

**Modelling Energy Loss Mechanisms  
and a Determination of the  
Electron Energy Scale for the CDF  
Run II  $W$  Mass Measurement**

**Thomas Riddick**

University College London

Submitted to University College London in fulfilment of the requirements for  
the award of the degree of Doctor of Philosophy 15<sup>th</sup> June, 2012.

# Declaration

I, Thomas Cameron Riddick confirm that the work presented in this thesis is my own. Where information has been derived from other sources, I confirm that this has been indicated in the thesis.

# Abstract

The calibration of the calorimeter energy scale is vital to measuring the mass of the  $W$  boson at CDF Run II. For the second measurement of the  $W$  boson mass at CDF Run II, two independent simulations were developed. This thesis presents a detailed description of the modification and validation of Bremsstrahlung and pair production modelling in one of these simulations, UCL Fast Simulation, comparing to both GEANT4 and real data where appropriate. The total systematic uncertainty on the measurement of the  $W$  boson mass in the  $W \rightarrow e\nu_e$  channel from residual inaccuracies in Bremsstrahlung modelling is estimated as  $6.2 \pm 3.2$  MeV/ $c^2$  and the total systematic uncertainty from residual inaccuracies in pair production modelling is estimated as  $2.8 \pm 2.7$  MeV/ $c^2$ . Two independent methods are used to calibrate the calorimeter energy scale in UCL Fast Simulation; the results of these two methods are compared to produce a measurement of the  $Z$  boson mass as a cross-check on the accuracy of the simulation.

# Summary of Contribution

The second CDF Run II  $W$  mass analysis is a complex measurement and the analysis itself is the work of a number of people at several institutions. This thesis focuses on my own contributions to this analysis, however necessarily utilises code written by others and in certain sections summarises the work of others. Two independent simulations are used for the  $W$  mass analysis; my work was on UCL Fast Simulation, which is used to cross-check important results.

My own work was to implement new models of Bremsstrahlung and pair production in UCL Fast Simulation and validate these models against GEANT4 using virtual test beam experiments (see Chapter 6). I also validated the modelling of Bremsstrahlung (and to a limited extent pair production) against available experimental data and tabulated theoretical results (also see Chapter 6). The results of my validations of Bremsstrahlung modelling against experimental data were used to improve the accuracy of the baseline analysis of CEM energy scale [1]. I implemented a two element model of the silicon tracker in UCL Fast Simulation (see Chapter 7). I estimated the systematic uncertainties on the  $W$  mass measurement due to residual mis-modelling of Bremsstrahlung and pair production in the silicon tracker and COT (see Chapter 8); some of these systematics were considered in the baseline analysis of the CEM energy scale [1]. I performed an independent measurement of the CEM energy scale for the  $W$  mass analysis using UCL Fast Simulation as a useful cross-check of the baseline analysis (see Chapter 9). The work on Bremsstrahlung and pair production presented in this thesis contributed to references [1, 2, 3, 4].

During my PhD I also assisted in the maintenance of the collaboration wide CDF Run II calibration database [5] for about a year and half (up till the end of CDF and Tevatron operations). The calibration database is a relational database containing tables of appropriate calibrations for the recorded electronic readout from the various components of the CDF Run II detector. Calibration runs, for example pulsing the calorimeter channels with laser light, were performed between Tevatron stores. This allowed changes in the required calibration of individual components over time, due to

the ageing of the detector and changing conditions, to be observed on a regular basis. New versions of each table were created when necessary to reflect these changes. The calibration in the CDF Run II calibration database were the main corrections applied to the data. (Some analysis, such as the  $W$  mass analysis applied further analysis specific corrections). I was responsible for associating the correct sets of calibration tables with newly recorded data as part of the CDF off-line data processing chain; this task was partly performed using automatic processing scripts I was responsible for monitoring and partly performed by running a number of scripts manually.

# Acknowledgements

I would like to thank all the people I have worked with on the  $W$  mass analysis: Dan Beecher, Emily Nurse, Mark Lancaster, Sarah Malik, Chris Hays, Ashutosh Kotwal, Bodhitha Jayatilaka, Derek Thompson and Oliver Stelzer-Chilton. I would like to thank in particular Ilija Bizjak and my supervisor David Waters for all the help they have given me. I would also like to thank my parents for their support.

# Contents

<b>1</b>	<b>The Standard Model of Particle Physics and Beyond</b>	<b>20</b>
1.1	The Standard Model as a Quantum Field Theory . . . . .	20
1.2	The Strong Interaction . . . . .	23
1.3	The Weak Interaction . . . . .	24
1.4	Electroweak Unification . . . . .	27
1.5	The Higgs Mechanism . . . . .	31
1.6	Physics Beyond The Standard Model . . . . .	33
<b>2</b>	<b>The Tevatron and CDF</b>	<b>37</b>
2.1	The Tevatron . . . . .	37
2.2	CDF . . . . .	39
2.2.1	Co-ordinate Systems . . . . .	41
2.2.2	Silicon Tracker . . . . .	43
2.2.3	Central Outer Tracker . . . . .	44
2.2.4	Central Calorimetry . . . . .	47
2.2.5	Muon Systems . . . . .	49
2.2.6	Forward Detectors . . . . .	51
2.2.7	Trigger . . . . .	51
2.2.8	Material Mapping . . . . .	54
<b>3</b>	<b><math>W</math> Mass Measurement</b>	<b>61</b>
3.1	Why Measure the $W$ Mass? . . . . .	61
3.2	Why Measure the $W$ Mass at CDF? . . . . .	63

<b>4</b>	<b>Overview of the Second CDF Run II <math>W</math> Mass Measurement</b>	<b>67</b>
4.1	Principles of Measuring the $W$ Mass at CDF Run II . . . . .	67
4.2	Template Fitting . . . . .	71
4.3	Event Selection . . . . .	72
4.3.1	Electron Selection . . . . .	73
4.3.2	$W$ and $Z$ Boson Selection . . . . .	75
4.4	Backgrounds . . . . .	77
4.5	Event Generation . . . . .	78
4.6	Detector Simulation . . . . .	80
4.6.1	Lepton and Photon Interactions . . . . .	81
4.6.2	Material Scale Determination . . . . .	85
4.6.3	Modelling Momentum Measurement . . . . .	86
4.6.4	Modelling of the Calorimeter . . . . .	88
4.6.5	Efficiencies . . . . .	88
4.7	Setting the Tracker Momentum Scale . . . . .	89
4.8	The Recoil Model . . . . .	90
<b>5</b>	<b>Theoretical Models of Bremsstrahlung and Pair Production</b>	<b>94</b>
5.1	Electron Bremsstrahlung . . . . .	94
5.1.1	Introduction . . . . .	94
5.1.2	Basic Model of Bremsstrahlung Differential Cross Section $y$ -Spectrum . . . . .	96
5.1.3	GEANT4 4.9.0 Model of the Bremsstrahlung Differential Cross Section $y$ -Spectrum . . . . .	97
5.1.4	GEANT4 4.9.2 Model of the Bremsstrahlung Differential Cross Section $y$ -Spectrum . . . . .	105
5.1.5	Bremsstrahlung Total Cross Section Models . . . . .	108
5.1.6	Differences Between Bremsstrahlung for Electrons and Positrons . . . . .	109
5.2	Pair Production . . . . .	110
5.2.1	Introduction . . . . .	110

5.2.2	Basic Model of the Pair Production Differential Cross Section $x$ -Spectrum . . . . .	111
5.2.3	GEANT4 Model of Pair Production Differential Cross Section $x$ -Spectrum . . . . .	112
5.2.4	Pair Production Total Cross Section Models . . . . .	116
<b>6</b>	<b>Monte Carlo Models of Bremsstrahlung and Pair Production</b>	<b>118</b>
6.1	Introduction . . . . .	118
6.2	The Modelling of Bremsstrahlung in the UCL Fast Simulation . . . . .	119
6.2.1	Strategy . . . . .	119
6.2.2	GEANT4 Virtual Test Beam Experiment . . . . .	120
6.2.3	UCL Fast Simulation Virtual Test Beam Experiment . . . . .	123
6.2.4	Bremsstrahlung GEANT4 4.9.0 Model $y$ -Spectrum Validation and Modification . . . . .	124
6.2.5	Bremsstrahlung GEANT4 4.9.0 Model Total Cross Section Validation and Modification . . . . .	132
6.2.6	Bremsstrahlung GEANT4 4.9.2 Model $y$ -Spectrum Validation and Modification . . . . .	136
6.2.7	Bremsstrahlung GEANT4 4.9.2 Model Total Cross Section Validation and Modification . . . . .	144
6.2.8	Summary . . . . .	147
6.3	Comparison of GEANT4 4.9.2 and GEANT4 4.9.0 Bremsstrahlung Models with Experimental Data . . . . .	147
6.3.1	Introduction . . . . .	147
6.3.2	Comparison in the Low- $y$ Region . . . . .	149
6.3.3	Comparison to Tabulated Theoretical Results in the High- $y$ Region . . . . .	158
6.3.4	Conclusion . . . . .	160
6.4	Modelling of Pair Production in UCL Fast Simulation . . . . .	162
6.4.1	Virtual Test Beam Experiments . . . . .	162

6.4.2	Pair Production $x$ -Spectrum Validation and Modification . . . . .	163
6.4.3	Pair Production Total Cross Section Validation and Modification	168
<b>7</b>	<b>Modelling the Composition of the CDF Run II Inner Detector</b>	<b>176</b>
7.1	Overview . . . . .	176
7.2	Simple Estimate of the Effect on the $W$ Mass Measurement . . . . .	178
7.3	Modelling the Composition of the Silicon Tracker using a Two Element Model . . . . .	178
7.4	Variants of the Two Element Model Implemented . . . . .	181
7.4.1	Cu/Be Model . . . . .	182
7.4.2	Si/Cu-Si/Be Model . . . . .	185
7.5	Modelling of Hybrid Layers in the Silicon Tracker . . . . .	186
<b>8</b>	<b>Bremsstrahlung and Pair Production Modelling Systematic Uncertainties on the <math>W</math> Mass Measurement</b>	<b>189</b>
8.1	Bremsstrahlung Modelling Systematic Uncertainties . . . . .	189
8.1.1	Half-LPM . . . . .	194
8.1.2	High- $y$ Re-weighted to GEANT4 4.9.0 $y$ -Spectrum . . . . .	196
8.1.3	High- $y$ Re-weighted to a $y$ -Spectrum that Approximates the EEDL Tabulated Theoretical Results . . . . .	197
8.1.4	Silicon Only . . . . .	201
8.1.5	Cu/Be Model . . . . .	201
8.2	Pair Production Modelling Systematic Uncertainties . . . . .	201
8.2.1	Basic Spectrum . . . . .	202
8.2.2	Pegged Total Cross Section . . . . .	203
8.3	Total Combined Systematic Uncertainty from Bremsstrahlung and Pair Production . . . . .	203
<b>9</b>	<b>Determination of the Electron CEM Energy Scale for the CDF Run II <math>W</math> Mass Measurement</b>	<b>205</b>
9.1	Overview of CEM Energy Scale Calibration . . . . .	205

9.2	CEM Energy Scale Analysis using UCL Fast Simulation . . . . .	210
9.3	Analysis using UCL Leakage, Coil Energy Loss and Non-Linearity Models	212
9.3.1	Tower-by-Tower Energy Scale and $\kappa$ Fits . . . . .	212
9.3.2	Material Scale Fits . . . . .	213
9.3.3	Separate $W \rightarrow e^+\nu$ and $W \rightarrow e^-\nu$ CEM Energy Scale Fits . . . . .	216
9.3.4	UCL Particle-by-Particle Calorimeter Non-Linearity . . . . .	217
9.3.5	CEM Energy Scale Results . . . . .	220
9.4	Analysis using Duke Leakage, Coil Energy Loss and Non-Linearity Models	225
9.4.1	Duke Particle-by-Particle Calorimeter Non-Linearity with a Log-arithmic Form . . . . .	225
9.4.2	Duke Leakage and Coil Energy Loss Model . . . . .	226
9.4.3	Tower-by-Tower Energy Scale and $\kappa$ Fits . . . . .	228
9.4.4	CEM Energy Scale Results . . . . .	229
9.5	Final CEM Energy Scale Calibration Results . . . . .	234
9.6	Possible Causes of the Inconsistent $Z$ Mass Measurement . . . . .	235
<b>10</b>	<b>Conclusions and <math>W</math> Mass Measurement Results</b>	<b>240</b>
10.1	Conclusions . . . . .	240
10.2	$W$ Mass Measurement Results . . . . .	242
	<b>Appendix A The CDF Run II Electromagnetic Clustering Algorithm</b>	<b>250</b>
	<b>Appendix B Non Iterative Method for the Evaluation of LPM and Di-electric Variables</b>	<b>252</b>
	<b>Appendix C Details of the Pair Production Sampling and Rejection Procedure</b>	<b>255</b>
	<b>Bibliography</b>	<b>257</b>

# List of Figures

1.1	Divergent $W$ boson Feynman diagrams . . . . .	27
1.2	Divergences cancelled by the $Z$ boson . . . . .	28
2.1	Run II store peak luminosities . . . . .	40
2.2	Schematic of CDF Run II . . . . .	42
2.3	Three COT supercells . . . . .	45
2.4	1/6 section of one of the COT endplates . . . . .	46
2.5	Positioning of muon scintillator counters . . . . .	50
2.6	The trigger system and data flow . . . . .	52
2.7	Conversion maps of the CDF Run II silicon tracker . . . . .	58
2.8	Distribution of photon conversions as a function of radius $r$ for the region $-45 < z < -15$ cm . . . . .	59
2.9	Distribution of photon conversions as a function of radius $r$ for the region $ z  < 15$ cm . . . . .	59
2.10	Distribution of photon conversions as a function of radius $r$ for the region $15 < z < 45$ cm . . . . .	60
3.1	The one-loop radiative $W$ mass correction from top and bottom quarks .	62
3.2	The one-loop radiative $W$ mass corrections from the Higgs boson . . . . .	62
3.3	The one-loop radiative $W$ mass corrections from squarks . . . . .	63
3.4	$m_W$ and $m_t$ constraints on the SM Higgs mass . . . . .	64
3.5	Existing $W$ mass measurements . . . . .	66
4.1	$W$ and $Z$ boson production diagrams . . . . .	68

4.2	Contributions to electron energy loss . . . . .	83
4.3	Contributions to photon energy loss . . . . .	84
4.4	Examples of $\Delta\rho$ distributions . . . . .	87
4.5	Comparison of recoil components in data and simulation . . . . .	92
5.1	Dominant Bremsstrahlung Feynman diagram . . . . .	95
5.2	Dominant pair production diagrams . . . . .	111
5.3	Limits on the pair production $x$ -range . . . . .	115
6.1	Virtual test beam setup . . . . .	121
6.2	Comparison of GEANT4 4.9.0 to a basic theory $y$ -spectra . . . . .	122
6.3	Ratio of the UCL Fast Simulation Basic Version $y$ -spectrum to theory .	125
6.4	Ratio of the UCL Fast Simulation Basic Version $y$ -spectrum to theory neglecting multiple Bremsstrahlung . . . . .	126
6.5	Comparison of the GEANT4 4.9.0, UCL Fast Simulation Basic Version and theory $y$ -spectra . . . . .	127
6.6	Ratio of the GEANT4 4.9.0 and UCL Fast Simulation Basic Version $y$ - spectra to theory . . . . .	128
6.7	Ratio of the GEANT4 4.9.0 and UCL Fast Simulation Bremsstrahlung Modification A $y$ -spectra to theory . . . . .	129
6.8	Ratio of GEANT4 4.9.0 and UCL Fast Simulation Bremsstrahlung Modi- fication A $y$ -spectra to theory . . . . .	130
6.9	Comparison of the GEANT4 4.9.0, UCL Fast Simulation Bremsstrahlung Modification B and theory $y$ -spectra . . . . .	132
6.10	Ratio of GEANT4 4.9.0 and UCL Fast Simulation Bremsstrahlung Modi- fication B $y$ -spectra to theory . . . . .	133
6.11	Absolute number of Bremsstrahlung events plotted against $y$ for GEANT4 4.9.0 and the final version of UCL Fast Simulation Modification B . . .	134
6.12	Tuning of the UCL Fast Simulation Bremsstrahlung Modification B total cross section as a function of incident electron energy . . . . .	135

6.13 Comparison of the UCL Fast Simulation Basic Version, GEANT4 4.9.2 Bremsstrahlung and theory $y$ -spectra . . . . .	137
6.14 Ratio of GEANT4 4.9.2 and UCL Fast Simulation Basic Version Brem- sstrahlung $y$ -spectra to theory . . . . .	138
6.15 Comparison of the GEANT4 4.9.2, UCL Fast Simulation Bremsstrahlung Modification C $y$ -spectra and theory . . . . .	140
6.16 Ratio of GEANT4 4.9.2 and UCL Fast Simulation Bremsstrahlung Modi- fication C $y$ -spectra to theory . . . . .	141
6.17 Ratio of GEANT4 4.9.2 pseudo-data to UCL Fast Simulation Bremsstrah- lung Modification C pseudo-data $y$ -spectra . . . . .	141
6.18 Comparison of the GEANT4 4.9.2, UCL Fast Simulation Bremsstrahlung Modification C $y$ -spectra and theory for 5 GeV electrons . . . . .	142
6.19 Ratio of GEANT4 4.9.2 and UCL Fast Simulation Bremsstrahlung Modi- fication C $y$ -spectra to theory for 5 GeV electrons . . . . .	143
6.20 Ratio of GEANT4 4.9.2 pseudo-data to UCL Fast Simulation Bremsstrah- lung Modification C pseudo-data $y$ -spectra for 5 GeV electrons . . . . .	143
6.21 Comparison of the GEANT4 4.9.2 and GEANT4 4.9.0 $y$ -distributions . . .	150
6.22 Comparison of Bremsstrahlung $k$ -spectra experimental data from three experiments performed at SLAC . . . . .	153
6.23 Comparison of the Bremsstrahlung $k$ -spectrum in GEANT4 pseudo-data and SLAC data for 25 GeV electrons incident on 6% $X_0$ of carbon . . .	154
6.24 Ratio of the GEANT4 pseudo-data to the SLAC data Bremsstrahlung $k$ -spectrum for 25 GeV electrons incident on 6% $X_0$ of carbon . . . . .	155
6.25 Comparison of the Bremsstrahlung $k$ -spectrum in GEANT4 pseudo-data and SLAC data for 25 GeV electrons incident on 2% $X_0$ of carbon . . .	156
6.26 Ratio of the GEANT4 pseudo-data to the SLAC data Bremsstrahlung $k$ -spectrum for 25 GeV electrons incident on 2% $X_0$ of carbon . . . . .	157
6.27 Ratio of the EEDL and theoretical GEANT4 4.9.0 $y$ -spectra to the theo- retical GEANT4 4.9.2 $y$ -spectra . . . . .	161

6.28	Comparison of the UCL Fast Simulation and theory pair production $x$ -spectra . . . . .	163
6.29	Comparison of the the UCL Fast Simulation, GEANT4 and theory pair production $x$ -spectra . . . . .	165
6.30	Ratio of GEANT4 and UCL Fast Simulation pair production $x$ -spectra to theory . . . . .	166
6.31	Comparison of the the UCL Fast Simulation, GEANT4 and theory pair production $x$ -spectra at 100 MeV . . . . .	167
6.32	Ratio of GEANT4 and UCL Fast Simulation pair production $x$ -spectra to theory at 100 MeV . . . . .	168
6.33	Comparison of the UCL Fast Simulation Pair Production Modification A, GEANT4 and theory pair production $x$ -spectra . . . . .	169
6.34	Comparison of the UCL Fast Simulation Pair Production Modification A, GEANT4 and theory pair production $x$ -spectra at 100 MeV . . . . .	170
6.35	Ratio of GEANT4 and UCL Fast Simulation Pair Production Modification A $x$ -spectra to theory . . . . .	171
6.36	Ratio of GEANT4 and UCL Fast Simulation Pair Production Modification A $x$ -spectra to theory at 100 MeV . . . . .	171
6.37	Ratio of the GEANT4 to UCL Fast Simulation Pair Production Modification A total cross section . . . . .	173
6.38	Comparison of the GEANT4, NIST data, UCL Fast Simulation Pair Production Modification A total cross sections . . . . .	174
6.39	Ratio of the GEANT4 to UCL Fast Simulation Pair Production Modification B total cross section . . . . .	175
7.1	Comparison of energy weighted Bremsstrahlung $y$ -spectra for beryllium, silicon and copper . . . . .	177
7.2	Comparison of GEANT4 4.9.2, UCL Fast Simulation Bremsstrahlung Modification C $y$ -spectra and theory for copper . . . . .	183
7.3	Logic of the Si/Cu-Si/Be Model . . . . .	185

8.1	Ratios of the EEDL and theoretical GEANT4 4.9.0 $y$ -spectra to the theoretical GEANT4 4.9.2 $y$ -spectra for several different energies . . . . .	199
9.1	Comparison of the best fitting template to data for the $W \rightarrow e\nu$ $E/p$ CEM energy scale fit using the UCL leakage, coil energy loss and non-linearity models . . . . .	208
9.2	Comparison of the best fitting template to data for the $Z \rightarrow e^+e^-$ mass CEM energy scale fit using the UCL leakage, coil energy loss and non-linearity models . . . . .	209
9.3	Comparison of the best fitting template to data for the material scale fit	214
9.4	Comparison of the best fitting template to data for the material scale fit using $Z$ events . . . . .	215
9.5	The particle-by-particle non-linearity best fit simulation pseudo-data and data $E/p$ distributions of individual $E_T$ slices for $W$ events . . . . .	221
9.6	The particle-by-particle non-linearity best fit simulation pseudo-data and data $E/p$ distributions of individual $E_T$ slices for $Z$ events . . . . .	222
9.7	Mean $E/p$ of each $E_T$ slice plotted against slice $E_T$ as a particle-by-particle non-linearity fit control distribution . . . . .	223
9.8	Ratio of the mean $E/p$ of each $E_T$ slice for simulation pseudo-data to that for data plotted against slice $E_T$ as a particle-by-particle non-linearity fit control distribution . . . . .	224
9.9	Comparison of the best fitting template to data for an $W \rightarrow e\nu$ $E/p$ CEM energy scale fit using the Duke leakage, coil energy loss and non-linearity models . . . . .	230
9.10	Comparison of the best fitting template to data for an $Z \rightarrow e^+e^-$ $E/p$ CEM energy scale fit using the Duke leakage, coil energy loss and non-linearity models . . . . .	232
9.11	Comparison of the best fitting template to data for a $Z \rightarrow e^+e^-$ mass CEM energy scale fit using the Duke leakage, coil energy loss and non-linearity models . . . . .	233

10.1	Comparisons of the best fitting templates to data for $m_W$ fits using the transverse mass distribution . . . . .	244
10.2	Comparisons of the best fitting templates to data for $m_W$ fits using the lepton transverse momentum distribution . . . . .	245
10.3	Comparisons of the best fitting templates to data for $m_W$ fits using the reconstructed neutrino transverse momentum distribution . . . . .	246
10.4	$m_W$ and $m_t$ constraints on the SM Higgs mass including the new CDF Run II $W$ mass measurement . . . . .	249

# List of Tables

1.1	The quark and lepton doublets . . . . .	22
1.2	The gauge bosons . . . . .	22
1.3	Fermion weak isospin and weak hypercharge . . . . .	31
2.1	Pseudo-rapidity coverage of the silicon tracker . . . . .	43
2.2	Pseudo-rapidity coverage of the muon systems . . . . .	50
2.3	Radial thickness of the various components of the CDF Run II detector . . . . .	55
4.1	The tight electron cut set . . . . .	75
4.2	The $W$ and $Z$ cut sets . . . . .	77
5.1	Bremsstrahlung differential cross section formulae properties . . . . .	99
6.1	Parameters of the total cross section retuning in UCL Fast Simulation Bremsstrahlung Modification B . . . . .	135
6.2	Parameters of the total cross section retuning in UCL Fast Simulation Bremsstrahlung Modification C . . . . .	146
6.3	Summary of the different versions of UCL Fast Simulation . . . . .	148
7.1	Geometric criteria for application of the Au/Be Model . . . . .	187
8.1	Formulae used to calculate uncertainties on $m_W$ shifts due the statistical uncertainties on the various retuned parameters . . . . .	191
8.2	Final retuned CEM energy scales and $\kappa$ 's for Bremsstrahlung systematics . . . . .	193
8.3	Final retuned material scales for Bremsstrahlung systematics . . . . .	193
8.4	Final Bremsstrahlung systematic uncertainties on the $m_W$ . . . . .	194

8.5	Final retuned CEM energy scales and $\kappa$ 's for pair production systematics	202
8.6	Final retuned material scales for pair production systematics . . . . .	202
8.7	Final pair production systematic uncertainties on the $m_W$ . . . . .	203
9.1	Tower-by-tower $W \rightarrow e\nu$ $E/p$ CEM energy scale and CEM $\kappa$ fit results .	213
9.2	Tower-by-tower $W \rightarrow e\nu$ $E/p$ CEM energy scale and CEM $\kappa$ fit results using the Duke leakage, coil energy loss and non-linearity models . . . .	229
10.1	Fitted $m_W$ values for the second CDF Run II $W$ mass measurement . .	243
10.2	Electron channel systematic uncertainties on $m_W$ . . . . .	247
10.3	Combined electron and muon channel uncertainties on $m_W$ . . . . .	247

# Chapter 1

## The Standard Model of Particle Physics and Beyond

### 1.1 The Standard Model as a Quantum Field Theory

The Standard Model of Particle Physics [6] is a highly successful model of the dynamics of elementary particles.

The basis of this model is Quantum Field Theory (QFT) [7]. Historically the idea of quantisation was first applied to particles to produce Quantum Mechanics. However when Quantum Mechanics is combined with special relativity you find the number of particles within any system is no longer conserved because of the possibility of the creation of particle-antiparticle pairs. This makes finding a relativistic quantum theory based on equations for one or any other fixed number of particles impossible. In QFT the idea of quantisation is applied to classical fields, particles then occur as partially localised excitations of the quantum field. Any QFT can accommodate any number of particles, hence it is possible to construct QFTs that are fully consistent with relativity. QFTs can be characterised by a Lagrangian density  $\mathcal{L}$ , usually referred to simply as a Lagrangian. It is possible to choose a Lagrangian such that the field quantises to produce particles named fermions which obey Fermi-Dirac statistics and have half-integral spin or such that it quantises to produce particles named bosons which obey Bose-Einstein statistics and have integral spin. Multiple QFTs may be linked together by interaction

terms within a joint Lagrangian describing them.

Using QFTs it is possible to calculate the quantum amplitude (hence the cross section) for the basic local interactions, i.e. the scattering, creation/annihilation and decay of particles. A simple way to represent such interactions is using Feynman diagrams. Furthermore it is possible to derive Feynman rules to calculate the quantum amplitude for a given Feynman diagram. These rules associate with each vertex and line in the diagram a mathematical term to be added to the scattering amplitude. The overall scattering amplitude for a process can hypothetically be found by summing all the possible Feynman diagrams for that process. Unfortunately if you don't restrict the number of vertices the number of Feynman diagrams for a process will be infinite. Fortunately the greater the number of vertices in a diagram the less it contributes to the total scattering amplitude<sup>1</sup>. Thus amplitudes are always calculated including only diagrams with a given number of vertices or less.

The Standard Model (SM) comprises a set of fermionic fields and a set of bosonic gauge fields. A further bosonic field is added as part of the Higgs Mechanism. The fermionic fields quantise to produce three doublets (sometimes known as families) of particles called leptons and three doublets of particles called quarks. These quark and lepton doublets are shown in table 1.1. Each lepton doublet consists of a massive lepton with unit negative electric charge (an electron, muon or tau) and an electrically neutral neutrino (an electron/muon/tau neutrino). While in the SM all neutrinos are assumed to be massless, extensions to the SM can accommodate neutrino masses. Each quark doublet consists of two massive quarks with electric charges of  $\frac{2}{3}e$  and  $-\frac{1}{3}e$ . The different kinds of quark are referred to as different flavours. All atomic matter is constructed from the up and down quark (the constituents of both the proton and neutron) from the first quark doublet and the electron from the first leptonic doublet; while a range of other composite particles are constructed from various combinations of quarks and/or antiquarks. Composite particles constructed from quarks are called hadrons.

---

<sup>1</sup>For some diagrams infinite amplitudes may be calculated initially, however these infinities will disappear after renormalisation. There are also exceptions in some QFTs where the contribution of diagrams to the total scattering amplitude does *not* decrease as the number of vertices increases; these exceptions can be treated using non-perturbative techniques.

$$\overline{\begin{pmatrix} u \\ d \end{pmatrix}} \quad \overline{\begin{pmatrix} c \\ s \end{pmatrix}} \quad \overline{\begin{pmatrix} t \\ b \end{pmatrix}} \qquad \overline{\begin{pmatrix} \nu_e \\ e^- \end{pmatrix}} \quad \overline{\begin{pmatrix} \nu_\mu \\ \mu^- \end{pmatrix}} \quad \overline{\begin{pmatrix} \nu_\tau \\ \tau^- \end{pmatrix}}$$

(a) (b)

Table 1.1: The quark doublets (a) and lepton doublets (b).

Gauge boson	Symbol	Interaction
Photon	$\gamma$	Electromagnetic
Gluon	$g$	Strong
$W$ boson	$W^-/W^+$	Weak
$Z$ boson	$Z^0$	Weak

Table 1.2: The gauge bosons and the interactions they correspond to.

The bosonic fields quantise to produce particles called gauge bosons (and also the Higgs boson). Interactions between the fermionic fields occur through terms in the SM Lagrangian that couple one or two of the fermionic fields to the bosonic fields. Such interactions are often thought of in terms of the exchange of gauge bosons by fermions. The gauge bosons are listed in table 1.2. The starting point for the SM was the theory of Quantum Electrodynamics (QED), a QFT which successfully describes the electromagnetic interaction as the exchange of photons by electrons. An analogous theory of the strong interaction was later discovered called Quantum Chromodynamics (QCD), in which quarks (and thus composite particles constructed from quarks) interact via the exchange of gluons. Meanwhile electroweak unification extended the ideas of QED to describe the now combined electromagnetic and weak interactions as the exchange of photons,  $W$  bosons and  $Z$  bosons by fermions. All of these theories are gauge theories, this means they are invariant under the local transformations of a certain characteristic gauge group and hence have additional non-physical degrees of freedom corresponding to a choice of gauge. The gauge group of QED is  $U(1)$ , while for QCD it is  $SU(3)$  and for the electroweak interaction it is  $SU(2)_L \times U(1)_Y$ . Thus the full gauge group of the SM is  $SU(3) \times SU(2)_L \times U(1)_Y$ .

The development of the SM has variously been both driven by and directed experimental particle physics research. For example the ‘zoo’ of particles discovered in the 1950’s and 60’s led to the development of the quark model, while results like the discov-

ery of parity violation in 1957 and the discovery of CP violation in 1964 led theorists to formulate the electroweak model. These developments then made many predictions such as the existence of the charm, bottom and top quarks; neutral weak currents; and the  $W$  and  $Z$  bosons which experimentalist devoted much effort to confirming. At the time of writing the only particle from the SM that remains to be discovered is the Higgs boson. The SM is not in itself a complete theory of nature. It has a number of failings, that is to say its success is limited to its realm of applicability. Gravity is not included in the SM and attempts to extend the SM to include a gravitational exchange boson (the hypothetical graviton) break down when detailed calculations are attempted. The SM as it was originally proposed assumed the neutrino to be massless; this has since been contradicted by experimental evidence. However, unlike gravity, neutrino masses (and neutrino oscillations) can be incorporated into the SM.

## 1.2 The Strong Interaction

QCD [8], the theory of the strong interaction, is a non-abelian gauge field theory based around the symmetry group  $SU(3)$ . In the QCD Lagrangian quark fields are coupled to a set of eight gluon gauge fields. Each quark carries a colour charge (colour charges are unrelated to the quarks' electromagnetic charge) of either blue, green or red, while each antiquark carries anti-blue, anti-red or anti-green. Gluons carry both a colour and anti-colour charge and each colour/anti-colour is conserved at interaction vertices within Feynman diagrams. As gluons themselves carry colour charge they can self-interact through gluon-only vertices. An important result of this self-coupling is the energy required to separate two quarks increases proportional to their separation. Qualitatively this is because as the quarks separate the gluons they exchange attract each other to form a tube of gluons which requires energy to extend. Thus quarks are only observed in composite particles with overall wavefunctions that are colour neutral through the correct superposition of states which individually have an overall colour charge.

### 1.3 The Weak Interaction

QED describes the electromagnetic interactions of all three charged leptons and all six quarks with photons. It is in itself a very experimentally successful theory predicting for example the anomalous magnetic moment of the electron to an accuracy of 1 part in  $10^8$ . However QED can be generalised to include the weak interaction thus forming electroweak gauge theory.

The weak interaction started out as a point-like four-fermion coupling proposed by Fermi to explain nuclear  $\beta$ -decay. However it later became clear that it was not point-like, but instead merely very short ranged. This short range arises because the exchange particles of the weak force, the  $W^+$ ,  $W^-$  and  $Z^0$  bosons<sup>2</sup>, are all relatively massive. This constrains the range over which a virtual weak boson exchange can take place. Their high mass also means high energies are needed to produce real weak bosons. This is in contrast with the exchange particle of the electromagnetic force, the photon, which is long ranged and readily produced.

The weak interaction can, like the strong and electromagnetic interactions, be described using QFT (though a weak QFT in isolation would not be renormalisable thus electroweak unification is required). The weak exchange bosons can interact with both quarks and leptons (and also with other weak exchange bosons).  $W$  boson vertices (charged current (CC) vertices) in Feynman diagrams either involve a coupling between a charged lepton and its associated neutrino or between two quarks of different flavour. The coupling constant of leptonic CC interactions is universal, the same for all three lepton families. Changes of lepton family at a vertex are forbidden. (In extensions to the SM that include massive neutrinos, changes of lepton family can occur through neutrino mixing as neutrinos propagate through space. However even in such extensions, changes in lepton family *at a weak interaction vertex* remain forbidden.)

For quarks the situation is more complex. The quark eigenstates of the weak interaction are not the same as the mass eigenstates, instead three weak doublets are

---

<sup>2</sup>The  $W^+$  and  $W^-$  are antiparticles of each other, and hence often are referred to generically as the  $W$  boson. The superscript is often also dropped from the  $Z^0$  and thus it is often referred to as just the  $Z$  boson.

formed by unitary transformations among the quark doublets. This is parameterised in the CKM matrix. Once the quark mass eigenstates have been rotated into the quark weak eigenstates, CC interactions involve couplings only between quarks within a weak quark doublet and the strength of the interaction is the same as that for leptons.

A parity inversion is a transformation of a system into its mirror image; mathematically that means reversing the sign of all the spatial (cartesian) co-ordinates used to describe the system. Both the strong and electromagnetic interactions are invariant under parity inversions, this means all results for a given process are the same for the parity inversion of that process. Charge conjugation is transforming a system by swapping all particles in the system for their antiparticle and visa-versa. Both the strong and electromagnetic interactions are also invariant under charge conjugation. Experimental evidence shows the weak interaction is not invariant under parity inversion or charge conjugation. Furthermore for interactions involving quarks it's not even invariant under the combined action of charge conjugation followed by parity inversion (referred to as CP).

Individually parity inversion and charge conjugation invariance violation can be accounted for by the form of the weak interaction term in the SM Lagrangian. Acting on the quantum field of a massless fermion with the chirality operator (an operator which extracts the chirality of a particle, for a massless particle this is equivalent to the projection of the particle's spin along its direction of motion<sup>3</sup>) results in the field being split into a right-handed chiral component and a left-handed chiral component. The quantum field of a massive fermion can also be split into a right-handed chiral component and a left-handed chiral component in this way with the exception of a mass term which couples the right- and left- handed chiral components of the field. In the SM Lagrangian there are no interaction terms for  $W$  bosons to interact with the right-handed component of fermionic fields. Thus CC interactions only involve the left-handed component of fermionic fields.

Parity inversion does not affect the spin of a fermion but switches the direction of

---

<sup>3</sup>A general definition of chirality uses the Poincaré symmetry group and is not given here. It is sufficient for the purpose of this discussion to simply view chirality as a mathematical property of quantum fields.

its momentum and hence its chirality. Thus after a parity inversion is applied to a CC weak process we find the component that used to be the left-handed component is now right-handed and hence does not interact, while the component that used to be the right-handed component is now left-handed and hence does interact. As the left-handed and right-handed components of a fermionic quantum field are not generally the same the process has changed under parity inversion.

In the SM Lagrangian there are only  $W$  boson interaction terms for right-handed fermion antiparticles. The charge conjugation operator does not change the chirality of a particle. Thus if we apply charge conjugation to a weak process we find the left-handed particles become left-handed antiparticles and thus no longer interact, and the opposite is true for right-handed particles. So the process has changed under charge conjugation.

However if we apply both charge conjugation and then parity inversion to a weak process left-handed particles become right-handed antiparticles while right-handed particles become left-handed antiparticles and so forth. The interactions of a left-handed particle are identical to those of a right-handed antiparticle. Thus the weak interaction is invariant under the action of charge conjugation followed by parity inversion for interactions involving leptons and would be so for quarks too were it not for a further complication due to the arbitrary phase that can be introduced to the CKM matrix which allows for CP violation.

$Z$  boson vertices (neutral current (NC) vertices) cannot change quark flavour (nor can they change between lepton families), instead they can perform all the same interactions as photons, and in addition can form neutrino scattering and creation/annihilation vertices. The SM Lagrangian has interaction terms for  $Z$  bosons with both right-handed and left-handed fermionic fields. However the coupling strength (a constant in the mathematical expression associated with a vertex in Feynman rules) is different for right-handed and left-handed NC interaction vertices. Also there are no NC interactions for right-handed neutrinos. This is all explained very neatly by electroweak unification. As the neutrino is uncharged and in the SM assumed to be massless, there are no interactions for right-handed neutrinos in the SM and in fact right-handed neutrinos are

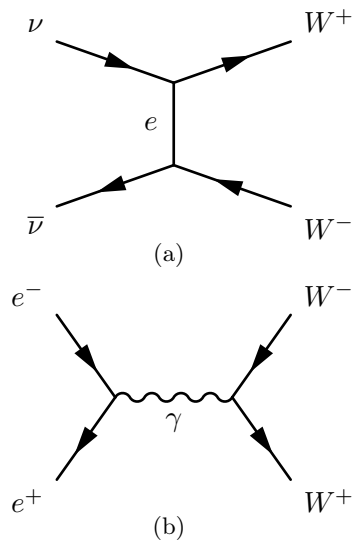


Figure 1.1: Divergent Feynman diagrams after the introduction of the  $W$  boson.

assumed not to exist within the SM. Right-handed neutrinos have never been observed in nature.

## 1.4 Electroweak Unification

The early point-like theories of the weak interaction suffered from divergences at high energies, causing violations of unitarity (transition probabilities greater than one, clearly unphysical). These were solved by introducing the  $W$  boson, however this then generated new divergences, some in diagrams with all weak vertices, some in diagrams with a mixture of weak and electromagnetic processes (see fig. 1.1 for examples of these). These could themselves be solved by introducing a neutral weak boson, the  $Z$  boson, which then added additional Feynman diagrams that cancelled out these divergences (see fig. 1.2). In order for cancellations to occur between diagrams with both weak and electromagnetic vertices (such as fig. 1.1(b)) and those with purely weak vertices (such as fig. 1.2(b)) the electromagnetic coupling constant  $e$ , must be roughly equal to the weak coupling constant  $g$ . This then predicts the mass of the  $W$  and  $Z$  bosons to be of the order of  $100 \text{ GeV}/c^2$ .

This parity between the weak and electromagnetic coupling constants led to the possibility of the unification of the two interactions. Glashow, Weinberg, Salam and

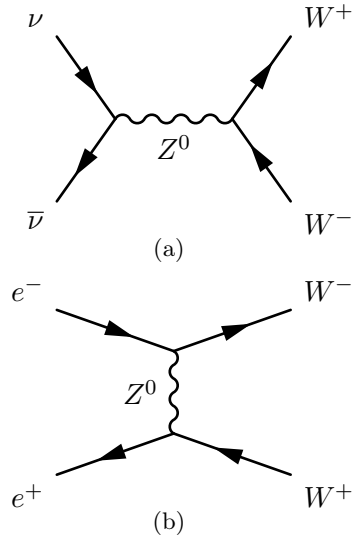


Figure 1.2: Diagrams that cancel divergences after the introduction of the  $Z$  boson. Technically speaking diagram (b) only completely cancels the divergences in the process  $e^+e^- \rightarrow W^+W^-$  if we neglect electron mass. Without this simplification some residual divergences will remain, these can be cancelled by the introduction of the Higgs boson (see section 1.5).

Ward achieved such an electroweak unification in the late 1960's [9, 10, 11] by first introducing four electroweak quantum gauge fields,  $\mathbf{W}_\mu \equiv W_\mu^{(1)}, W_\mu^{(2)}, W_\mu^{(3)}$  and  $B_\mu$  (where the subscript index  $\mu$  specifies the components of a space-time vector, these are all vector fields). Then by taking appropriate linear combinations of these fields they recovered the photon and three massless weak bosons (the  $W^\pm$  bosons and  $Z$  boson). Finally they restored the mass of the weak bosons (and the fermions) using the Higgs mechanism.

The electromagnetic interaction term in a QED Lagrangian can be written as:

$$\mathcal{L} = eJ_\mu^{\text{em}}A_\mu \quad (1.1)$$

where  $A_\mu$  is the electromagnetic field (sometimes referred to as the electromagnetic four-potential) interacting with an electromagnetic current  $J_\mu^{\text{em}}$  at an electromagnetic interaction vertex. The coupling constant is the charge of the electron  $e$ . In electroweak unification the electromagnetic current is replaced by two new currents, namely a weak isospin current and a weak hypercharge current.

Weak isospin  $I$ , is associated with the symmetry  $SU(2)$ . It is named weak isospin

in analogy to normal isospin which is also associated with this symmetry, otherwise the two isospins are unrelated. The irreducible representation of  $SU(2)$  for  $I = 1$  is a triplet of states labelled by the third component of weak isospin  $I_3 = \{1, 0, -1\}$ . We assign a weak isospin  $I = 1$  to the three fields  $\mathbf{W}_\mu$ , giving each a different  $I_3$ . We assign a weak isospin  $I = 0$  (which is represented by a singlet state) to  $B_\mu$ .

Weak hypercharge  $Y$ , is associated with the symmetry  $U(1)$ . It is defined as:<sup>4</sup>

$$Y \equiv Q - I_3 \tag{1.2}$$

where  $Q$  is the (electromagnetic) charge. The full symmetry of the electroweak interaction is the product of the symmetry of weak hypercharge and weak isospin, namely  $SU(2)_L \times U(1)_Y$  as noted previously.

So the electroweak interaction term in the SM Lagrangian can be written:

$$\mathcal{L} = g\mathbf{J}_\mu \cdot \mathbf{W}_\mu + g' J_\mu^Y B_\mu \tag{1.3}$$

where  $\mathbf{J}_\mu$  is the weak isospin current and  $J_\mu^Y$  is the weak hypercharge current.  $g$  and  $g'$  are two non-identical coupling constants. From the definition of weak hypercharge we can trivially derive:

$$J_\mu^Y = J_\mu^{\text{em}} - J_\mu^{(3)} \tag{1.4}$$

where  $J_\mu^{(3)}$  is the third component of weak isospin. We recover the  $W$  boson (the  $W_\mu^\pm$  fields) by taking superpositions of  $W_\mu^{(1)}$  and  $W_\mu^{(2)}$ :

$$W_\mu^\pm = \frac{1}{\sqrt{2}} \left[ W_\mu^{(1)} \pm W_\mu^{(2)} \right] \tag{1.5}$$

$W_\mu^{(3)}$  and  $B_\mu$  are linear combinations of the  $Z$  boson (the  $Z_\mu$  field) and the photon (the

---

<sup>4</sup>It is sometimes defined with an additional factor of 2 to give  $Y \equiv 2(Q - I_3)$  like strong hypercharge, however this convention has not been adopted here.

$A_\mu$  field):

$$W_\mu^{(3)} = \frac{gZ_\mu + g'A_\mu}{\sqrt{g^2 + g'^2}} \quad (1.6)$$

$$B_\mu = \frac{-g'Z_\mu + gA_\mu}{\sqrt{g^2 + g'^2}} \quad (1.7)$$

Defining:

$$J_\mu^\pm \equiv J_\mu^{(1)} \pm iJ_\mu^{(2)} \quad (1.8)$$

and introducing the Weinberg angle  $\theta_W$  (also referred to as the weak mixing angle) to parameterise the relative strength of the coupling constants:

$$\frac{g'}{g} \equiv \tan \theta_W, \quad (1.9)$$

we can use eqs. (1.4) to (1.7) to rewrite eq. (1.3) as

$$\mathcal{L} = \frac{g}{\sqrt{2}}(J_\mu^- W_\mu^+ + J_\mu^+ W_\mu^-) + \frac{g}{\cos \theta_W}(J_\mu^{(3)} - \sin^2 \theta_W J_\mu^{\text{em}})Z_\mu + g \sin \theta_W J_\mu^{\text{em}} A_\mu \quad (1.10)$$

We can identify the first term in this Lagrangian as the weak CC interaction, the second term as the weak NC interaction and the third term as the electromagnetic interaction. We can infer that the electromagnetic coupling constant  $e = g \sin \theta_W$ . Thus we have unified the electromagnetic and weak forces. However it still remains to introduce a mass to the weak bosons using the Higgs mechanism, this will be discussed in section 1.5.

In order to ensure only left-handed particles can interact via weak CC interactions we assign all right-handed fermions to weak isospin singlets ( $I = 0$  states). The right-handed neutrino is not included in the SM, but if it were then it would have both  $I = 0$  and  $Y = 0$  hence not undergo any interactions.

The irreducible representation of  $SU(2)$  for  $I = 1/2$  is a doublet of states labelled by the third component of weak isospin  $I_3 = \{1/2, -1/2\}$ . We assign the left-handed electron and left-handed neutrino to this  $I = 1/2$  doublet giving the electron  $I_3 = -1/2$  and the neutrino  $I_3 = 1/2$ . Note both will have the same weak hypercharge  $Y = -1/2$ .

Similarly we assign the left-handed  $u$  quark and the left-handed CKM rotated  $d'$

Fermion	$Q$	$I$	$I_3$	$Y$
$\nu_e, \nu_\mu, \nu_\tau$	0	1/2	+1/2	-1/2
$e_L^-, \mu_L^-, \tau_L^-$	-1	1/2	-1/2	-1/2
$e_R^-, \mu_R^-, \tau_R^-$	-1	0	0	-1
$u_L, c_L, t_L$	+2/3	1/2	+1/2	+1/6
$d_L', s_L', b_L'$	-1/3	1/2	-1/2	+1/6
$u_R, c_R, t_R$	+2/3	0	0	+2/3
$d_R', s_R', b_R'$	-1/3	0	0	-1/3

Table 1.3: The electromagnetic charge, weak isospin and weak hypercharge values of the various fermions. Fermions are given a subscript L or R to indicate if they are left- or right-handed. As there are no right-handed neutrinos in the SM the L subscript is omitted for the (left-handed) neutrinos.

quark (you only need to rotate one quark in each doublet to achieve the correct electroweak quark eigenstates) to an  $I = 1/2$  doublet giving the  $u$  quark  $I_3 = +1/2$  and the  $d'$  quark  $I_3 = -1/2$ ; again they will both have the same weak hypercharge  $Y = +1/6$ . We assign the right-handed  $u$  and  $d'$  quark to weak isospin singlets with  $I = 0$ ; thus they will have  $Y = +2/3$  and  $Y = -1/3$  respectively.

The same assignments of  $I$ ,  $I_3$  and  $Y$  are made for the other two families in both the cases of quarks and of leptons. The weak isospin and weak hypercharge of all the fermions is summarised in table 1.3. As noted previously this electroweak unification neatly explains the chirality dependent coupling strength of weak NC interactions; the left-handed component couples to weak isospin currents while both the left- and the right-handed components couple to electromagnetic currents.

## 1.5 The Higgs Mechanism

The electroweak model presented in the previous section predicts massless weak gauge bosons. This is not what is observed in nature. Unfortunately it is not possible to add in mass terms to the Lagrangian for the  $\mathbf{W}_\mu$  and  $B_\mu$  fields directly as such terms are not gauge invariant. Gauge is a non-physical degree of freedom in the description of the system; so gauge invariance must be maintained to ensure our results are not dependent on our choice of gauge. Actually we have a further problem, as mentioned before mass terms for fermionic fields couple the left- and right- handed components

of the field. But in electroweak theory we have given different values of weak isospin and weak hypercharge to the left- and right- handed components of the field, thus if we couple them the weak isospin and hypercharge current we have introduced will not be conserved. This too would constitute a violation of gauge invariance.

The Higgs mechanism [12, 13] is an ingenious way to add mass terms for both fermions and weak gauge bosons to the SM Lagrangian while preserving gauge invariance. Often in nature a dynamical system with degenerate ground states may have a certain symmetry. However the ground states themselves may not have this symmetry. In this case when we arbitrarily make a choice of ground state we may hide the symmetry; the system itself still has the symmetry but the system plus the choice of ground state does not. The ground state of a QFT is the vacuum and it is very important as QFTs essentially rely on making perturbative expansions around the vacuum. Normally QFTs choose a vacuum expectation value (VEV) that is zero and thus can be quantised perturbatively using their original Lagrangian. The idea of the Higgs mechanism is to introduce a new quantum field with a degenerate vacuum that has a non-zero VEV. The original Lagrangian of this quantum field will be gauge invariant, however in order to make perturbative expansions we need to arbitrarily choose a particular vacuum state thus hiding the gauge symmetry of the Lagrangian. We redefine the Lagrangian in order to perturbatively expand around our chosen vacuum. This redefined Lagrangian is not manifestly gauge invariant because it describes not only the dynamics of the quantum field itself but the gauge symmetry violating choice of vacuum. We say the symmetry has been spontaneously broken, however this terminology is somewhat misleading, the symmetry has actually been hidden not broken. If we let the new quantum field couple to the fermionic and electroweak bosonic gauge fields the process of redefining the Lagrangian generates new mass terms for these fields not present in the original gauge invariant Lagrangian. This is the Higgs mechanism, in the context of the SM we want to hide the symmetry  $SU(2)_L \times U(1)_Y$ . The Higgs vacuum states do have the symmetry  $U(1)_Q$  which is the symmetry associated with QED, thus allowing the photon to remain massless.

An extremely important result of the Higgs mechanism is that by introducing a

Higgs quantum field it predicts the existence of the Higgs boson. The Higgs boson was already mentioned in the context of fig. 1.2 as cancelling residual divergences in the process  $e^+e^- \rightarrow W^+W^-$  that remain after the introduction of the  $Z$  boson. The Higgs boson is the only particle predicted by the SM that has still not been discovered [14]. The mass of the Higgs boson is not directly predicted within the SM; it is a free parameter of the theory. However it can be constrained indirectly from experimental measurement of other SM parameters; this is discussed in section 3.1. Experimental searches at LEP have ruled out Higgs masses less than  $114.4 \text{ GeV}/c^2$ . In recent years both the Tevatron and the LHC have been racing to find a Higgs more massive than this. The good performance of the LHC last year (and the end of Tevatron operations last September) make it look increasingly likely that the Higgs will actually be discovered by the LHC within the next few years; it is possible the first hints of the Higgs existence have already been observed there. (Possible hints have also been observed at the Tevatron.) Of course the Higgs boson may simply not exist, if this is the case then considerable reformulation of the SM will be needed; there are potential replacements for the Higgs mechanism such as  $W$  substructure.

## 1.6 Physics Beyond The Standard Model

The SM constitutes a *nearly* complete model of the dynamics of elementary particles which agrees with *almost* all known experimental results. Thus two reasons to look for physics beyond the SM are to attempt to find an absolutely complete model of elementary particle dynamics and to find modifications to the SM to cover its experimental failings. With about 20 free parameters and lots of seemingly ad-hoc features (for example fractional quark charges) the SM is a rather inelegant model, so a third reason to look for physics beyond the SM is to attempt to find the underlying reasons for the form of the SM and the values of its free parameters. Particle physics has an important role to play in cosmology and so a fourth reason to look for physics beyond the standard model is to help to solve outstanding cosmological problems. This fourth possibility is not considered further in this thesis.

The SM is incomplete because it does not include gravity. Attempts to formulate a gravitational quantum field theory (quantum gravity) with the hypothetical graviton as its exchange particle are not renormalisable and suffer high energy divergences. These divergences are linked to the point-like nature of particles. One possible candidate for a theory that can incorporate both QFT and gravity is superstring theory [15, 16]. In string theory particles are replaced by strings and hence the high energy divergences that plague quantum gravity disappear. Unfortunately string theory is both at present theoretically incomplete and extremely difficult to test experimentally because of its extremely high natural energy scale of  $\sim 10^{19}$  GeV.

The SM assumption that neutrinos are massless appears to be incorrect; this is at present the only known major disagreement between the SM and experimental observation. (Neglecting recent evidence suggesting that neutrinos may be able to travel faster than light; this being as yet unconfirmed and possibly due merely to an unaccounted for systematic uncertainty on the measurement.) There is now extremely strong evidence from solar, atmospheric, reactor and accelerator neutrino experiments for neutrino oscillations caused by non-zero neutrino mass [14]. It is proposed that the neutrino interaction eigenstates are not the same as the neutrino mass eigenstates. Rotated neutrino interaction eigenstates can be formed from superpositions of the mass eigenstates using the Pontecorvo-Maki-Nakagawa-Sakata (PMNS) mixing matrix, which is somewhat akin to the CKM mixing matrix from the quark sector. Almost all neutrino oscillation data to date can be accounted for by this simple mixing mechanism. Extending the SM to include neutrino mixing and mass adds a further seven free parameters. As neutrinos are electrically neutral it is possible they are Majorana fermions (i.e. fermions that are their own antiparticle) instead of the normal Dirac fermions; insufficient experimental data exists at present to determine if this is the case.

Given the success of electroweak unification it is natural to ask if we can go further and find a theory that unifies the strong interaction with the electroweak interaction. Theories that achieve this are called grand unified theories (GUTs). The starting point of a GUT is to find an appropriate symmetry group that can incorporate the existing  $SU(3)$  and  $SU(2)_L \times U(1)_Y$  SM symmetry groups. An early candidate for this unifying

symmetry was  $SU(5)$  [17], though this particular example has now largely been excluded by experimental upper limits on the rate of (as yet unobserved) proton decay. The great advantage of GUTs is they may show ad-hoc features of the SM to actually be manifestations of this new symmetry. For example GUTs can explain the fractional charge of quarks and the similarity between lepton and quark doublets, both of which must simply be accepted as quirks of nature in the SM itself. GUTs must only be manifest at very high energies otherwise they would have been detected already. We can estimate from the running of coupling constants (the change of coupling constants with energy, this being a consequence of renormalisation) that the typical unification energy for a GUT might be of order  $10^{16}$  GeV.

One major problem with GUTs, and in fact any new physics that is manifest at extremely high energies, is the hierarchy problem. The mass of the Higgs boson is adjusted by radiative corrections associated with virtual particle loops where the Higgs emits and subsequently reabsorbs some other particle. Introducing new theories manifest at very high energy scales causes these radiative corrections to become extremely large which will cause the Higgs mass to become divergent. A solution to this is to find a mechanism by which such radiative corrections can be cancelled out by a second radiative correction of the opposite sign. Supersymmetry (SUSY) [18], a symmetry between fermions and bosons, can achieve such a cancellation. SUSY proposes that each particle have a SUSY partner, for a boson this will be an otherwise identical fermion, for a fermion this will be an otherwise identical boson. This symmetry must then be spontaneously broken somehow to allow SUSY partners to have different masses from their counterparts (if they had the same masses as their regular particle counterparts they would presumably have been detected already). However even after symmetry breaking SUSY particles would still have the same couplings as their regular particle counterparts. Bosonic loops give radiative corrections of the opposite sign to fermionic loops, hence each particle and its SUSY partner would give radiative corrections to the Higgs mass that would cancel out. So SUSY would ‘protect’ the mass of the Higgs upon the introduction of GUTs that are manifest at very high energy scales. Most SUSY theories assume that SUSY particles would be produced in association (i.e. in particle-antiparticle pairs) and

would then seek to decay to the lightest possible SUSY particle. The simplest possible SUSY model consistent with the SM is the minimal supersymmetric extension of the Standard Model (known as the Minimal Supersymmetric Standard Model).

## Chapter 2

# The Tevatron and CDF

### 2.1 The Tevatron

Situated in the outer suburbs of Chicago, Illinois at the Fermi National Accelerator Laboratory (Fermilab), the Tevatron [19, 20] was a superconducting magnet synchrotron that collided protons with antiprotons. It remains the second highest energy particle collider built to date, having been superseded by the LHC at CERN. Collisions were first observed at the Tevatron on October 13th 1985, and it was permanently shut down on September 30th 2011. The Tevatron's operations are commonly divided into three distinct periods: Run 0, Run I and Run II, between which occurred major shut downs to allow major upgrades to the accelerator and the detectors. In Run II the beam energy was 980 GeV, thus producing collisions with a centre of mass energy just under 2 TeV.

Two general purpose detectors were situated at the Tevatron, CDF and DØ. In 1995 CDF and DØ finally discovered the long predicted top quark [21, 22]. They also found evidence for  $D^0$ - $\bar{D}^0$  oscillations; single-top,  $WZ$  and  $ZZ$  production; observed  $B_s$  oscillations and discovered the  $\Sigma_b$  [23], amongst many other things.

For data taking at the CDF and DØ detectors the Tevatron was setup in a steady state known as a 'store'. In this state two counter rotating beams (one of protons, one of antiprotons) circled the Tevatron continuously with a constant energy of 980 GeV per beam, colliding at interaction points in the centre of the CDF and DØ detectors. Each beam comprised of 36 distinct bunches of particles and at each interaction point there

was a bunch crossing every 396 ns. A series of superconducting NbTi electromagnets (each cryogenically cooled to 4.6 K) constrained the beam to its circular path, while further superconducting magnets focused the beam. A set of 8 RF (Radio Frequency) cavities applied an oscillating electric field to accelerate the particles in each bunch as they passed through with each successive turn. This compensated for any loss of energy from synchrotron radiation; the RF cavities were also used at the start of the store to ramp up the energy of the beam.

The initial setup of a store required the use of a chain of smaller accelerators to generate particles with an energy and degree of collimation sufficient for injection into the Tevatron itself. The beginning of the process was the generation of  $H^-$  ions by the Pre-accelerator, these being hydrogen atoms with an extra electron. The  $H^-$  ions were passed to the Linear Accelerator which then accelerated them to 400 MeV using RF cavities. The 400 MeV hydrogen ions were then passed to a synchrotron called the Booster, which removed the electrons from the  $H^-$  to produce protons and accelerated these to 8 GeV. From the Booster the protons were passed to the Main Injector, a larger synchrotron which further accelerated them to 120 GeV for antiproton production or 150 GeV for injection into the Tevatron. Both the Booster and the Main Injector used a combination of RF cavities for acceleration and magnets to constrain the beam in a similar fashion to the Tevatron itself.

Antiprotons were produced by striking a nickel alloy target with 120 GeV protons from the Main Injector to produce a spray of particles from which 8 GeV antiprotons were selected using magnets. These were then directed to the Debuncher and Accumulator, a pair of rounded triangle shaped synchrotrons (which shared the same tunnel) designed to capture and cool the antiprotons coming from the target without further accelerating them. The antiprotons were then transferred to the Recycler (the name of which relates to a long abandoned plan to recycle antiprotons from the Tevatron), which was a storage ring that shared a tunnel with the Main Injector, for further cooling using beams of electrons to absorb the excess heat (spread of momenta) from the antiproton beam. They were then ‘stashed’ in the Recycler until they were needed. The rate at which antiprotons were generated was rather slow, and if the stash was depleted then it

would take several hours before sufficient antiprotons could be stashed to setup a new store. During the setup of a new store first the protons were created and injected into the Tevatron via the Main Injector, then the stash of antiprotons was transferred to the Main Injector where they were accelerated to 150 GeV for injection into the Tevatron. Once both protons and antiprotons were circulating in the Tevatron at 150 GeV then both beams were accelerated by the RF cavities to 980 GeV. Simultaneous to this the power of the Tevatron's electromagnets was ramped up to maintain the orbit of the increasingly energetic beams. The orbits of the protons and antiprotons within the accelerator fractionally differed to prevent collisions under normal circumstances. When acceleration was complete and any stray particles had been removed using collimators the beams were deliberately brought together at the two interaction points.

Once collisions had been initiated data was recorded at CDF and DØ continuously for the duration of the store (unless technical issues occurred). No further particles were added during the store, so the luminosity of the beams fell as particles were lost through collisions or imperfect confinement of the beam. As the rate of data taking for many processes of interest was proportional to the luminosity, once sufficient antiprotons had been stashed the store was usually terminated (by dumping the beams) and a new store setup. During my own shifts on CDF in late 2010 the average length of store when the Tevatron was running smoothly was about 16 hours with a typical initial luminosity of  $\sim 350 \times 10^{30} \text{cm}^{-2} \text{sec}^{-1}$ . Figure 2.1 is a plot of the peak luminosity of each store in Run II. The total integrated luminosity collected at CDF Run II was  $\approx 10 \text{fb}^{-1}$ .

## 2.2 CDF

CDF (Collider Detector at Fermilab) [24, 25] was the older of the two detectors on the Tevatron. It was a multi-component detector designed to track, identify and determine the energy and momentum of particles produced in high energy proton-antiproton collisions at its centre. CDF studied a wide range of high energy physics phenomena ranging from making precision electroweak measurements to searches for evidence of supersymmetry. However the experimental signatures that needed to be detected and measured

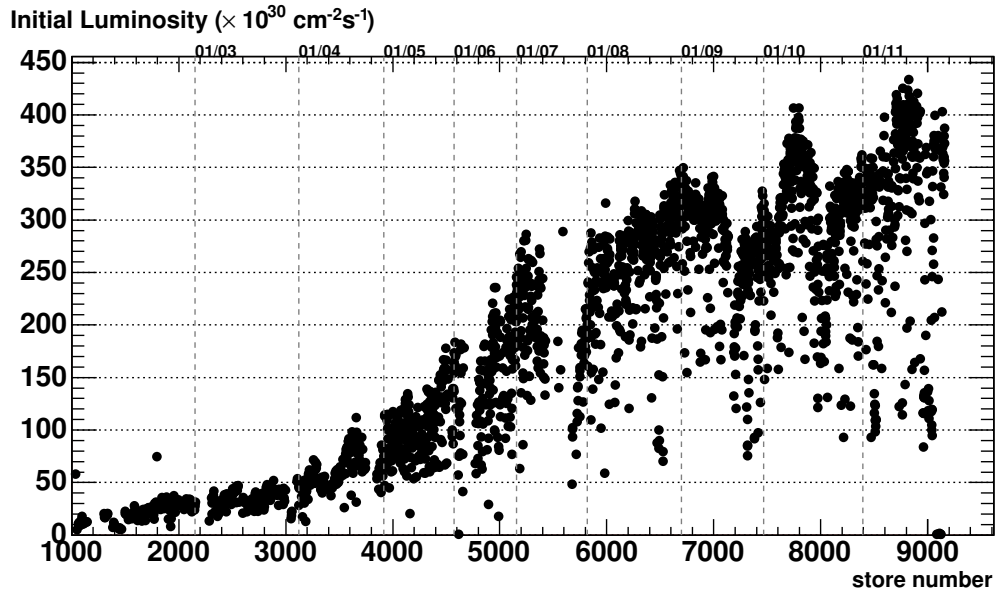


Figure 2.1: Store peak luminosity for Tevatron Run II. The dotted vertical lines indicate the store number reached at the start of each year; the labels along the upper edge of the graph give the date represented by each line in the format month/year.

almost always consisted of tracking a few basic kinds of particle. Electrons will both leave a track in a tracking detector, that combined with a magnetic field allows their momentum to be measured and deposit all their energy in a calorimeter, allowing their energy to be measured. Muons will also leave a track in a tracking detector but will pass through a calorimeter only depositing minimal energy. As they are the only charged particle which is so penetrating it is possible to identify muons by placing further tracking detectors on the far side of the calorimeter. Photons will not be visible in a tracker however will deposit all their energy in a calorimeter. Charged hadrons will produce a track and deposit all their energy in a calorimeter, however they can be distinguished from an electron because they will penetrate much further into the calorimeter. Neutral hadrons will produce a signal similar to that of a photon except that neutral hadrons will penetrate further into the calorimeter. Hadronic physics signatures will not usually consist of a single particle but a spray of many low energy particles (both hadrons and more rarely photons or leptons) created by secondary QCD interactions (in a process called ‘hadronisation’) occurring very close to the interaction point almost immediately after the initial interaction. These sprays of particles may leave multiple tracks and

then deposit a large amount of energy in the calorimeter and are commonly referred to as jets. Neutrinos will not leave any track or energy in the detector but their presence can be inferred from missing transverse energy.

The CDF detector was upgraded between Run I and Run II, the upgraded detector being known as CDF Run II or CDF II; the description given in this thesis relates to the CDF Run II detector. The entire CDF detector was built around the Tevatron beam pipe; at its centre was the B0 interaction point. The central section consisted of various components arranged in concentric cylindrical layers. Moving outward the components were a silicon tracker (which was actually sub divided further into three separate components: Layer 00, SVX II and ISL), an open cell drift chamber referred to as the Central Outer Tracker (COT), a Time of Flight Detector (TOF), the solenoid coil that produced the magnetic field for the inner detector (i.e. the silicon tracker and COT), an electromagnetic calorimeter referred to as the Central Electromagnetic Calorimeter (CEM), a hadronic calorimeter (which was actually divided further into two components: the central CHA and the forward ‘wall’ WHA), and finally various muon detectors. The detector was capped at either end by plug calorimeters to cover the forward regions with layers arranged perpendicular to the beam pipe; the muon systems also extended into the forward regions. A schematic of the CDF Run II detector is presented in fig. 2.2.

### 2.2.1 Co-ordinate Systems

Two co-ordinate systems are commonly used to describe the CDF detector. Both take the centre of the detector, the B0 interaction point, as their origin. Cartesian co-ordinates take the plane perpendicular to the beam pipe as the  $x$ - $y$  plane (this plane is known as the transverse plane), with  $x$  pointing in the direction outwards from the Tevatron ring (north) and  $y$  pointing upwards. The  $z$ -axis lays along the beam pipe, with the positive  $z$ -direction being the direction of the proton beam (east). The other co-ordinate system commonly used describes positions within the plane perpendicular to the beam pipe using the radius  $r$  from the centre of the detector *within that plane* and the azimuthal angle  $\phi$ .  $z$ -position is described using pseudo-rapidity  $\eta$ , defined

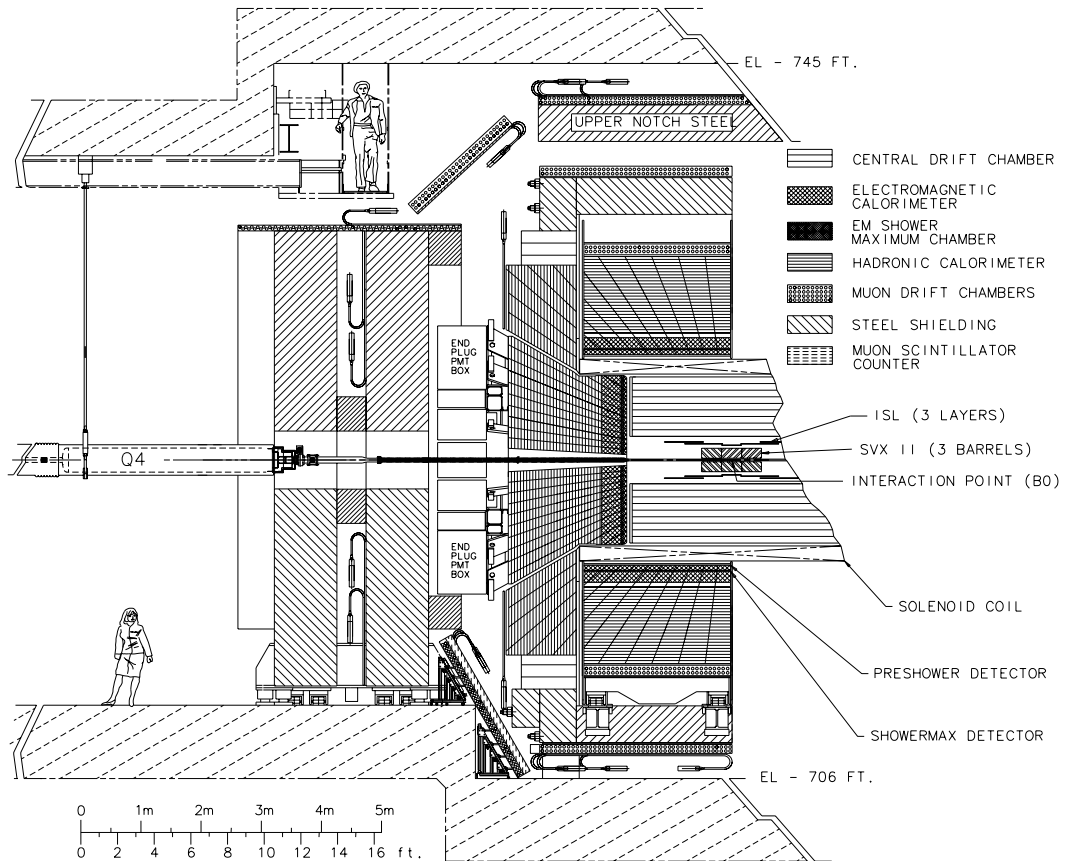


Figure 2.2: 'Elevation view' schematic of CDF Run II detector. See main text for further details.

Detector	Pseudo-Rapidity Coverage
L00	$ \eta  \leq 4$
SVX II	$ \eta  \leq 2$
ISL	$ \eta  \leq 2$

Table 2.1: Pseudo-rapidity coverage of the silicon tracker at CDF Run II

as  $\eta = -\ln(\tan(\theta/2))$  where  $\theta$  is the polar angle measured from the  $z$ -axis. Pseudo-rapidity is the same as rapidity in the limit of zero mass (or equivalently infinite energy) yet is itself defined without any reference to the kinematics of a particular event, hence it is a useful third co-ordinate to use.

### 2.2.2 Silicon Tracker

The CDF Run II silicon tracker [26] was designed to study the displaced secondary vertices characteristic of the decay of heavy quarks. Resolving such displaced secondary vertices required very high accuracy position measurements and this degree of positional accuracy could not be achieved using the COT. The CDF Run II silicon tracker was designed to achieve an accuracy of less than  $20 \mu\text{m}$  for tracks with energies above 2 GeV and therefore be able to provide excellent resolution of displaced vertices. Because of this the silicon tracker had an important role in the study of top physics, B physics and searches for both supersymmetry and the Higgs boson.

The silicon tracker consisted of three separate components. The innermost component was Layer 00 (L00), a single sensor layer which was affixed to the outside of the beam pipe at a radius of 1.3 cm. The SVX II consisted of 5 sensor layers between the radii of 2.5 cm and 10.6 cm. The Intermediate Silicon Layers (ISL) consisted of further layers at the radii of 20.2 cm and 29.1 cm. L00 could determine the position of hits to within  $\sim 11$  microns, while for the SVX this figure was  $\sim 9$  microns. The pseudo-rapidity coverage of the tracker is presented in table 2.1.

The information from the silicon tracker is not used in the  $W$  mass measurement. However the correct simulation of the passage of particles through the tracker's physical structure is important to the measurement.

### 2.2.3 Central Outer Tracker

The CDF Run II COT [27] was a large cylindrical drift chamber immersed in a 1.4 T magnetic field, used to track charged particles and determine their momentum by measuring the curvature of the track.

Drift chambers are a variant design of Multi-Wire Proportional Chamber (MWPC). A MWPC is a gas-filled chamber strung with rows of anode wires (also known as sense wires). Between the rows of wires are thin cathode plates (also known as field plates). A potential difference is maintained between the anode wires and the cathode plates. A passing charged particle may ionise the gas, producing an electron and a positive ion. The electron will be accelerated by the electric field towards the nearest anode wire. If the electron gains sufficient kinetic energy it may generate secondary ionisations, which may themselves generate secondary ionisations and so on; hence leading to a cascade of electrons. The cascade of electrons will be detected as a small electric current in the anode wire. The potential difference between the anode and cathode wires is chosen such that the charge reaching the anode is proportional to the number of primary ion-electron pairs created, hence the name proportional chamber. The positive ion will be accelerated towards the nearest cathode plate and if sufficiently energetic will similarly lead to cascades of positive ions.

A drift chamber is a variant of MWPC where the drift time of the electron is used to estimate the position of the initial ionisation between the anode wires and thus the position of the track of the passing particle. Additional field shaping wires are added between the anode wires to maintain a uniform drift field. The strength of the drift field is low, however in a region very close to the anode wires a much higher strength field is generated. Thus the primary electron drifts much of the distance to the anode without causing any further ionisation, however once it gets very close to the anode an avalanche occurs to create a detectable current.

The COT had 30,420 gold-plated tungsten sense wires, arranged in 96 concentric sense wire layers. The layers were themselves grouped into eight concentric ‘superlayers’. The superlayers alternated between ‘axial’ superlayers in which the wires ran exactly

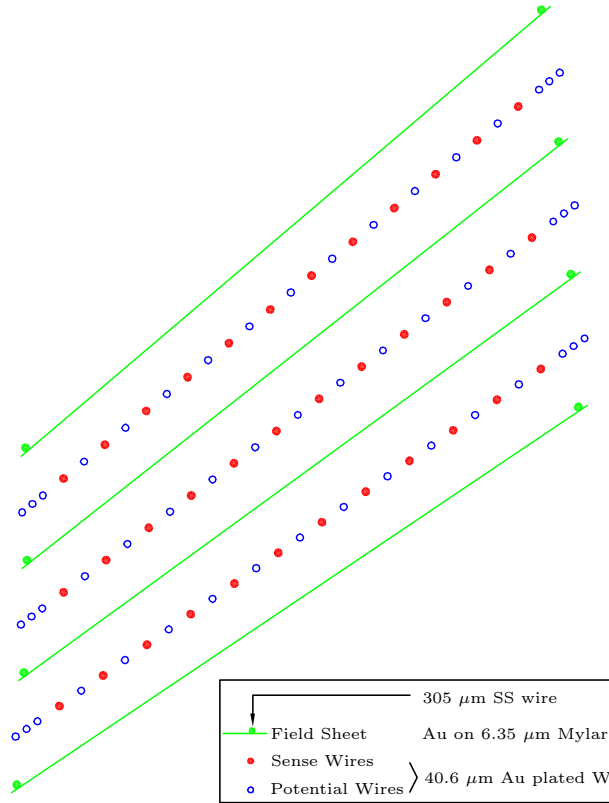


Figure 2.3: Position within the transverse plane (i.e. looking along  $z$  direction) of sense wires, potential wires and field sheets for three supercells in superlayer 2.

parallel to the  $z$  axis and ‘stereo’ superlayers in which the wires were offset from the  $z$  axis by  $2^\circ$ . This allowed for the reconstruction of tracks in the  $z$  plane in addition to the  $r$ - $\phi$  plane. Between each sense wire layer was a layer of field shaping wires (referred to as potential wires), also made from gold-plated tungsten. In each superlayer a plane of 12 sense wires from different layers (and the potential wires between them) offset by  $35^\circ$  from the radial direction constituted a ‘supercell’. A field sheet consisting of a sheet of Mylar with gold vapour deposited on both sides separated adjacent supercells. Figure 2.3 shows the layout of three supercells in superlayer 2 while fig. 2.4 illustrates the arrangement of supercells and superlayers in the  $r$ - $\phi$  plane. The COT was initially filled with a near 50:50 mixture of argon and ethane gas with trace of isopropyl. A small quantity of oxygen was later added to this to reduce the slow degradation of the COT due to polymer build-up on the wires. The COT covered  $|\eta| \lesssim 1$ .

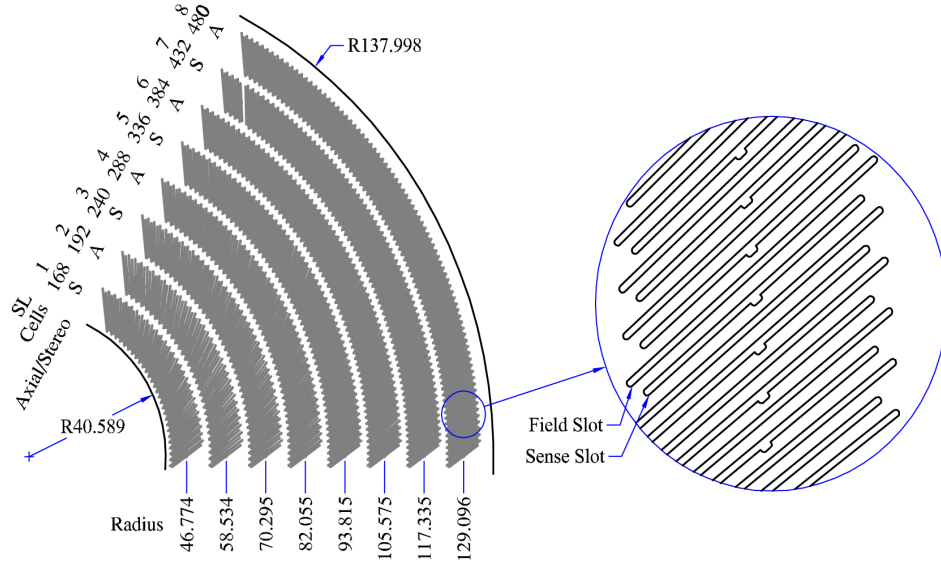


Figure 2.4: 1/6 section of one of the COT endplates illustrating the arrangement of superlayers and supercells. Distances given in cm. A field sheet was positioned along the precision machined edge of each field slot and a plane of sense wires was positioned along the precision machined edge of each sense slot.

If the maximum drift time (the maximum amount of time an electron took to reach the nearest anode) in the COT was greater than the time between bunch crossings it would be possible for new initial ionisations to occur while the electrons from the previous event were still in transit, hence confusing the readout considerably. A simple way to avoid this problem was to ensure the COT had a maximum drift time less than the bunch spacing of 396 ns. The COT design was such that the maximum distance an electron could drift was 0.88 cm, which for the mixture of gases used gave a maximum drift time of 177 ns. The strength of the drift field was 1.9 kV/cm, while the strength of the field on the surface of the sense wires was  $\sim 180$  kV/cm. The typical size of an avalanche resultant from an initial electron-ion pair was  $\sim 2 \times 10^4$  electrons.

The COT could measure the position of hits (primary ionisations) from a passing particle to within  $\sim 140$  microns. The magnetic field in the COT bent the tracks of particles traversing it. From the Lorentz equation (and the mechanics of circular

motion) the curvature of a track can be related to its transverse momentum:

$$\mathbf{F} = q(\mathbf{E} + (\mathbf{v} \times \mathbf{B})) \quad (2.1)$$

$$\frac{mv^2}{R} = |q|vB \quad (2.2)$$

$$p_T = |q|BR \quad (2.3)$$

where  $q$  is the charge of the particle,  $\mathbf{B}$  the magnetic field strength and  $R$  the radius of curvature in the  $r$ - $\phi$  plane. The momentum resolution achieved by the COT alone was  $\frac{\sigma(p_T)}{p_T} = 0.15\% \times p_T$  [GeV/c] $^{-1}$ , while if the COT was combined with the SVX and ISL the resolution improved to  $\frac{\sigma(p_T)}{p_T} = 0.07\% \times p_T$  [GeV/c] $^{-1}$ . Where applicable the COT momentum measurement could be improved by constraining the track to originate from the beam spot. The beam constrained COT only momentum resolution was  $\frac{\sigma(p_T)}{p_T} = 0.05\% \times p_T$  [GeV/c] $^{-1}$ .

The time-of-flight detector (TOF) was positioned between the COT and the solenoid magnet. It was designed to accurately measure the time of incidence of particles and hence determine their velocity. It is not used in the  $W$  mass measurement, though it is included in the model of the composition of the detector outside of the COT.

## 2.2.4 Central Calorimetry

CDF Run II utilised calorimeters [28] to measure the energy and position of particles exiting the COT (and potentially very forward particles that had escaped the  $\eta$  coverage of the COT).

The central calorimeter of CDF Run II was divided into two separate barrels by the  $z = 0$  plane. Each barrel had ten projective towers, each of which roughly covered  $\Delta\eta \approx 0.11$  and was also split azimuthally into 24 wedges each subtending an angle of 0.26 radians. Overall the central calorimeter covered  $|\eta| < 1.1$ . Radially the inner section of the central calorimeter was the CEM [29], designed to measure the energy and position of electromagnetic showers, while the outer section comprised of the CHA and WHA [30], which were designed to measure hadronic showers.

A calorimeter's basic function is to make a destructive measurement of a parti-

cle's energy as the particle loses most or all of its energy through interacting with the calorimeter to create a shower or cascade of daughter particles. The entire calorimeter can be designed to detect the cascade (a homogenous calorimeter) or the cascade can be sampled by active detector layers sandwiched by passive layers of absorber (a heterogeneous or sampling calorimeter). Electromagnetic cascades occur when a photon or electron is incident on a calorimeter. In an electromagnetic cascade successive pair production and Bremsstrahlung interactions occur, increasing the number of particles in the cascade and reducing the energy of the individual particles. This will continue until the particles' energies are reduced below some critical energy. Below this critical energy the energy of the particles will be dissipated by ionisation and excitation without generating any further particles. A hadronic cascade is more complicated with a range of charged and neutral hadrons being produced by various inelastic scattering mechanisms. Some secondary particles, especially the  $\pi^0$ , decay immediately into two photons which then form electromagnetic cascades. Unlike in an electromagnetic cascade where almost all of the energy is finally dissipated through detectable ionisation, in a hadronic cascade roughly 30 % of the energy dissipates through undetectable mechanisms. Hadronic cascades develop over greater distances than electromagnetic cascades, it is hence common for the first section of a calorimeter to be primarily designed to measure electromagnetic cascades (though still able to measure the initial stages of hadronic cascades too) and the second section to be designed to measure hadronic cascades.

A common choice for the active detector component of calorimeters are scintillators. Scintillators are materials that emit light (scintillate) when their atoms are excited by ionisation occurring within them; this scintillation is then recorded using photomultiplier tubes.

The CEM was a sampling calorimeter comprised of alternate radial layers of scintillator (31 layers) and lead-aluminium plates (30 layers). At a distance of about six radiation lengths into the CEM from the inner wall (including the width of the solenoid) a set of strip and wire chambers made a determination of the position (to a precision of 2 mm at 50 GeV) and transverse width of electromagnetic cascades based on charge deposited on the strips and wires. The distance from the inner wall was chosen such

that the strip and wire chambers were positioned at the point where an electromagnetic cascade was expected to deposit the most energy. These strip and wire chambers were called the central electromagnetic shower maximum detector (CES). The CEM energy resolution was  $\sigma(E)/E = 13.5\%/\sqrt{E \sin(\theta)}$  (GeV) + 2%.

The CHA consisted of 32 layers of steel interleaved with 32 layers of scintillator and covered  $|\eta| < 0.6$ . The energy resolution of the CHA was  $\sigma(E)/E = 0.5/\sqrt{E}$  (GeV). The WHA extended the central hadronic calorimeter beyond the edge of the central barrel of the detector (necessary if the central hadronic calorimeter was to have roughly the same angular coverage as other central detector components) to cover the region  $0.6 < |\eta| < 1.1$  and consisted of 15 layers of steel interleaved with 15 layers of scintillator.

### 2.2.5 Muon Systems

CDF Run II identified and tracked muons outside the COT and calorimeters using a combination of drift chambers and scintillator detectors. The drift chambers tracked the muons while the scintillator detectors provided precise timing information so the muon tracks could be associated with the correct bunch crossing. The central muon systems [31, 32] consisted of the central muon detector (CMU), a proportional drift chamber directly outside the CHA; the central muon upgrade (CMP), also a proportional drift chamber, which covered the same solid angle as the CMU but was separated from it by a 60 cm thick layer of steel<sup>1</sup>; the central scintillator upgrade counters (CSP), which were attached to the outside of the CMP; the central muon extension drift chambers (CMX), placed outside the steel detector support structure at either end of the central barrel of the detector and the central muon extension scintillator counters (CSX), placed on the inner and outer wall of the CMX. The pseudo rapidity coverage of both the central and forward muon detectors is summarised in table 2.2. The positioning of the various forward and central muon scintillator counters is shown in fig. 2.5.

---

<sup>1</sup>The shielding that separated the CMP from the CMU allowed the small fraction of pions that escaped the central calorimeter and faked muon tracks in the CMU to be correctly identified.

Detector	Type	Pseudo-Rapidity Coverage
<i>Central</i>		
CMU	Drift Chambers	$ \eta  \lesssim 0.6$
CMP	Drift Chambers	$ \eta  \lesssim 0.6$
CSP	Scintillator Counters	$ \eta  \lesssim 0.6$
CMX	Drift Chambers	$0.6 \lesssim  \eta  \lesssim 1$
CSX	Scintillator Counters	$0.6 \lesssim  \eta  \lesssim 1$
<i>Forward</i>		
IMU	Drift Chambers and Scintillator Counters	$1.0 \lesssim  \eta  \lesssim 1.5$

Table 2.2: Pseudo-rapidity coverage of the various muon systems at CDF Run II.

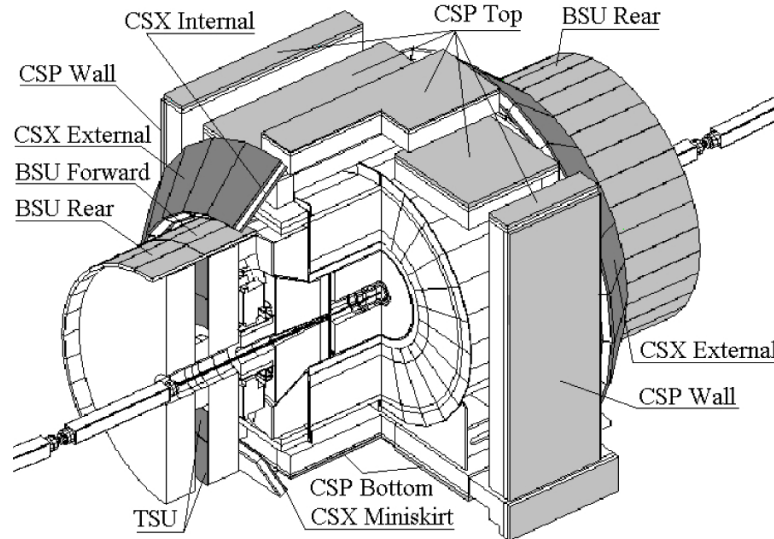


Figure 2.5: Positioning of central and forward muon scintillator counters at CDF Run II.

### 2.2.6 Forward Detectors

The CDF Run II forward detectors consisted of the plug electromagnetic calorimeter (PEM), the plug hadronic calorimeter (PHA), Cherenkov luminosity counters (CLC), the barrel muon chambers (BMU), the barrel scintillator upgrade (BSU) and the toriod scintillator upgrade (TSU). The BMU, BSU and TSU together made up the intermediate muon detector (IMU) [32]. There was no forward gaseous tracker in CDF Run II, however the silicon trackers wide pseudo-rapidity coverage allowed for silicon only tracking in the forward region. The plug calorimeters were similar in design to their central counterparts and covered  $1.1 \lesssim |\eta| < 3.6$ . The IMU detectors were also similar to their central counterparts; their pseudo-rapidity coverage is given in table 2.2.

The CLC [33] was used to measure the average number of interactions per beam crossing, from which the luminosity could be accurately estimated. The CLC consisted of very long and thin cone shaped Cherenkov counters arranged around the beam pipe (inside the gap in the plug calorimeters), each of which was filled with isobutane gas. Particles passing through the CLC with velocities greater than the speed of light in the medium emitted Cherenkov radiation which was collected by photomultiplier tubes. The CLC counters covered the very high pseudo-rapidity region  $3.7 < |\eta| < 4.7$ .

### 2.2.7 Trigger

The rate at which beam crossings occurred at CDF Run II was determined by the 396 ns bunch spacing as roughly 2.5 MHz. This was several orders of magnitude greater than the rate at which detector readout data could be written to magnetic tape (still considered the best medium for mass data storage) or otherwise stored. Hence a trigger system was required to filter through the events occurring and select only the most interesting for storage. This triggering needed to happen in near real time to cope with the incoming flow of data. When the readout buffers used to temporarily store detector information were full and the system was still busy processing the events in these buffers the system was ‘dead’ to new events. Any new event occurring while the system was dead had to be rejected without being considered. Time when the system was dead was

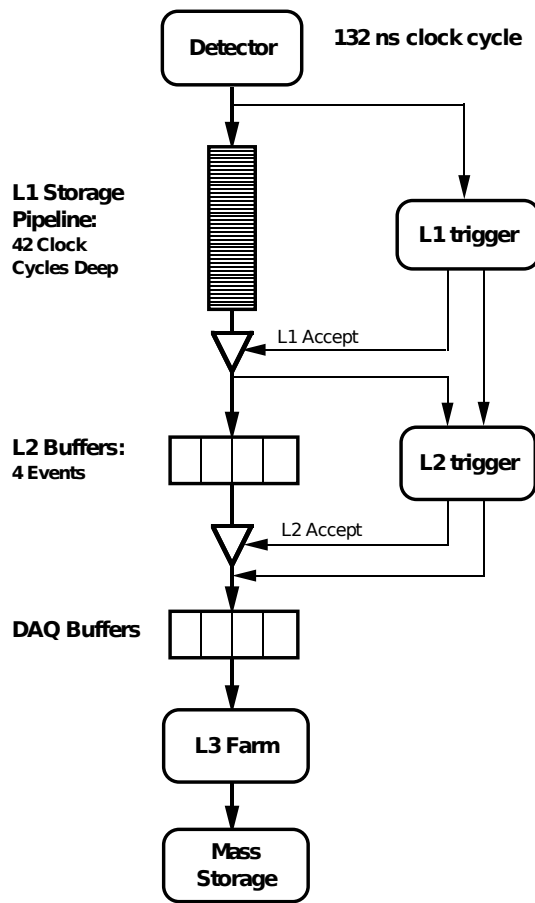


Figure 2.6: A schematic of the trigger system and data flow at CDF Run II.

called ‘deadtime’ and it was desirable to keep this to an absolute minimum so that rare events of particular interest were not missed.

In order to achieve near real time filtering the trigger actually consisted of a chain of three trigger levels. At each level a large fraction of the input events were rejected as uninteresting, considerably reducing the input data rate to the next level. Thus the triggering criteria of the successive levels could be increasingly complex, and therefore time consuming to evaluate, without increasing deadtime. The three trigger levels in the chain were called level 1, level 2 and level 3. A schematic overview of the trigger system is given in fig. 2.6.

Level 1 was the first level of the chain; it was designed around a 132 ns clock

cycle<sup>2</sup> and could process one event per clock cycle. Level 1 did not make a decision about an event in a single clock cycle however, instead it processed events by passing them through a decision chain that was exactly 42 clock cycles long and could have up to 42 events at different steps in the chain simultaneously<sup>3</sup>. Meanwhile the readout information from the detector was placed in a storage pipeline synchronised to the level 1 trigger decision chain. In order to implement this synchronised system the level 1 trigger was necessarily built using custom designed hardware.

The level 1 trigger decision chain consisted of three separate processing streams that were run in parallel. The first stream considered data from the axial COT superlayers, if sufficient sense wires had registered charge above a certain threshold then the extremely fast tracker (XFT) tried to reconstruct a track<sup>4</sup>. If this was successful then the track extrapolator (XTRP) calculated the expected  $\phi$  of such a track in the calorimeter and muon systems to allow electron and muon candidates to be formed. The second stream considered information from the calorimeter, using the ratio of electromagnetic to hadronic energy in each tower to identify electron candidates. The third stream considered information from the muon chambers. All this information was put together to form trigger primitives (electron/muon/photon candidates, jets, XFT tracks, total energy, missing energy) on which a final level 1 decision was made. The level 1 accept rate for events was around 25 kHz and was limited by level 2 deadtime. The level 1 trigger itself had no deadtime at all.

The level 2 trigger used more sophisticated clustering algorithms for the calorimeter to allow more stringent cuts to be applied to calorimeter based primitives, while also adding information from the CES. Level 2 also used information from the silicon tracker which was reconstructed by the silicon vertex tracker (SVT). The SVT allowed level 2

---

<sup>2</sup>Two different modes of Tevatron operation for Run II were initially considered at the design stage, one was to use 108 bunches and a 132 ns bunch separation and the other was to use 36 bunches and a 396 ns bunch separation. The latter was eventually chosen. Many components of the CDF Run II detector were thus designed for either 36 or 108 bunches.

<sup>3</sup>Given the 2.5 MHz beam crossing rate of the Tevatron, level 1 was actually only processing 14 events at a time.

<sup>4</sup>The XFT was upgraded in 2006 and again in 2007. The first upgrade allowed it to consider information from the outer three stereo superlayers to confirm tracks reconstructed using the axial superlayers. The second upgrade allowed the full reconstruction of tracks using stereo superlayers for the level 2 trigger.

to consider displaced vertices in its trigger decisions. Level 2 was not synchronised and used a mixture of hardware and software. It could process events at a maximum rate of about 25 kHz. Four buffers were available to store events that were being processed, if all four buffers were full then no further events could be accepted from level 1 and CDF was dead till one of the buffers cleared. Level 2 deadtime varied greatly according to the luminosity at the time but would typically be 5%. The level 2 accept rate for events was originally about 350 Hz but later could rise as high as 900 Hz at times.

The level 3 trigger was software based and consisted of a farm of 300 PCs running Linux. Many events could be processed simultaneously by the level 3 farm. Level 3 used the full detector readout information from all the detector subsystems and fully reconstructed events before making a decision. Accepted events were sent to a data logger system from where they were transferred to the Feynman Computing Centre (across the road from the CDF building) to be written to tape. The level 3 accept rate for events was about 75 Hz. Level 3 deadtime was possible however in practice was usually avoided by adjusting the trigger criteria for level 2.

### 2.2.8 Material Mapping

Correctly modelling particle energy loss in the CDF Run II detector requires an accurate description (map) of the material composition of the detector. Energy loss in the inner detector (the silicon tracker and COT) reduced the resolution of measurements of a particle's momentum and position, so the inner detector was designed to minimise such energy losses by minimising the quantity of material present and choosing 'light' materials that generated comparatively small energy losses. Approximate estimates of the radial thickness of various detector components in the central region are given in table 2.3.

The main map of the material composition of the CDF Run II detector is contained in the code of the CDF collaboration's main simulation of the detector, CdfSim. The basis for this map was a component-by-component description of the detector based on technical drawings and notes compiled during the construction/upgrading of the detector. (The upgrades to the detector made between Run I and Run II were sufficiently

Detector Component	Thickness
Beam Pipe and Silicon Tracker	0.03 to 0.20 $X_0$
COT Inner Can	0.01 $X_0$
COT Active Volume	0.02 $X_0$
COT Outer Can, TOF and Solenoid	1 $X_0$
CEM	18 $X_0$
CHA	4.5 $\lambda_I$

Table 2.3: Approximate estimates of the radial thickness of the various detector components of the CDF Run II detector in the central region. Thicknesses are given in terms of radiation lengths ( $X_0$ ), or for the hadronic calorimeter, nuclear interaction lengths ( $\lambda_I$ ).

significant as to render material mapping information from Run I obsolete.) For most individual components of the detector the mass and dimensions of the component were known. The fractional material composition of components was not always known; sometimes it was necessary to estimate this from the known mass and dimensions of a component combined with the known densities of its constituents. When the fractional composition of a component was known, its mass could be calculated from its dimensions and then compared to the measured value for this mass as a cross-check. (Note that the term ‘component’ is used in this thesis to refer to both sub-systems of detector as a whole, e.g. the silicon tracker, and to individual pieces of such sub-systems, e.g. a length of copper wiring. The correct definition should be clear from the context.) References [34, 35, 36] describe some of the key components of the inner detector included in the map, however the only comprehensive version of the map is that contained in the code itself. To accurately simulate the effect of energy loss on momentum measurements, the key component of the detector to model is the silicon tracker.

The initial CdfSim material map of the silicon tracker and COT inner wall was validated against experimental data taken during CDF Run II, using three different techniques:

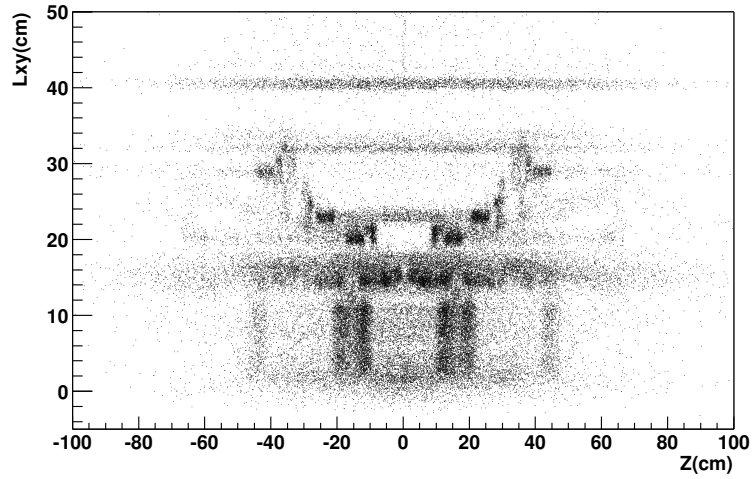
- $W \rightarrow e\nu$  and  $Z \rightarrow e^+e^-$   $E/p$  fits: Monte-Carlo to data fits of the radiative tail of the distribution of lepton energy measured in the calorimeter divided by lepton momentum measured in the tracker ( $E/p$ ) for  $W \rightarrow e\nu$  and  $Z \rightarrow e^+e^-$  events [37].

These fits are very similar to the material scale fits made for the  $W$  mass analysis (see section 4.6.2), however these studies used considerable less data ( $100 \text{ pb}^{-1}$ ) than the  $W$  mass analysis and also differed in other details.

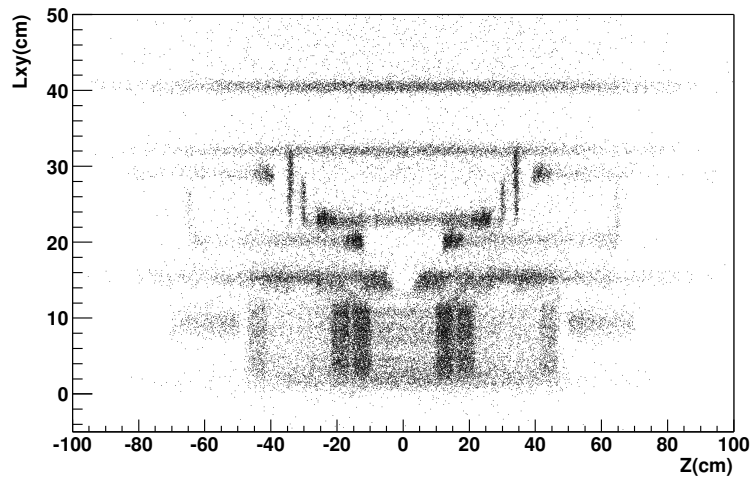
- $J/\psi \rightarrow \mu^+ \mu^-$  mass fits: Monte-Carlo to data fits of the reconstructed  $J/\psi$  mass distribution for  $J/\psi \rightarrow \mu^+ \mu^-$  events as a function of  $J/\psi$   $p_T$  [38]. The measured momentum of a muon is affected by the energy lost by the muon through ionisation in the silicon tracker. The absolute energy loss of high  $p_T$  muons is almost independent of muon  $p_T$ ; thus the relative effect is reduced as the  $p_T$  increases and the measured  $J/\psi$  mass will be sensitive to  $p_T$  if ionisation energy losses are not modelled correctly. We constrain the  $J/\psi$  mass to the world average and fit the required adjustment to the ionisation energy losses in the simulation. From this adjustment we can estimate the accuracy of our simulation of the total quantity of radiative material in the silicon tracker.
- Photon conversion mapping: The dominant energy loss mechanism for high energy (energies above approximately 100 MeV if the medium is carbon) photons in matter is pair production. When a photon converts to an electron-positron pair, the electron and positron will both leave tracks and these tracks will curve in opposite directions in a magnetic field. Thus it is possible in a tracker to construct the point (vertex) at which the photon converted. As the probability of a pair production event occurring is proportional to the number of radiation lengths of material traversed by a photon, reconstructed pair production vertices can be used to produce a three dimensional conversion map of the material in a detector. Such a conversion map was produced using early CDF Run II data for the CDF Run II silicon tracker (and beam pipe and COT inner wall) [39]. A simulated conversion map was also produced using CdfSim. The data and simulation conversion maps for the  $r$ - $z$  plane are given in fig. 2.7. Figures 2.8 to 2.10 compare the data and simulation distributions of conversions as a function of  $r$  for three different  $z$  regions; these distributions effectively show the (radiation length normalised) thickness of material traversed by a particle travelling normal to the beam line.

The thickness of the inner can of the COT is well known and used to normalise the simulated distributions to data. Photon conversion mapping provides the most detailed information on the radiative material present in the CDF Run II inner detector out of these three techniques.

From the results of these three validation techniques, especially the photon conversion mapping, it was concluded that the amount of material being simulated in CdfSim was an underestimate of the amount of material present in the actual detector. It was hypothesised that this was because of mis-modelling of the copper wiring in the silicon tracker. Unfortunately it was not possible to verify this as the silicon tracker was inaccessible while CDF was running. Thus to improve the modelling of the material in the silicon tracker a number of ‘phantom layers’ were added to the CdfSim model to account for this extra material. Further simulated conversion maps were produced using the improved version of CdfSim and by further comparisons it was possible to tune these ‘phantom layers’ such as to best model the data. The conversion maps also highlighted extraneous heat exchangers in the simulation which were removed.



(a)



(b)

Figure 2.7: Maps of the location in the  $r$ - $z$  plane of reconstructed photon conversion vertices in the CDF Run II silicon tracker for data (a) and simulation (b). (Note  $Lxy \equiv r$ .) Note the extraneous heat exchangers in the simulated map at approximately  $|z| = 60$  cm,  $Lxy = 10$  cm. There is a clear excess of events in the data at approximately  $Lxy = 15$  cm compared to the simulation. Reproduced from reference [39].

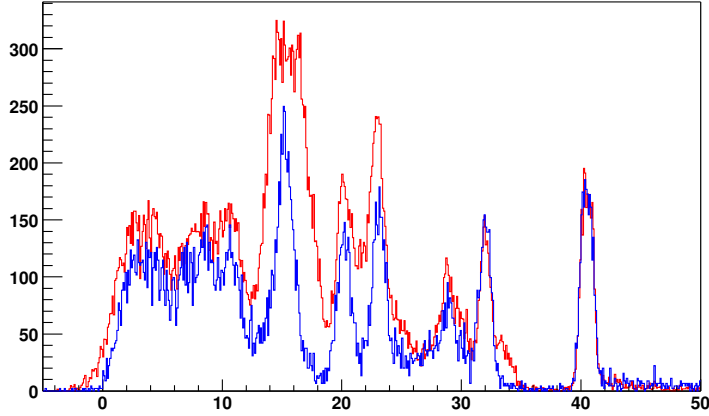


Figure 2.8: Comparison of the distribution of reconstructed photon conversion vertices for data (red histogram) and simulation (blue histogram) as a function of signed radius  $r$  for the region  $-45 < z < -15$  cm. The  $y$ -axis variable is number of events; the  $x$ -axis variable is signed radius (in cm). The simulation histogram is normalised to the data histogram using the peak at  $r \approx 40$  cm (the COT inner can). These distributions effectively show the (radiation length normalised) thickness of material traversed by a particle travelling normal to the beam line. Negative values of signed radius occur when a photon conversion vertex is mis-reconstructed in the opposite side of the detector (in the transverse plane) to true vertex of the photon conversion. Reproduced from reference [39].

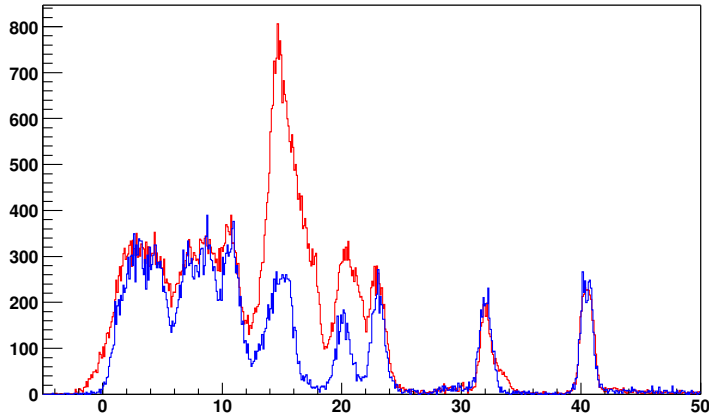


Figure 2.9: Comparison of the distribution of reconstructed photon conversion vertices for data (red histogram) and simulation (blue histogram) as a function of signed radius  $r$  for the region  $|z| < 15$  cm. The  $y$ -axis variable is number of events; the  $x$ -axis variable is signed radius (in cm). The simulation histogram is normalised to the data histogram using the peak at  $r \approx 40$  cm (the COT inner can). These distributions effectively show the (radiation length normalised) thickness of material traversed by a particle travelling normal to the beam line. Negative values of signed radius occur when a photon conversion vertex is mis-reconstructed in the opposite side of the detector (in the transverse plane) to true vertex of the photon conversion. Reproduced from reference [39].

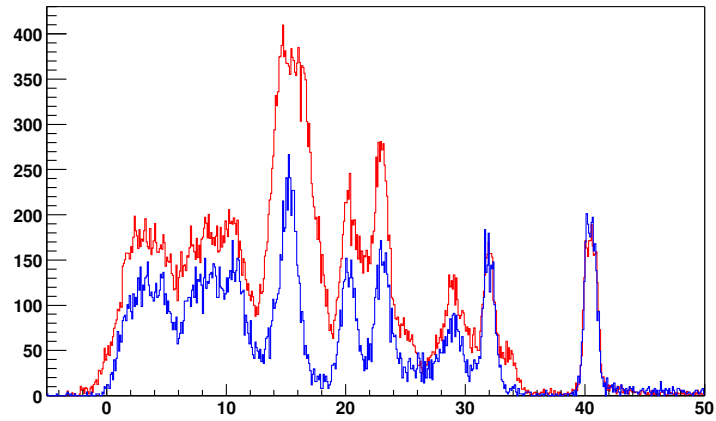


Figure 2.10: Comparison of the distribution of reconstructed photon conversion vertices for data (red histogram) and simulation (blue histogram) as a function of signed radius  $r$  for the region  $15 < z < 45$  cm. The  $y$ -axis variable is number of events; the  $x$ -axis variable is signed radius (in cm). The simulation histogram is normalised to the data histogram using the peak at  $r \approx 40$  cm (the COT inner can). These distributions effectively show the (radiation length normalised) thickness of material traversed by a particle travelling normal to the beam line. Negative values of signed radius occur when a photon conversion vertex is mis-reconstructed in the opposite side of the detector (in the transverse plane) to true vertex of the photon conversion. Reproduced from reference [39].

# Chapter 3

## $W$ Mass Measurement

### 3.1 Why Measure the $W$ Mass?

Precision measurement is a very important aspect of modern high energy physics. This is particularly true for parameters of the electroweak interaction for which the SM makes specific predictions. Generally, precision measurements can be used firstly to confirm the validity of the SM and then, once a sufficient level of accuracy has been achieved, to search for minor deviations from the SM that might indicate new physics that is explicitly manifest at higher energy scales than have so far been probed. The motivations for precision measurements of the  $W$  boson mass differ from this generality because of the unknown mass of the as yet undiscovered Higgs boson. The  $W$  mass and the Higgs mass are connected; thus measurements of the  $W$  mass can be used either to constrain the Higgs mass within the SM or combined with direct constraints on the Higgs mass (or direct measurements of the Higgs mass when/if the Higgs is discovered) to test for deviations from the SM.

The SM electroweak theory allows the  $W$  mass to be predicted with great precision using the values of a number of other SM parameters. The SM prediction for the  $W$  mass (in the ‘on-shell’ renormalisation scheme) is [40, 41]:

$$m_W^2 = \frac{\hbar^3}{c} \frac{\pi\alpha_{\text{em}}}{\sqrt{2}G_F} \frac{1}{(1 - m_W^2/m_Z^2)(1 - \Delta r)} \quad (3.1)$$

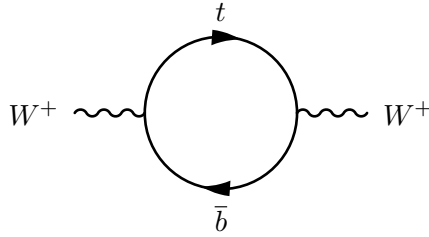


Figure 3.1: Diagram for the one-loop radiative correction to the  $W$  mass from top and bottom quarks. Adapted from reference [41].



Figure 3.2: Diagrams for the one-loop radiative correction to the  $W$  mass from the Higgs boson. Adapted from reference [41].

where  $m_Z$  is the  $Z$  boson mass,  $G_F$  is the Fermi weak coupling constant measured using the lifetime of the muon,  $\alpha_{\text{em}}$  is the electromagnetic coupling constant at the renormalisation energy scale  $Q = m_Z c^2$  and  $\Delta r$  contains all radiative corrections. Except for  $\Delta r$  all the parameters in eq. (3.1) are already known very precisely,  $m_Z$  having been measured with very great precision at LEP. The uncertainty on the radiative corrections to the  $W$  mass are potentially large. There are three main contributions to this uncertainty. Firstly the uncertainty on the mass of the top quark  $m_t$ , in the top and bottom quark loop correction (see fig. 3.1). Secondly there is a correction from Higgs loops (see fig. 3.2). Thirdly there are potential corrections from supersymmetric particles (mostly from the SUSY partner of the quark which is called the squark) if they exist (see fig. 3.3). Higgs loop radiative corrections would decrease the  $W$  mass while SUSY loop corrections would tend to increase the  $W$  mass. The magnitude of Higgs loop corrections is proportional to the logarithm of the Higgs mass.

Figure 3.4 uses the latest world experimental averages to fit for the SM Higgs mass derived by considering these corrections (not including the SUSY corrections) as a function of the value of  $m_W$  and  $m_t$ . Significantly, at the moment the  $m_W$  uncertainty makes a greater contribution to the uncertainty on the fit than the  $m_t$  uncertainty. Given the direct lower limit on the Higgs mass from LEP and the current state of this

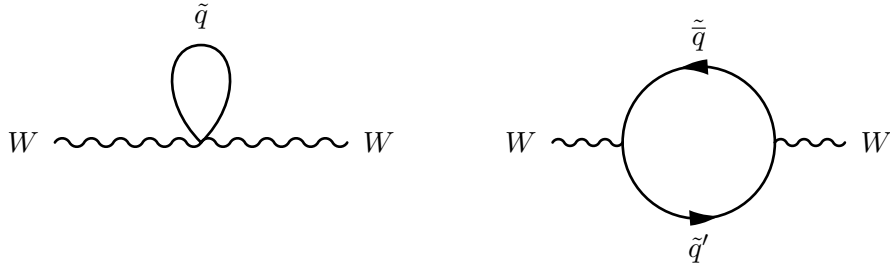


Figure 3.3: Diagrams for the one-loop radiative correction to the  $W$  mass from squarks. Squark loops are the dominant contribution to radiative corrections to the  $W$  mass from SUSY particles. Adapted from reference [41].

fit, it is possible that by reducing the uncertainty on or changing the central values of either  $m_W$  and  $m_t$  this fit could exclude the SM Higgs at some confidence level. This could be an indication the Higgs boson doesn't exist. Alternatively it could be an indication of the minimal supersymmetric extension of the Standard Model being required to introduce additional radiative corrections that increase the predicted  $W$  mass value thus allowing the fit to be consistent with a larger Higgs mass. Given that we will know if the Higgs exists from direct searches very soon regardless, it could be argued that the latter possibility is a far more important reason to measure the  $W$  mass.

### 3.2 Why Measure the $W$ Mass at CDF?

High precision measurements of the  $W$  mass have been made by the four experiments that were situated at the LEP II  $e^+e^-$  collider (which has subsequently been dismantled and replaced by the LHC) and the two experiments situated on the Tevatron. Two methods were used at LEP II to measure the  $W$  mass. The first method compared the predicted  $\sigma(e^+e^- \rightarrow W^+W^-)$  to that measured experimentally for collisions with centre of mass energies near the  $W$  boson pair production threshold; this cross section is a strong function of  $m_W$  near the aforementioned threshold and therefore this comparison provides a precise measurement of the  $W$  mass. The second method completely reconstructed the  $W$  boson invariant mass in  $W$  boson pair production events using the known centre of mass collision energy. Both measurement techniques at LEP II benefited from the 'clean' collisions produced by a lepton collider. Each LEP II experi-

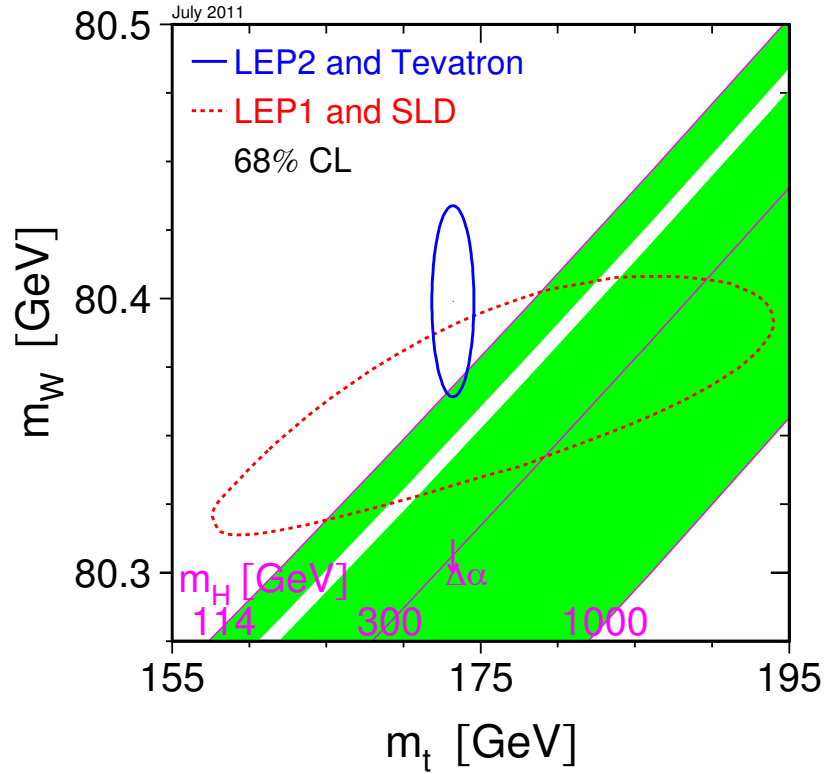


Figure 3.4: Diagram showing the 68% confidence level limit imposed on the SM Higgs boson mass through a combination of  $m_W$  and  $m_t$  by LEP II and the Tevatron (blue, by direct measurements of  $m_W$  and  $m_t$ ), and LEP I and SLD (red, by indirect measurements of  $m_W$  and  $m_t$ ). The upper edge of the green area is the lower bound on the Higgs boson mass imposed by direct searches at LEP. If the fit were to lay in the region above this bound the Minimal Supersymmetric Standard Model would be favoured. The white band within the green area is imposed by direct searches at the Tevatron and LHC around 160 GeV ( $2 \times m_W$ ). The lower edge of the green area is imposed as an upper bound on the Higgs boson mass, since for Higgs boson masses above 1 TeV/ $c^2$ , the SM and its formulae do not make sense. Reproduced from reference [42].

ment produced a final  $W$  mass measurement by combining both methods; these results were then combined (appropriately accounting for common uncertainties) to produce an overall LEP II average measurement of  $m_W = 80.376 \pm 0.033 \text{ GeV}/c^2$ . This average is dominated by the results from the direct reconstruction technique.

The Tevatron measurements are impaired by the ‘messy’ collisions produced by a hadron collider. However, the  $W$  production cross section at the Tevatron (about 5.5 nb including a factor for the fraction of  $W$ ’s that decay to the muon or electron channels useful for hadron collider precision measurements) was very considerably higher than that at LEP II (where the cross section for the dominant  $W$  production channel,  $e^+e^- \rightarrow W^+W^-$ , was between roughly 4 pb and 18 pb depending on the centre of mass collision energy). Thus measurements at the Tevatron are able to achieve a similar precision to those made at the LEP II experiments. A prior measurement of the  $W$  mass was made at CDF Run II using similar techniques (though slightly less refined) as the latest CDF Run II measurement discussed herein, but with a considerably smaller sample of collision data ( $200 \text{ pb}^{-1}$ ). DØ Run II have measured the  $W$  mass using fits to the transverse mass, electron energy and missing energy distributions for the  $W \rightarrow e\nu$  decay channel using  $1 \text{ fb}^{-1}$  of collision data. Prior to the CDF analysis discussed herein, this DØ measurement was the most precise single measurement of the  $W$  mass to date. The current combined average measurement for the Tevatron (including some older results from Run I, excluding the latest CDF analysis discussed herein) is  $m_W = 80.420 \pm 0.031 \text{ GeV}/c^2$ . The current world average, combining all the LEP II and Tevatron Run II results (and some older results from Tevatron Run I, excluding the latest CDF analysis discussed herein) is  $m_W = 80.399 \pm 0.023 \text{ GeV}/c^2$ . The values and uncertainties of existing  $W$  mass measurements are summarised in fig. 3.5.

The  $200 \text{ pb}^{-1}$  of collision data used in the previous (first) CDF Run II  $W$  mass measurement was only a small fraction of the available data set. The accuracy achieved by this measurement was  $48 \text{ MeV}/c^2$ . This total uncertainty included a  $34 \text{ MeV}/c^2$  contribution from statistical uncertainties and a  $34 \text{ MeV}/c^2$  contribution from systematic uncertainties. The second CDF Run II  $W$  mass measurement, the analysis described in

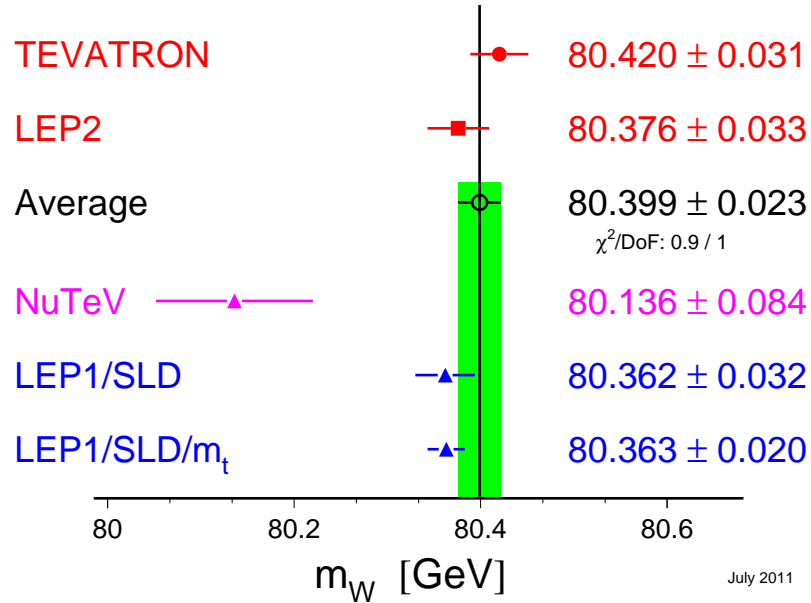


Figure 3.5: Summary of the values and uncertainties of existing  $W$  mass measurements (as of the time of writing, excluding the new CDF analysis discussed herein). The average combines the Tevatron and LEP II results. The NuTeV and LEP I/SLD results are indirect measurement of the  $W$  mass calculated from a combination of other electroweak results. Reproduced from reference [42].

this thesis, aimed to reduce both its statistical uncertainty (by using a larger dataset of about  $2.2 \text{ fb}^{-1}$  of collision data) and its systematic uncertainty (by an increased sophistication in the modelling of  $W$  decay events). The aim of the measurement was to reduce the total uncertainty to about  $25 \text{ MeV}/c^2$ . Thus this measurement aimed to have a significant impact on the world average  $m_W$  and hence on the indirect SM Higgs mass predicted by considering the combination of the  $W$  mass and top quark mass. Measuring the  $W$  mass at CDF would also provide further valuable experience of making precision measurements at a hadron collider that could be carried forward to a program of precision measurements at the LHC.

## Chapter 4

# Overview of the Second CDF Run

## II $W$ Mass Measurement

### 4.1 Principles of Measuring the $W$ Mass at CDF Run II

The main process through which  $W$  and  $Z$  bosons were produced at the Tevatron was the quark-antiquark annihilation of  $u$  and/or  $d$  valence quarks (see fig. 4.1). There was an additional contribution of  $\sim 20\%$  from sea quarks. The  $W$  boson has a mean lifetime of  $\sim 10^{-25}$  s; thus the distance it travels before decaying is negligible compared to the size of a proton. Roughly 67% of  $W$  bosons decay via hadronic channels, however such channels have very large QCD backgrounds and hence are not useful for high precision measurements. Roughly 11% of  $W$  bosons decay to each of the three leptonic decay channels  $W \rightarrow \ell\nu$ . The  $\tau$  has a short mean lifetime of  $\sim 300 \times 10^{-15}$  s and therefore  $\tau$ 's decay very close to the interaction point and are thus difficult to identify; hence the  $\tau$  decay channel is also not used. The  $W \rightarrow e\nu$  and  $W \rightarrow \mu\nu$  decay channels were the dominant source of isolated high  $p_T$  electrons and muons in the Tevatron. Electrons and muons can be triggered on very effectively and their kinematic properties can be measured very accurately. Thus the electron and muon decay channels are used to measure the  $W$  mass at CDF. In this thesis I concentrate on the electron channel.

When a  $W$  (or  $Z$ ) boson is produced in a proton-antiproton collision the remnants of the proton and antiproton that collided will hadronise to form new particles. Addi-

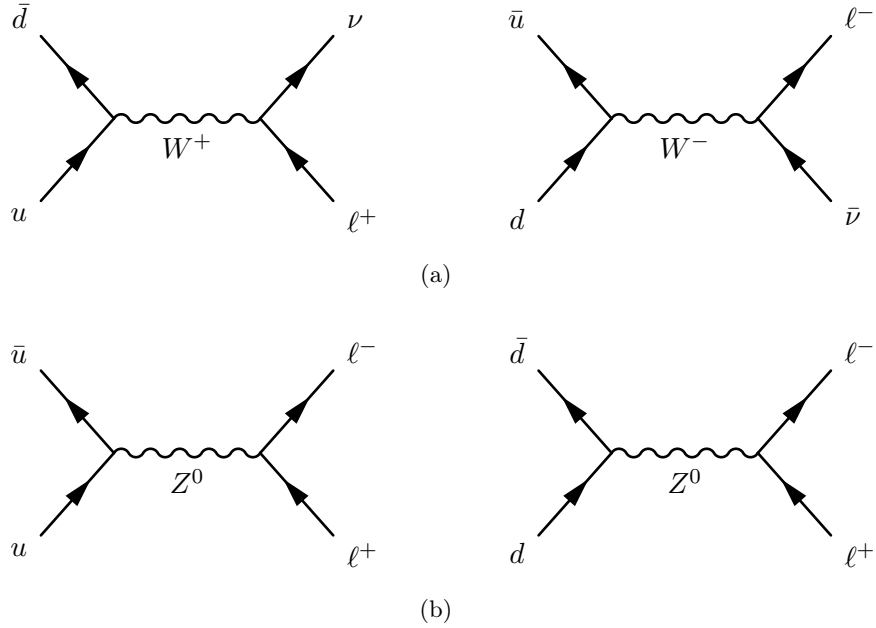


Figure 4.1: Important first order Feynman diagrams for the production of  $W$  bosons (a) and  $Z$  bosons (b) in proton-antiproton collisions at the Tevatron.

tionally some rarer  $W$  boson production processes may involve (often high  $p_T$ ) gluons and quarks being emitted from the interacting quark or antiquark and these too will hadronise to form new particles and possibly form jets. Particles not associated with the decay of the  $W$  boson are collectively referred to as the underlying event; it is common for some such particles to escape along the beam pipe and not be detected.

For leptonic  $W$  boson decays the observables will be either the energy and momentum (for electrons) or the momentum only (for muons) of the charged lepton and the energy deposited in the calorimeter by the underlying event. The neutrino will escape undetected and not be observable. The fraction of the beam energy carried by the quarks/antiquarks that are directly involved in the  $W$  boson production will not be known; thus the initial momentum of the  $W$  boson is not known. It cannot be inferred from the vector sum of the underlying event energy due to some particles from the underlying event escaping along the beam pipe. As a result of both the neutrino and initial  $W$  boson momenta being unknown it is not possible to reconstruct leptonic  $W$  boson decays fully in three dimensions. Instead a template fitting procedure is used to measure  $m_W$  (as described in section 4.2); this requires the simulation of  $W$  boson

production and decay events.

The initial  $p_T$  of the interacting proton and antiproton is zero and the transverse momenta carried by particles that escape along the beam pipe will be negligible. The transverse momentum of the  $W$  boson  $\vec{p}_T^W$ , is thus inferred to be opposite in direction and equal in magnitude to the hadronic recoil vector  $\vec{u}_T$ , the vector sum of the energy deposited in the calorimeter not associated with the charged lepton (i.e.  $\vec{p}_T^W = -\vec{u}_T = -\sum_{i,j}(\vec{E}_T)_{ij}$ , where  $i$  is an index over the calorimeter towers in a  $\phi$  wedge that are not associated with the lepton and  $j$  an index over the  $\phi$  wedges of the calorimeter). A measure of the neutrino's momentum  $\vec{p}_T^\nu$ , is then  $\vec{p}_T^\nu = -(\vec{p}_T^\ell + \vec{u}_T)$  where  $\vec{p}_T^\ell$  is the momentum of the charged lepton.  $\vec{p}_T^\nu$  can be used to construct the 'transverse mass' of the  $W$  boson, defined as:

$$m_T \equiv \sqrt{2p_T^\ell p_T^\nu (1 - \cos \Delta\phi)} \quad (4.1)$$

where  $\Delta\phi$  is the angle between the charged lepton and  $\vec{p}_T^\nu$  in the transverse plane. Fitting the  $W$  transverse mass distribution provides the most statistically precise measurement of the  $W$  mass.  $m_T$  is largely independent of the production dynamics of the  $W$  boson; it is not directly sensitive to  $p_z^W$  (the  $z$  component of the  $W$  boson's momentum) and is only sensitive to  $p_T^W$  to  $\mathcal{O}((p_T^W/M_W)^2)$ . However  $m_T$  is sensitive to the measurement of  $\vec{u}_T$ .

Two alternatives to the transverse mass are the charged lepton transverse momentum and reconstructed neutrino transverse momentum distributions. The charged lepton transverse momentum distribution is not directly sensitive to the measurement of  $\vec{u}_T$  but is sensitive to true  $p_T^W$  to  $\mathcal{O}(p_T^W/M_W)$ . The reconstructed neutrino transverse momentum distribution is sensitive to both the measurement of  $\vec{u}_T$  and to  $p_T^W$  to  $\mathcal{O}(p_T^W/M_W)$ . Both these distributions are statistically less precise than the transverse mass. All three distributions are fitted separately for both channels and cross-checked against each other; the weighted average, taking into account correlations, of these six individual fits is then used as the final measured value of the  $W$  mass.

$Z$  boson production has similar vector boson production kinematics to  $W$  boson production and furthermore the  $Z$  boson decay channels  $Z \rightarrow e^+e^-$  and  $Z \rightarrow \mu^+\mu^-$

also produce leptons of a comparable energy (to within roughly 5 GeV) to leptonic  $W$  boson decays (though the number of leptons per event differs). Therefore the accurate simulation of  $Z$  boson decays in these two channels requires many elements similar to the simulation of leptonic  $W$  boson decays. The  $Z$  mass has already been measured to an extremely high accuracy at LEP and these  $Z$  boson decay channels are fully reconstructable; thus they are used as important control samples for the  $W$  mass measurement.

The  $W$  mass measurement in the muon (decay) channel is made using COT information (along with the beam spot constraint) to measure the muon transverse momentum  $p_T^\mu$  and the calorimeter to measure the hadronic recoil. The COT's momentum measurements are calibrated using samples of  $J/\psi \rightarrow \mu\mu$  and  $\Upsilon(1S) \rightarrow \mu\mu$  decays from CDF Run II. (A more detailed breakdown of the various elements of the measurement in both the muon and electron channels is given in section 4.6.)

For the electron (decay) channel the transverse energy of the electron is defined as  $E_T = E \times \sin \theta$  where  $E$  is the energy of the electron measured in the electromagnetic calorimeter (energy leaking into the hadronic calorimeter is not included in this measurement) and  $\theta$  is measured using the trajectory of the track in the COT. The energy resolution of the calorimeter is more accurate than the momentum resolution of the tracker for a 40 GeV electron typical of  $W$  decays in this channel. Thus we replace  $p_T^e$  with  $E_T$  in the definition of all the kinematic variables used to fit  $m_W$  in the electron channel<sup>1</sup>. (This includes the  $p_T^e$  distribution itself, which now effectively becomes the  $E_T$  distribution.) The calorimeter is used to measure the hadronic recoil.

Two different methods are considered to calibrate the calorimeter's electron energy measurements. Both methods derive an energy scale  $S_{\text{CEM}}$  that is then applied to the energy of simulated electrons. The first is to fit for  $S_{\text{CEM}}$  using the distribution  $E_T/p_T^e$ , where the momentum measurement uses the same calibration as for muons. The second is to fit for  $S_{\text{CEM}}$  in  $Z \rightarrow e^+e^-$  events using the reconstructed  $Z$  mass distribution with templates being generated using the world average  $Z$  mass. Both methods are applied and their agreement is an important cross-check of the validity of the simulation used.

---

<sup>1</sup>As the mass of the electron is negligible  $p_T = E_T$ .

The final  $S_{\text{CEM}}$  used is the weighted average of the two methods. Any non-linearity in the calorimeter’s electron energy response is also modelled, using parameters obtained from fits to data.

$W$  production and decay events are simulated using a custom fast simulation of the detector response combined with an appropriate event generator. A custom fast simulation is chosen instead of the full GEANT-based CDF detector simulation (CdfSim); the fast simulation code runs much faster than CdfSim, and allows the modelling of the detector response to be tailored specifically for accurate  $W$  mass measurement. The high computational speed of the fast simulation allows the many high statistics studies necessary to calculate systematic uncertainties to be made. The baseline measurement is performed using a fast simulation called Duke Fast Simulation. This thesis describes and presents results from an independent simulation program called UCL Fast Simulation used to cross-check important results.

As important to any precision measurement as the measured value of the parameter itself is the uncertainty on that value. Thus it is vital to the  $W$  mass analysis to evaluate possible systematic uncertainties on the fitted mass, including (but not limited to) systematic uncertainties on  $m_W$  arising from the statistical uncertainties on parameters of the simulation estimated by fitting to data. All known possible systematic uncertainties must be combined with the statistical uncertainties on the fitted values of  $m_W$  using standard error propagation techniques to give an overall uncertainty on the  $W$  mass measurement.

## 4.2 Template Fitting

As leptonic  $W$  boson decays cannot be fully reconstructed it is necessary to measure the  $W$  mass by a template fitting procedure. A model of  $W$  boson production and decay is used to simulate the observable kinematic distributions of  $W \rightarrow e\nu$  and  $W \rightarrow \mu\nu$  events. This is repeated for a range of different discrete hypotheses for  $m_W$ . A simulated kinematic distribution for a given  $W$  mass hypothesis is called a template. The kinematic distributions of  $W$  boson decay cannot be described analytically; the distri-

butions are produced numerically as histograms (binned frequency distributions) using the Monte-Carlo method. Comparison of the templates to the data distribution (also binned into a histogram) is then used to measure the value of  $m_W$  using maximum likelihood estimation. Each template is compared to data and the likelihood  $L$ , is calculated as:

$$L = \prod_{i=1}^N \frac{e^{-m_i} n_i^{m_i}}{n_i!} \quad (4.2)$$

where  $i$  is an index over the  $N$  bins of the template,  $n_i$  is the number of observed data events in bin  $i$  and  $m_i$  is the number of simulation events in bin  $i$ . The  $m_W$  hypothesis of the template which minimises  $-\ln L$  is taken as the best fit value of  $m_W$  and the  $\pm 1\sigma$  uncertainties on  $m_W$  are the values which increase  $-\ln L$  to  $(-\ln L)_{\text{minimum}} + 0.5$  (its value at the minimum plus a half). In this fitting procedure  $m_W$  is known as the estimated parameter; analogous template fitting procedures are used to estimate other parameters of  $W$  boson decay events such as the calorimeter energy scale. For some other parameters limited Monte-Carlo statistics are maximised by fitting a parabola to a graph of  $-\ln L$  as a function of the estimated parameter and taking the parabola's minimum as the best fit value<sup>2</sup>. Any possible bias in the final measured  $m_W$  value due to background events (events that are not actually  $W$  boson decays in the electron/muon channel) still present in the data sample after event selection cuts have been applied is minimised by adding background distributions to the templates used.

### 4.3 Event Selection

The aim of event selection is to maximise the number of  $W$  decay events selected from the available data sample while minimising the fraction of background events selected. It is also important to ensure the  $W$  decay events selected are of a high quality, i.e. do not have any features that are difficult to simulate and which might bias the measurement, such as having the lepton in a poorly instrumented region of the detector (i.e. cracks).

---

<sup>2</sup>For some parameters we minimise  $\chi^2 = \sum_{i=1}^N (n_i - m_i)^2 / ((\sigma_m)_i^2 + (\sigma_n)_i^2)$  instead of  $-\ln L$  where  $(\sigma_n)_i = \sqrt{n_i}$  is the error on the number of data events in bin  $i$  and  $(\sigma_m)_i$  is the error on the number of simulation events in bin  $i$ . Further discussion of likelihood and  $\chi^2$  minimisation is given in reference [43].

The experimental data sample being used for the second CDF Run II  $W$  mass measurement comprises data taken between February 4th 2002 and August 4th 2007 (i.e. CDF data periods 0-13, datasets bhel/bhmu 0d to 0j). The specific datasets used contain events within this data sample collected from trigger chains that required at least one high- $p_T$  central ( $|\eta| \leq 1$ ) lepton. Details of the triggers used to record these datasets are given in reference [41]. Both  $W$  and  $Z$  boson decay events are selected from these datasets. Each possible  $W$  boson ( $Z$  boson) event recorded within this dataset is known as a  $W$  ( $Z$ ) candidate event.

The event selection this analysis uses is based on cuts on the lepton, the reconstructed neutrino and the hadronic final state (i.e. recoil). This cuts-based selection technique is applied to both  $W$  and  $Z$  candidate events in both the muon and the electron channels. This thesis only gives the cuts that apply to the electron channel; the cuts for the muon channel are given in reference [44].

### 4.3.1 Electron Selection

Each  $W \rightarrow e\nu$  candidate event is reconstructed by clustering the energy deposited by electromagnetic showers in the CEM using the CDF Run II electromagnetic clustering algorithm (see Appendix A). The tracks of the electron candidates in an event are reconstructed by fitting a trajectory to hits recorded in the COT; this is constrained to originate from the beam spot position in the transverse plane to improve the accuracy of the fit and thus the  $p_T$  resolution. COT tracks are extrapolated to the calorimeter and matched to clusters to form electron candidates. The energy of a cluster associated with an electron track is referred to as the reconstructed energy of the electron. A ‘tight’ cut set is defined for electrons<sup>3</sup>. The full set of tight electron cuts is applied to each electron candidate, if it passes then it is called a ‘tight’ electron.

Selection cuts for electron candidates are applied to the following variables:

- $N_{\text{SL}}^{\text{axial}}$  ( $N_{\text{SL}}^{\text{stereo}}$ ): Number of axial (stereo) super-layers in the COT with  $\geq 5$  hits recorded for the track. A minimum requirement is placed on these variables to

---

<sup>3</sup>The nomenclature is derived from the muon channel where both a ‘tight’ and a ‘loose’ cut set are defined.

ensure only good quality tracks are selected.

- $z_0$ : The distance along the beam between the origin and the trajectory at its point of closest approach to the beam. An appropriate cut on this variable ensures the point of origin of the track is consistent with the longitudinal beam spot and thus the track is from a  $p\bar{p}$  collision.
- $p_T$ : The transverse momentum of the beam-constrained COT track. For the tracks of low  $p_T$  electrons the trigger track-finding efficiency is  $p_T$  dependent. An appropriate cut on this variable eliminates such tracks. An appropriate cut on this variable also reduces backgrounds.
- $E_T$ : The transverse energy of the reconstructed electron (as defined previously). Appropriate cuts on this variable reduce backgrounds.
- CES  $z$ : Local  $z$  co-ordinate of the energy-weighted centre of the electromagnetic shower at the CES within the electron's calorimeter tower (i.e the calorimeter tower that the extrapolated COT track is matched to). Appropriate cuts on this variable and CES  $x$  (see below) ensure the shower occurs in a well instrumented region of the calorimeter.
- CES  $x$ : Local  $x$  co-ordinate of the energy weighted centre of the electromagnetic shower at the CES within the electron's calorimeter tower.
- $E/p$ : The ratio of the electron's reconstructed energy to the electron's momentum measured in the tracker. (Note that  $E/p \equiv E_T/p_T^e$ .) An appropriate cut on this variable and on the variables  $E_{\text{had}}/E_{\text{em}}$ ,  $\Delta z$  and  $L_{\text{shr}}$  (see below) reduces multi-jet backgrounds.
- $E_{\text{had}}/E_{\text{em}}$ : The ratio of the energy measured in the electromagnetic calorimeter to the energy measured in the hadronic calorimeter for the electron's cluster.
- $\Delta z$ : The distance in the  $r$ - $z$  plane between the energy weighted centre of the electromagnetic shower at the CES and the extrapolated COT track.

Variable	Cut
$N_{\text{SL}}^{\text{axial}}$	$\geq 3$
$N_{\text{SL}}^{\text{stereo}}$	$\geq 3$
$ z_0 $	$< 60$ cm
$p_T$	$> 18$ GeV/c
$E_T$	$> 30$ GeV, $< 65$ GeV
$ \text{CES } z $	$> 9$ cm, $< 230$ cm
$ \text{CES } x $	$< 18$ cm
$E/p$	$< 1.6$
$E_{\text{had}}/E_{\text{em}}$	$< 0.1$
$ \Delta z $	$< 5$ cm
$L_{\text{shr}}$	$< 0.3$
Tower number	$\neq 9$

Table 4.1: Selection cuts a tight electron candidate is required to *pass*. (A cut is *passed* if the stated inequality is *true*.)

- $L_{\text{shr}}$ : The electron lateral shower profile; this is derived by comparing the energy measured in the towers adjacent to the seed tower to test beam data.
- Tower number: Calorimeter tower 9 leaks more of the energy of electromagnetic showers into the hadronic calorimeter than other towers; electrons matched to clusters in this tower are rejected.

The values of the tight electron cuts are given in table 4.1.

### 4.3.2 $W$ and $Z$ Boson Selection

A set of cuts is used to define  $W$  events. For each tight electron candidate in a  $W$  event candidate, the event is reconstructed assuming that electron is the primary electron from  $W \rightarrow e\nu$  decay (henceforth referred to as the primary electron) and then tested against the event cuts. If none of the electrons in an event passes all the electron and event cuts then the event candidate is rejected. Otherwise the event candidate is accepted. The highest  $E_T$  tight electron candidate that passes all the event cuts is considered to be the primary electron. The set of the accepted  $W$  candidate events is called the signal event sample.

Event selection cuts for  $W$  candidate events are applied to the following variables:

- $m_T$ : Transverse mass of the  $W$  boson. Appropriate cuts on this variable and on

$\cancel{p}_T$  reduce background.

- $E_T$ : The transverse energy of the electron (as defined previously). A cut on this variable is also included in the tight lepton cut set; it is included again here as an event cut with a more restrictive value on the upper bound for  $W$  candidate events. (This cut is intended to reduce backgrounds; as  $Z \rightarrow e^+e^-$  backgrounds are negligible there is no event cut on this variable for  $Z$  candidate events.)
- $u_T$ : The magnitude of the recoil vector. An appropriate cut on this variable removes events with poor  $\cancel{p}_T$  resolution and reduces multi-jet and  $Z \rightarrow e^+e^-$  backgrounds.
- $\cancel{p}_T$ : The missing transverse energy (or equivalently momentum) in the event (as defined previously).
- ‘ $Z$ -veto’: A flag; set to be *true* if there are any tracks (discounting tracks that would emanate from a displaced vertex if the beam constraint were not applied) with  $p_T > 20$  GeV/ $c$  that are of opposite charge to the tight lepton candidate and extrapolate to a poorly instrumented region of the calorimeter. Otherwise set to be *false*. Requiring this veto to be false reduces  $Z \rightarrow e^+e^-$  backgrounds where the second electron energy is mis-measured by the calorimeter and thus the event passes the  $u_T$  cut. More details of the  $Z$ -veto are given in reference [41]; note the track isolation requirement described in this reference is no longer required.

The values of the  $W$  event selection cuts are given in table 4.2.

$Z$  candidate events are reconstructed by a similar procedure to  $W$  bosons. Each  $Z$  decay is reconstructed from the energy of two tight electron candidates of opposite sign measured in the electromagnetic calorimeter.  $Z$  candidate events are required to pass  $Z$  event selection cuts. The set of the accepted  $Z$  candidate events is called the  $Z$  event sample.

Event selection cuts for  $Z$  candidate events are applied to the following variables:

- $m_{ee}$ : The invariant mass of the  $Z$  boson reconstructed from two electrons (using their reconstructed energies and directional information from their COT tracks).

Cut Set	Variable	Cut
$W$ Candidate Events	$m_T$	$> 60 \text{ GeV}/c^2, < 100 \text{ GeV}/c^2$
	$E_T$	$< 55 \text{ GeV}$
	$u_T$	$< 15 \text{ GeV}$
	$\not{p}_T$	$> 30 \text{ GeV}/c, < 55 \text{ GeV}/c$
	$Z$ -veto	is <i>false</i>
$Z$ Candidate Events	$m_{ee}$	$> 66 \text{ GeV}/c^2, < 116 \text{ GeV}/c^2$
	$p_T^Z$	$< 30 \text{ GeV}/c$

Table 4.2: Selection cuts  $W$  and  $Z$  candidate events are required to *pass*. (A cut is *passed* if the stated inequality is *true*. The  $Z$ -veto cut is *passed* if the value of the flag is *false*.)

- $p_T^Z$ : Transverse momentum of the  $Z$  reconstructed from two electrons (using their reconstructed energies and directional information from their COT tracks).

The values of  $Z$  event selection cuts are also given in table 4.2.

## 4.4 Backgrounds

Despite the careful selection of  $W$  candidate events, due to imperfect detector coverage and resolution, a few background events will mimic the characteristics of a leptonic  $W$  decay sufficiently accurately to pass all the lepton and events cuts<sup>4</sup>. Any bias in the fitted  $W$  mass due to such background events can be minimised by adding an estimate of their contribution to the appropriate kinematic distribution to each set of templates used in  $m_W$  fits. To do this requires an estimate both of the fraction of the signal event sample that is actually background events and of the shape of the relevant kinematic distribution of such background events.

Backgrounds to the electron channel can be divided into electroweak backgrounds and ‘multi-jet’ background. The main electroweak backgrounds to the electron channel are  $Z \rightarrow e^+e^-$  and  $W \rightarrow \tau\nu$  events. In multi-jet background events a hadronic jet is incorrectly reconstructed as a lepton and a large  $\not{p}_T$  is measured due to a second hadronic jet’s energy being either reduced by a semi-leptonic decay or mis-reconstructed. A

<sup>4</sup>In fact it is possible for individual  $W \rightarrow \tau\nu$  background events to be kinematically indistinguishable from signal events even without misconstruction or imperfect detector coverage, although the average kinematics of this background are different from those of signal events.

similar electroweak background exists for the muon channel alongside other backgrounds not applicable to the electron channel. The treatment of muon channel background is not considered in this thesis but is detailed in reference [41].

Electroweak backgrounds are modelled using the event generator PYTHIA and CdfSim. Partial mis-reconstruction of the event (for example failure to reconstruct one of the leptons in a  $Z \rightarrow e^+e^-$  event) is typical of electroweak background events that pass the  $W$  event selection procedure. CdfSim is chosen to model such events (instead of using UCL Fast Simulation) as it provides a comprehensive treatment of such event mis-reconstructions.

Multi-jet background events are selected from the same datasets as the  $W$  event candidate sample using a set of ‘anti-electron’ cuts to create an anti-electron event sample. The shapes of kinematic distributions for the multi-jet background are taken from this anti-electron event sample. The fraction of the signal event sample that is actually multi-jet background events is estimated by fitting simulated  $\cancel{p}_T$  distribution templates for a range of different fractions to data. The templates include PYTHIA/CdfSim simulations of the processes  $W \rightarrow e\nu$ ,  $Z \rightarrow e^+e^-$  and  $W \rightarrow \tau\nu$ . The multi-jet background component uses the data-derived shape detailed above. All variables other than the fraction of multi-jet background events are kept fixed. The data sample used is selected by the same procedure as the signal event sample with the exception that the minimum  $\cancel{p}_T$  requirement is now omitted from the set of event selection cuts. This omission thus includes in the  $\cancel{p}_T$  distribution a low  $\cancel{p}_T$  kinematic region dominated by multi-jet background.

The systematic uncertainty on  $m_W$  arising from the modelling of backgrounds is estimated and used in the calculation of the overall uncertainty on  $m_W$ .

## 4.5 Event Generation

The simulation of events for the CDF Run II  $W$  mass analysis can be divided between the simulation of  $W$  and  $Z$  boson production and decay and the simulation of the propagation of the decay products through the CDF detector. The former is known

as event generation; the event generation process used to provide events to UCL Fast Simulation is briefly outlined in this section. A fuller treatment of this process is described in reference [45].

$W$  and  $Z$  production and decay events for UCL Fast Simulation are simulated by the Monte-Carlo event generator HORACE [46, 47]. This event generator evaluates the leading order (LO) production and decay Feynman diagrams and also includes all electroweak next-to-leading (NLO) corrections to these diagrams. (LO diagrams have the smallest number of vertices of all possible diagrams for a particular process. NLO diagrams have the second smallest number of vertices.) HORACE does not include NLO QCD corrections; unfortunately there is no currently available event generator that includes both NLO QCD and NLO electroweak corrections. The most important NLO QCD correction is the radiation of initial state gluons; these may alter the  $p_T$  of the  $W$  boson. To model this, the decay products of  $W$  decay events generated by HORACE are boosted in the transverse plane according to a  $p_T^W$  distribution calculated by the event generator RESBOS [48, 49, 50] (which includes NLO QCD corrections) with the important ‘ $g_2$ ’ parameter tuned by a fit to this analysis’s  $Z \rightarrow \ell^+\ell^-$  event samples [45]. The final product of the event generation procedure is the kinematic properties of the lepton(s) and any photons produced by the  $W$  or  $Z$  decay as they leave the interaction point and enter the detector. This is known as the generator level event information.

The set of parton distribution functions (PDF’s) used is CTEQ6M [51]. The uncertainties on the PDF’s are propagated to  $m_W$ . The total PDF uncertainty on the  $W$  mass measurement is roughly  $10 \text{ MeV}/c^2$ ; without improvements in the PDF uncertainties themselves this will be a limiting factor on the possible accuracy achievable in future  $W$  mass measurements at proton-antiproton colliders. Other systematic uncertainties on  $m_W$  arising from event generation are also estimated and used in the calculation of the overall  $m_W$  uncertainty.

## 4.6 Detector Simulation

The detector simulation uses the generator level event information from each simulated event and models the passage of particles through the CDF detector and the detector response to these particles to create simulated versions of the observable kinematic distributions used to fit  $m_W$ . The specific detector simulation detailed here is UCL Fast Simulation. As indicated below some aspects of UCL Fast Simulation are treated in this section while others are treated in either subsequent sections of this chapter or in later chapters. Note that the tracker momentum scale and calorimeter energy scale and non-linearity applied by this analysis can be regarded (both conceptually and practically) as either final calibrations applied to the data<sup>5</sup> or as an aspect of the simulation depending on the exact definition of the *observable* kinematic distributions used in fits for  $m_W$ . UCL Fast Simulation applies the calorimeter energy scale in the simulation and the tracker momentum scale as a correction to the data.

Simulating the muon channel requires models of energy loss by muons through interactions with material in the silicon tracker (see later in this section), muon energy deposition in the calorimeter (see later in this section), the dependence of various muon efficiencies on  $\eta$ ,  $\phi$ ,  $\vec{u}_T$  and  $p_T^\mu$  (see later in this section), the measurement of muon momenta in the COT (see later in this section and section 4.7) and the hadronic recoil (see section 4.8). The modelling of secondary photons and electrons in muon events is also necessary; the treatment of these is essentially as described below for the electron channel.

Simulating the electron channel requires models of energy loss by electrons and photons through interaction with material in the silicon tracker and COT (see later in this section), energy deposition in the TOF detector and solenoid by electrons and photons (see later in this section), the leakage of energy from the electromagnetic calorimeter into the hadronic calorimeter (see later in this section), the dependence of various electron efficiencies on  $\eta$ ,  $\phi$ ,  $\vec{u}_T$  and  $p_T^\mu$  (see later in this section), the measurement of

---

<sup>5</sup>Both momenta measured in the COT and energies measured in the calorimeter are reconstructed from electronic readout information using standard collaboration wide calibrations; any scalings specific to this analysis are applied in addition to these.

electron momenta in the COT (see later in this section and section 4.7), the calorimeter energy scale (see section 9.1), the calorimeter non-linearity (see section 9.3.4) and the hadronic recoil (see section 4.8).

Simulated events are reconstructed and selected using the same event selection procedure as data events as far as possible. However some cuts cannot be meaningfully applied to simulated events due to simplifications made in the simulation. Any bias on the measured  $m_W$  due to these differences is minimised by the accurate modelling of acceptances and efficiencies.

### 4.6.1 Lepton and Photon Interactions

It is important to model the passage of the primary electron or muon through the silicon tracker and COT. It is also important to model the passage of any other electrons or photons generated in the simulated event. The important effects of Bremsstrahlung and pair production are discussed in detail in later chapters; this section provides an overall introduction to lepton and photon interactions and discusses ionisation in detail. Photons are produced in  $W$  decay events as either initial or final state radiation emitted during the  $W$  boson production and decay event, or by Bremsstrahlung occurring in the detector. Additional electrons are produced through photon pair production. In the electron channel if these photons and secondary electrons deposit their energy in the same tower and  $\phi$  wedge (or in a neighbouring tower in the same  $\phi$  wedge) of the calorimeter as the primary electron their energy will not be individually resolved and instead will be added to the measured energy of the primary electron; this is called recombination. Note the momentum of the primary electrons (or muons) measured in the COT is not affected by the presence of secondary particles (in other words, there is no recombination from the point of view of the  $p_T$  measurement). In the electron channel the  $E/p$  calibration of the energy scale is thus highly sensitive to the modelling of secondary particles. In both channels the energy of secondary particles detected in the calorimeter adds to the recoil vector, except for those that recombine with a primary electron or are excluded because they are in the primary muon's (or electron's) 'knock-out' region (see section 4.8).

Thus simulated muons, electrons and photons (including those generated through interactions occurring in the detector) are individually propagated through the silicon tracker and the COT to the calorimeter (and for muons, on through to the muon chambers) in UCL Fast Simulation. Leptons and photons lose energy by a variety of mechanisms as they pass through matter.

The typical muon from a  $W$  decay has an energy of roughly 40 GeV; the dominant energy loss mechanism for such muons as they traverse the silicon tracker is ionisation. The mean rate of energy loss for a muon from ionisation is predicted by the Bethe-Bloch equation [14]:

$$-\frac{dE}{dx} = K \frac{Z}{A} \frac{1}{\beta^2} \left[ \frac{1}{2} \ln \frac{2m_e c^2 \beta^2 \gamma^2 T_{\max}}{I^2} - \beta^2 - \frac{\delta(\beta\gamma)}{2} \right] \quad (4.3)$$

where  $-\frac{dE}{dx}$  is the muon's energy loss per unit length (normalised by density),  $Z$  and  $A$  are the atomic number and atomic mass of the media being traversed respectively,  $m_e$  is the mass of the electron,  $\beta$  and  $\gamma$  are relativistic kinematic variables with their usual meaning,  $T_{\max}$  is the maximum kinematic energy that can be imparted to a free electron in a single collision,  $I$  is the mean excitation energy and  $\delta(\beta\gamma)$  is the density effect correction to the ionisation energy loss.  $K$  is defined as  $K = 4\pi N_A r_e^2 m_e c^2$  where  $N_A$  is Avogadro's number and  $r_e$  is the classical electron radius. UCL Fast Simulation initially modelled the energy loss in each layer of the tracker as equal to exactly this mean value. However poor modelling of the mass resolution of  $J/\psi$  and  $\Upsilon(1S)$  data samples used in the calibration of the tracker momentum scale necessitated the implementation of a more sophisticated model of energy losses through ionisation. This revised implementation samples the energy loss in each layer from a Landau distribution with a maximum energy loss cut-off applied. The value of the cut-off is chosen to keep the mean energy loss equal to the Bethe-Bloch equation prediction.

The typical energy of an electron from a  $W$  decay is 40 GeV. Figure 4.2 shows the contributions of various energy loss mechanisms to overall electron energy losses. The dominant energy loss mechanism for electrons from a  $W$  boson decay as they traverse material in the silicon tracker is Bremsstrahlung. However there is also a small but

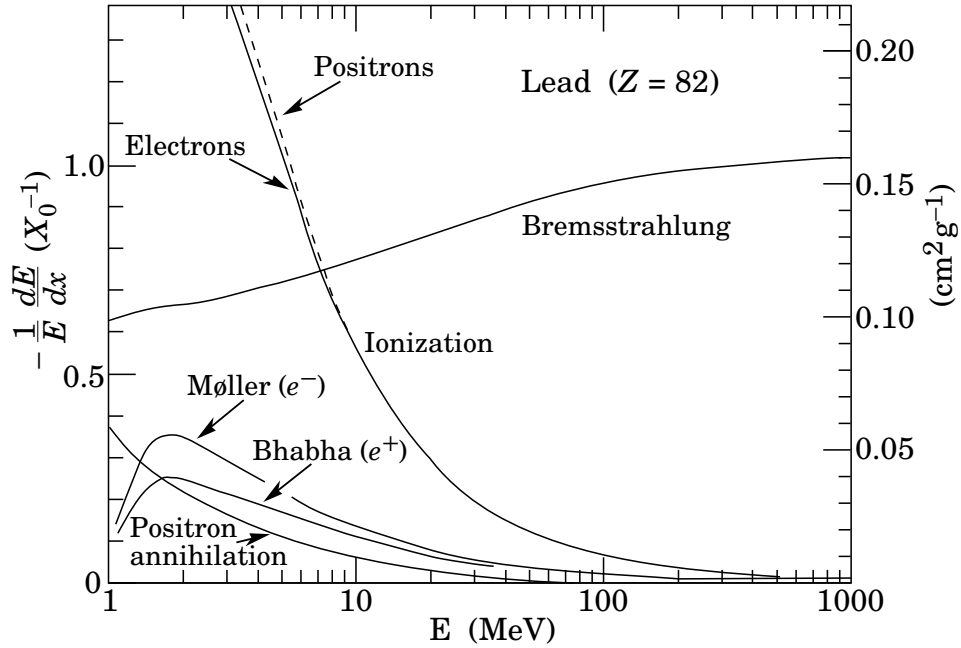


Figure 4.2: The fractional energy loss per radiation length in lead as a function of electron (or positron) energy for a variety of electron energy loss mechanisms. Reproduced from reference [14].

significant contribution to the energy loss from ionisation. The modelling of electron energy loss by ionisation is essentially identical to that for muons. The modelling of Bremsstrahlung in UCL Fast Simulation is discussed very extensively in Chapters 5 to 8.

Figure 4.3 shows the contributions of various energy loss mechanisms to overall photon energy losses. The dominant energy loss mechanism for photons with energies of interest to this analysis (between several hundred MeV and several GeV) is pair production. A small but important contribution to energy loss for such photons is also made by Compton scattering. The modelling of pair production is discussed extensively in Chapters 5, 6 and 8. A very basic model of Compton scattering is also implemented in UCL Fast Simulation.

All of these energy loss mechanisms depend on both the nature and thickness of the media being traversed. UCL Fast Simulation models energy loss in the silicon tracker (and the inner wall of the COT) using a material map (called SiliMap) [52] which

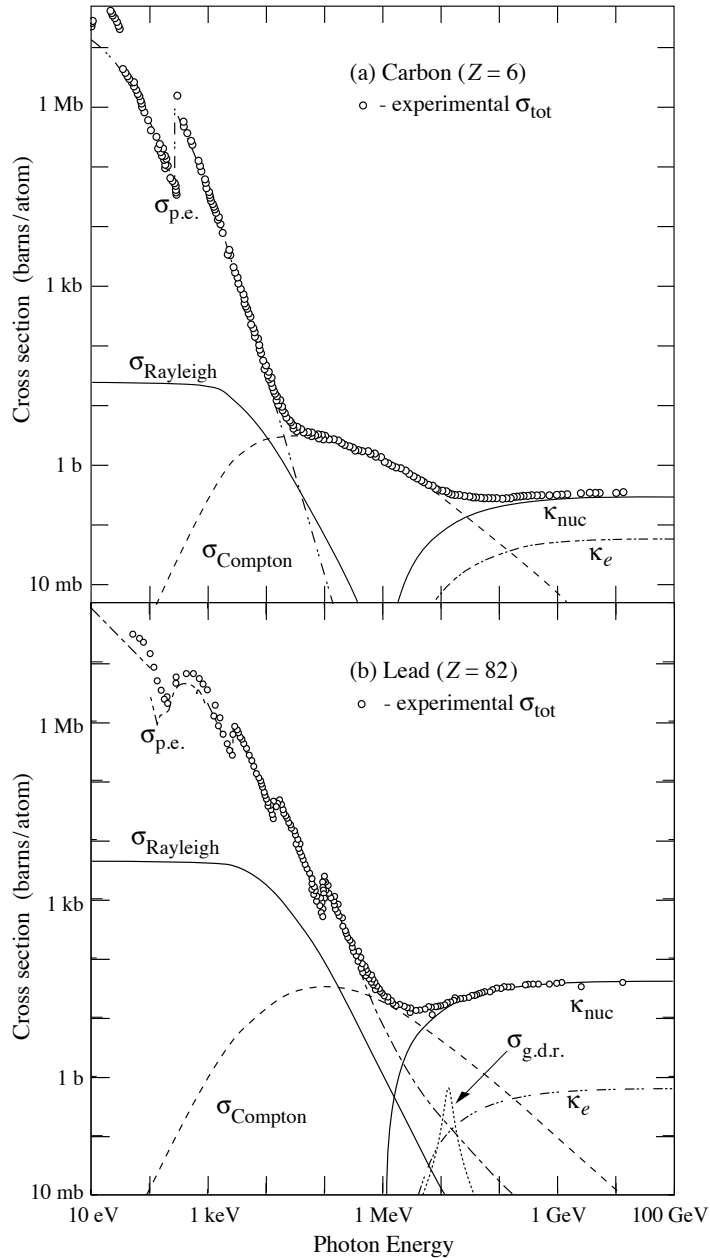


Figure 4.3: Total cross sections for the variety of processes through which photons interact with matter as a function of incident photon energy. The processes are:

- $\sigma_{\text{p.e.}}$  = Atomic photoelectric effect (electron ejection, photon absorption)
- $\sigma_{\text{Rayleigh}}$  = Rayleigh (coherent) scattering - atom neither ionized nor excited
- $\sigma_{\text{Compton}}$  = Incoherent scattering (Compton scattering off an electron)
- $\sigma_{\text{nuc}}$  = Pair production, nuclear field
- $\sigma_{\text{e}}$  = Pair production, electron field
- $\sigma_{\text{g.d.r.}}$  = Photonuclear interactions, most notably the Giant Dipole Resonance. In these interactions the target nucleus is broken up.

Figure reproduced from reference [14].

consists of a set of persistent look-up tables, rather than a complete model of the full detector geometry. SiliMap splits the silicon tracker into concentric logical layers based on the actual physical layers of material in the tracker and sub-divides each layer into bins in  $z$  and  $\phi$ . SiliMap provides the necessary parameters of the material in each bin in each logical layer required to correctly model energy losses in that bin. (In fact some key information required for the accurate modelling of Bremsstrahlung is actually lacking from SiliMap, see Chapter 7 for further details.) Bremsstrahlung interactions by electrons (by far the most significant energy loss mechanism) in the COT are also modelled. As the COT is mostly filled with gas, a medium in which only minimal energy losses occur, all other energy loss mechanisms in the COT are neglected.

The systematic uncertainty on  $m_W$  arising from residual mis-modelling of lepton and photon interactions is estimated and used in the calculation of the overall uncertainty on  $m_W$ . Estimates of the uncertainties on  $m_W$  due to residual mis-modelling of Bremsstrahlung and pair production are given in Chapter 8.

#### 4.6.2 Material Scale Determination

Both the total cross section for Bremsstrahlung for an electron and the total cross section for pair production and Compton scattering for a photon are dependent on the fractional number of radiation lengths of material traversed by the electron or photon ( $dX_0$ ). This information is provided for each bin in SiliMap and is appropriately adjusted according to the angle of incidence of the electron or photon on the bin. We multiply the  $dX_0$  value given in SiliMap for each bin by a global material scale factor  $S_{\text{mat}}$ . This scale factor is estimated by fitting the  $E/p$  distribution in three bins in the region  $0.8 < E/p < 1.6$  for simulated  $W$  events to the signal event sample. The size of the three  $E/p$  bins used is unequal; the first bin spans the range  $0.8 < E/p < 1.2$  while the other two bins span the range  $1.2 < E/p < 1.4$  and  $1.4 < E/p < 1.6$ . The high  $E/p$  tail of the  $E/p$  distribution consists mostly of events where a large fraction of the primary electron's energy has been transferred to a photon through Bremsstrahlung in the silicon tracker and so is highly sensitive to the total cross section for Bremsstrahlung. The peak of the  $E/p$  distribution around  $E/p \approx 1$  is less sensitive to the total cross section for Bremsstrahlung. Thus

this fit provides a statistically precise estimate of  $S_{\text{mat}}$  by comparing the magnitude of the peak and the upper tail of the  $E/p$  distribution. An  $E/p$  background distribution is added to the templates for this fit; this background is produced using the same techniques as are used to produce backgrounds for fits to estimate  $m_W$ . Examples of the comparison of the best fit template to data for material scale fits are given in section 9.3.2.

### 4.6.3 Modelling Momentum Measurement

Individual COT hits are not modelled in UCL Fast Simulation, instead the resolution of COT momentum measurements is modelled by combining information from CdfSim studies with fits to  $Z \rightarrow \mu^+ \mu^-$  data. The variable  $\Delta\rho$  is defined:

$$\Delta\rho \equiv \left(\frac{q}{p_T}\right)_{\text{gen.}} - \left(\frac{q}{p_T}\right)_{\text{meas.}} \quad (4.4)$$

where  $\left(\frac{q}{p_T}\right)_{\text{gen.}}$  is the generator level value of the lepton's curvature (its charge divided by its transverse momentum) and  $\left(\frac{q}{p_T}\right)_{\text{meas.}}$  is the measured value of the lepton's curvature. Separate  $\Delta\rho$  distributions are obtained from CdfSim simulations of  $W \rightarrow \mu\nu$  events for four possible types of track:

- Tracks with  $N_{\text{SL}}^{\text{axial}} = 3$  and  $N_{\text{SL}}^{\text{stereo}} = 3$
- Tracks with  $N_{\text{SL}}^{\text{axial}} = 3$  and  $N_{\text{SL}}^{\text{stereo}} = 4$
- Tracks with  $N_{\text{SL}}^{\text{axial}} = 4$  and  $N_{\text{SL}}^{\text{stereo}} = 3$
- Tracks with  $N_{\text{SL}}^{\text{axial}} = 4$  and  $N_{\text{SL}}^{\text{stereo}} = 4$

Examples of typical  $\Delta\rho$  distributions are given in fig. 4.4. For each track simulated in UCL Fast Simulation the type of track is decided by sampling from the  $N_{\text{SL}}^{\text{axial}}$  and  $N_{\text{SL}}^{\text{stereo}}$  distributions. (These distribution having been measured in  $Z \rightarrow \mu^+ \mu^-$  data.) A  $\Delta\rho$  is then sampled from the appropriate CdfSim distribution. For each track the

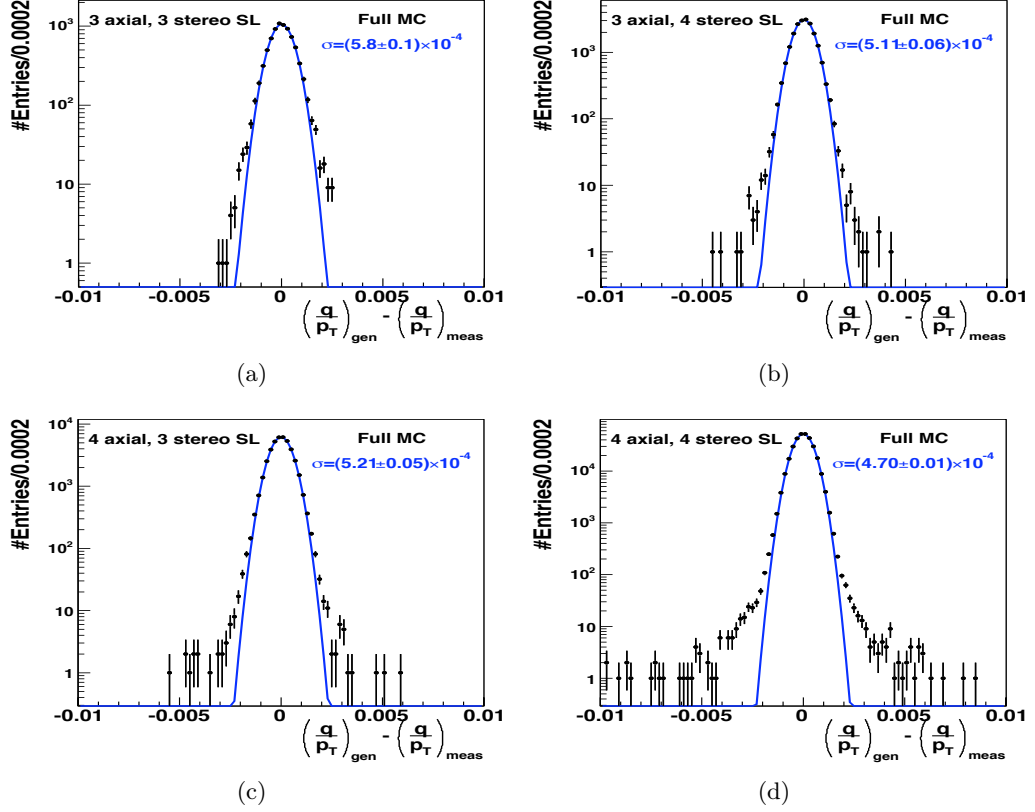


Figure 4.4: Examples of typical  $\Delta\rho$  distributions for tracks with: (a)  $N_{\text{SL}}^{\text{axial}} = 3$  and  $N_{\text{SL}}^{\text{stereo}} = 3$ ; (b)  $N_{\text{SL}}^{\text{axial}} = 3$  and  $N_{\text{SL}}^{\text{stereo}} = 4$ ; (c)  $N_{\text{SL}}^{\text{axial}} = 4$  and  $N_{\text{SL}}^{\text{stereo}} = 3$ ; and (d)  $N_{\text{SL}}^{\text{axial}} = 4$  and  $N_{\text{SL}}^{\text{stereo}} = 4$ . These are actually the distributions that were used in UCL Fast Simulation in a previous analysis of the  $W$  boson width and are included here for illustrative purposes; the distribution in UCL Fast Simulation for the  $W$  mass analysis have been subsequently updated. The distributions are parameterised in the simulation by as gaussians (shown in the plots in blue), though it is evident the data has a non-gaussian component. Reproduced from[53].

lepton's measured momentum is corrected according to:

$$\left(\frac{q}{p_T}\right)_{\text{meas.}} = \left(\frac{q}{p_T}\right)_{\text{gen.}} + (S_{\text{res.}} \times \Delta\rho) \quad (4.5)$$

where  $S_{\text{res.}}$  is estimated by fitting the invariant  $Z$  mass reconstructed from the muon momenta in  $Z \rightarrow \mu^+\mu^-$  data. The effect of finite beam spot size on measured momenta through the beam constraint is also simulated, as (for electrons) is the effect of Bremsstrahlung radiation occurring in the silicon tracker and COT.

#### 4.6.4 Modelling of the Calorimeter

Electrons and photons are assigned to calorimeter towers according to the geometry of the CEM. The energy of incident particles is adjusted to account for energy losses in the TOF and solenoid, leakage of energy into the hadronic calorimeter (all three of these effects are modelled by sampling from distributions obtained from CdfSim) and by the application of the non-linearity (see section 9.3.4). The energy in each tower is then taken as the sum of the energies of all the particles incident on that tower and the CDF clustering algorithm is simulated. A contribution from underlying event energy (a phenomenon described in section 4.8) is added to the energy of each cluster. This contribution is sampled from the distribution of energy in two-tower clusters in  $W \rightarrow e\nu$  events at the same  $\eta$  but a different  $\phi$  to the electron and then scaled according to its observed dependence on the total energy in the event. The energy leaked into the hadronic calorimeter is recorded and a basic model of the hadronic calorimeter response is used to simulate the  $E_{\text{had}}/E_{\text{em}}$  cut.

The small quantity of energy deposited in the calorimeter by muons (important in the simulation of certain cuts applied to muon candidates) is modelled by sampling from cosmic ray data. The energy of any photons or secondary electrons that enter the same tower as the muon are added to this energy. A contribution from underlying event energy is also added to this energy; the modelling of this is the same as that for electrons described above.

#### 4.6.5 Efficiencies

The efficiency of a selection requirement is defined as:

$$\epsilon \equiv \frac{N_{\text{pass}}}{N_{\text{total}}} \quad (4.6)$$

where  $N_{\text{pass}}$  is the number of events passing the selection requirement and  $N_{\text{total}}$  is the total number of events tested against the requirement. The simplified model of the detector used in UCL Fast Simulation necessitates the estimation and explicit modelling of the  $\eta$  and  $\phi$  dependencies of the muon reconstruction efficiency, lepton trigger efficiency

and track hit efficiency as such dependencies may affect the shape of the kinematic distributions used to fit  $m_W$ . These efficiencies and their  $\eta$  and  $\phi$  dependencies are measured from data and then modelled accordingly. It is also necessary to model the  $\vec{u}_T$  and  $p_T^\mu$  dependencies of lepton cut efficiencies; these are studied using the full detector geometry in CdfSim and then parameterised in UCL Fast Simulation. A detailed account of the modelling of efficiencies is given in reference [54].

## 4.7 Setting the Tracker Momentum Scale

The absolute scale of momentum measurements made in the COT can be determined very accurately using a combination of fits to the mass distribution (reconstructed from COT momentum measurements) of the  $Z \rightarrow \mu^+\mu^-$  event sample and the mass distributions (also reconstructed from COT momentum measurements) of  $J/\psi \rightarrow \mu\mu$  and  $\Upsilon(1S) \rightarrow \mu\mu$  events samples, selected with suitable cuts. In each case the absolute momentum scale is the estimated parameter; the masses of the  $Z$  boson,  $J/\psi$  and  $\Upsilon(1S)$  used in the simulation are the (very well known) world averages for these particles and are held constant. The cross section for  $J/\psi \rightarrow \mu\mu$  events at the Tevatron was large; thus fits to the  $J/\psi$  mass distribution are very statistically accurate. However the  $J/\psi$  mass is only  $\sim 3 \text{ GeV}/c^2$  and hence the momentum of the tracks from  $J/\psi \rightarrow \mu\mu$  events is considerably smaller than that from leptonic  $W$  decays. The mass of the  $\Upsilon(1S)$  is  $\sim 10 \text{ GeV}/c^2$  so  $\Upsilon(1S) \rightarrow \mu\mu$  events provide a second high statistics calibration of the momentum scale for higher momentum tracks<sup>6</sup>.  $Z \rightarrow \mu^+\mu^-$  events provide a third calibration for tracks with momenta similar to those produced by leptonic  $W$  decay events. The momentum scale is applied as a correction to the data.

COT alignment and curvature corrections are also applied to the data. The alignment correction is derived by analysing cosmic ray data, while the curvature correction is derived by considering differences in the  $E/p$  distribution between positrons and electrons in  $W \rightarrow e\nu$  data. The calibration of the tracker momentum scale and application

---

<sup>6</sup>The precision of the momentum scale determined from  $J/\psi \rightarrow \mu\mu$  and  $\Upsilon(1S) \rightarrow \mu\mu$  events is roughly similar; the  $J/\psi$  event sample is considerably larger than the  $\Upsilon(1S)$  event sample but there is also a larger systematic error on the  $J/\psi$  calibration.

of COT alignment and curvature corrections are complex processes and it is not, for the sake of brevity, possible to include full details in this thesis; a more detailed description is given in reference [55]. The systematic uncertainty on  $m_W$  arising from the calibration of the tracker momentum scale is estimated and used in the calculation of the overall uncertainty on  $m_W$ .

## 4.8 The Recoil Model

Both  $m_T$  and  $\not{p}_T$  have a strong dependence on the recoil vector  $\vec{u}_T$ ; thus the accurate modelling of this vector in simulated  $W$  events (for both the muon and electron decay channels) is essential for the accurate measurement of the  $W$  mass. The modelling of the recoil is very complex and it is only possible to give a brief overview of it here; a detailed description is given in reference [56].

Though  $\vec{u}_T$  is used as a measure of the  $\vec{p}_T^W$ , the relationship between the observed recoil and the true  $W$  transverse momentum is very complex and they are perhaps best regarded (for the purposes of recoil modelling) as separate but closely related variables. It is important to accurately model the experimentally measured value of  $\vec{u}_T$  used in forming the  $m_T$  and  $\not{p}_T$  kinematic distributions.  $\vec{u}_T$  is defined as the vector sum of the energy measured in all the central and plug calorimeter towers. This sum excludes the ‘knock-out region’, a set of towers around (and including) the primary lepton’s calorimeter tower. The exclusion of this knock-out region is intended to separate energy deposited by the primary lepton from recoil energy. The exact definition of the knock-out region differs between the electron and muon channels and is based on studies of the leakage of energy of electromagnetic clusters into neighbouring towers. (It also excludes towers with  $|\eta| > 2.6$  where less than 5 GeV of energy are deposited.) A scale factor is applied to the energy in each tower; this scale factor differs between plug towers and central towers such as to give a uniform response across both calorimeters once applied.

There are three phenomena that contribute to the recoil vector: Bremsstrahlung photons (and secondary electrons) from the primary lepton that are emitted at wide angles and deposit energy in towers outside the knock-out region; energy from the

radiation of initial state gluons that recoil against the  $W$  boson, referred to as the ‘hard’ QCD sub-process; and ‘soft’ underlying event energy from the proton and antiproton remnant’s interactions and any additional  $p\bar{p}$  collisions that occur during the same bunch crossing. Bremsstrahlung photons and secondary electrons are explicitly simulated as described in previous sections of this chapter. The other contributions to the recoil vector are too complex to model from first principles; instead such contributions are modelled using a parameterisation of  $Z \rightarrow \ell^+\ell^-$  data. The  $Z$  data sample is suitable for this because the hadronisation process characteristic of the ‘hard’ QCD contributions for  $Z$  and  $W$  production will be very similar and  $p_T^Z$  is known for  $Z$  events from the leptons, and thus the true recoil of such events is known. The parameterisation splits the recoil vector into a component parallel to the boson  $p_T$  that is sensitive to the hard QCD sub process (predominately initial state gluon radiation) and a component perpendicular to the boson  $p_T$  that is sensitive to the soft underlying event. Knock-out regions are excluded around both of the leptons in the calculation of the observed recoil of  $Z$  data events; for the parameterisation to be an accurate model of  $W$  data it is important that  $Z$  and  $W$  events are analysed consistently. Comparisons of this parameterisation of the recoil to  $W$  data are given in fig. 4.5.

The knock-out region is modelled in the simulation. Simulated leptons and photons that enter knock-out region towers are not included in the simulated recoil vector. Some of the energy deposited in the knock-out region removed in data will not be associated with the primary lepton but instead be true recoil energy or underlying event energy. This is modelled by sampling from the distribution of the total energy measured in ‘pseudo knock-out regions’ in  $W \rightarrow \ell\nu$  data and subtracting the sampled energy from  $u_T$ . These pseudo knock-out regions are defined at  $\Delta\phi = \pm 90^\circ$  to the actual knock-out region and are otherwise identical to the actual knock-out region. The dependence of the energy in the pseudo knock-out region on the projection of the recoil in the direction of the (pseudo) knock-out region, luminosity and  $\eta$  in data is parameterised; the energy subtracted from the simulation is then scaled using this parameterisation according to the characteristics of the event. The knock-out region is also modelled in the simulation of  $Z$  events.

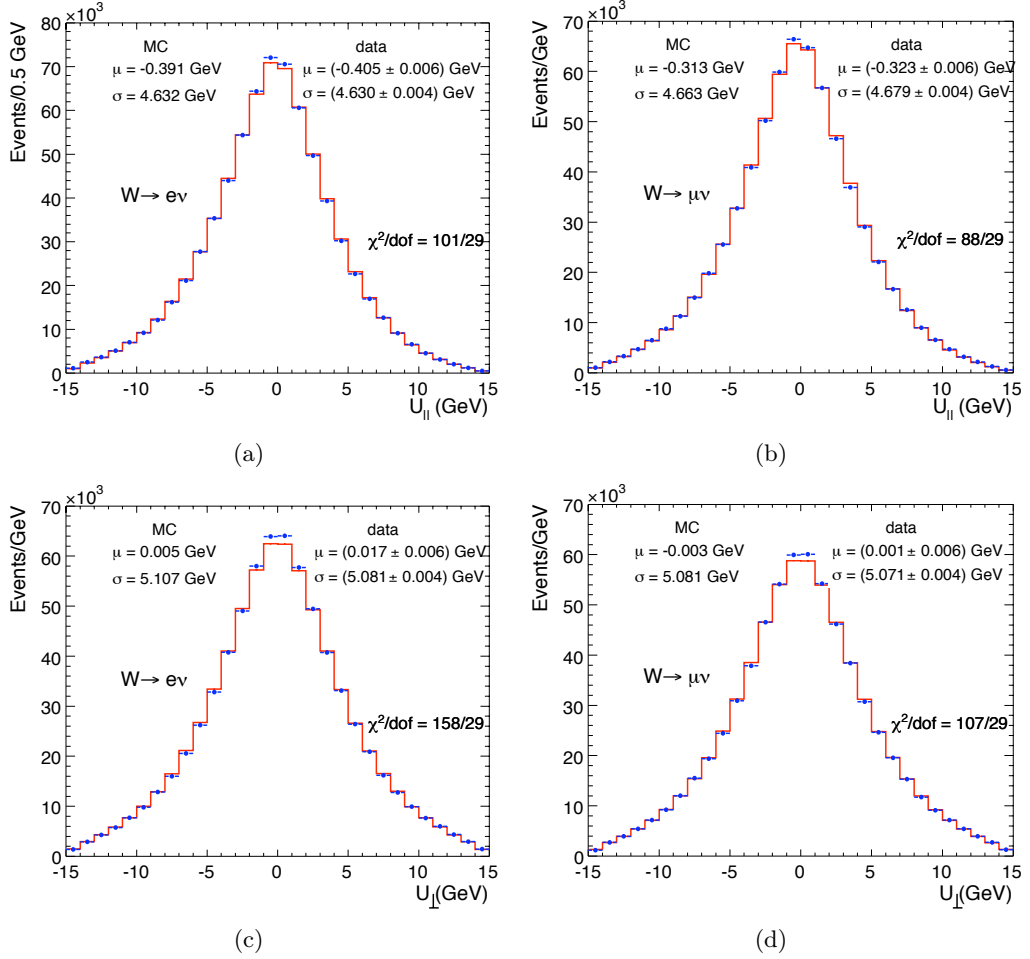


Figure 4.5: Comparison of the components of the recoil parallel (a)(b) and perpendicular (c)(d) to the direction of the primary lepton for  $W$  data and simulation. The projections parallel and perpendicular to the lepton are used here as the  $p_T^W$  is unknown. Reproduced from reference [56].

The systematic uncertainty on  $m_W$  arising from the modelling of the recoil is estimated and used in the calculation of the overall uncertainty on  $m_W$ .

## Chapter 5

# Theoretical Models of Bremsstrahlung and Pair Production

### 5.1 Electron Bremsstrahlung

#### 5.1.1 Introduction

An electron cannot radiate a photon in a vacuum (except if the electron is passing through a magnetic field) because such a process cannot conserve both energy and momentum. However when an electron passes through an atom, it is accelerated and decelerated by the electric field of the nucleus (the electric field of the atomic electrons can also have an affect), causing it to lose energy by radiating photons. The nucleus recoils in this process, allowing energy and momentum to be conserved. This process is called Bremsstrahlung (meaning ‘braking radiation’ in German) [57]. The dominant Feynman diagrams for this process are shown in fig. 5.1. Note that they are closely related to those for pair production (see section 5.2).

Bremsstrahlung events can occur in the CDF Run II detector in the silicon tracker and it is necessary to accurately simulate them in UCL Fast Simulation. Bremsstrahlung events can also occur in the COT and these too are modelled in UCL Fast Simulation.

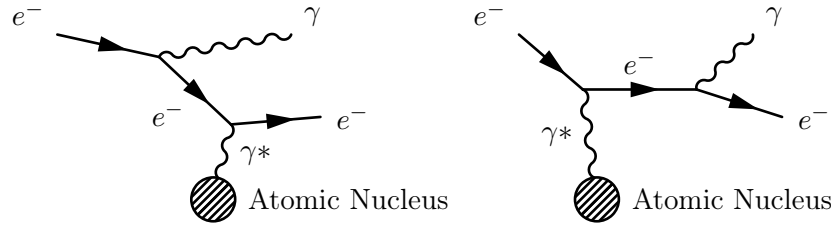


Figure 5.1: The two dominant Bremsstrahlung Feynman diagrams.

To simulate Bremsstrahlung events requires a model of the total Bremsstrahlung cross section as a function of incident electron energy and also the differential cross section as a function of the variable  $y$ , which is the fractional energy lost by the electron through the radiation of photons, i.e.:

$$y \equiv \frac{k}{E} \quad (5.1)$$

where  $E$  is the energy of the incident electron and  $k$  the energy of the radiated photon. It is assumed that radiated photons are co-linear with the electron, which is a very good approximation at high energies. Hence the angular distribution of radiated photons is not discussed here. In UCL Fast Simulation the differential and total cross sections are treated separately. Three models of the Bremsstrahlung differential cross section  $y$ -spectrum are discussed below; the basic functional form as given by reference [58] (including a modification of this that accounts for the LPM effect), the GEANT4 version 4.9.0 model and the newer GEANT4 version 4.9.2 model. Three possible models of the Bremsstrahlung total cross section are discussed below; the first model is the integral of the basic functional form for the differential cross section given in reference [58], the second model is the model used by GEANT4 4.9.0 (for all incident electron energies) and the third model is the model used by GEANT4 4.9.2 for incident electron energies greater than 1 GeV. The second model is also used by GEANT4 4.9.2 for incident electron energies less than 1 GeV.

### 5.1.2 Basic Model of Bremsstrahlung Differential Cross Section $y$ -Spectrum

The most basic functional form for the Bremsstrahlung differential cross section  $y$ -spectrum at high energies (given in review [58]) is:

$$\frac{d\sigma}{dy} = \frac{A}{yX_0N_A} \left( \frac{4}{3} - \frac{4}{3}y + y^2 \right) \quad (5.2)$$

where  $A$  is the atomic mass number of the absorber,  $X_0$  is the radiation length of the absorber (in  $\text{g cm}^{-2}$ ) and  $N_A$  is Avogadro's number. This formula is based on many assumptions and will be inaccurate near  $y = 1$  and  $y = 0$ . The inaccuracy near  $y = 1$  is because eq. (5.2) assumes that the screening of the nuclear Coulomb charge by the atomic electrons is complete (i.e. the reduction in strength of the nuclear Coulomb field acting on the electron due to the screening always takes its maximum value), but at very high- $y$  this may not be true as for such a large energy exchange the interaction will occur very close to the nucleus. The inaccuracy near  $y = 0$  is due to two effects - dielectric suppression and the Landau-Pomeranchuk-Migdal (LPM) effect (described below). Equation (5.2) also assumes that an ultra-relativistic limit applies (defined as  $E \gg m_e c^2$ ,  $(E - k) \gg m_e c^2$  and  $k \gg m_e c^2$ ); this assumption may contribute to the inaccuracy of eq. (5.2). Note eq. (5.2) is actually a simplified version of the 'Complete Screening Formula' given in reference [59]; in the former a small term is discarded to allow the Bremsstrahlung differential cross section to be defined in terms of a generic material property, radiation length. This may also contribute to the inaccuracy of eq. (5.2).

The LPM effect is due to Bremsstrahlung interactions at low- $y$  being spread across a relatively long distance, this being possible because the momentum transfer is smaller, allowing the virtual exchange particle a relatively long lifetime. The distance the interaction is spread over is called the formation length. If this becomes comparable with the distance between scattering centres (i.e. atomic nuclei) then quantum interference can occur between the amplitudes for Bremsstrahlung at different centres [58]. The LPM effect only becomes important for Bremsstrahlung interactions with a  $y$ -value below a

certain threshold, which is given in reference [58] as:

$$y < \frac{E}{E + E_{\text{LPM-1}}}. \quad (5.3)$$

Here  $E_{\text{LPM-1}}$  is dependent on the radiation length of the interaction medium in question<sup>1</sup>, and is defined:

$$E_{\text{LPM-1}} \equiv \frac{\alpha(m_e c^2)^2 X_0}{2hc\rho} \approx 7.7 \times \frac{X_0}{\rho} \text{ TeV/cm} \quad (5.4)$$

where  $\rho$  is the density of the medium. For energies below this  $y$ -value, the Bremsstrahlung differential cross section is suppressed by a factor of  $S_{\text{LPM}}$ . A good approximation for this is given by:

$$S_{\text{LPM}} = \sqrt{\frac{kE_{\text{LPM-1}}}{E^2}} \quad (5.5)$$

This gives values that are within about 10% of a more detailed calculation performed by Migdal [60, 61]. A basic differential cross section  $y$ -spectrum including the LPM effect can be achieved by applying this suppression to eq. (5.2). This is henceforth referred to as the Basic Bremsstrahlung Differential Cross Section Model.

### 5.1.3 GEANT4 4.9.0 Model of the Bremsstrahlung Differential Cross Section $y$ -Spectrum

GEANT4 4.9.0's implementation for the Bremsstrahlung differential cross section  $y$ -spectrum [62]<sup>2</sup>, in terms of physics, differs from that of the Basic Bremsstrahlung Differential Cross Section Model in two respects. Firstly it samples photon energies from a more sophisticated  $y$ -spectrum, that considers the possibility of incomplete screening of the nuclear Coulomb field by atomic electrons, does not require the assumption that an ultra-relativistic limit applies (a novel technique is used to circumvent the lack of screened Bremsstrahlung differential cross section formula that does not assume an ultra-relativistic limit applies) and does not discard any small terms. Secondly it calcu-

<sup>1</sup>A different definition of  $E_{\text{LPM}}$  is used later. To distinguish the two definitions we append a number to the subscript, hence we have either  $E_{\text{LPM-1}}$  (as defined here) or  $E_{\text{LPM-2}}$  (as defined later).

<sup>2</sup>This reference is actually for the GEANT4 4.9.1 Physics Reference Manual. However the details of the Bremsstrahlung and pair production treatment given also apply to GEANT4 4.9.0.

lates the effect of dielectric suppression in addition to that of LPM suppression at low  $y$ -values.

GEANT4 4.9.0 uses a parameterisation fitted to the  $y$ -spectra of Seltzer and Berger [63] for various elements. The Seltzer and Berger tables are themselves based on the synthesis of various theoretical results and they agree with theoretical and experimental results to within 5% for incident electrons with energies greater than 50 MeV.

Bremsstrahlung can occur both in the Coulomb field of an atomic nucleus (henceforth referred to as electron-nucleus Bremsstrahlung) and in the Coulomb field of atomic electrons (henceforth referred to as electron-electron Bremsstrahlung). The electron-nucleus Bremsstrahlung cross section is the dominant contribution to the overall Bremsstrahlung cross section (for 40 GeV electrons incident on silicon, roughly 90% of the total Bremsstrahlung cross section will be due to electron-nucleus Bremsstrahlung); the remainder of the discussion in this paragraph refers to electron-nucleus Bremsstrahlung. It is not possible to calculate the exact matrix element for Bremsstrahlung because such a matrix element would require the exact Dirac wave functions of the initial and final electrons and the Dirac wave equation can not be solved in closed form for an electron in a Coulomb field. It is hence necessary to either assume an ultra-relativistic limit applies (defined as  $E \gg m_e c^2$ ,  $(E - k) \gg m_e c^2$  and  $k \gg m_e c^2$ ) and use approximate relativistic Dirac wave functions for an electron in a Coulomb field or use free particle wave functions perturbed to first order in  $Z$  (where  $Z$  is the atomic number of the media being traversed); this later case is known as the Born approximation. (A further possibility is to assume a non-relativistic limit applies and use approximate Schrödinger wave functions for an electron in a Coulomb field; this approach has met with very limited success and is not relevant to this discussion). Bremsstrahlung differential cross section  $y$ -spectra formulae calculated using approximate relativistic Dirac wave functions (henceforth referred to as Coulomb-corrected formulae) differ from similar formulae calculated using the Born approximation (henceforth referred to as Born approximation formulae) by an additional additive correction factor known as the Coulomb correction. The effect of atomic screening of the nuclear Coulomb field can be included in both Coulomb-corrected and Born approximation Bremsstrahlung differential cross section

Formula Type	Valid Only in Ultra-Relativistic Limit?	Includes the Effect of Atomic Screening?	Includes the Coulomb Correction?
Coulomb-corrected	yes	yes	yes
Screened Born approximation	yes	yes	no
Unscreened Born approximation	no	no	no

Table 5.1: Summary of the properties of three types of Bremsstrahlung differential cross section formulae.

$y$ -spectra formulae, such formulae that include this effect are henceforth referred to as screened formulae. Born approximation Bremsstrahlung differential cross section formulae that do not include the effect of atomic screening of the nuclear Coulomb field (henceforth referred to as unscreened formulae) exist for all energy regimes and do not require the approximation of either a non-relativistic or ultra-relativistic limit applying. The available screened Born approximation Bremsstrahlung differential cross section  $y$ -spectra formulae require the approximation of an ultra-relativistic limit applying; it is not clear if this is because it is not possible to calculate screened Born approximation differential cross section formulae for all energy regimes or simply that such formulae have not been calculated outside the ultra-relativistic limit because of the limited interest in Born approximation differential cross section  $y$ -spectra at lower incident electron energies where the Born approximation will be less accurate. Screened Bremsstrahlung differential cross section  $y$ -spectra formulae can be obtained for either the most general case of arbitrary screening (possibly requiring the numerical evaluation of atomic form factors) or for a range of simplified cases requiring various approximations (e.g. the complete screening approximation as discussed in section 5.1.2). The properties of these various types of Bremsstrahlung differential cross section formula are summarised in table 5.1. Reference [64] gives a detailed review of the different Bremsstrahlung cross section formulae available.

The starting point for the Seltzer and Berger tabulated theoretical results is the unscreened Born approximation electron-nucleus Bremsstrahlung differential cross section  $y$ -spectrum. This is valid in all energy regimes and does not require the assumption of

an ultra-relativistic limit applying. Two corrections are then applied to this unscreened Born approximation formula: a Coulomb correction and a correction for the screening of the nuclear Coulomb field by atomic electrons; thus an approximate Coulomb-corrected screened electron-nucleus Bremsstrahlung differential cross section  $y$ -spectrum with no requirement to assume an ultra-relativistic limit applies can be expressed:

$$\chi_{\text{electron-nucleus}} = \chi_{\text{Born}}^{\text{unscreened}} + \delta_{\text{screen}} + \delta_{\text{Coul}} \quad (5.6)$$

where  $\chi_{\text{electron-nucleus}}$  is the approximate Coulomb-corrected screened (using arbitrary screening) electron-nucleus Bremsstrahlung differential cross section  $y$ -spectrum and  $\chi_{\text{Born}}^{\text{unscreened}}$  the unscreened Born approximation electron-nucleus Bremsstrahlung differential cross section  $y$ -spectrum, both expressed in term of the dimensionless quantity  $\chi$ , which is defined as:

$$\chi \equiv [4\alpha r_e^2 Z^2]^{-1} k \frac{d\sigma}{dk}. \quad (5.7)$$

In this equation  $\alpha$  is the fine structure constant,  $r_e$  is the classical electron radius,  $Z$  is the atomic number of the media traversed and  $k$  is the energy of the radiated photon.

The correction for the screening of the nuclear Coulomb field by the atomic electrons is:

$$\delta_{\text{screen}} = {}^{\text{HE}}\chi_{\text{Born}}^{\text{screened}} - {}^{\text{HE}}\chi_{\text{Born}}^{\text{unscreened}} \quad (5.8)$$

where  ${}^{\text{HE}}\chi_{\text{Born}}^{\text{screened}}$  and  ${}^{\text{HE}}\chi_{\text{Born}}^{\text{unscreened}}$  are the screened and unscreened Born approximation electron-nucleus Bremsstrahlung differential cross section  $y$ -spectra assuming an ultra-relativistic limit applies. The correction is evaluated with Hartee-Fock form factors; this evaluation is not discussed in this thesis. The Coulomb correction is evaluated using a synthesis of several different techniques with varying regions of applicability, this evaluation is also not discussed here.

A further correction is made to the Seltzer and Berger results for the effect of electron-electron Bremsstrahlung. By combining the unscreened born level Bremsstrahlung differential cross section formulae with corrections derived in the ultra-relativistic limit the Seltzer and Berger results give the best possible approximation of a Brem-

sstrahlung differential cross section formulae with a general applicability to all energies regimes. The Seltzer and Berger results do not include LPM and dielectric suppression.

The GEANT4 4.9.0 parameterisation reproduces the Seltzer and Berger tables to on average within 2-3%, at most differing by about 10%. For the case of incident electrons with energies higher than 1 MeV (which is the only case which we are interested in here), the GEANT4 4.9.0 parameterisation is:

$$\frac{d\sigma}{dk} = \frac{C}{k} \times ((1 - a_h y)F_1(\delta) + b_h y^2 F_2(\delta)), \quad (5.9)$$

where  $C$  is a normalisation constant (to be fixed later by eq. (5.42)),  $k$  is the energy of the radiated photon, and  $\delta$  is a function of  $y$  given below<sup>3</sup>. The  $y$  dependence of eq. (5.9) is not immediately obvious, given  $F_1$  and  $F_2$  are both complicated functions of  $y$  themselves through  $\delta$ , though with knowledge of the kinetic and total energy of the electron it can be calculated<sup>4</sup>.  $F_1$  and  $F_2$  depend on the atomic number ( $Z$ ) of the material in question (for silicon  $Z = 14$ ) and are given by:

$$\delta \equiv \frac{136m_e}{Z^{1/3}E} \cdot \frac{y}{1-y} \quad (5.10)$$

$$F_1(\delta) = F_0(42.392 - 7.796\delta + 1.96\delta^2 - F) \quad \delta \leq 1 \quad (5.11)$$

$$F_2(\delta) = F_0(41.734 - 6.484\delta + 1.250\delta^2 - F) \quad \delta \leq 1 \quad (5.12)$$

$$F_1(\delta) = F_2(\delta) = F_0(42.24 - 8.368 \ln(\delta + 0.952) - F) \quad \delta > 1 \quad (5.13)$$

$$F_0 \equiv \frac{1}{42.392 - F} \quad (5.14)$$

$$F \equiv 4 \ln Z - 0.55(\ln Z)^2. \quad (5.15)$$

$a_h$  and  $b_h$  are the parameters that are fitted to the results of Seltzer and Berger. They

<sup>3</sup>The use of  $\delta$  here is unrelated to that in eq. (5.8).

<sup>4</sup>In fact the total and kinetic energies can be assumed to be the same at the energies we are interested in.

take the form:

$$a_h = 1 + \frac{a_{h1}}{u} + \frac{a_{h2}}{u^2} + \frac{a_{h3}}{u^3} \quad (5.16)$$

$$b_h = 0.75 + \frac{b_{h1}}{u} + \frac{b_{h2}}{u^2} + \frac{b_{h3}}{u^3} \quad (5.17)$$

where:

$$u \equiv \ln \left( \frac{T}{m_e} \right) \quad (5.18)$$

where  $T$  is the kinetic energy of the incident electron.  $a_{hi}$  and  $b_{hi}$  are themselves second order polynomials in the variable:

$$v \equiv [Z(Z + 1)]^{1/3}. \quad (5.19)$$

There are therefore 18 free parameters in total. These parameters are given in the GEANT4 4.9.0 code.

Equation (5.9) is similar to the screened Coulomb-corrected Bethe-Heitler formula [59, 65]; however it differs from the screened Coulomb-corrected Bethe-Heitler formula in two respects. In eq. (5.9), the parameters  $a_h$  and  $b_h$  are functions of incident electron energy and the atomic number of the absorber, whereas in the screened Coulomb-corrected Bethe-Heitler formula they are fixed ( $a_h = 1$ ,  $b_h = 0.75$ ). This difference is expected as the the screened Coulomb-corrected Bethe-Heitler formula is valid in the high-energy (ultra-relativistic) limit while the Seltzer and Berger tabulated theoretical results are based on a Bethe-Heitler formulae that is valid for all energy regimes. Equation (5.9) also uses a different function  $F$  from the screened Coulomb-corrected Bethe-Heitler formula; the function  $F$  used by eq. (5.9) is better behaved in the limit  $y \rightarrow 1$ .

In addition to the LPM effect Bremsstrahlung is suppressed at low- $y$  by the dielectric effect. It is possible for Compton scattering of the radiated photons to take place during the Bremsstrahlung formation length (i.e. during the spread out Bremsstrahlung interaction). In the case this is forward Compton scattering, then the scattering can be coherent causing a shift in the photon's phase. If this phase shift is large across the formation length, then it will cause a loss of coherence, suppressing the photon

emission [60].

GEANT4 4.9.0 uses the following parameterisation to calculate the suppression factor for the dielectric effect,  $S_p$ :

$$S_p = \frac{k^2}{k^2 + C_p \cdot E^2} \quad (5.20)$$

where:

$$C_p \equiv \frac{r_0 \lambda_e^2 n}{\pi} \quad (5.21)$$

with:

$r_0$  : classical electron radius  $\equiv e^2/4\pi\epsilon_0 m_e c^2$

$\lambda_e$  : electron Compton wavelength  $\equiv h/m_e c$

$n$  : electron density in the material.

This parameterisation (eqs. (5.20) and (5.21)) is nearly identical to the formulation given in reference [60]<sup>5</sup>, although a little shuffling of constants is required to see this. While reference [60] compares this with experimental data and generally gets agreement within 5%, the conclusions of this paper are both disparate and complex, so it hard to tell if this confirms the form of eqs. (5.20) and (5.21).

The dielectric effect and LPM effect both act over the same length scale, the formation length, and it is incorrect to simply suppress the differential cross section by a combined factor of ( $S_p \times S_{\text{LPM}}$ ). Instead, according to the Physics Reference Manual of GEANT4 4.9.0 [62] they must be combined non-trivially using:

$$\frac{1}{S} = 1 + \frac{1}{S_p} + \frac{S}{S_{\text{LPM}}^2} \quad (5.22)$$

to give  $S$ , the total suppression factor. This formula is derived in reference [66]. This can be solved to give:

$$S = \frac{\sqrt{S_{\text{LPM}}^4 \cdot (1 + \frac{1}{S_p})^2 + 4 \cdot S_{\text{LPM}}^2} - S_{\text{LPM}}^2 \cdot (1 + \frac{1}{S_p})}{2} \quad (5.23)$$

---

<sup>5</sup>Equation (5.20) is indeed identical to equation 12 of reference [60]. However while the basic form of eq. (5.21) appears to be very similar to that given in reference [60], they don't appear to match exactly.

This parameterisation of the low- $y$  suppression is henceforth referred as GEANT4 4.9.0 Bremsstrahlung Parameterisation A. However it is not clear how GEANT4 4.9.0 applies this suppression factor. The manual [62] appears to indicate that, for emissions satisfying inequality (5.3) (i.e. below the LPM threshold)<sup>6</sup>, it performs a suppression by comparing  $S/S_p$  to a random number in the range zero to one, and discounting the photon emission if the random number is greater. While examination of the GEANT4 4.9.0 code [67] confirms a random number rejection procedure using  $S/S_p$ , and that  $S_{\text{LPM}}$  and  $S_p$  are calculated using equations eqs. (5.5) and (5.20), the way  $S$  is calculated in GEANT4 4.9.0 does not agree with eq. (5.23) as given in the GEANT4 4.9.0 Physics Reference Manual [62].

The GEANT4 4.9.0 code instead gives the following formulation for calculating the value of  $S$ :

$$S = \frac{\sqrt{w^2 + 4 \cdot S_{\text{LPM}}^2} - w}{\sqrt{w^2 + 4} - w} \quad (5.24)$$

with:

$$w = S_{\text{LPM}}^2 \cdot (3 - S_p) \quad \text{if } (1 - S_p) < 1 \times 10^{-6} \quad (5.25)$$

$$w = S_{\text{LPM}}^2 \cdot \left(1 + \frac{1}{S_p}\right) \quad \text{otherwise.} \quad (5.26)$$

This parameterisation of the the low- $y$  suppression is henceforth referred to as GEANT4 4.9.0 Bremsstrahlung Parameterisation B. Notice that putting eq. (5.26) into eq. (5.24) gives the same numerator as eq. (5.23), hence eq. (5.23) is a limiting case of eq. (5.24) as  $w \rightarrow 0$ . This formulation seems to have more sensible limits than eq. (5.23); in particular it approaches one as you approach the LPM threshold. No justification for this formulation has been found in the literature, and why GEANT4 4.9.0 differs from the implementation given in its manual is unknown. Furthermore it is not clear if there is a further factor due to dielectric suppression integrated into the GEANT4 4.9.0 code elsewhere. However, given the time constraints of the  $W$  mass analysis further

---

<sup>6</sup>Actually GEANT4 4.9.0 does not use inequality (5.3) explicitly here but uses the limiting case of this inequality when  $E \ll E_{\text{LPM-1}}$ . Due to the large magnitude of  $E_{\text{LPM-1}}$  compared to the incident electron energies of interest in this note, this limiting case will be a good approximation to inequality (5.3) for the purposes of this analysis.

investigation into this matter has not been undertaken.

#### 5.1.4 GEANT4 4.9.2 Model of the Bremsstrahlung Differential Cross Section $y$ -Spectrum

GEANT4 4.9.2 [68] has a new parameterisation for the Bremsstrahlung differential cross section  $y$ -spectrum for incident electrons with energies greater than 1 GeV which is valid in the high energy (ultra-relativistic) limit. It is a Coulomb-corrected screened Bremsstrahlung differential cross section formula including both electron-nucleus and electron-electron Bremsstrahlung and uses the complete screening approximation. (Reference [59] notes the complete screening formula will be valid ‘when the energy is high, and if one is not particularly concerned with the detailed shape at the high-energy tip of the Bremsstrahlung spectrum’). This is then adjusted to account for the two matter effects, LPM suppression and the dielectric suppression effect, to give:

$$\frac{d\sigma}{dk} = \frac{4\alpha r_e^2}{3k} \left[ \left( \xi(s) \{y^2 G(s) + 2[1 + (1-y)^2] \phi(s)\} \right. \right. \\ \left. \left. \times [Z^2(F_{\text{el}} - f) + ZF_{\text{inel}}] \right) + (1-y) \frac{Z^2 + Z}{3} \right] \times S_{\text{G4.9.2}}(k) \quad (5.27)$$

where  $k$  is the energy of the radiated photon,  $Z$  is the atomic number of the medium,  $r_e$  is the classical electron radius and  $\alpha$  is the fine structure constant.  $F_{\text{el}}$  is the elastic form factor, describing the scattering of electrons by the nucleus, while  $F_{\text{inel}}$  is the inelastic form factor, describing the scattering of electrons by the atomic shell electrons (hence this term is dependent on  $Z$  instead of  $Z^2$ ). For  $Z > 4$  these terms are given by:

$$F_{\text{el}} = \log \left( \frac{184.15}{Z^{\frac{1}{3}}} \right) \quad (5.28)$$

and:

$$F_{\text{inel}} = \log \left( \frac{1194.0}{Z^{\frac{2}{3}}} \right). \quad (5.29)$$

$f$  is the Coulomb correction, given by<sup>7</sup>:

$$f = \alpha^2 Z^2 \sum_{n=1}^{\infty} \frac{1}{n(n^2 + \alpha^2 Z^2)} \quad (5.30)$$

The complete screening approximation differential cross section (the basis for eq. (5.27)) is initially derived in the Born approximation; the addition of  $f$  corrects this to a Coulomb-corrected formula as defined in section 5.1.3. The LPM suppression functions,  $G(s)$  and  $\phi(s)$ , represent the LPM suppression of the parts of the differential cross section corresponding to an electron spin-flip and no electron spin-flip respectively. They are defined as:

$$G(s) = 24s^2 \left( \frac{\pi}{2} - \int_0^{\infty} e^{-st} \frac{\sin(st)}{\sinh\left(\frac{t}{2}\right)} dt \right) \quad (5.31)$$

and<sup>8</sup>:

$$\phi(s) = 12s^2 \left( -\frac{\pi}{2} + \int_0^{\infty} e^{-st} \sin(st) \coth\left(\frac{t}{2}\right) dt \right) \quad (5.32)$$

The suppression function  $\xi(s)$  and the suppression variable  $s$  are defined recursively by the relations:

$$s = \sqrt{\frac{E_{\text{LPM-2}k}}{8E(E-k)\xi(s)}} \quad (5.33)$$

and:

$$\xi(s) = 2 \quad (s < s_1) \quad (5.34)$$

$$\xi(s) = 1 + \ln(s)/\ln(s_1) \quad (s_1 < s < 1) \quad (5.35)$$

$$\xi(s) = 1 \quad (s \geq 1) \quad (5.36)$$

---

<sup>7</sup>The formula for the Coulomb correction given in equation 3.3 of reference [59] is incorrect. The corrected formula is given in an erratum to this paper; this corrected formula agrees with the formula given here.

<sup>8</sup>The GEANT4 manual appears to be mistaken on its definition of  $\phi$ , using a factor of  $\sinh$  instead of  $\coth$  as is used by both the original reference [61] and other subsequent authors. The formula here is that used by the original reference.

where  $s_1 \equiv Z^{2/3}/(184.15^2)$  (in GEANT4 4.9.2, see footnote<sup>9</sup>) and:

$$E_{\text{LPM-2}} \equiv \frac{\alpha(m_e c^2)^2 X_0}{4hc\rho} \quad (5.37)$$

(This differs from  $E_{\text{LPM-1}}$  by a factor of 2). The term  $S_{\text{G4.9.2}}(k)$  is an additional multiplicative factor for dielectric suppression. It is defined as:

$$S_{\text{G4.9.2}}(k) = \left[ \frac{k^2}{k^2 + k_p^2} \right] \quad (5.38)$$

where:

$$k_p \equiv \hbar w_p \frac{E_e}{m_e c^2} = \frac{\hbar E_e}{m_e c^2} \cdot \sqrt{\frac{n_e e^2}{\epsilon_0 m_e}} \quad (5.39)$$

with:

$w_p$  : plasma frequency of media  $\equiv \sqrt{n_e e^2 / \epsilon_0 m_e}$

$m_e$  : rest mass of an electron

$n_e$  : electron density in the material

$\epsilon_0$  : permittivity of free space.

A non-iterative method for solving for  $\xi(s)$  and  $s$  is given by Stanev et al. [69, 70]. Because the LPM and dielectric suppression mechanisms both act to reduce the effective formation length of photons it is necessary to modify this method to treat both suppression mechanisms consistently within a single parameterisation [71]. Details of the modified method are given in Appendix B.

Aside from the LPM suppression function and the additional multiplicative factor for dielectric suppression, eq. (5.27) is essentially the same as the ‘Complete Screening Formula’ given in reference [59].

For incident electrons of energies below 1 GeV, GEANT4 4.9.2 uses a modified version

---

<sup>9</sup>Other authors give slightly different definitions of  $s_1$ . Reference [69] defines  $s_1 \equiv Z^{2/3}/(191^2)$ ; reference [70] defines  $s_1 \equiv Z^{2/3}/(184^2)$ . The reason for this variation in the definition of  $s_1$  is unknown.

of the GEANT4 4.9.0 parameterisation (c.f. eq. (5.9)). The modifications remove the combined dielectric and LPM suppression from this parameterisation and replace them with a treatment of only the dielectric effect, hence neglecting the LPM effect. As sub 1 GeV electrons are of only marginal interest to us, we do not further discuss these modifications in this thesis.

### 5.1.5 Bremsstrahlung Total Cross Section Models

A basic model of the Bremsstrahlung total cross section defines the expected number of Bremsstrahlung interactions with a  $y$ -value in the range  $y_{\min} < y < y_{\max}$  occurring within a slice of material  $dX_0$  radiation lengths thick as:

$$\lambda_\gamma = dX_0 \times \frac{4}{3} \left[ \ln(y_{\max}/y_{\min}) - (y_{\max} - y_{\min}) + \frac{3}{8}(y_{\max} - y_{\min})^2 \right]. \quad (5.40)$$

In a Monte Carlo simulation, the number of Bremsstrahlung photon emitted within that layer is then generated according to a Poisson distribution with a mean of  $\lambda_\gamma$ . This is henceforth referred to as the Basic Bremsstrahlung Total Cross Section Model. Note that this model does not account for LPM suppression (or dielectric suppression), so the LPM (LPM/dielectric) suppression should be applied to it as an explicit rejection of events and consequent reduction in the total cross section.

GEANT4 4.9.0 divides electron energy loss due to Bremsstrahlung into a ‘soft’ component represented by a continuous energy loss and ‘hard’ component for which photon emission is explicitly simulated. The boundary between these two components is set at a cut-off emitted photon energy,  $k_c$  (GEANT4 4.9.0 sets the value for explicit secondary particle generation cut-offs by a complicated procedure intended to be consistent across a range of processes hence the exact value of  $k_c$  used is not clear, but examination of test beam pseudo-data indicates  $k_c = 10$  keV). For the ‘hard’ component a parameterisation of the Bremsstrahlung total cross section based on the EEDL (Evaluated Electrons Data Library) [72, 73] data set is used. The total cross section for explicit photon emission is defined as:

$$\sigma(Z, T, k_c) = \int_{k_c}^T \frac{d\sigma(Z, T, k)}{dk} dk \quad (5.41)$$

where  $T$  is the kinetic energy of the incident electron, and  $Z$  is the atomic number of the medium the electron is traversing. The parameterisation for the total cross section is:

$$\sigma(Z, T, k_c) = Z(Z + \xi_\sigma) \left(1 - c_{\text{sigh}} Z^{1/4}\right) \left[\frac{T}{k_c}\right]^\alpha \frac{f_s}{N_A} \quad (5.42)$$

where  $N_A$  is Avogadro's number,  $\xi_\sigma$ ,  $c_{\text{sigh}}$  and  $\alpha$  are constants.  $f_s$  is a tenth order polynomial in  $x = \log_{10}(T)$  with  $Z$ -dependent coefficients for  $x < x_l$  and  $f_s = 1$  for  $x \geq x_l$ , where  $x_l$  is a fixed constant. For incident electron kinetic energies lower than a limit  $T_{\text{lim}}$  (where  $T_{\text{lim}} = 10$  MeV) eq. (5.42) should be multiplied by:

$$\left(\frac{T_{\text{lim}}}{T}\right)^{c_l} \cdot \left(1 + \frac{a_l}{\sqrt{ZT}}\right) \quad (5.43)$$

where  $c_l$  and  $a_l$  are constants. The values of the constants and the coefficients of  $f_s$  can be found in the GEANT4 4.9.0 code. The LPM effect is not considered within this parameterisation, instead it is accounted for by randomly rejecting Bremsstrahlung events according to a suppression function (c.f. eq. (5.24)).

GEANT4 4.9.2 uses the same model for the total cross section as GEANT4 4.9.0 for incident electron energies less than 1 GeV. For incident electron energies greater than 1 GeV it uses the integral of the differential cross section given by eq. (5.27) in the range  $y_{\text{min}} < y < 1$ , where  $y_{\text{min}}$  is the  $y$ -value corresponding to the cut-off emitted energy.

### 5.1.6 Differences Between Bremsstrahlung for Electrons and Positrons

All the above treatments of Bremsstrahlung are for electrons. According to [68], cross sections (both total and differential) for positron Bremsstrahlung can differ from those for electrons. However such differences are mostly of importance for low incident electron energies and high values of  $Z$ , and basic enumeration shows they would be negligible for the electron energies considered in this analysis.

## 5.2 Pair Production

### 5.2.1 Introduction

The conversion of a photon into an electron-positron pair cannot occur in vacuum as momentum cannot be conserved in such a process. However in the presence of an atomic electron or nucleus such a conversion can proceed, via the two Feynman diagrams shown in fig. 5.2. The Feynman diagrams for pair production are variants of those for Bremsstrahlung, hence the two processes are closely related. In order to simulate pair production we must determine the total cross section as a function of incident photon energy and the fraction of the photon's energy transferred to the pair produced electron. We assume that the electron and positron are produced co-linear with the incident photon, which is a very good approximation at high energy, hence the angular distribution of the electron is not simulated and thus not discussed here.

The differential cross section for pair production is defined in terms of  $x$ , the fraction of the photon's energy transferred to the pair produced electron, i.e.:

$$x \equiv \frac{E_{e^-}}{k} \tag{5.44}$$

where  $E_{e^-}$  is the total energy of the pair produced electron and  $k$  the incident photon energy. The total energy of the pair produced positron is then:

$$E_{e^+} = (1 - x)k. \tag{5.45}$$

Due to the inherent symmetry of the electron and positron any differential cross section spectrum should be symmetric about  $x = 0.5$ . The pair production differential cross section  $x$ -spectrum can be derived from basic principles [74, 75, 76, 77]; this is discussed in a review article by Tsai [59]. Another useful review article on the topic is Motz, Olsen and Koch [78].

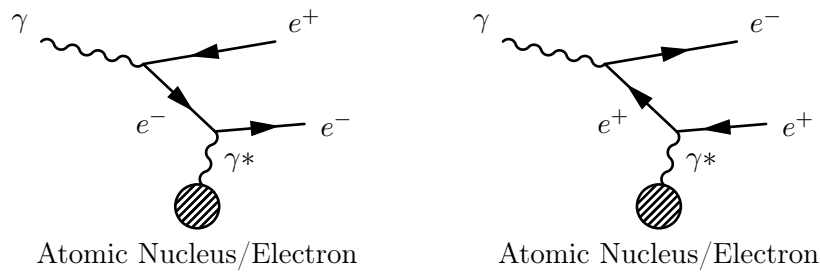


Figure 5.2: The two dominant Feynman diagrams for pair production in the electric field of a nucleus or atomic electron. Adapted from reference [59].

### 5.2.2 Basic Model of the Pair Production Differential Cross Section $x$ -Spectrum

The most basic equation for the pair production  $x$ -spectrum, which can be derived from the results presented in Tsai by both neglecting the Coulomb correction and assuming the ‘complete screening’ case, then further neglecting a numerically insignificant second term in the resultant expression, is:

$$\frac{d\sigma}{dx} = \frac{A}{X_0 N_A} \left[ 1 - \frac{4}{3}x(1-x) \right] \quad (5.46)$$

where  $A$  is the atomic mass number of the absorber,  $X_0$  is the radiation length of the absorber and  $N_A$  is Avogadro’s number. Because of the assumptions it is based on, this formula will only be accurate in the high energy limit. Also it will fail at very low and high values of  $x$ . This equation is taken from reference [58]. Note the similarity of this equation to the Bremsstrahlung spectrum given by eq. (5.2). Pair production and Bremsstrahlung have similar Feynman diagrams, hence we might expect to derive similar expressions for their basic spectra if we use the same approximations, as is the case here.

### 5.2.3 GEANT4 Model of Pair Production Differential Cross Section $x$ -Spectrum

In GEANT4 (both versions 4.9.0 and 4.9.2) a more sophisticated expression for the pair production  $x$ -spectrum is adopted:

$$\begin{aligned} \frac{d\sigma(Z, x)}{dx} = & \alpha r_e^2 Z [Z + \xi(Z)] \left\{ \left[ x^2 + (1-x)^2 \right] \left[ \Phi_1(\delta(x)) - \frac{F(Z)}{2} \right] \right. \\ & \left. + \frac{2}{3} x(1-x) \left[ \Phi_2(\delta(x)) - \frac{F(Z)}{2} \right] \right\} \end{aligned} \quad (5.47)$$

where  $r_e$  is the classical electron radius and  $\alpha$  is the fine structure constant. This is a version of the Bethe-Heitler formula incorporating various corrections and is essentially formula 3.9 of Tsai, although the treatment of atomic electrons takes a significantly different form here from that given in Tsai. The treatment in Tsai adds additional  $x$ -dependent terms to the Bethe-Heitler formula to account for pair production in the field of atomic electrons, whereas in eq. (5.47) pair production in the field of atomic electrons and pair production in the field of the nucleus are assumed to yield the same  $x$ -spectral shape and atomic electrons are accounted for by adding the  $\xi(Z)$  term to the overall normalisation.

The  $\Phi_1$  and  $\Phi_2$  terms are screening functions, accounting for the screening of the nuclear Coulomb field by the atomic electrons, and are defined in terms of a screening variable  $\delta$ , itself defined as:

$$\delta(x) \equiv \frac{136}{Z^{1/3}} \frac{x_0}{x(1-x)}, \quad (5.48)$$

with:

$$x_0 \equiv \frac{m_e c^2}{k}. \quad (5.49)$$

$Z$  is the atomic number of the absorber,  $m_e$  is the electron mass and  $k$  is the incident

photon energy. The screening functions themselves are then defined as:

$$\begin{aligned}
\text{for } \delta \leq 1 \quad \Phi_1(\delta) &= 20.867 - 3.242\delta + 0.625\delta^2, \\
\Phi_2(\delta) &= 20.209 - 1.930\delta - 0.086\delta^2, \\
\text{for } \delta > 1 \quad \Phi_1(\delta) &= \Phi_2(\delta) = 21.12 - 4.184 \ln(\delta + 0.952).
\end{aligned} \tag{5.50}$$

The  $F(Z)$  term in eq. (5.47) is the Coulomb correction function. Like its Bremsstrahlung equivalent the Bethe-Heitler pair production formula is derived in the Born approximation and the purpose of the Coulomb correction is the same as described for Bremsstrahlung in section 5.1.3. The Coulomb correction function is:

$$\begin{aligned}
\text{for } k < 50 \text{ MeV} : \quad F(Z) &= 8/3 \ln Z, \\
\text{for } k \geq 50 \text{ MeV} : \quad F(Z) &= 8/3 \ln Z + 8f_c(Z),
\end{aligned} \tag{5.51}$$

with:

$$\begin{aligned}
f_c(Z) &= (\alpha Z)^2 \left[ \frac{1}{1 + (\alpha Z)^2} \right. \\
&\quad \left. + 0.20206 - 0.0369(\alpha Z)^2 + 0.0083(\alpha Z)^4 - 0.0020(\alpha Z)^6 + \dots \right].
\end{aligned} \tag{5.52}$$

The  $\xi(Z)$  term in eq. (5.47) accounts for the contribution of pair production in the field of the atomic electrons. It is given by:

$$\xi(Z) = \frac{\ln(1440/Z^{2/3})}{\ln(183/Z^{1/3}) - f_c(Z)}. \tag{5.53}$$

For silicon it is approximately  $\sim 1.3$ . Note because this is dependent only on  $Z$  and appears only as part of an overall multiplier in eq. (5.47), it does not affect the shape of the pair production  $x$ -spectrum, only its normalisation. In both GEANT4 and UCL Fast Simulation the pair production total cross section is treated separately and only the spectral shape is taken from eq. (5.47), so its normalisation is irrelevant.

The kinematical limits on  $x$  are:

$$x_0 \leq x \leq 1 - x_0 \quad (5.54)$$

but it is sometimes possible for eq. (5.47) to become negative for values of  $x$  inside this range. This happens if:

$$\delta(x) > \delta(x_1) = \exp \left[ \frac{42.24 - F(Z)}{8.368} \right] - 0.952 \quad (5.55)$$

where  $x_1$  is the fixed value of  $x$  for which the cross section is zero. (This expression is derived by substituting the definitions of  $\Phi_1$  and  $\Phi_2$  for  $\delta > 1$  into eq. (5.47).) Thus from the definition of  $\delta(x)$  the values of  $x$  for which eq. (5.47) becomes negative are:

$$x < x_1 = \frac{1}{2} - \frac{1}{2} \sqrt{1 - \frac{\delta_{min}}{\delta(x_1)}}, \quad (5.56)$$

with:

$$\delta_{min} = \delta \left( x = \frac{1}{2} \right) = \frac{136}{Z^{1/3}} 4x_0. \quad (5.57)$$

Hence the limits on  $x$  are:

$$x \in [x_{min} = \max(x_0, x_1), 1 - x_{min}]. \quad (5.58)$$

For the case of silicon (i.e.  $Z = 14$ )  $x_0$  is greater than  $x_1$  for all incident photon energies above  $\sim 3.5$  MeV, as seen in fig. 5.3. Note for photon energies below  $\sim 1.7$  MeV the cross section is negative for all  $x$ , hence  $\sim 1.7$  MeV is the minimum value for which pair production can occur. This is slightly higher than the kinematic limit of about  $\sim 1.0$  MeV.

It should be noted that while eq. (5.47) is considerably more sophisticated than eq. (5.46), it is still based on a number of approximations. Its original QED derivation is exact to order  $\alpha^3$ , but expressions are required for both atomic and nuclear form factors<sup>10</sup>. The latter of these are ignored in eq. (5.47), which is justified for a highly

---

<sup>10</sup>Atomic form factors account for the Coulomb field of the nucleus and its screening by atomic

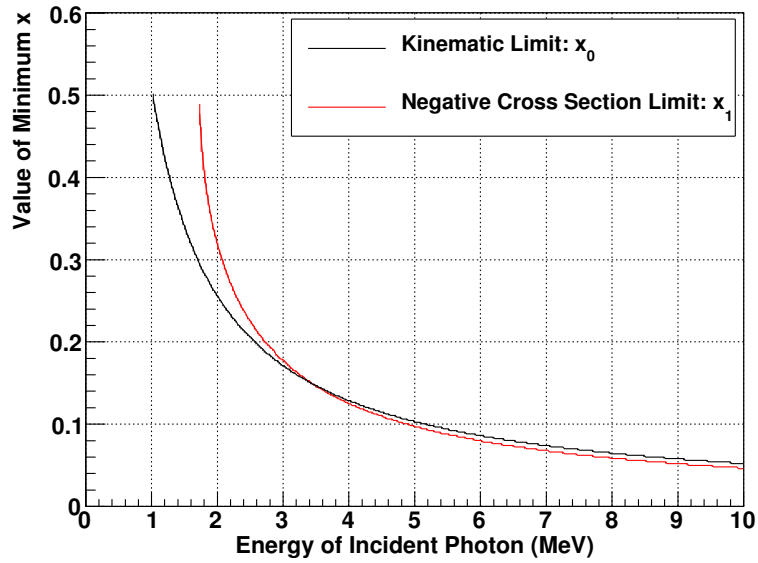


Figure 5.3: The kinematic limit ( $x_0$ ) and negative cross section limit ( $x_1$ ) on the range of  $x$  for pair production. The higher value, at any given incident photon energy, is  $x_{min}$ , the minimum value of  $x$  for which pair production can occur and  $1 - x_{min}$  is the maximum value of  $x$  for which pair production can occur. Due to the symmetry in the  $x$ -spectrum if  $x_{min} > 0.5$  then there are no allowable values of  $x$  and hence no pair production can occur according to eq. (5.47). Note this only shows incident photon energies below 10 MeV. However the trend seen here remains the same above 10 MeV and further plots (not included in this thesis) show that the kinematic limit is greater than the negative cross section limit between  $\sim 3.5$  MeV and at least 100 GeV.

relativistic system where pair production occurs mostly in the forward direction. Atomic form factors (which are not ignored in eq. (5.47)) can only be calculated exactly for Hydrogen and Helium, so here also we have to use an approximation. Equation (5.47) also ignores the effects of recoil of the nucleus/atomic electron involved in the pair production; again this can be ignored for high energies and small angles.

#### 5.2.4 Pair Production Total Cross Section Models

Integrating eq. (5.46) gives the high energy limit of the pair production total cross section as:

$$\sigma = \frac{7}{9} (A/X_0 N_A) \quad (5.59)$$

where  $X_0$  is the radiation length of the absorber,  $A$  is the atomic mass of the absorber and  $N_A$  is Avogadro's constant. Reference [58] notes this is accurate to within a few percent down to incident photon energies as low as 1 GeV, especially for high- $Z$  materials. However we are interested in both photon energies less than 1 GeV and greater than 1 GeV for silicon which has a low atomic number (specifically  $Z = 14$ ) so eq. (5.59) is possibly insufficiently accurate for our purposes. A more accurate theoretical expression for the pair production total cross section could be obtained by integrating eq. (5.47). However this is not the line that has been followed either by us or by GEANT4. Instead it is preferable to use experimental data and avoid relying on theoretical models for the total cross section.

GEANT4's approach is to fit to data in the range  $1 \leq Z \leq 100$  and for incident photon energies between 1.5 MeV and 100 GeV. This produces the parameterisation:

$$\sigma(Z, k) = Z(Z + 1) \left[ F_1(X) + F_2(X)Z + \frac{F_3(X)}{Z} \right] \quad (5.60)$$

where  $X = \ln(k/m_e c^2)$  and  $F_1(X)$ ,  $F_2(X)$ ,  $F_3(X)$  are fifth order polynomials in  $X$  with coefficients determined by a least squares fit to the data. The accuracy of the fit is estimated as  $\frac{\Delta\sigma}{\sigma} \leq 5\%$  with a mean of  $\approx 2.2\%$ . Our own approach is also data driven

---

electrons. They also account for the Coulomb fields of atomic electrons and their screening by the nucleus. Nuclear form factors account for the charge distribution within the nucleus itself.

and is a fit to data between 0.001 MeV and 100 GeV. This will be discussed in section 6.4.3.

## Chapter 6

# Monte Carlo Models of Bremsstrahlung and Pair Production

### 6.1 Introduction

To simulate the  $W \rightarrow e\nu_e$  channel it is necessary to model the effect of Bremsstrahlung on electrons and pair production on photons as they pass through the silicon tracking detector. The original UCL Fast Simulation (utilised in a prior analysis of the width of the  $W$  boson [79]) used simplified models for Bremsstrahlung and pair production based on the treatment in the Particle Data Group's review of the Passage of Particles Through Matter [58]. For Bremsstrahlung these models are the Basic Bremsstrahlung Differential Cross Section Model and the Basic Bremsstrahlung Total Cross Section Model as described in Chapter 5; their Monte Carlo implementation is discussed below. The basic pair production model is discussed in section 6.4. This chapter details the implementation and validation of more comprehensive models of these effects based on the models used in the GEANT4 detector simulation program [80].

For Bremsstrahlung both the GEANT4 4.9.0 and GEANT4 4.9.2 models (see Chapter 5), which differ significantly, are considered. These two models are compared to

available data and tabulated theoretical results (see section 6.3). In the light of the results of these studies it was decided to implement the newer GEANT4 4.9.2 model in UCL Fast Simulation.

The GEANT4 4.9.2 Bremsstrahlung model is dependent on the interaction media; hence to model the varied composition of the CDF Run II silicon tracker a ‘two element model’ was implemented in UCL Fast Simulation. The compositional modelling of the regions of the detector where multilayer thick film ceramic hybrids with electronic readout chips mounted on them are positioned (these hybrids are positioned in all three subcomponents of the silicon tracker and known variously as the Layer 00, SVXII and ISL hybrids) is treated separately from the remainder of the silicon tracker using a different variant of the two element model; this was introduced as a late modification postdating the rest of the work on Bremsstrahlung modelling. The two element model (including the late modification to the modelling of the hybrid regions) is discussed in Chapter 7.

An estimate of the resultant error on the measured  $W$  boson mass from any residual mis-modelling of Bremsstrahlung and pair production is presented in Chapter 8.

## 6.2 The Modelling of Bremsstrahlung in the UCL Fast Simulation

### 6.2.1 Strategy

For the purposes of validation we have compared the total cross section and differential cross section  $y$ -spectrum for electron Bremsstrahlung in UCL Fast Simulation to GEANT4, and modified UCL Fast Simulation accordingly to match the GEANT4 models. As far as was possible the GEANT4 models were cross-checked with published theoretical models of Bremsstrahlung. Importantly, the alterations made to UCL Fast Simulation did not slow down the simulation significantly.

Rather than compare the simulation in the context of the actual detector geometry of CDF for these two models, a virtual test beam experiment was setup. This allowed us to compare the two models isolated from any other possible differences. Within

each test beam experiment only a single physics process, Bremsstrahlung, would be simulated, all other processes being disabled. The typical energy of an electron produced in the  $W \rightarrow e\nu_e$  channel is 40 GeV, hence the initial comparisons were done using a 40 GeV beam of electrons. To validate the energy dependence of the UCL Fast Simulation model, further test beam comparisons were made for a range of incident electron energies.

Both the GEANT4 version 4.9.0 and version 4.9.2 physics models were separately implemented and validated within UCL Fast Simulation, a switch within the code allowing the user to choose which of these two models to use.

### 6.2.2 GEANT4 Virtual Test Beam Experiment

A virtual test beam experiment was set up in GEANT4. Tests were performed in both GEANT4 versions 4.9.0 (specifically version 4.9.0 patch-01) and 4.9.2. The virtual experiment consisted of a  $10 \text{ m}^3$  world volume, at the centre of which was placed a  $10 \text{ cm}^2$  silicon plate orientated parallel to the  $x$ - $y$  plane. The plate had a thickness of 1 mm. A test beam of 40 GeV electrons (i.e. electrons with an initial kinetic energy of 40 GeV) was fired at the plate along the  $z$ -axis, striking it at an angle of 90 degrees. Any electron and photon tracks passing more than 1 cm in the  $z$  direction beyond the centre of the plate were recorded (see fig. 6.1). Each event consisted of the firing of one electron, then the tracking of it and any secondary photons produced through Bremsstrahlung until they reached the edge of the world volume.

All physics processes in GEANT4 were disabled except for electron Bremsstrahlung. A number of histograms were defined and filled at run time, many of these - primary vertex energy, electron momentum, photon momentum etc. - simply confirmed the details of the experimental setup. The histogram most pertinent to this analysis is that of the differential cross section against  $y_{\text{eff}}$ , where  $y_{\text{eff}}$ , effective  $y$ , is defined as the fraction of the electron's energy radiated through the emission of photons, i.e. for the emission of a single photon,  $y_{\text{eff}}$  equals  $y$  as defined by eq. (5.1) and used throughout section 5.1. This was plotted on both logarithmic and linear scales. First the number of events against  $y_{\text{eff}}$  was histogrammed at run time. To correctly convert the logarithmic

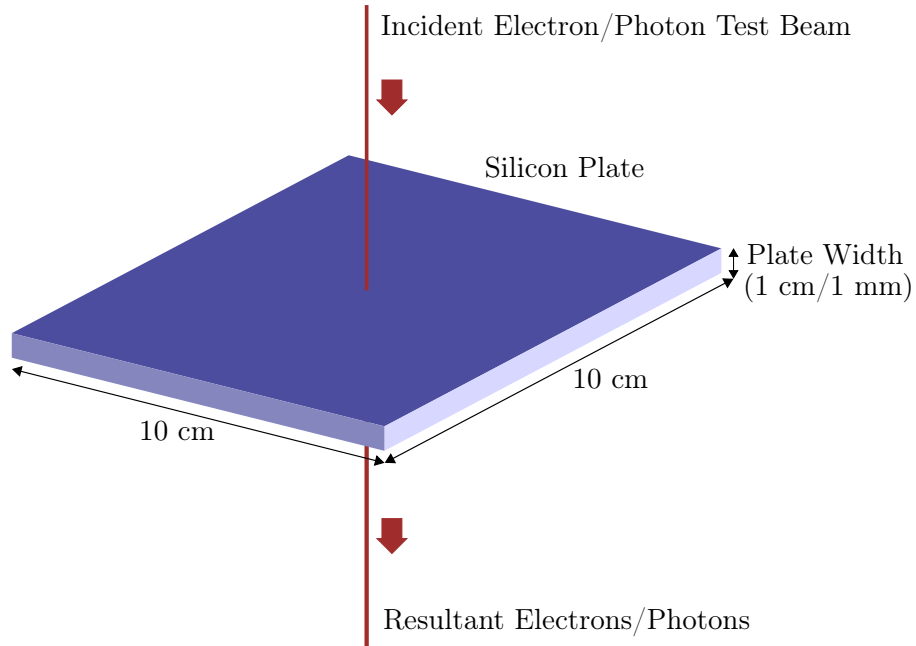


Figure 6.1: The setup of the virtual test beam experiment in GEANT4.

scale plot to one of differential cross section against  $y_{\text{eff}}$ , it was necessary to divide the content of each bin by the bin width. In the case of the linear histogram, events where no Bremsstrahlung occurred were not plotted, hence removing the dominant peak at  $y_{\text{eff}} = 0$ .

It was observed from early plots that in total roughly 11% of the electrons underwent Bremsstrahlung while passing through the silicon plate. This agreed with simple calculations based on the radiation length of electrons in silicon, and confirmed that 1 mm was, for Bremsstrahlung, a suitable choice of plate thickness. A significantly thicker plate would result in too many events with more than one photon being radiated, this would tend to skew the  $y_{\text{eff}}$ -spectrum as will be seen later; a significantly thinner plate would mean a very large number of events would be needed to get satisfactory statistics.

To confirm that the output of GEANT4 was being interpreted correctly, a curve following the basic theoretical  $y$ -spectrum given by eq. (5.2) was overlaid on both the linear and logarithmic  $y_{\text{eff}}$  histograms. The overall constant of proportionality of eq. (5.2) was determined to match the histogram scaling rather than calculated from theory. This was done by requiring that the integral of the theory curve and of the histogram matched

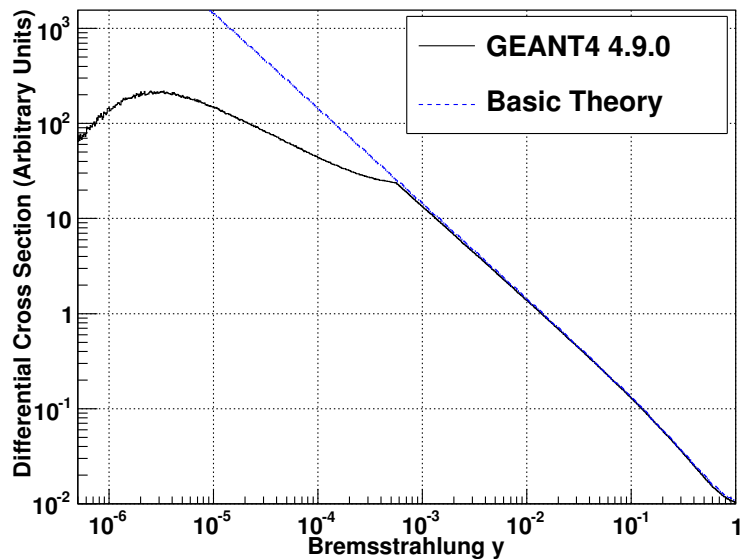


Figure 6.2: GEANT4 4.9.0  $y_{\text{eff}}$ -spectrum pseudo-data compared to a basic theory curve given by eq. (5.2), on logarithmic axis scales. The incident electron energy is 40 GeV. A good agreement is observed between the pseudo-data and theory spectra except at low- $y$ . A discrepancy between pseudo-data and theory also exists at high- $y$  but this is not visible on the axis scale used in this plot.

in a region of good agreement (in terms of line shape), this region being defined by  $0.01 < y < 0.1$ . The normalisation thus determined, a good agreement was observed between GEANT4 pseudo-data and theory shapes, except at very high- $y$ , and at low- $y$  below the LPM cut off. This can be seen in fig. 6.2, which compares GEANT4 4.9.0  $y_{\text{eff}}$ -spectrum pseudo-data to the theoretical  $y$ -spectrum given by eq. (5.2) on a logarithmic scale.

The value of  $y_{\text{eff}}$  for a given event is calculated by subtracting the energy of the electron after it has passed through the plate from its energy at the primary vertex (i.e. the fixed energy of the test beam). It was confirmed that this gave completely equivalent results to calculating  $y_{\text{eff}}$  by summing the energy of any photons radiated. It was also confirmed that if the test beam particle was changed to an  $e^+$  exactly the same results were found.

### 6.2.3 UCL Fast Simulation Virtual Test Beam Experiment

The original UCL Fast Simulation (similar to the simulation detailed in reference [79]), henceforth referred to as UCL Fast Simulation Basic Version, adopts eq. (5.2) as its  $y$ -spectrum, but also accounts for the LPM effect. Each layer of silicon in UCL Fast Simulation is split into 4 sublayers, and as an electron passes through each sublayer a number of Bremsstrahlung photons are generated randomly according to the Basic Bremsstrahlung Total Cross Section Model with  $y_{min} = 1 \times 10^{-4}$  and  $y_{max} = 1$ ; this usually gives either zero or one photon(s), although multiple photon emission is possible. The energy of any photons generated is randomly sampled from eq. (5.2). If the generated  $y$  is below the LPM threshold (according to inequality (5.3)) then an LPM suppression is applied. This suppression is made by generating a random number in the range zero to one; if this is greater than the LPM suppression factor  $S_{LPM}$  given by eq. (5.5) then the photon is discarded. Any remaining photons are then propagated separately henceforth, and their energy is deducted from that of the electron. This is an implementation of the Basic Bremsstrahlung Differential Cross Section Model.

UCL Fast Simulation was modified to provide an analogous setup to that used in GEANT4. UCL Fast Simulation propagates lepton and photon paths through a series of layers - a series of silicon tracker layers, the COT, the time-of-flight scintillators, the solenoid etc. This was modified by turning off all the layers but a single layer of silicon, and modifying this to be 1 mm thick. Then 40 GeV electrons were fired outwards perpendicular to the silicon layer from the interaction point, one per event. The initial and final energy of the electrons was recorded, allowing  $y_{eff}$  to be calculated. Histograms of differential cross section against effective  $y$  were produced for both logarithmic and linear scales. Again it was confirmed that changing the test beam particle to an  $e^+$  had no effect on the results.

Simulation results are compared to theory by taking the ratio,  $R = \frac{d\sigma_{\text{histogram}}}{d\sigma_{\text{theory}}}$ . Figure 6.3 was made by replacing the content of each histogram bin with the ratio  $R = \frac{d\sigma_{\text{histogram}}}{d\sigma_{\text{theory}}}$ , where  $d\sigma_{\text{histogram}}$  is UCL Fast Simulation Basic Version pseudo-data and  $d\sigma_{\text{theory}}$  is taken from eq. (5.2). Note that even above the LPM cut off, the ratio

$\frac{d\sigma_{\text{histogram}}}{d\sigma_{\text{theory}}}$  is not constant. The  $y$  we are plotting in histograms is an effective  $y$ , the total amount of energy that the electron has lost through photon emission, while the spectrum given by eq. (5.2) is the spectrum for single photon emission. Secondary or further photon emission shifts events to higher  $y$ 's than predicted by the single emission spectrum. While such events are reasonably rare, there are enough to distort the ratio plot in the observed way. This is henceforth referred to as the 'multiple photon emission effect'. To confirm this, UCL Fast Simulation Basic Version was run with only one simulation step being used in calculating the passage of the electron through the silicon and limiting the maximum number of photons generated per electron to one. Any multiple photon emission events predicted by the simulation were treated as single photon emissions. As can be seen in fig. 6.4, an entirely uniform ratio plot was then observed in the appropriate region. The effect of multiple photon emission can also be seen in a plot of GEANT4 simulated data to the spectrum it follows (as given by eq. (5.9)) but, since GEANT4 cannot be manipulated in the same way to turn off multiple photon emission, it cannot be tested in the same way that the slope is due to multiple photon emission.

#### 6.2.4 Bremsstrahlung GEANT4 4.9.0 Model $y$ -Spectrum Validation and Modification

In fig. 6.5 the GEANT4 4.9.0 and UCL Fast Simulation Basic Version  $y_{\text{eff}}$ -spectra are compared to the basic theoretical  $y$ -spectrum given by eq. (5.2) (normalised against the GEANT4 4.9.0 histogram) on logarithmic axis scales. The incident electron energy is 40 GeV. The discrepancies at high- $y$  and low- $y$  were expected as UCL Fast Simulation Basic Version samples from the spectrum given by eq. (5.2), adding in LPM suppression at low- $y$ , while GEANT4 4.9.0 samples from a more complex spectrum given by eq. (5.9) and implements both LPM and dielectric suppression at low- $y$ . In fig. 6.6, the ratio  $R = \frac{d\sigma_{\text{histogram}}}{d\sigma_{\text{theory}}}$  is shown for GEANT4 4.9.0 and UCL Fast Simulation Basic Version, where  $d\sigma_{\text{theory}}$  is taken from eq. (5.2). The incident electron energy is 40 GeV.

It was decided to modify UCL Fast Simulation such that it samples from eq. (5.9) and so that it uses a low- $y$  suppression calculated by considering both the LPM effect

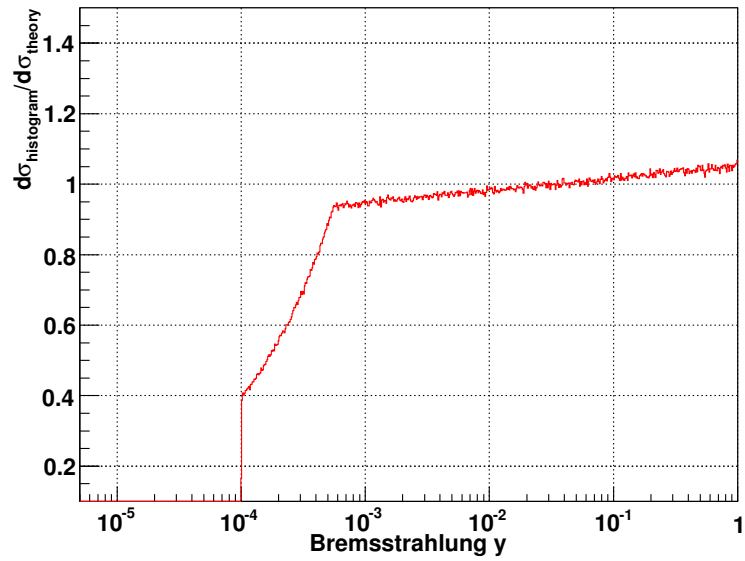


Figure 6.3: The ratio of the UCL Fast Simulation Basic Version Bremsstrahlung  $y_{\text{eff}}$ -spectrum to the theoretical  $y$ -spectrum given by eq. (5.2) on a logarithmic  $x$ -axis scale. Note the slight slope from  $y = 1$  down to  $y = 5.5 \times 10^{-4}$ . In this region there is good agreement with the theoretical spectrum, the slope being due to multiple photon emission. At  $y = 5.5 \times 10^{-4}$ , the LPM cut-off is reached; below this value eq. (5.2) proves inaccurate. The ratio is zero below  $y = 1 \times 10^{-4}$ , the minimum value of  $y$  simulated in UCL Fast Simulation Basic Version.

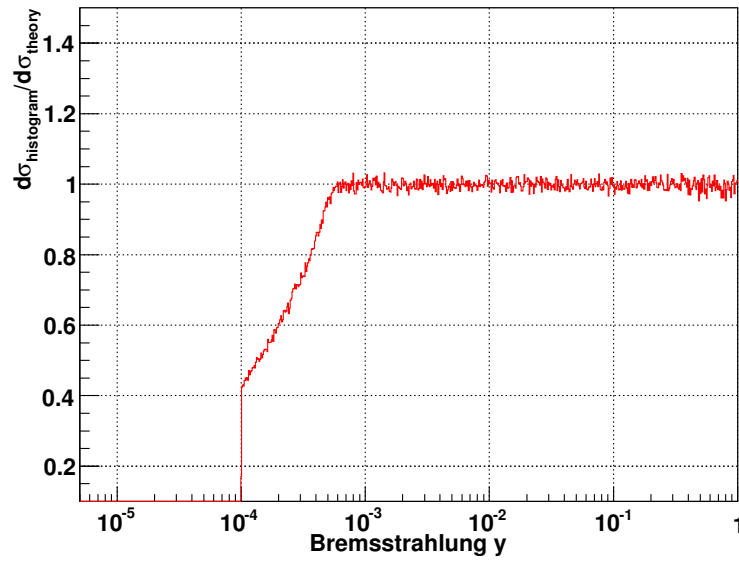


Figure 6.4: The ratio of the UCL Fast Simulation Basic Version Bremsstrahlung  $y_{\text{eff}}$ -spectrum to the theoretical  $y$ -spectrum given by eq. (5.2) on a logarithmic  $x$ -axis scale with no multiple Bremsstrahlung. Note the ratio is constant from  $y = 1$  down to  $y = 5.5 \times 10^{-4}$ , indicating perfect agreement between UCL Fast Simulation Basic Version and eq. (5.2) in this region. Below  $y = 5.5 \times 10^{-4}$  eq. (5.2) proves inaccurate and  $y = 1 \times 10^{-4}$  is the minimum value of  $y$  simulated by UCL Fast Simulation Basic Version.

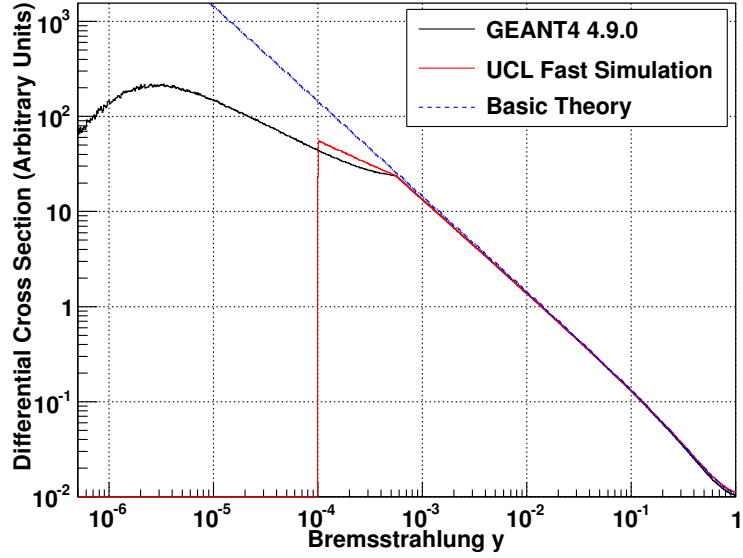


Figure 6.5: GEANT4 4.9.0 and UCL Fast Simulation Basic Version Bremsstrahlung  $y_{\text{eff}}$ -spectra compared to a basic theory curve given by eq. (5.2), on logarithmic axis scales. The incident electron energy is 40 GeV. Note the good agreement from  $y = 1$  down to the LPM cut-off at  $y = 5.5 \times 10^{-4}$ , and the divergence of all three lines below this. The UCL Fast Simulation Basic Version line is zero below  $y = 1 \times 10^{-4}$ , the minimum value of  $y$  simulated in UCL Fast Simulation Basic Version.

and the dielectric effect. This was done in two stages.

Firstly UCL Fast Simulation Basic Version was modified to sample from eq. (5.9), but continued to use the Basic Bremsstrahlung Differential Cross Section Model implementation of the low- $y$  suppression, i.e. suppressing the Bremsstrahlung differential cross section  $y$ -spectrum below the LPM cut-off (given by inequality (5.3)) by a factor of  $S_{\text{LPM}}$  (given by eq. (5.5)). Henceforth this is referred to as UCL Fast Simulation Bremsstrahlung Modification A. In fig. 6.7, the ratio  $R = \frac{d\sigma_{\text{histogram}}}{d\sigma_{\text{theory}}}$  is plotted, where  $d\sigma_{\text{theory}}$  is given by eq. (5.2). The incident electron energy is 40 GeV. It can be seen from this ratio plot that UCL Fast Simulation Bremsstrahlung Modification A and GEANT4 4.9.0 now agree except in the low- $y$  region. Both deviate from eq. (5.2) at high- $y$ .

Theory curves henceforth use the  $y$ -spectrum given by eq. (5.9). Initial attempts to implement GEANT4 4.9.0 Bremsstrahlung Parameterisation A (see section 5.1) low- $y$  suppression in a theory curve seemed to indicate that, despite being the method given in the documentation, the dielectric effect is not implemented in this fashion in GEANT4.

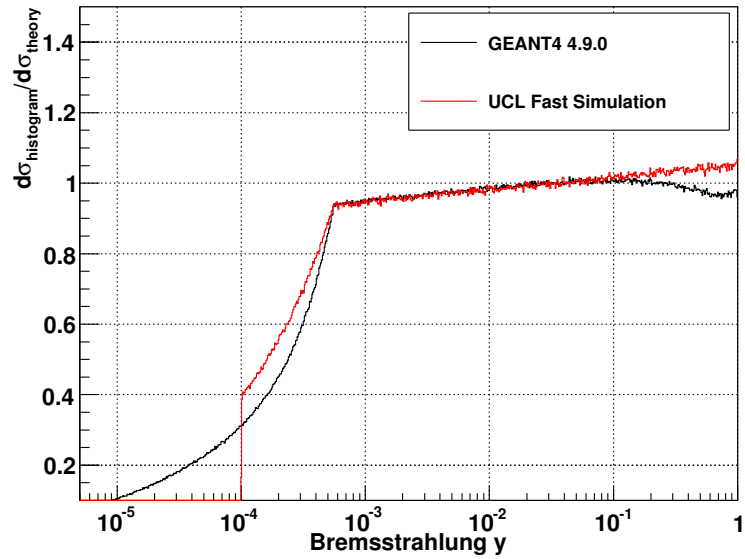


Figure 6.6: The ratio of GEANT4 4.9.0 and UCL Fast Simulation Basic Version Bremsstrahlung  $y_{\text{eff}}$ -spectra to the theoretical  $y$ -spectrum given by eq. (5.2) on a logarithmic  $x$ -axis scale. The incident electron energy is 40 GeV. Note that above the LPM cut-off at  $y = 5.5 \times 10^{-4}$  UCL Fast Simulation Basic Version's line agrees well with eq. (5.2), displaying a slope due to the possibility of multiple photon emission. GEANT4 4.9.0 also shows good agreement with eq. (5.2) over most of this range, but deviates a little at high- $y$ . Below  $y = 5.5 \times 10^{-4}$  both GEANT4 4.9.0 and UCL Fast Simulation Basic Version differ from eq. (5.2). The UCL Fast Simulation Basic Version line is zero below  $y = 1 \times 10^{-4}$ , the minimum value of  $y$  simulated in UCL Fast Simulation Basic Version.

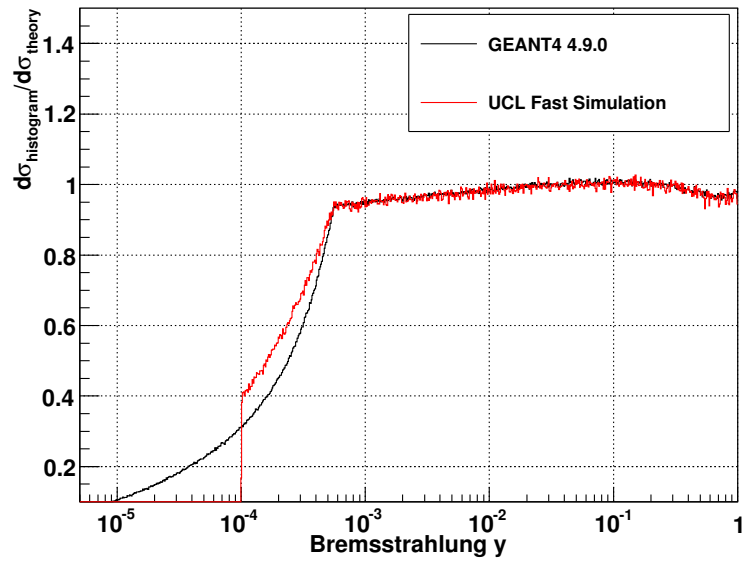


Figure 6.7: The ratio of GEANT4 4.9.0 and UCL Fast Simulation Bremsstrahlung Modification A  $y_{\text{eff}}$ -spectra to the basic theoretical  $y$ -spectrum given by eq. (5.2) on a logarithmic  $x$ -axis scale. The incident electron energy is 40 GeV. Note the good agreement between GEANT4 4.9.0 and UCL Fast Simulation Bremsstrahlung Modification A above  $y = 5.5 \times 10^{-4}$ , including in the very high- $y$  region. Both curves deviate from eq. (5.2) at very high- $y$ . Below  $y = 5.5 \times 10^{-4}$  disagreement occurs between GEANT4 4.9.0 and UCL Fast Simulation Modification A, and both deviate from eq. (5.2).

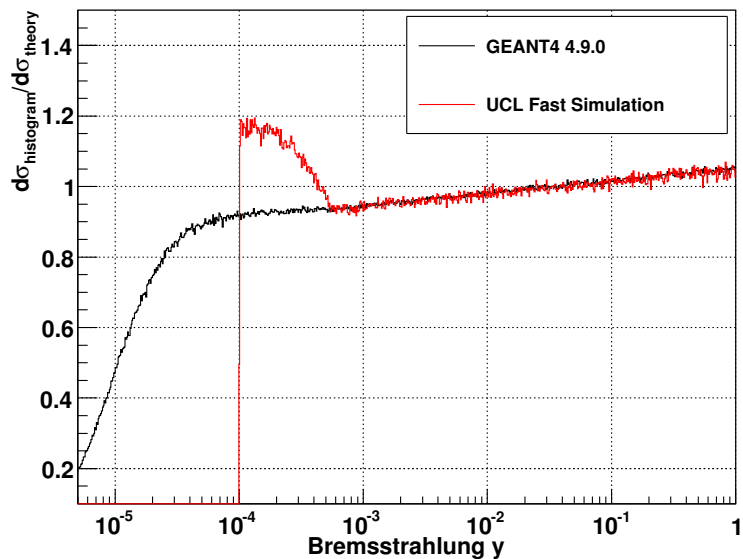


Figure 6.8: The ratio of GEANT4 4.9.0 and UCL Fast Simulation Bremsstrahlung Modification A  $y_{\text{eff}}$ -spectra to an advanced theoretical  $y$ -spectrum given by eq. (5.9) and using GEANT4 4.9.0 Bremsstrahlung Parameterisation B for low- $y$  suppression. A logarithmic  $x$ -axis scale is used. The incident electron energy is 40 GeV. Note the agreement of GEANT4 4.9.0 and UCL Fast Simulation Bremsstrahlung Modification A above the LPM cut-off (the slope being due to the possibility of multiple photon emission), the deviation of UCL Fast Simulation Bremsstrahlung Modification A below the LPM cut off from the GEANT4 4.9.0 results, and the deviation of GEANT4 4.9.0 below  $y = 5.5 \times 10^{-4}$  from a ratio of one.

Examination of the code proves this to be the case. The exact way that GEANT4 4.9.0 implements low- $y$  suppression in the code is complex, and not fully understood by us. However, a satisfactory parameterisation based on the GEANT4 4.9.0 implementation was seen to be GEANT4 4.9.0 Bremsstrahlung Parameterisation B (see section 5.1), using eqs. (5.5), (5.20) and (5.24). Figure 6.8 shows  $R$  for GEANT4 4.9.0 and UCL Fast Simulation Bremsstrahlung Modification A compared to this more complex theoretical expectation. The incident electron energy is 40 GeV. Equation (5.9), with the GEANT4 4.9.0 Bremsstrahlung Parameterisation B of low- $y$  suppression, is used for  $d\sigma_{\text{theory}}$ . Note there is still a discrepancy between GEANT4 4.9.0 Bremsstrahlung Parameterisation B and GEANT4 4.9.0 below about  $y = 5.5 \times 10^{-4}$  - the reason for this is unknown.

Adding the dielectric suppression as given by GEANT4 4.9.0 Bremsstrahlung Parameterisation B (see section 5.1) with eqs. (5.5), (5.20) and (5.24), to UCL Fast Simulation

Bremsstrahlung Modification A gives figs. 6.9 and 6.10. The incident electron energy is 40 GeV. The minimum value of  $y$  simulated was reduced to  $y = 1 \times 10^{-5}$ . This is henceforth referred to as UCL Fast Simulation Bremsstrahlung Modification B. This eliminates the discrepancies at low- $y$  down to about  $y = 5 \times 10^{-5}$ , although poor statistics and numerical fluctuations caused by the insufficient integration points during the integration of eq. (5.2) add a lot of noise to the ratio plot at low- $y$ . Hence we have good agreement between UCL Fast Simulation Bremsstrahlung Modification B and GEANT4 4.9.0 in the range  $y = 1$  to  $y = 5 \times 10^{-5}$  but below this value we observe a discrepancy of unknown origin. For the purposes of this validation exercise UCL Fast Simulation Bremsstrahlung Modification B was set to simulate values of  $y$  down to  $y = 1 \times 10^{-5}$ , however the final version of UCL Fast Simulation Bremsstrahlung Modification B simulates values of  $y$  down to  $y = 5 \times 10^{-5}$ , the point below which it no longer accurately reproduces the results of GEANT4 4.9.0. The fraction of events with  $y$ -values less than  $5 \times 10^{-5}$  is small but not negligible ( $\sim 4.6$  % of the total number of Bremsstrahlung events occurring for a 40 GeV incident electron - see fig. 6.11, which shows the absolute number of events against  $y_{\text{eff}}$ ). However the energy weighted fraction is negligible, hence not simulating  $y$ -values below  $y = 5 \times 10^{-5}$  is expected to have a negligible effect on the measured  $W$  mass. A quantitative estimate of the error was made using numerical integration of the model's spectrum combined with various approximations and a small set of pseudo-data. This estimate indicates the error on  $m_W$  is of the order of a hundred keV/ $c^2$ , which is negligible compared to other sources of uncertainty in the  $W$  mass analysis.

Further test beam comparisons of UCL Fast Simulation Bremsstrahlung Modification B and GEANT4 4.9.0 at a range of other incident electron energies (0.5 GeV, 1 GeV, 5 GeV and 20 GeV) display a similar level of agreement between UCL Fast Simulation Bremsstrahlung Modification B and GEANT4 4.9.0. Hence we conclude that UCL Fast Simulation Bremsstrahlung Modification B is a satisfactory implementation of the GEANT4 4.9.0 Bremsstrahlung model for the  $W$  mass analysis across the relevant range of incident electron energies.

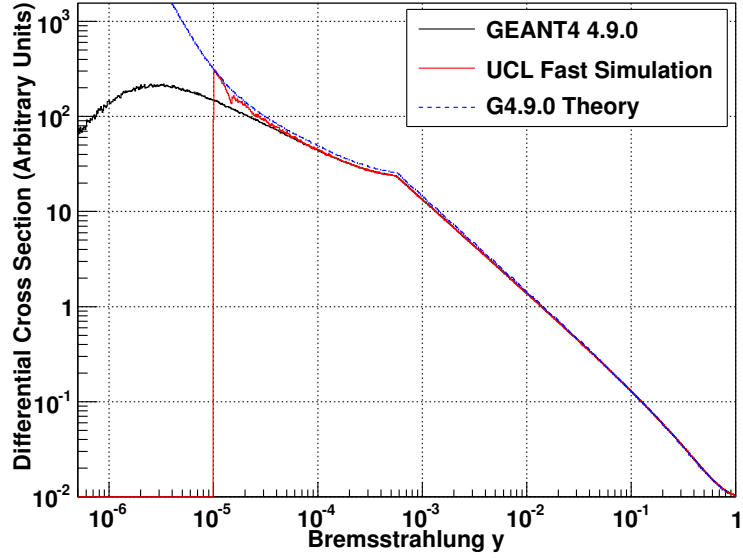


Figure 6.9: GEANT4 4.9.0 and UCL Fast Simulation Bremsstrahlung Modification B  $y_{\text{eff}}$ -spectra compared to an advanced theory curve given by eq. (5.9) with GEANT4 4.9.0 Bremsstrahlung Parameterisation B used for low- $y$  suppression, on logarithmic axis scales. The incident electron energy is 40 GeV. Note the good agreement between GEANT4 4.9.0 and UCL Fast Simulation Bremsstrahlung Modification B in the range  $y = 5 \times 10^{-5}$  to  $y = 1$ , both above and below the LPM cut-off.

### 6.2.5 Bremsstrahlung GEANT4 4.9.0 Model Total Cross Section Validation and Modification

An incident electron energy dependent adjustment is applied to the total cross section of UCL Fast Simulation Bremsstrahlung Modification B. For incident electron energies of 1, 2, 3, 5, 10, 20, 40 and 50 GeV we calculated the ratio:

$$R = \frac{\int_{0.0001}^1 N_{\text{GEANT4}} dy_{\text{eff}}}{\int_{0.0001}^1 N_{\text{FastSim}} dy_{\text{eff}}} \quad (6.1)$$

where  $N_{\text{GEANT4}}$  is the number of GEANT4 4.9.0 pseudo-data events and  $N_{\text{FastSim}}$  is the number of initial UCL Fast Simulation Bremsstrahlung Modification B pseudo-data events. A three variable function of incident electron energy of the form  $R(E) = A \cdot E^{-B} + C$  is fitted to the calculated  $R$  values. The fitted parameters  $A$ ,  $B$ ,  $C$  of  $R(E)$  are presented in table 6.1. The fitted three variable function of the incident electron energy  $R(E)$  and the calculated  $R$  values are compared in fig. 6.12. The UCL Fast Sim-

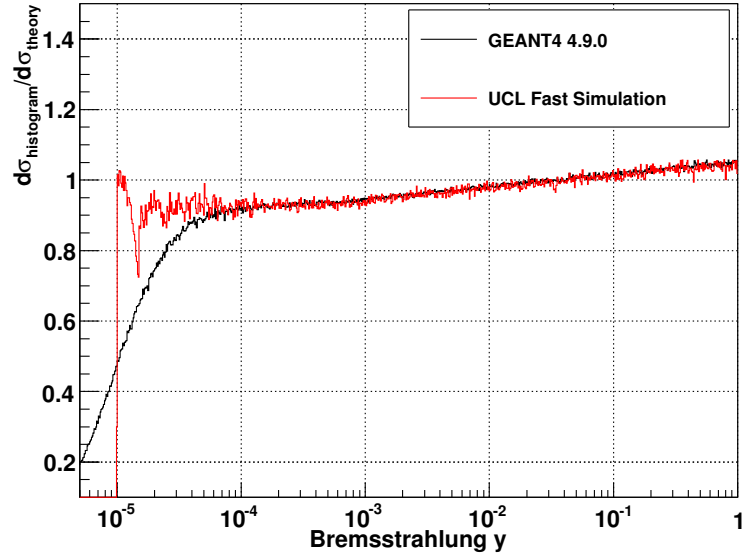


Figure 6.10: The ratio of GEANT4 4.9.0 and UCL Fast Simulation Bremsstrahlung Modification B  $y_{\text{eff}}$ -spectra to the theoretical  $y$ -spectrum given by eq. (5.9) with GEANT4 4.9.0 Bremsstrahlung Parameterisation B used for low- $y$  suppression. A logarithmic  $x$ -axis scale is used. The incident electron energy is 40 GeV. Note the good agreement between GEANT4 4.9.0 and UCL Fast Simulation Bremsstrahlung Modification B in the range  $y = 5 \times 10^{-5}$  to  $y = 1$ , both above and below the LPM cut-off. The reason for the discrepancy below  $y = 5 \times 10^{-5}$  is unknown. Poor statistics and numerical calculation errors account for the large degree of fluctuation of UCL Fast Simulation Bremsstrahlung Modification B at low- $y$ . The UCL Fast Simulation Bremsstrahlung Modification B ratio is zero below  $y = 1 \times 10^{-5}$ , the minimum value of  $y$  UCL Fast Simulation Bremsstrahlung Modification B simulates.

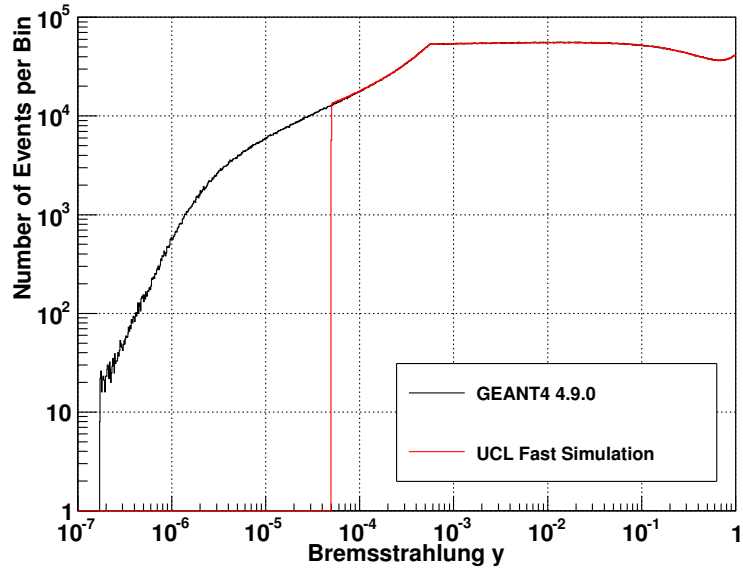


Figure 6.11: Absolute number of Bremsstrahlung events per bin plotted against  $y_{\text{eff}}$  for GEANT4 4.9.0 and the final version of UCL Fast Simulation Modification B (only simulating events for  $y$ -values above  $y = 5 \times 10^{-5}$ ). Logarithmic axis scales are used and a fine grained logarithmic binning is used. The incident electron energy is 40 GeV. The total number of incident electrons is  $2.5 \times 10^8$ . Note that the actual number of events falls considerably at low- $y$ .

ulation Bremsstrahlung Modification B Bremsstrahlung total cross section is multiplied by  $R(E)$  for incident electron energies greater than 1 GeV. To prevent a divergence as  $E \rightarrow 0$  the UCL Fast Simulation Bremsstrahlung Modification B Bremsstrahlung total cross section is multiplied by  $R(E = 1 \text{ GeV})$  for incident electron energies less than 1 GeV. Further  $R$  values calculated using pseudo-data generated using UCL Fast Simulation Bremsstrahlung Modification B including this energy dependent total cross section adjustment for incident electron energies of 0.5, 1, 5, 20 and 40 GeV are equal to 1 to within a tolerance of 0.2% (except for at a 0.5 GeV incident electron energy, for which the tolerance is  $\sim 1.0\%$ )<sup>1</sup>.

<sup>1</sup>The interdependence of the Bremsstrahlung differential cross section  $y_{\text{eff}}$ -spectrum shape and the integral of the pseudo-data  $y_{\text{eff}}$ -distribution over any  $y$ -range narrower than the full  $0 < y < 1$  observed in UCL Fast Simulation Bremsstrahlung Modification C in section 6.2.7 will also occur in UCL Fast Simulation Bremsstrahlung Modification B. However for UCL Fast Simulation Bremsstrahlung Modification B an iterative derivation of the total cross section adjustment was deemed unnecessary as the technique described here produces sufficiently accurate results.

Parameter	Value
A	12.8240
B	0.860239
C	1.00258

Table 6.1: The parameters of  $R(E)$ , where  $E$  is incident electron energy in MeV.

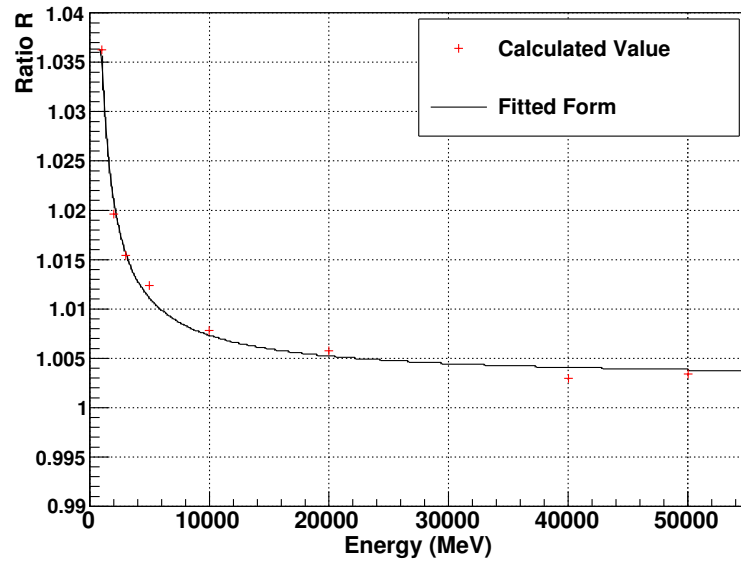


Figure 6.12: Comparison of the fitted three variable function of the incident electron energy  $R(E)$  and the  $R$  values calculated for a range of incident electron energies from eq. (6.1).

### 6.2.6 Bremsstrahlung GEANT4 4.9.2 Model $y$ -Spectrum Validation and Modification

In fig. 6.13 the GEANT4 4.9.2 and UCL Fast Simulation Basic Version  $y_{\text{eff}}$ -spectra are compared to the theoretical spectrum defined by eq. (5.2) for an incident electron energy of 40 GeV using a logarithmic scale. The theoretical spectrum is normalised to the GEANT4 4.9.2 histogram in the region  $0.01 < y < 0.1$ . Good agreement is observed between UCL Fast Simulation Basic Version and theory from  $y = 1$  to the LPM cut-off (as defined in inequality (5.3) using  $E_{\text{LPM-1}}$ ) at  $y = 5.5 \times 10^{-4}$ . At lower values of  $y$  they are highly discrepant, as expected. Excellent agreement is observed between GEANT4 4.9.2 and UCL Fast Simulation Basic Version from  $y = 1$  to the soft LPM cut-off (as characterised by  $E_{\text{LPM-2}}$ ) at  $y \sim 10^{-3}$ . The same features are evident in fig. 6.14, a plot of  $R = \frac{d\sigma_{\text{histogram}}}{d\sigma_{\text{theory}}}$  for GEANT4 4.9.2 and UCL Fast Simulation Basic Version. In the region  $y \sim 10^{-3}$  to  $y = 1$  the small linearly varying discrepancy between UCL Fast Simulation Basic Version and theory is to be expected because of the multiple photon emission effect (see section 6.2.3). The discrepancies observed between UCL Fast Simulation Basic Version and GEANT4 4.9.2 are due to the more sophisticated modelling of the LPM effect and the addition of a model of the dielectric effect in GEANT4 4.9.2. The GEANT4 4.9.2 model includes a numerically small term proportional to  $1 - y$  which is neglected in UCL Fast Simulation Basic Version and which may also contribute to the discrepancy.

It was decided to modify UCL Fast Simulation Basic Version to use eq. (5.27) for its  $y$ -spectral shape for incident electrons with energies greater than 1 GeV and to use the GEANT4 4.9.0 model (see sections 6.2.4 and 6.2.5) for incident electrons with energies less than 1 GeV. This will henceforth be referred to as UCL Fast Simulation Bremsstrahlung Modification C. As part of this modification it was also decided to reduce the minimum value of  $y$  simulated in UCL Fast Simulation from  $y = 10^{-4}$  to  $y = 5 \times 10^{-5}$ . (A minimum simulated  $y$ -value of  $y = 10^{-4}$  equates to a possible 4 MeV error on the simulation of the energy of a 40 GeV electron; however, because of the LPM/dielectric suppression of the Bremsstrahlung spectrum in the low- $y$  region, only a small fraction

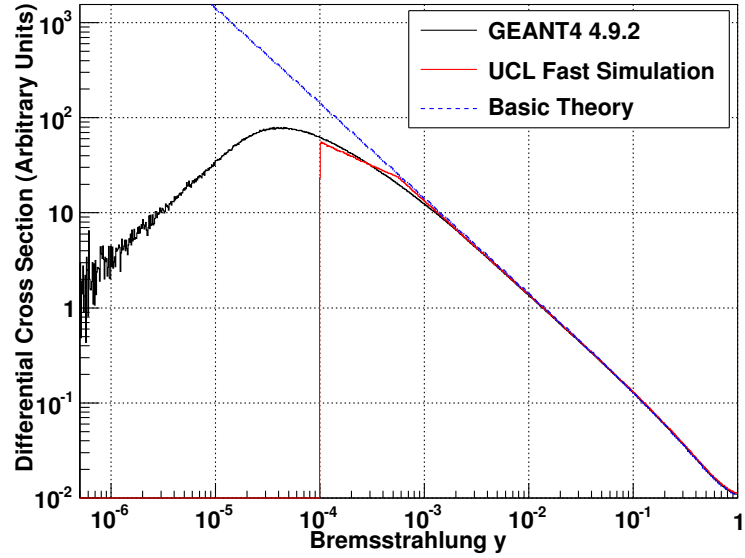


Figure 6.13: UCL Fast Simulation Basic Version and GEANT4 4.9.2 Bremsstrahlung  $y_{\text{eff}}$ -spectra pseudo-data compared to the theoretical spectrum given by eq. (5.2) on logarithmic axis scales. The incident electron beam energy is 40 GeV. The differential cross section is given in arbitrary units and the theoretical spectrum is normalised to the GEANT4 pseudo-data histogram in the region  $0.01 < y < 0.1$ . Good agreement is observed between UCL Fast Simulation Basic Version and theory from  $y = 1$  to the LPM cut-off (as defined in inequality (5.3) using  $E_{\text{LPM-1}}$ ) at  $y = 5.5 \times 10^{-4}$ ; at lower values of  $y$  they are highly discrepant, as expected. Excellent agreement is observed between GEANT4 and UCL Fast Simulation Basic Version from  $y = 1$  to the soft LPM cut-off (as characterised by  $E_{\text{LPM-2}}$ ) at  $y \sim 10^{-3}$ . The UCL Fast Simulation Basic Version spectrum is zero for  $y$  values less than  $y = 1 \times 10^{-4}$ , the minimum value of  $y$  simulated in UCL Fast Simulation Basic Version.

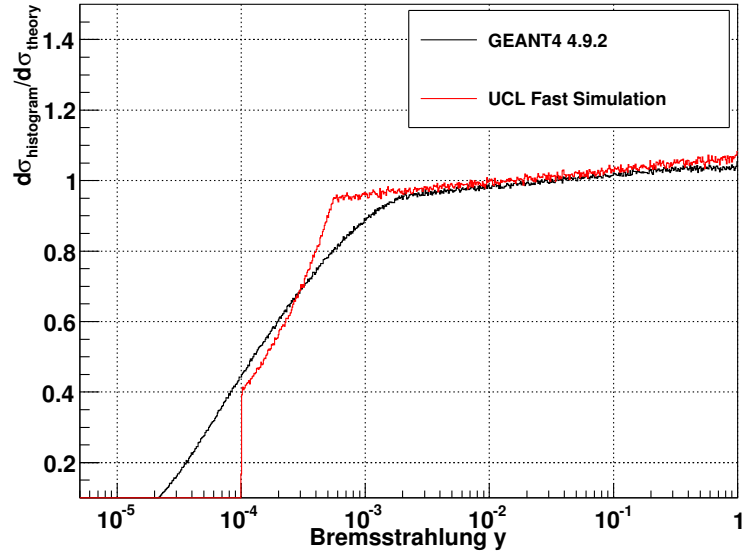


Figure 6.14: The ratio of the GEANT4 4.9.2 and UCL Fast Simulation Basic Version Bremsstrahlung  $y_{\text{eff}}$ -spectra to the theoretical spectrum given by eq. (5.2) on a logarithmic  $x$ -axis scale. The incident electron beam energy is 40 GeV. The theoretical spectrum is normalised to the GEANT4 pseudo-data histogram in the region  $0.01 < y < 0.1$ . Note that the UCL Fast Simulation Basic Version histogram is not normalised to the GEANT4 4.9.2 histogram, however the number of incident electrons used to generate the GEANT4 4.9.2 and UCL Fast Simulation Basic Version Bremsstrahlung  $y_{\text{eff}}$ -spectra is the same. The small linear variation of both ratios observed in the region  $y \sim 10^{-3}$  to  $y = 1$  is due to multiple photon emission (see section 6.2.3). The small constant difference between the GEANT4 4.9.2 and UCL Fast Simulation Basic Version histograms observed in the  $y \sim 10^{-3}$  to  $y = 1$  region is due to both the observed differences in the Bremsstrahlung differential cross section  $y$ -spectrum shape and differences in the Bremsstrahlung total cross section. The integrals of the GEANT4 4.9.2 and UCL Fast Simulation Basic Version histograms for the range  $0 < y < 1$  differ by  $\sim 2\%$  indicating a difference in total cross section.

of electron channel  $W$  decay events will be affected by this error. Thus the actual error on  $m_W$  due to using  $y = 10^{-4}$  as the minimum value of  $y$  simulated is expected to be negligible. Reducing the minimum simulated  $y$ -value by a factor of 2 is simply a further ‘safety measure’ to improve the accuracy of our simulation and ensure this error on  $m_W$  due to the minimum simulated  $y$ -value is negligible.) This modification also includes adjustments to the total Bremsstrahlung cross section as detailed in section 6.2.7. The error on the measured  $W$  mass due to not simulating  $y$ -values less than  $y = 5 \times 10^{-5}$  is expected to be negligible. This was not specifically studied for UCL Fast Simulation Bremsstrahlung Modification C, but the arguments for this error being negligible made for the case of UCL Fast Simulation Bremsstrahlung Modification B (see section 6.2.4) will apply equally to this case.

In fig. 6.15 the GEANT4 4.9.2 and UCL Fast Simulation Bremsstrahlung Modification C  $y$ -spectra are compared to the theoretical  $y$ -spectrum defined by eq. (5.27) for an incident electron energy of 40 GeV using a logarithmic scale. Now the GEANT4 4.9.2 histogram and the UCL Fast Simulation Bremsstrahlung Modification C histogram are in excellent agreement from  $y = 1$  to the minimum  $y$  simulated in UCL Fast Simulation Bremsstrahlung Modification C,  $y = 5 \times 10^{-5}$ . Good agreement is observed between GEANT4 4.9.2 and the theoretical  $y$ -spectrum as expected; however a small discrepancy is visible at low values of  $y$ , this is due to multiple photon emission (as discussed previously, see section 6.2.3). The same features are evident in fig. 6.16, a plot of  $R = \frac{d\sigma_{\text{histogram}}}{d\sigma_{\text{theory}}}$  for GEANT4 4.9.2 and UCL Fast Simulation Bremsstrahlung Modification C. Figure 6.17, a plot of  $R = \frac{d\sigma_{\text{GEANT4 4.9.2 histogram}}}{d\sigma_{\text{UCL Fast Simulation Modification C histogram}}}$ , confirms the accurate agreement between GEANT4 4.9.2 and UCL Fast Simulation Modification C.

The Bremsstrahlung GEANT4 4.9.2  $y$ -spectrum is dependent on the energy of the incident electron; hence it is interesting to compare UCL Fast Simulation Modification C and GEANT4 4.9.2 at a second energy. In fig. 6.18 the GEANT4 4.9.2 and UCL Fast Simulation Bremsstrahlung Modification C  $y$ -spectra are compared to the theoretical  $y$ -spectrum defined by eq. (5.27) for an incident electron energy of 5 GeV using a logarithmic scale. Again the GEANT4 4.9.2 histogram and the UCL Fast Simulation Bremsstrahlung Modification C histogram are in excellent agreement from  $y = 1$  to

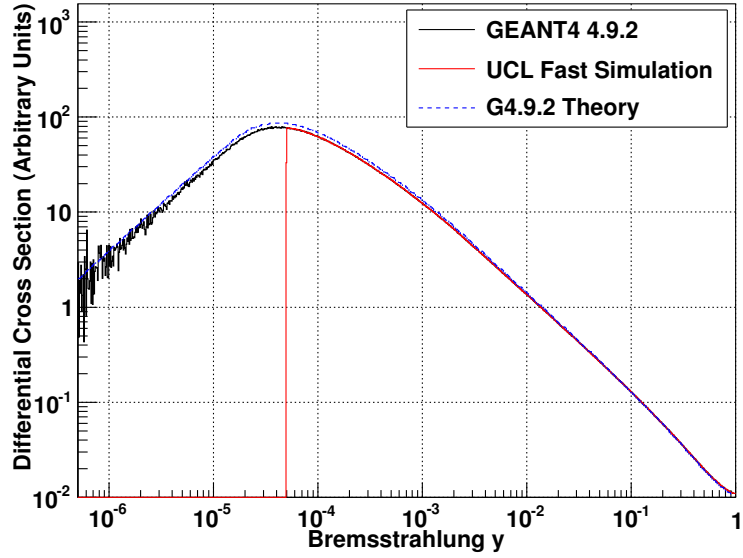


Figure 6.15: GEANT4 4.9.2 and UCL Fast Simulation Bremsstrahlung Modification C  $y_{\text{eff}}$ -spectra pseudo-data compared to the theoretical spectrum given by eq. (5.27) on logarithmic axis scales. The incident electron beam energy is 40 GeV. The differential cross section is given in arbitrary units and the theoretical spectrum is normalised to the GEANT4 pseudo-data histogram in the region  $0.01 < y < 0.1$ . The GEANT4 4.9.2 histogram and the UCL Fast Simulation Bremsstrahlung Modification C histogram are in excellent agreement from  $y = 1$  to the minimum  $y$  simulated in UCL Fast Simulation Bremsstrahlung Modification C,  $y = 5 \times 10^{-5}$ . Good agreement is observed between GEANT4 4.9.2 and the theoretical  $y$ -spectrum as expected; however a small discrepancy is visible at low values of  $y$ , due to multiple photon emission.

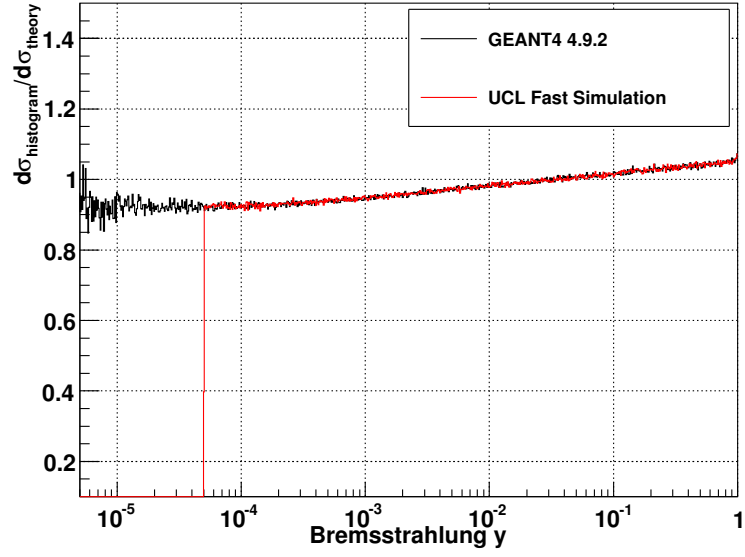


Figure 6.16: The ratio of the GEANT4 4.9.2 and UCL Fast Simulation Bremsstrahlung Modification C  $y_{\text{eff}}$ -spectra to the theoretical spectrum given by eq. (5.27) on a logarithmic  $x$ -axis scale. The incident electron beam energy is 40 GeV. The theoretical spectrum is normalised to the GEANT4 pseudo-data histogram in the region  $0.01 < y < 0.1$ .

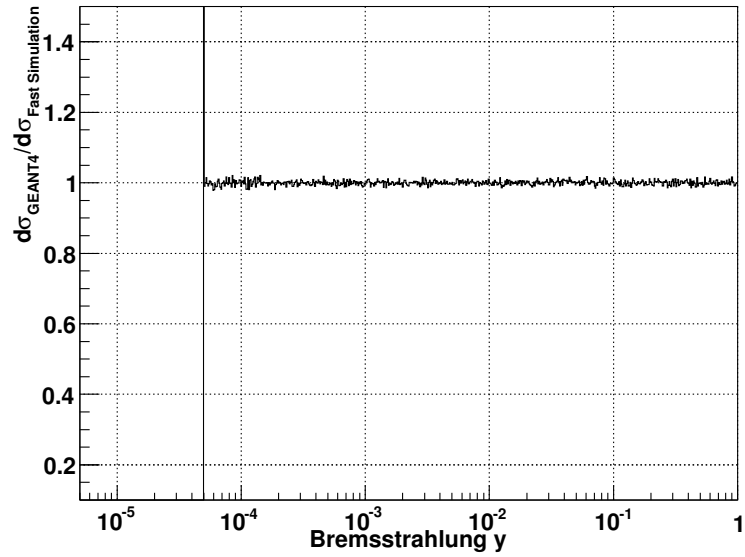


Figure 6.17: The ratio of the GEANT4 4.9.2 pseudo-data  $y_{\text{eff}}$ -spectrum to the UCL Fast Simulation Bremsstrahlung Modification C pseudo-data  $y_{\text{eff}}$ -spectrum on a logarithmic  $x$ -axis scale. The incident electron beam energy is 40 GeV.

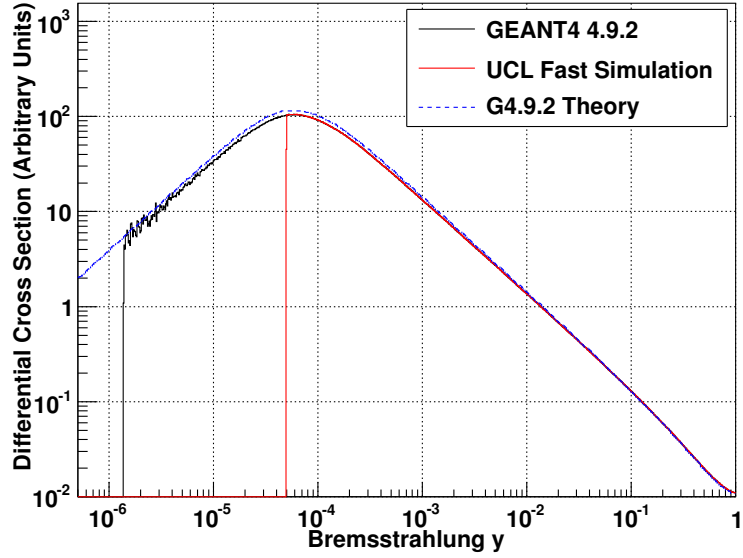


Figure 6.18: GEANT4 4.9.2 and UCL Fast Simulation Bremsstrahlung Modification C  $y_{\text{eff}}$ -spectra pseudo-data compared to the theoretical spectrum given by eq. (5.27) on logarithmic axis scales. The incident electron beam energy is 5 GeV. The differential cross section is given in arbitrary units and the theoretical spectrum is normalised to the GEANT4 pseudo-data histogram in the region  $0.01 < y < 0.1$ . The GEANT4 4.9.2 histogram and the UCL Fast Simulation Bremsstrahlung Modification C histogram are in excellent agreement from  $y = 1$  to the minimum  $y$  simulated in UCL Fast Simulation Bremsstrahlung Modification C,  $y = 5 \times 10^{-5}$ . Good agreement is observed between GEANT4 4.9.2 and the theoretical  $y$ -spectrum as expected. However a small discrepancy is visible at low values of  $y$ , due to multiple photon emission. (GEANT4 4.9.2 does not simulate discrete Bremsstrahlung events which generate photons of energies less than 0.01 MeV, hence the observed cut-off in the GEANT4 4.9.2 histogram at  $y = 2 \times 10^{-6}$  for this incident electron energy.)

the minimum  $y$  simulated in UCL Fast Simulation Bremsstrahlung Modification C,  $y = 5 \times 10^{-5}$ . Good agreement is observed between GEANT4 4.9.2 and the theoretical  $y$ -spectrum as expected; however a small discrepancy is visible at low values of  $y$ , due to multiple photon emission. The same features are evident in fig. 6.19, a plot of  $R = \frac{d\sigma_{\text{histogram}}}{d\sigma_{\text{theory}}}$  for GEANT4 4.9.2 and UCL Fast Simulation Modification C. Figure 6.20, a plot of  $R = \frac{d\sigma_{\text{GEANT4 4.9.2 histogram}}}{d\sigma_{\text{UCL Fast Simulation Modification C histogram}}}$ , confirms the accurate agreement between GEANT4 4.9.2 and UCL Fast Simulation Modification C.

Comparisons at a range of other energies (1.01 GeV, 1.5 GeV, 2 GeV, 10 GeV, 20 GeV, 30 GeV, 50 GeV, 60 GeV, 70 GeV, 80 GeV, 90 GeV, 100 GeV and 110 GeV) also display excellent agreement between GEANT4 4.9.2 and UCL Fast Simulation Brem-

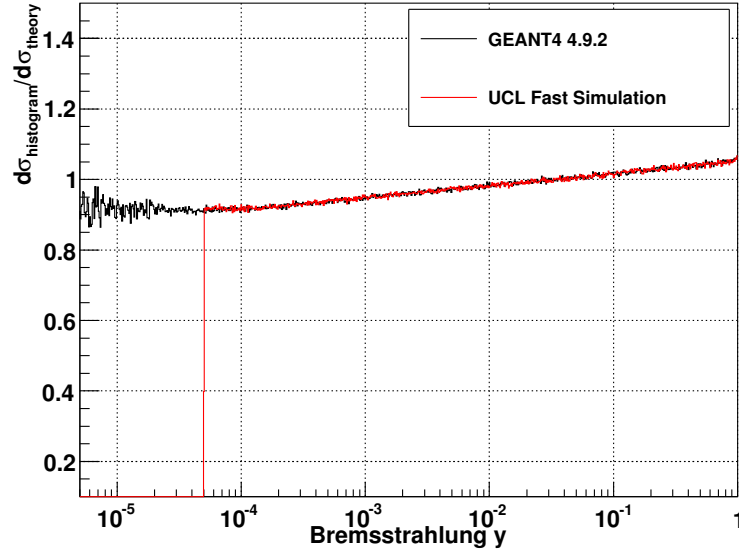


Figure 6.19: The ratio of the GEANT4 4.9.2 and UCL Fast Simulation Bremsstrahlung Modification C  $y_{\text{eff}}$ -spectra to the theoretical spectrum given by eq. (5.27) on a logarithmic  $x$ -axis scale. The incident electron beam energy is 5 GeV. The theoretical spectrum is normalised to the GEANT4 pseudo-data histogram in the region  $0.01 < y < 0.1$ .

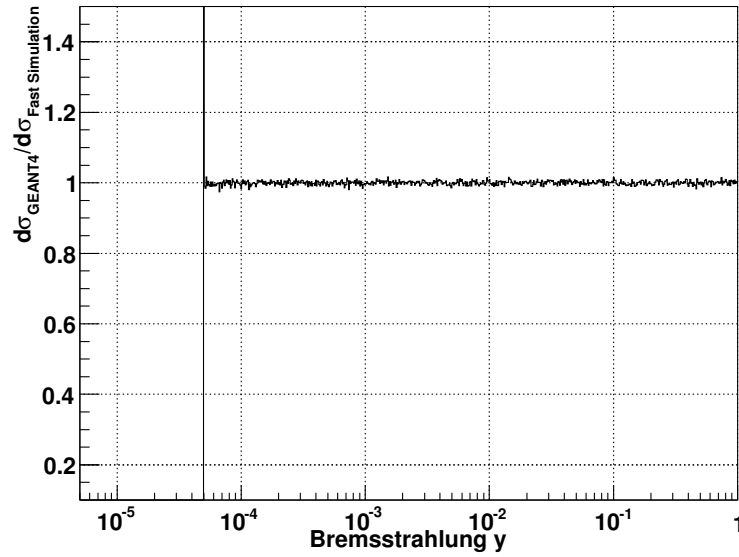


Figure 6.20: The ratio of the GEANT4 4.9.2 pseudo-data  $y_{\text{eff}}$ -spectrum to the UCL Fast Simulation Bremsstrahlung Modification C pseudo-data  $y_{\text{eff}}$ -spectrum on a logarithmic  $x$ -axis scale. The incident electron beam energy is 5 GeV.

strahlung Modification C. Comparisons at an energy below 1 GeV (0.99999 GeV) displayed good agreement between GEANT4 4.9.0 and UCL Fast Simulation Bremsstrahlung Modification C as expected. Good agreement is seen for all  $y$  across the entire range of energies of interest to us, hence we conclude that eq. (5.27) has been successfully implemented as the  $y$ -spectral shape in UCL Fast Simulation Bremsstrahlung Modification C for incident electrons with energies greater than 1 GeV.

### 6.2.7 Bremsstrahlung GEANT4 4.9.2 Model Total Cross Section Validation and Modification

The minimum  $y$ -value for which Bremsstrahlung events are simulated is higher for UCL Fast Simulation Bremsstrahlung Modification C than GEANT4 4.9.2, hence it is not consistent to compare their total cross sections directly. Instead we compare the integral of the  $y_{\text{eff}}$ -distribution for a range with a lower bound greater than the minimum  $y$ -value for which Bremsstrahlung is simulated in UCL Fast Simulation Bremsstrahlung Modification C. Included in UCL Fast Simulation Bremsstrahlung Modification C is an energy dependent adjustment of the Bremsstrahlung total cross section such that the integral of the UCL Fast Simulation Bremsstrahlung Modification C pseudo-data  $y_{\text{eff}}$ -distribution for the range  $0.0001 < y < 1$  is equal (within a tolerance of less than 0.1%) to the GEANT4 4.9.2 pseudo-data  $y_{\text{eff}}$ -distribution for the same range, at a range of incident electron energies from 1.01 GeV to 100 GeV; the derivation of this energy dependent adjustment is described below.

For UCL Fast Simulation Bremsstrahlung Modification C and GEANT4 4.9.2 the spectral shape of the Bremsstrahlung differential cross section  $y_{\text{eff}}$ -spectrum and the integral of a pseudo-data  $y_{\text{eff}}$ -distribution (for any  $y$ -range apart from  $0 < y < 1$ ) are weakly interdependent. The integral of a pseudo-data  $y_{\text{eff}}$ -distribution (for any  $y$ -range apart from  $0 < y < 1$ ) depends upon the spectral shape. The spectral shape depends upon the frequency of multiple photon emission, and the frequency of multiple photon emission in turn depends on the total cross section. Hence the required energy dependent adjustment for the total Bremsstrahlung cross section must be derived through an iterative cycle of comparison and further adjustment. Four iterations were required to

achieve an energy dependent adjustment to the total cross section sufficiently accurate to satisfy the required equality (see above) to within a tolerance of 0.1%.

In the first iteration UCL Fast Simulation Bremsstrahlung Modification C and GEANT4 4.9.2 pseudo-data was generated for 40 GeV incident electrons only. The following adjustment factor was calculated:

$$f_{\text{adj},1} = \frac{\int_{0.0001}^1 N_{\text{GEANT4}} dy_{\text{eff}}}{\int_{0.0001}^1 N_{\text{FastSim}} dy_{\text{eff}}} \quad (6.2)$$

where  $N_{\text{GEANT4}}$  is the number of GEANT4 4.9.2 pseudo-data events and  $N_{\text{FastSim}}$  is the number of UCL Fast Simulation Bremsstrahlung Modification C pseudo-data events. The initial UCL Fast Simulation Bremsstrahlung Modification C total Bremsstrahlung cross section was then multiplied by  $f_{\text{adj},1}$ .

In the second iteration UCL Fast Simulation Bremsstrahlung Modification C (including the adjustment of the total cross section by  $f_{\text{adj},1}$ ) pseudo-data was generated for 40 GeV incident electrons only. A second adjustment factor  $f_{\text{adj},2}$ , analogous to the first was calculated using this new pseudo-data. The initial UCL Fast Simulation Bremsstrahlung Modification C total Bremsstrahlung cross section was then multiplied by a combined factor of  $f_{\text{adj},1} \times f_{\text{adj},2}$ .

In the third iteration UCL Fast Simulation Bremsstrahlung Modification C (including the adjustment of the total cross section by  $f_{\text{adj},1} \times f_{\text{adj},2}$ ) pseudo-data was generated for 1.01, 1.5, 2, 5, 10, 20, 30, 40, 50, 60, 70, 80, 90 and 100 GeV incident electrons. At each energy a third adjustment factor  $f_{\text{adj},3}$ , analogous to the first was calculated using this new pseudo-data. An energy dependent adjustment function  $f_{\text{adj},3}(E)$ , was then calculated by performing a polynomial fit to  $f_{\text{adj},3}$  across the range of incident electron energies, with different sets of coefficients for two different sub-ranges. The initial UCL Fast Simulation Bremsstrahlung Modification C total Bremsstrahlung cross section was then multiplied by a combined factor of  $f_{\text{adj},1} \times f_{\text{adj},2} \times f_{\text{adj},3}(E)$ .

The fourth iteration was performed by the same technique as the third, although in this case the polynomial fit used only one set of coefficients for the entire range of energies. In the final version of UCL Fast Simulation Bremsstrahlung Modification C the initial

Adjustment Functions	
$f_{\text{adj},1}$	$= 0.797454$
$f_{\text{adj},2}$	$= 0.985503$
$f_{\text{adj},3}(E)$	$= \begin{cases} \begin{pmatrix} 1.10774 & \text{if } E \leq 2009.166 \text{ MeV} \\ -2.59124 \times 10^{-5} E \\ +5.32290 \times 10^{-9} E^2 \end{pmatrix} \\ \begin{pmatrix} 1.08297 & \text{otherwise} \\ -2.94215 \times 10^{-6} E \\ +2.67988 \times 10^{-11} E^2 \\ -1.58269 \times 10^{-16} E^3 \\ +3.93827 \times 10^{-22} E^4 \end{pmatrix} \end{cases}$
$f_{\text{adj},4}(E)$	$= 1.00469 - 1.41998 \times 10^{-7} E + 6.14205 \times 10^{-13} E^2$

Table 6.2: The functional forms and numerical values of the four adjustment functions:  $f_{\text{adj},1}$ ,  $f_{\text{adj},2}$ ,  $f_{\text{adj},3}(E)$  and  $f_{\text{adj},4}(E)$ . The numerical values given are for incident electron energies  $E$ , in units of MeV.

UCL Fast Simulation Bremsstrahlung Modification C total Bremsstrahlung cross section is multiplied by an energy dependent adjustment of  $f_{\text{adj},1} \times f_{\text{adj},2} \times f_{\text{adj},3}(E) \times f_{\text{adj},4}(E)$ . To ensure a consistent treatment of very high energy electrons in the final version of UCL Fast Simulation Bremsstrahlung Modifications C, for electrons with incident electron energies greater than 100 GeV the initial UCL Fast Simulation Bremsstrahlung Modification C total Bremsstrahlung cross section is multiplied by a fixed adjustment of  $f_{\text{adj},1} \times f_{\text{adj},2} \times f_{\text{adj},3}(E = 100 \text{ GeV}) \times f_{\text{adj},4}(E = 100 \text{ GeV})$  instead of the energy dependent adjustment.

Further UCL Fast Simulation Bremsstrahlung Modification C pseudo-data was generated using this final version for the range of energies listed previously and used to confirm that the energy dependent adjustment fulfils its purpose. The functional forms and coefficients of the four adjustment functions are presented in table 6.2.

For incident electron energies less than 1 GeV UCL Fast Simulation Bremsstrahlung Modification C uses UCL Fast Simulation Bremsstrahlung Modification B (i.e. the GEANT4 4.9.0 Bremsstrahlung model). To prevent a discontinuity in the total cross section as a function of incident electron energy at 1 GeV, the final version of UCL Fast Simulation Bremsstrahlung Modification C scales the UCL Fast Simulation Bremsstrah-

lung Modification B total cross section such that the integral of the UCL Fast Simulation Bremsstrahlung Modification C pseudo-data  $y_{\text{eff}}$ -distribution for a 1.00001 GeV incident electron energy (over the range  $0.005 < y < 0.05$ ) is equal to the integral of the UCL Fast Simulation Bremsstrahlung Modification B pseudo-data  $y_{\text{eff}}$ -distribution for a 0.999999 GeV incident electron energy (over the same range).

### 6.2.8 Summary

Table 6.3 lists the different versions of UCL Fast Simulation detailed above. The Bremsstrahlung total cross section physics model and Bremsstrahlung differential cross section  $y$ -spectrum model used for each version are also stated.

## 6.3 Comparison of GEANT4 4.9.2 and GEANT4 4.9.0 Bremsstrahlung Models with Experimental Data

### 6.3.1 Introduction

The GEANT4 4.9.0 Bremsstrahlung model (eq. (5.9)) and the GEANT4 4.9.2 Bremsstrahlung model (eq. (5.27)) differ considerably for incident electrons with energies greater than 1 GeV. The differences affect two different regions of the Bremsstrahlung  $y$ -spectrum, the high- $y$  region (approximately  $0.1 < y < 1$  for a 40 GeV incident electron energy) and the low- $y$  region (approximately  $y < 2 \times 10^{-3}$  for a 40 GeV incident electron energy).

The GEANT4 4.9.0 Bremsstrahlung differential cross section  $y$ -spectrum model is a parameterisation of the differential cross section  $y$ -spectra of Seltzer and Berger [63] over a wide range of different incident electron energies and elements (see section 5.1.3). The GEANT4 4.9.2 Bremsstrahlung differential cross section  $y$ -spectrum model is an analytic representation which is valid in the high energy (ultra-relativistic) limit and uses the complete screening approximation (see section 5.1.4). This accounts for the difference observed in the high- $y$  region; these models both tend to the same limit as  $y \rightarrow 0$ .

UCL Fast Simulation Version	Bremsstrahlung Differential Cross Section $y$ -Spectrum Model	Bremsstrahlung Total Cross Section Model
Basic Version	Basic Bremsstrahlung Differential Cross Section Model: Equation (5.2) with a LPM suppression factor given by eq. (5.5) applied for $y$ -values satisfying inequality (5.3)	Basic Bremsstrahlung Total Cross Section Model: Equation (5.40) combined with explicit rejection of events to account for the LPM effect
Bremsstrahlung Modification A	Partial GEANT4 4.9.0: Equation (5.9) with a LPM suppression factor given by eq. (5.5) applied for $y$ -values satisfying inequality (5.3)	Formally unconstrained but of the same order of magnitude as the Basic Bremsstrahlung Total Cross Section Model
Bremsstrahlung Modification B	GEANT4 4.9.0: Equation (5.9) with GEANT4 4.9.0 Bremsstrahlung Parameterisation B low- $y$ suppression (models both LPM and dielectric suppression)	Adjusted to match the GEANT4 4.9.0 total cross section across a range of incident electron energies
Bremsstrahlung Modification C	GEANT4 4.9.2: Equation (5.27) (models both LPM and dielectric suppression) for incident electron energies greater than 1 GeV, Bremsstrahlung Modification B for incident electron energies less than 1 GeV	Adjusted to match the GEANT4 4.9.2 total cross section across a range of incident electron energies

Table 6.3: Summary of the different versions of UCL Fast Simulation detailed in section 6.2.

GEANT4 4.9.2 uses a more sophisticated treatment of the dielectric and LPM effects than GEANT4 4.9.0. This changes the shape of the Bremsstrahlung differential cross section  $y$ -spectrum in the LPM/dielectric suppressed region. It also changes from using a precisely defined threshold condition (a ‘hard cut-off’) for applying LPM/dielectric suppression (eq. (5.3)) to using a gradual threshold (‘soft cut-off’) for applying LPM/dielectric suppression; thus allowing a smooth intersection between the LPM/dielectric suppressed and non-suppressed regions of the differential cross section  $y$ -spectrum. This accounts for the differences observed in the low- $y$  region.

In fig. 6.21 the GEANT4 4.9.2 and GEANT4 4.9.0 pseudo-data  $y_{\text{eff}}$ -distributions are compared for an incident electron energy of 40 GeV using a logarithmic  $x$ -axis scale. Significant differences can be observed in both the high- $y$  region and the low- $y$  region as expected. Notice GEANT4 4.9.0 uses a ‘hard cut-off’ of LPM and dielectric suppression at  $y = 5.5 \times 10^{-4}$  while GEANT4 4.9.2 uses a ‘soft cut-off’ of LPM and dielectric suppression at roughly  $y \sim 10^{-3}$ .

Basic calculations indicated that the differences between these two models were possibly significant to the  $W$  mass analysis. It was unclear which of these models would most accurately model the differential cross section  $y$ -spectrum for Bremsstrahlung occurring in the CDF Run II silicon tracker at electron energies typical of this analysis ( $\sim 40$  GeV), hence it was decided to compare the GEANT4 models against experimental data. No single experimental data set of Bremsstrahlung  $y$ -spectrum data was found that covered the entire range of  $y$ -values at the incident electron energies of interest. Our studies are divided into those of the low- $y$  region where matter effects are important and the high- $y$  region where such matter effects are negligible.

### 6.3.2 Comparison in the Low- $y$ Region

The low- $y$  region (the region of LPM/dielectric suppression) has been probed by data sets taken at CERN SPS and at SLAC. Direct comparisons of both GEANT4 4.9.2 and GEANT4 4.9.1 (the modelling of Bremsstrahlung does not differ between GEANT4 4.9.0 and GEANT4 4.9.1) with the CERN SPS data are given in reference [81], this data covers the entire  $y$ -range. Comparisons are given for 149 GeV electrons incident

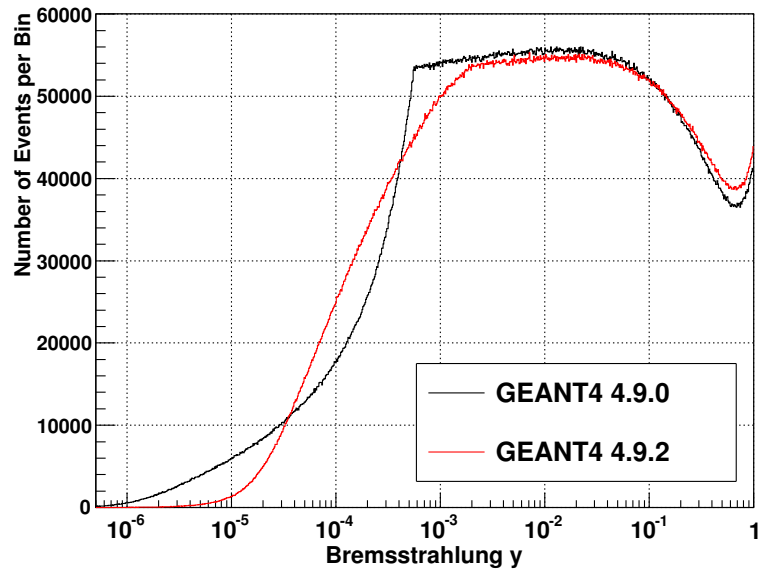


Figure 6.21: GEANT4 4.9.2 and GEANT4 4.9.0 pseudo-data  $y_{\text{eff}}$ -distributions compared on a logarithmic  $x$ -axis scale. The incident electron beam energy is 40 GeV. The total number of test beam events generated in the two pseudo-data samples is the same, however events in which no Bremsstrahlung interaction occurs are not included in the histograms. Significant changes can be observed in both the high- $y$  region  $0.1 < y < 1$  and the low- $y$  region  $y < 2 \times 10^{-3}$ . GEANT4 4.9.0 uses a ‘hard cut-off’ of LPM and dielectric suppression at  $y = 5.5 \times 10^{-4}$ ; GEANT4 4.9.2 uses a ‘soft cut-off’ of the LPM and dielectric suppression at roughly  $y \sim 10^{-3}$ .

on a tantalum ( $Z = 73$ ) target, 207 GeV electrons incident on an iridium ( $Z = 77$ ) target and 287 GeV electrons incident on a copper ( $Z = 29$ ) target. In all cases we see GEANT4 4.9.2 more accurately reproducing the data than GEANT4 4.9.1, and we can see that generally GEANT4 4.9.2 reproduces the experimental data with a good degree of accuracy. However these comparisons are at incident electron energies that are considerably higher than those of interest to us. Tantalum and iridium are heavy elements with high atomic numbers and we would not expect their radiative properties to be similar to those of silicon or other light elements that are abundant in the CDF Run II silicon tracker.

The SLAC experimental data is presented in a series of three papers. The first paper [82] presents a study of the production rate of 5-500 MeV photons from 8 and 25 GeV electron beams incident on thin gold and carbon targets, herein referred to as the ‘5-500 MeV PRL’ dataset. The second paper [83] presents a study of the production rate of 0.2-20 MeV photons from 8 and 25 GeV electron beams incident on thin gold and carbon targets, herein referred to as the ‘0.2-20 MeV PRL’ dataset. The third paper [60] presents a study of the production rate of 0.2-500 MeV photons from 8 and 25 GeV electron beams incident on a range of different materials (including carbon ( $Z = 6$ ) - a light element which is chemically similar to silicon), herein referred to as the ‘0.2-500 MeV PRD’ dataset. We compared the experimental data for 25 GeV electrons incident on a carbon (pyrolytic graphite) target from SLAC with GEANT4 4.9.2 and GEANT4 4.9.0 pseudo-data Bremsstrahlung differential cross section spectra derived in a test beam setup (as described in section 6.2.2). In the ‘0.2-20 MeV PRL’ and ‘0.2-500 MeV PRD’ datasets, carbon data is presented for target thicknesses of 2%  $X_0$  and 6%  $X_0$ . The ‘5-500 MeV PRL’ dataset only includes carbon data for a target thickness of 6%  $X_0$ . The ‘0.2-500 MeV PRD’ dataset includes data for aluminium ( $Z = 13$ ), also of possible interest to this analysis, however the results from the carbon data were considered sufficient and this data was not considered. These three SLAC experiments use the effective photon energy  $k_{\text{eff}} = \sum_i k_i$ , the summed energy of all the photons emitted from an electron, as the independent variable and photon intensity  $\frac{1}{X_0} \frac{dN}{d \log k}$ , as the dependent variable. ( $N$  is the number of events per photon energy bin per incident

electron.) This is equivalent to the Bremsstrahlung energy weighted differential cross section  $y$ -spectrum; it can be shown that:

$$\frac{1}{X_0} \frac{dN}{d \log k} \propto y \frac{d\sigma}{dy} \quad (6.3)$$

As a cross-check of the consistency of the data, fig. 6.22 compares the SLAC data for 25 GeV electrons incident on a 6 %  $X_0$  thick carbon plate from these three SLAC experiments. It was decided to use the ‘0.2-500 MeV PRD’ carbon dataset for comparison with GEANT4 as this provided consistent data over a large range of  $k$  values. Reference [60] notes that the carbon target used for that experiment had a measured density 4 % below the standard value. We used this reduced density of carbon in the GEANT4 test beam setups.

In fig. 6.23 the data from the ‘0.2-500 MeV PRD’ dataset is compared with pseudo-data generated in a test beam setup using both GEANT4 4.9.2 and GEANT4 4.9.0. Figure 6.24 is a plot of  $R = \frac{d\sigma_{\text{pseudo-data}}}{d\sigma_{\text{data}}}$  for this comparison. The target is carbon with a thickness of 6%  $X_0$ . The total cross section for Bremsstrahlung was not validated in this exercise, hence the GEANT4 Bremsstrahlung  $y$ -spectra for the low- $y$  region were normalised by hand to give an accurate match to the data. The GEANT4 4.9.2 Bremsstrahlung model reproduces the data accurately except at exceptionally low  $k$ -values ( $k < 1$  MeV). The GEANT4 4.9.0 Bremsstrahlung model does not reproduce the data accurately in the region where the LPM and dielectric effects are important. The observed ‘upturn’ in the data at exceptionally low  $k$ -values could be due to transition radiation and backgrounds, neither of which are modelled in the GEANT4 test beam setup. This is possibly the source of the discrepancy between the GEANT4 4.9.2 Bremsstrahlung model and the data at exceptionally low  $k$ -values ( $k < 500$  keV). In UCL Fast Simulation we only simulate Bremsstrahlung down to a minimum  $y$ -value of  $y = 5 \times 10^{-5}$ , hence such exceptionally low  $k$ -values would not be simulated for a typical  $\sim 40$  GeV electron.

It is also of interest to compare GEANT4 to the SLAC data for a thinner target to test the modelling of any edge effects (such effects being more pronounced for thinner targets). In fig. 6.25 the data from the ‘0.2-500 MeV PRD’ dataset is compared with

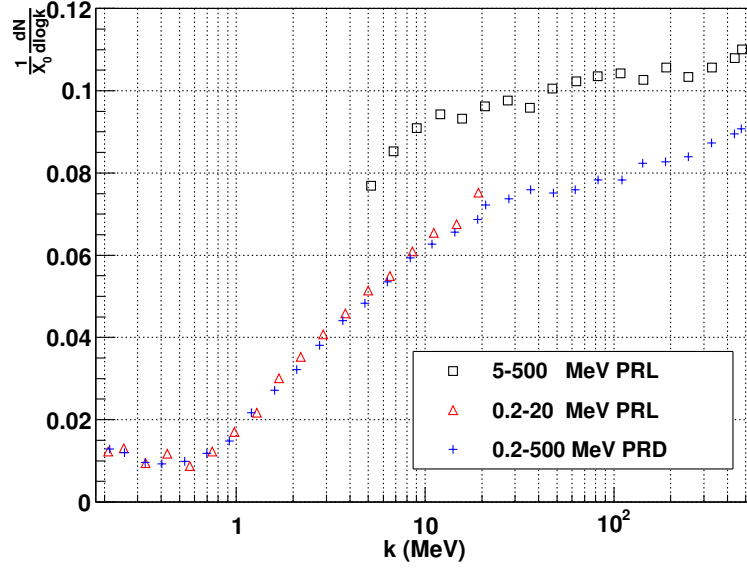


Figure 6.22: Comparison of SLAC experimental data for 25 GeV electrons incident on a 6 %  $X_0$  thick carbon plate from the ‘5-500 MeV PRL’, ‘0.2-20 MeV PRL’ and ‘0.2-500 MeV PRD’ datasets. The effective photon energy  $k_{\text{eff}} = \sum_i k_i$ , the summed energy of all the photons emitted from an electron, is the independent variable and photon intensity  $\frac{1}{X_0} \frac{dN}{d \log k}$ , is the dependent variable. The units of the photon intensity are unknown. The data presented in the ‘0.2-20 MeV PRL’ and ‘0.2-500 MeV PRD’ datasets appears to be in good agreement. The data from the ‘5-500 MeV PRL’ dataset agrees with the functional form of the  $k$ -spectrum of the data from the ‘0.2-500 MeV PRD’ dataset. However the normalisation of the data from the ‘5-500 MeV PRL’ dataset does not agree with that of the ‘0.2-500 MeV PRD’ dataset. This could be due to an additional cut (intended to reduce a significant experimental background) applied to the data from the ‘0.2-20 MeV PRL’ and ‘0.2-500 MeV PRD’ datasets but not used in the older data from the ‘5-500 MeV PRL’ dataset.

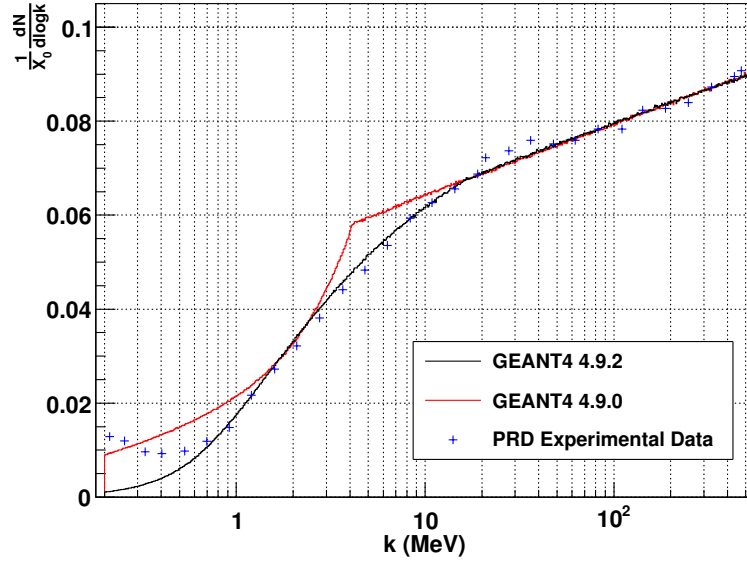


Figure 6.23: GEANT4 4.9.2 and GEANT4 4.9.0 pseudo-data  $k_{\text{eff}}$ -distributions compared to SLAC experimental data from the ‘0.2-500 MeV PRD’ dataset on a logarithmic  $k$ -scale. The incident electron beam energy is 25 GeV; the target is carbon with a thickness of 6%  $X_0$ . The units of the data values of photon intensity are unknown. The GEANT4 4.9.2 pseudo-data histogram is normalised by hand to best match the data. The GEANT4 4.9.0 pseudo-data histogram is then normalised to the GEANT4 4.9.2 pseudo-data histogram in the region  $100 < k < 500$  MeV. Both GEANT4 versions reproduce the data accurately above the region where the LPM and dielectric effects are important. GEANT4 4.9.2’s soft cut-off for the LPM and dielectric effects reproduces the data more accurately than GEANT4 4.9.0’s hard cut-off. GEANT4 4.9.2 reproduces the data more accurately than GEANT4 4.9.0 at very low  $k$ -values. For extremely low  $k$  neither model accurately reproduces the data; however this can possibly be attributed to the effect of transition radiation and backgrounds.

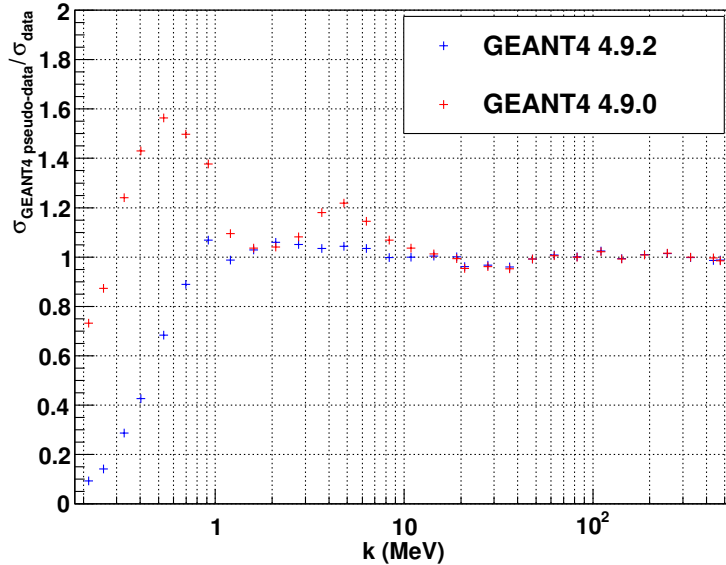


Figure 6.24: The ratio of GEANT4 4.9.2 and GEANT4 4.9.0  $k_{\text{eff}}$ -distributions to SLAC experimental data from the ‘0.2-500 MeV PRD’ dataset on a logarithmic  $k$ -scale. The incident electron beam energy is 25 GeV; the target is carbon with a thickness of 6%  $X_0$ . The GEANT4 4.9.2 pseudo-data is normalised by hand to best match the data. The GEANT4 4.9.0 pseudo-data is then normalised to the GEANT4 4.9.2 pseudo-data in the region  $100 < k < 500$  MeV.

pseudo-data generated in a test beam setup using both GEANT4 4.9.2 and GEANT4 4.9.0. Figure 6.26 is a plot of  $R = \frac{d\sigma_{\text{pseudo-data}}}{d\sigma_{\text{data}}}$  for this comparison. The target is carbon with a thickness of 2%  $X_0$ . The total cross section for Bremsstrahlung was not validated in this exercise, hence the GEANT4 Bremsstrahlung  $y$ -spectra for the low- $y$  region were normalised by hand to give an accurate match to the data. Neither GEANT4 model reproduces the data completely accurately in the region where the LPM and dielectric effects are important; however GEANT4 4.9.2 reproduces the data considerably more accurately than GEANT4 4.9.0 in this region. The observed discrepancy between GEANT4 4.9.2 and the data is similar to that observed by the authors of reference [60] between the data and their own Monte-Carlo simulation (see further discussion below). There is also a small feature in the data for  $k$ -values slightly higher than the region where the LPM and dielectric effects are important, this is unexplained and not captured by either GEANT4 model. The observed ‘upturn’ in the data at exceptionally low  $k$ -values could be due to transition radiation and backgrounds, neither of which are modelled in

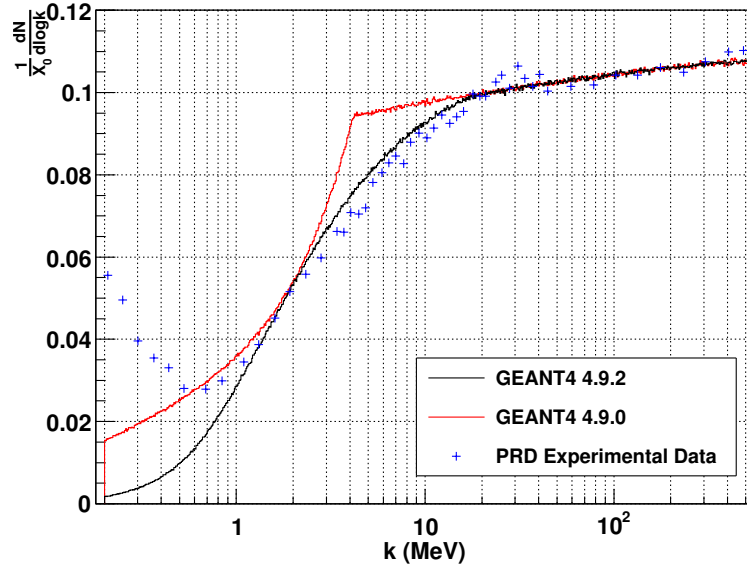


Figure 6.25: GEANT4 4.9.2 and GEANT4 4.9.0 pseudo-data  $k_{\text{eff}}$ -distributions compared to SLAC experimental data from the ‘0.2-500 MeV PRD’ dataset on a logarithmic  $k$ -scale. The incident electron beam energy is 25 GeV; the target is carbon with a thickness of 2%  $X_0$ . The units of the data values of photon intensity are unknown. The GEANT4 4.9.2 pseudo-data histogram is normalised by hand to best match the data. The GEANT4 4.9.0 pseudo-data histogram is then normalised to the GEANT4 4.9.2 pseudo-data histogram in the region  $100 < k < 500$  MeV. Both GEANT4 versions reproduce the data accurately for high  $k$ -values. In the region  $20 < k < 40$  MeV an unknown feature of the data is not reproduced accurately by either of the GEANT4 models. In the region  $k < 20$  MeV the LPM and dielectric effects are expected to be important; the GEANT4 4.9.2 model reproduces the data with a greater degree of accuracy in this region than the GEANT4 4.9.0 model, however neither model reproduces the data completely accurately in this region. For extremely low  $k$  neither model accurately reproduces the data; however this can possibly be attributed to the effect of transition radiation and backgrounds.

the GEANT4 test beam setup.

GEANT4 4.9.2 appears to satisfactorily model the data (except for exceptionally low  $k$ -values, which are unimportant for this analysis) for the 6%  $X_0$  carbon target, however it does not completely accurately model the data for the 2%  $X_0$  carbon target. Hence it appears that while GEANT4 4.9.2 accurately models the bulk media Bremsstrahlung  $y$ -spectrum at low- $y$ , it does not capture distortion of the Bremsstrahlung spectrum that may occur as the electron traverses the edges of the target (i.e. surface effects, see below). This is supported by evidence from reference [60] where a technique of ‘subtracting’ the data for the 2%  $X_0$  carbon target from the data for the 6%  $X_0$  carbon

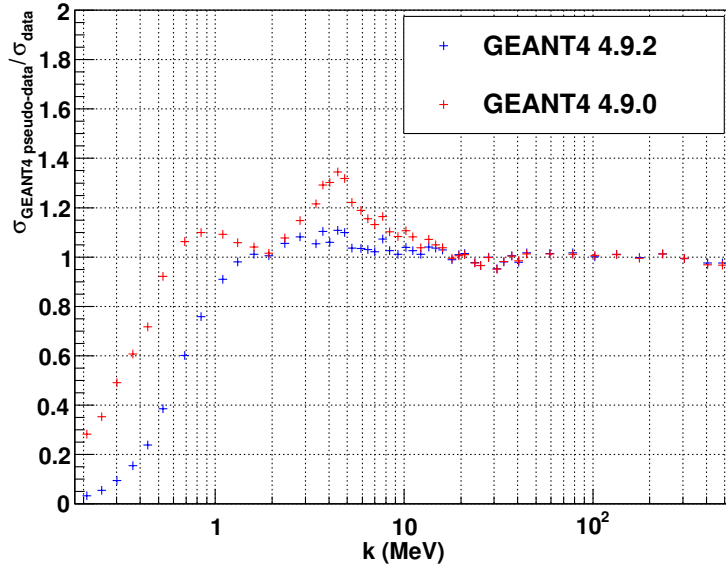


Figure 6.26: The ratio of GEANT4 4.9.2 and GEANT4 4.9.0  $k_{\text{eff}}$ -distributions to SLAC experimental data from the ‘0.2-500 MeV PRD’ dataset on a logarithmic  $k$ -scale. The incident electron beam energy is 25 GeV; the target is carbon with a thickness of 2%  $X_0$ . The GEANT4 4.9.2 pseudo-data is normalised by hand to best match the data. The GEANT4 4.9.0 pseudo-data is then normalised to the GEANT4 4.9.2 pseudo-data in the region  $100 < k < 500$  MeV.

target is used to isolate the bulk media Bremsstrahlung  $y$ -spectrum; this bulk media Bremsstrahlung  $y$ -spectrum is well modelled by the author’s own Monte-Carlo, which is similar to GEANT4 4.9.2.

One possible candidate for these surface effects might be conventional transition radiation<sup>2</sup>. However the authors of reference [60] also find a similar discrepancy between the data and their own Monte-Carlo simulation which includes conventional transition radiation for the 2%  $X_0$  carbon target; hence it would not appear that conventional transition radiation alone can explain the observed discrepancy.

Another candidate for these surface effects is a reduction in the dielectric/LPM suppression of the Bremsstrahlung  $y$ -spectrum near the target surface. If the formation length of a Bremsstrahlung interaction extends outside of the target then there are less scattering centres for destructive quantum interference, reducing the LPM suppression

<sup>2</sup>When an electron enters a medium, the electron’s electromagnetic field adjusts to the dielectric of the medium. This adjustment may cause part of the electron’s electromagnetic field to break-away and form a real photon. This radiation is known as transition radiation [70].

of the Bremsstrahlung  $y$ -spectrum. If the formation length of a Bremsstrahlung interaction extends outside the target this also reduces the number of centres for Compton scattering, hence reducing the dielectric suppression of the Bremsstrahlung  $y$ -spectrum. For extremely thin targets, when target thickness  $t < l_f = 2\hbar c (E / (m_e c^2))^2 / k$  (where  $E$  is the energy of the incident electron and  $k$  is the energy of the emitted photon), no LPM/dielectric suppression will occur. For a 40 GeV electron  $l_f \approx 2 \text{ keV}/k \text{ m}$ , hence we might expect to get no LPM/dielectric suppression of the emission of a 10 MeV photon in a layer of thickness  $\sim 100 \mu\text{m}$ .

However the observed discrepancy in the comparison between data and GEANT4 4.9.2 indicates an increase in LPM/dielectric suppression in the data. Reference [60] also observes this and describes it as ‘puzzling’; one plausible explanation is that the edge transition radiation and Bremsstrahlung from atomic electrons might interfere destructively. It is also possible that the specific material structure of the pyrolytic graphite carbon target can explain these surface effects.

### 6.3.3 Comparison to Tabulated Theoretical Results in the High- $y$ Region

For the high- $y$  region we validated against respected tabulated theoretical results to avoid the complexities commonly associated with comparisons with experimental data. Two sets of tabulated theoretical results were considered, those of Seltzer and Berger [63] and those of the Evaluated Electron Data Library (EEDL) [72, 73]<sup>3</sup>. We were unable to find a satisfactory procedure by which to normalise the results of Seltzer and Berger, hence this study proved inconclusive. The EEDL results are essentially an extension of the Seltzer and Berger results (S.M Seltzer is named as an author of the EEDL) to a larger range of incident electron energies and media. The EEDL results also provide a greater number of emitted photon energies ( $k$  values) than the Seltzer and Berger results.

Figure 6.27 is a plot of the ratios  $\frac{d\sigma_X}{d\sigma_{\text{GEANT4 4.9.2 } y\text{-spectrum}}}$  where  $X$  is the EEDL tabu-

---

<sup>3</sup>Unfortunately while the EEDL itself is available online, the original documentation associated with it is more difficult to obtain and rather incomplete.

lated theoretical Bremsstrahlung  $y$ -spectrum or the GEANT4 4.9.0 theoretical differential cross section  $y$ -spectrum as given by eq. (5.9) and the GEANT4 4.9.2  $y$ -spectrum is the GEANT4 4.9.2 theoretical differential cross section  $y$ -spectrum as given by eq. (5.27). A logarithmic  $x$ -axis scale is used. The incident electron energy is 100 GeV (the energy nearest to 40 GeV on a logarithmic scale for which EEDL tabulated theoretical results are given); the medium is silicon. The EEDL tabulated theoretical results do not include dielectric and LPM suppression, hence the GEANT4 4.9.2 and GEANT4 4.9.0  $y$ -spectra used in this figure do not include dielectric/LPM suppression (for GEANT4 4.9.2 this is achieved by setting the LPM parameters  $\xi(s) = 1$ ,  $G(s) = 1$ ,  $\phi(s) = 1$  and the dielectric parameter  $S(k) = 1$ ). The EEDL tabulated theoretical results and both of the GEANT4 spectra appear to tend to the same limit as  $y \rightarrow 0$ , hence we normalise the EEDL tabulated theoretical data and GEANT4 4.9.0 spectrum to the GEANT4 4.9.2 spectrum in the region  $0.00001 < y < 0.0001$ .

The EEDL tabulated theoretical results are not modelled accurately throughout the entire  $y$ -range by either of the GEANT4 models. They are better modelled by the GEANT4 4.9.0 model for  $y < 0.2$ , but better modelled by GEANT4 4.9.2 for  $y > 0.2$ . Note it is unlikely an event where Bremsstrahlung of a primary daughter electron of a  $W \rightarrow e\nu_e$  decay occurs with a  $y$ -value higher than  $y \sim 0.5$  will pass the cut imposed on the quantity  $E/p$  (the primary selection cut for material scale fits for the  $W$  mass analysis on  $E/p$  is currently to veto  $E/p > 1.6$ ), hence the modelling of very high- $y$  Bremsstrahlung is of little importance to this analysis. The Bremsstrahlung  $y$ -spectrum may display some dependence on the incident electron energy (certainly the GEANT4 4.9.0 model is incident electron energy dependent). We expect the general conclusion of comparisons made for 100 GeV incident electrons to remain valid at 40 GeV; however it is not clear if the exact regions of agreement between the EEDL tabulated values and GEANT4 4.9.0/GEANT4 4.9.2 would be the same at these two different energies. The discrepancies between GEANT4 4.9.2 and the EEDL tabulated values are possibly to be expected. The GEANT4 4.9.2 model uses a model that is valid in the high energy (ultra-relativistic) limit, additionally making the approximation of complete screening (of the nuclear Coulomb charge by atomic electrons); both the application of a high-energy

limit formula and the approximation of complete screening may be only partially valid for 100 GeV incident electrons.

GEANT4 4.9.0 uses a parameterised fit to the theoretical results of Seltzer and Berger across a large range of values of  $Z$  and incident electron energy; it is unclear why discrepancies occur between the GEANT4 4.9.0 model and the EEDL tabulated values. As discussed in section 8.1, a further comparison was made between the EEDL tabulated theoretical results, the GEANT4 4.9.0 model and the GEANT4 4.9.2 model for incident electron energies greater than 1 GeV (deliberately applied outside its normal range of applicability) at a lower incident electron energy of  $\sim 12$  MeV; in this case the EEDL tabulated theoretical values and GEANT4 4.9.0 model roughly agree and both deviate very considerably from the GEANT4 4.9.2 model for incident electron energies above 1 GeV. Hence it would appear that across a much wider range of energies than used in this analysis, the GEANT4 4.9.0 model does roughly model the dependency of the Bremsstrahlung differential cross section on the incident electron energy present in the EEDL tabulated theoretical results. However for the energy regime of interest to us GEANT4 4.9.0 does not model this incident energy dependency to an accuracy sufficient to make it a superior model to the GEANT4 4.9.2 model which uses a Bremsstrahlung differential cross section  $y$ -spectrum formulae valid for the high-energy limit.

### 6.3.4 Conclusion

GEANT4 4.9.2 appears to give a better description of the data for the important low- $y$  region. Neither of the GEANT4 models accurately describe the entire high- $y$  region, each models a different sub-section of this region reasonably accurately. The systematic uncertainty on the measured  $W$  mass associated with the inaccurate modelling of the high- $y$  region of the Bremsstrahlung  $y$ -spectrum by GEANT4 4.9.2 is considered in section 8.1. An estimate of the systematic error due to surface effects is also considered in this section.

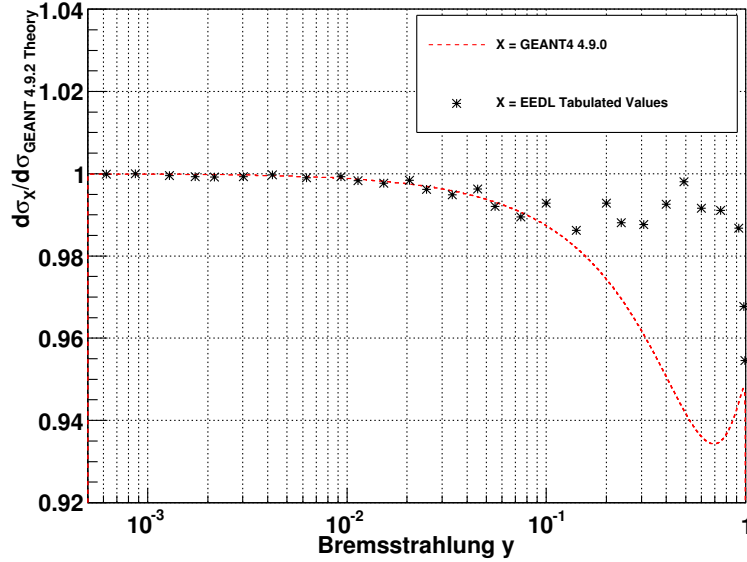


Figure 6.27: The ratios  $\frac{d\sigma_X}{d\sigma_{\text{GEANT4 4.9.2 } y\text{-spectrum}}}$  where  $X$  is the EEDL tabulated theoretical Bremsstrahlung  $y$ -spectrum or the GEANT4 4.9.0 theoretical differential cross section  $y$ -spectrum as given by eq. (5.9) and the GEANT4 4.9.2 theoretical differential cross section  $y$ -spectrum as given by eq. (5.27). A logarithmic  $x$ -axis scale is used. The incident electron energy is 100 GeV; the medium is silicon. The GEANT4 4.9.2 and GEANT4 4.9.0  $y$ -spectra used in this figure do not include dielectric/LPM suppression. The EEDL tabulated theoretical results agree with both GEANT4 models for  $y < 0.01$ . In the region  $0.01 < y < 0.2$  the EEDL tabulated theoretical results roughly agree with the GEANT4 4.9.0  $y$ -spectrum while diverging from the GEANT4 4.9.2  $y$ -spectrum. For  $0.2 < y < 0.9$  the EEDL tabulated theoretical results do not agree with either of the GEANT4  $y$ -spectra accurately, however they appear to roughly follow the GEANT4 4.9.2  $y$ -spectrum. For  $y$ -values higher than  $y \sim 0.9$  the differential cross section  $y$ -spectra of the EEDL tabulated theoretical results and of GEANT4 4.9.0 both diverge rapidly from the GEANT4 4.9.2  $y$ -spectrum.

## 6.4 Modelling of Pair Production in UCL Fast Simulation

### 6.4.1 Virtual Test Beam Experiments

The strategy for the validation of pair production was the same as that outlined in section 6.2.1 for Bremsstrahlung. Both the  $x$ -spectrum and the total cross section were considered of interest. We treated these separately. Again our strategy was to turn off all processes except that under investigation, i.e. pair production, and compare the GEANT4 and the UCL Fast Simulation spectra using a virtual test beam.

The test beam setup used for pair production was very similar to that used for Bremsstrahlung (as outlined in sections 6.2.2 and 6.2.3). However due to the differing nature of pair production and Bremsstrahlung, a number of alterations were made in the pair production case, as detailed below. As pair production was only seen in about 1% of cases using a 1 mm thick plate setup, a thicker 1 cm plate setup was used to reduce the overall number of events needed to get good statistics. The test beam in GEANT4 was changed to a  $\gamma$  beam and the pair production physics process was activated. Bremsstrahlung was deactivated and all the other physics processes (e.g. ionisation) were left inactive. The energy of any electron/positron tracks was recorded (emerging from either side of the silicon plate), along with that of the incident  $\gamma$ . 40 GeV photons are uncommon in the  $W$  mass analysis, so the test beam energy was reduced to 5 GeV, an energy more typical of photons simulated in the  $W$  mass analysis. The pair production spectrum is expected to have a strong dependence on the energy of the incident photon when this energy is low. To investigate this we changed the energy to a variety of energies from 5 GeV down to 100 MeV. (The pair production spectrum for incident photon energies significantly less than 100 MeV is not important to this analysis as the electrons produced by such low energy interactions will either curl-up in the magnetic field of the inner detector or be absorbed in the solenoid. However, the modelling of the total cross section for pair production interactions for incident photon energies less than 100 MeV is important to this analysis as this determines if such photons will reach the calorimeter.) A similar setup was used in the UCL Fast Simulation test beam.

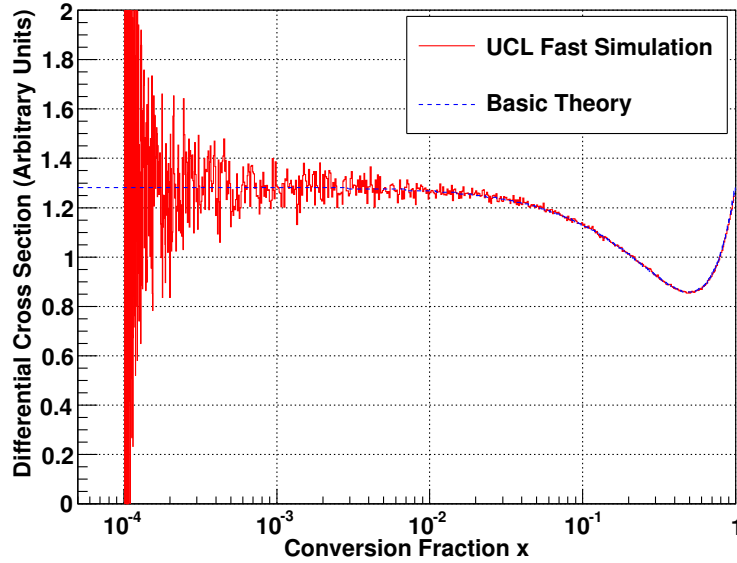


Figure 6.28: UCL Fast Simulation pair production  $x$ -spectrum pseudo-data compared to a basic theoretical spectrum defined by eq. (5.46), on a logarithmic  $x$ -axis scale. The incident photon beam energy is 5 GeV. The differential cross section is given in arbitrary units and the theoretical spectrum is normalised to the pseudo-data histogram in the region  $0.25 < x < 0.75$ . The increased statistical fluctuations at low- $x$  are an artefact of the logarithmic binning used. Note the kinematic limit visible in the pseudo data at  $x \approx 10^{-4}$ . Excellent agreement is observed between theory and pseudo-data as expected (see main text).

#### 6.4.2 Pair Production $x$ -Spectrum Validation and Modification

Historically UCL Fast Simulation used eq. (5.46) as its spectrum. In fig. 6.28 UCL Fast Simulation's  $x$ -spectrum is compared to the basic theoretical  $x$ -spectrum defined by eq. (5.46) for an incident photon energy of 5 GeV using a logarithmic scale. The theoretical spectrum is normalised to the histogram in the region  $0.25 < x < 0.75$ . The excellent agreement observed is expected. Unlike Bremsstrahlung it is impossible to get multiple pair productions in a single event within this test beam setup, so there is no need to define an equivalent of  $y_{\text{eff}}$  and it is sufficient to compare spectra using the true  $x$  exactly as defined in eq. (5.44).

In fig. 6.29 the GEANT4 and the UCL Fast Simulation  $x$ -spectra are compared to the theoretical  $x$ -spectrum defined by eq. (5.47) for an incident photon energy of 5 GeV using a logarithmic scale. The theoretical spectrum is normalised to the GEANT4 his-

togram in the region  $0.01 < x < 0.1$ . The excellent agreement between GEANT4 and the theoretical spectrum is to be expected since GEANT4 uses eq. (5.47) as its  $x$ -spectrum. Note the discrepancy between GEANT4 and UCL Fast Simulation starting below about  $x = 0.03$  and increasing steadily down to the kinematic limit at about  $x = 0.0001$ . A similar discrepancy will be observed at very high  $x$  because of the symmetry of the  $x$ -spectrum, however this is barely observable on this logarithmic scale. The same features are evident in fig. 6.30, a plot of  $R = \frac{d\sigma_{\text{histogram}}}{d\sigma_{\text{theory}}}$  for GEANT4 and UCL Fast Simulation. The discrepancy between UCL Fast Simulation and GEANT4 is largely due to the assumption of the ‘complete screening’ case in eq. (5.46), while eq. (5.47) accounts for the possibility of incomplete screening of the nucleus by the atomic electrons. Unlike eq. (5.46), eq. (5.47) also includes a Coulomb correction function and retains a numerically small second term, both of which also contribute to the discrepancy between UCL Fast Simulation and GEANT4.

As noted before the pair production spectral shape has a strong dependence on the energy of the incident photon; hence it is interesting to compare UCL Fast Simulation and GEANT4 at a second energy. In fig. 6.31 the GEANT4 and UCL Fast Simulation  $x$ -spectra are compared to the theoretical  $x$ -spectrum defined by eq. (5.47) for an incident photon energy of 100 MeV. Again GEANT4 and the theoretical spectrum show excellent agreement as expected. The agreement between the UCL Fast Simulation and GEANT4  $x$ -spectra shape is poor, even in the middle region of the  $x$ -spectrum, where for a 5 GeV incident photon energy we saw good agreement. This can be seen clearly in fig. 6.32, a plot of  $R = \frac{d\sigma_{\text{histogram}}}{d\sigma_{\text{theory}}}$  for GEANT4 and UCL Fast Simulation.

It was decided to modify UCL Fast Simulation to use eq. (5.47) for its  $x$ -spectral shape. This will henceforth be referred to as UCL Fast Simulation Pair Production Modification A. Note only the spectral shape was taken from eq. (5.47), the total cross section was left unchanged from the original UCL Fast Simulation implementation discussed in section 6.4.3. As part of this modification it was also decided not to propagate any electrons/positrons produced with energies below 1 MeV. Pair production events for values of  $x$  which would produce an electron or positron below this limit are still simulated and the higher energy lepton still propagated, but the sub 1 MeV lepton

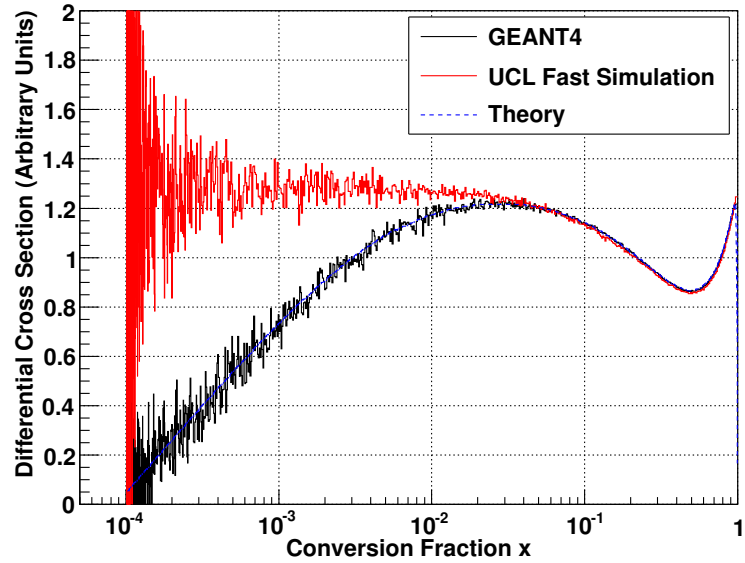


Figure 6.29: UCL Fast Simulation and GEANT4 pair production  $x$ -spectra pseudo-data compared to a theoretical spectrum defined by eq. (5.47) on a logarithmic  $x$ -axis scale. The theoretical spectrum line is partially obscured by the GEANT4 pseudo-data histogram (which it matches closely) but is visible on close examination. The incident photon beam energy is 5 GeV. The differential cross section is given in arbitrary units and the theoretical spectrum is normalised to the GEANT4 pseudo-data histogram in the region  $0.01 < x < 0.1$ . Excellent agreement is observed between theory and GEANT4 pseudo-data as expected. An increasing discrepancy is observed between the GEANT4 and the UCL Fast Simulation pseudo-data at low- $x$ , starting at about  $x = 0.03$  and increasing down to the kinematic limit at  $x \approx 10^{-4}$ .

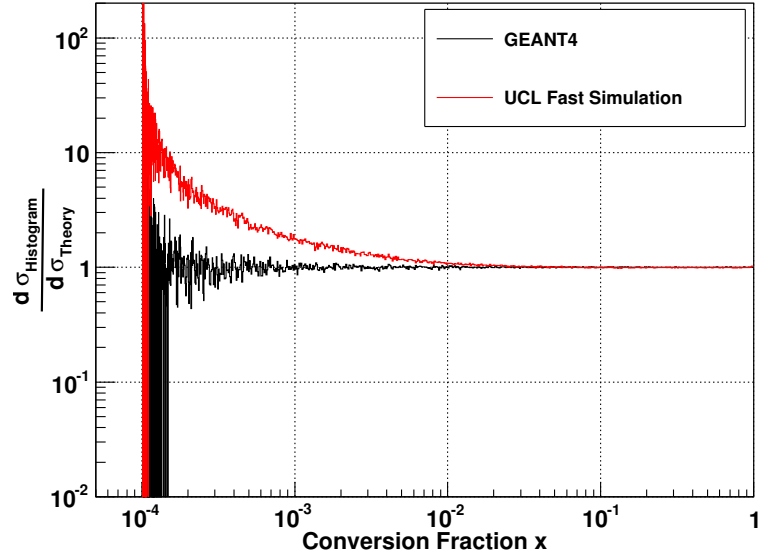


Figure 6.30: The ratio of GEANT4 and UCL Fast Simulation pair production  $x$ -spectra to the theoretical spectrum given by eq. (5.47) on logarithmic axis scales. The incident photon beam energy is 5 GeV. The theoretical spectrum is normalised to the GEANT4 pseudo-data histogram in the region  $0.01 < x < 0.1$ .

is discarded. This was done to maintain an efficient running speed for the UCL Fast Simulation code. Such low energy electrons are of no interest since they will be ‘swept up’ by the solenoid magnetic field in the inner detector and not reach the calorimeter. Some additional technical details regarding the sampling and rejection procedure used by UCL Fast Simulation Pair Production Modification A are given in Appendix C.

In fig. 6.33 the GEANT4 and UCL Fast Simulation Pair Production Modification A  $x$ -spectra are compared to the theoretical  $x$ -spectrum defined by eq. (5.47) for an incident photon energy of 5 GeV using a logarithmic scale. Now the GEANT4 histogram, UCL Fast Simulation Pair Production Modification A histogram and theoretical  $x$ -spectrum are all in excellent agreement across the entire  $x$ -range.

In fig. 6.34 the GEANT4 and UCL Fast Simulation Pair Production Modification A  $x$ -spectra are compared to the theoretical  $x$ -spectrum defined by eq. (5.47) for an incident photon energy of 100 MeV using a logarithmic scale. Again the GEANT4 histogram, UCL Fast Simulation Pair Production Modification A histogram and theoretical  $x$ -spectrum are all in excellent agreement across the entire  $x$ -range.

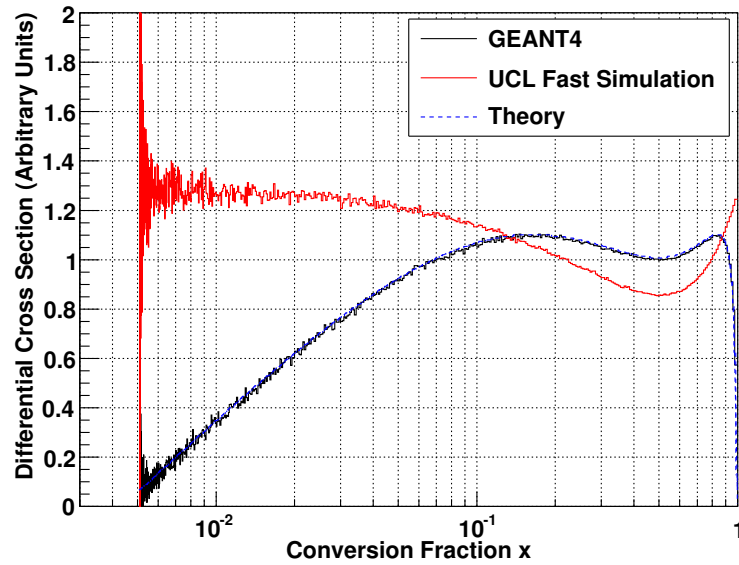


Figure 6.31: UCL Fast Simulation and GEANT4 pair production  $x$ -spectra pseudo-data compared to a theoretical spectrum defined by eq. (5.47) on a logarithmic  $x$ -axis scale. The theoretical spectrum line is partially obscured by the GEANT4 pseudo-data histogram (which it matches closely) but is visible on close examination. The incident photon beam energy is 100 MeV. The differential cross section is given in arbitrary units and the theoretical spectrum is normalised to the GEANT4 pseudo-data histogram in the region  $0.01 < x < 0.1$ . Excellent agreement is observed between theory and GEANT4 pseudo-data as expected. The agreement between GEANT4 and UCL Fast Simulation pseudo-data is poor even at mid-range  $x$ -values.

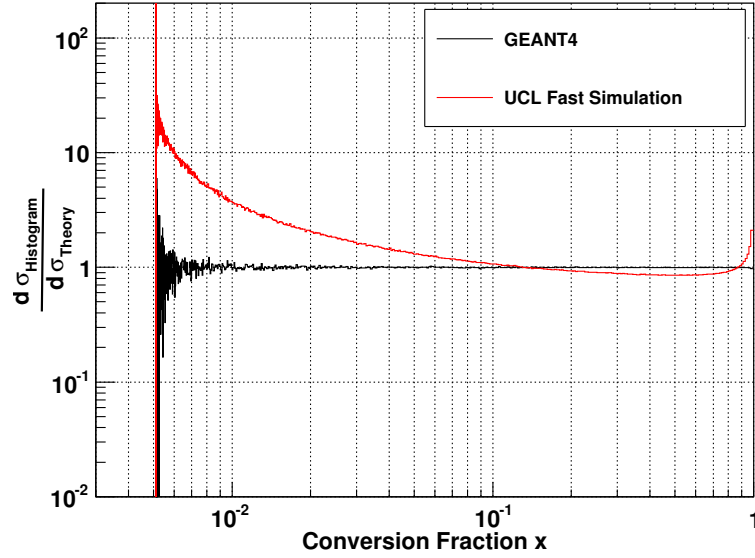


Figure 6.32: The ratio of GEANT4 and UCL Fast Simulation pair production  $x$ -spectra to the theoretical spectrum given by eq. (5.47) on logarithmic axis scales. The incident photon beam energy is 100 MeV. The theoretical spectrum is normalised to the GEANT4 pseudo-data histogram in the region  $0.01 < x < 0.1$ .

Comparisons at 500 MeV and 1 GeV also display excellent agreement between GEANT4 and UCL Fast Simulation Pair Production Modification A. To check this agreement in detail, the ratios  $R = \frac{d\sigma_{\text{histogram}}}{d\sigma_{\text{theory}}}$  were plotted for initial photon energies of both 5 GeV and 100 MeV, as shown in figs. 6.35 and 6.36. Good agreement is seen for all  $x$ , though as we approach the lower limit of  $x$  statistical fluctuations become very pronounced making the accuracy of the agreement inconclusive in this region. Hence we conclude that eq. (5.47) has been successfully implemented as the  $x$ -spectral shape in UCL Fast Simulation Pair Production Modification A.

### 6.4.3 Pair Production Total Cross Section Validation and Modification

The implementation of pair production in UCL Fast Simulation separates the treatment of the pair production total cross section from the sampling of the pair production differential cross section in  $x$ . Compton scattering and pair production events are generated according to the total photon interaction cross section, then split according to the frac-

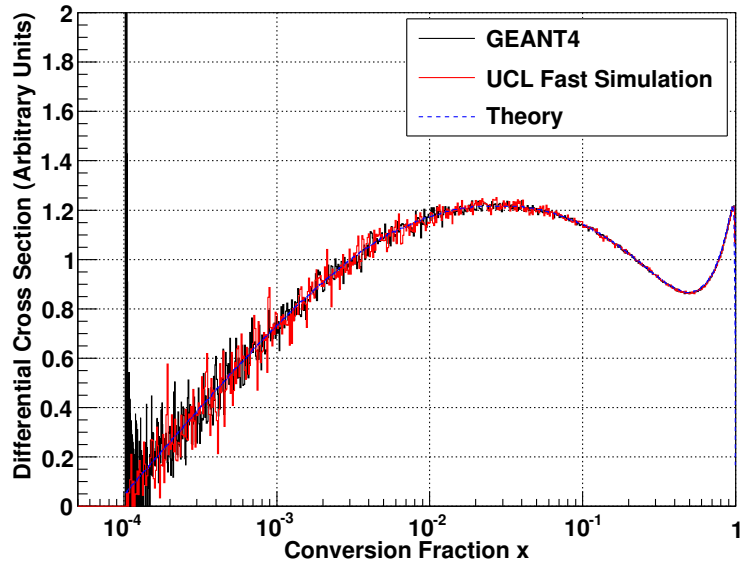


Figure 6.33: UCL Fast Simulation Pair Production Modification A and GEANT4 pair production  $x$ -spectra pseudo-data compared to a theoretical spectrum defined by eq. (5.47) on a logarithmic  $x$ -axis scale. The theoretical spectrum line is partially obscured by the pseudo-data histograms (which it matches closely) but is visible on close examination. The incident photon beam energy is 5 GeV. The differential cross section is given in arbitrary units and the theoretical spectrum is normalised to the GEANT4 pseudo-data histogram in the region  $0.01 < x < 0.1$ . Excellent agreement is observed between GEANT4 and UCL Fast Simulation Pair Production Modification A across the entire  $x$ -range. The UCL Fast Simulation Pair Production Modification A pseudo-data plotted here has been generated without the discarding of any sub 1 MeV electrons. This has been done specially in order to compare the spectral shape across the entire  $x$ -range for this plot and fig. 6.35 only, and is not the case anywhere else in the analysis.

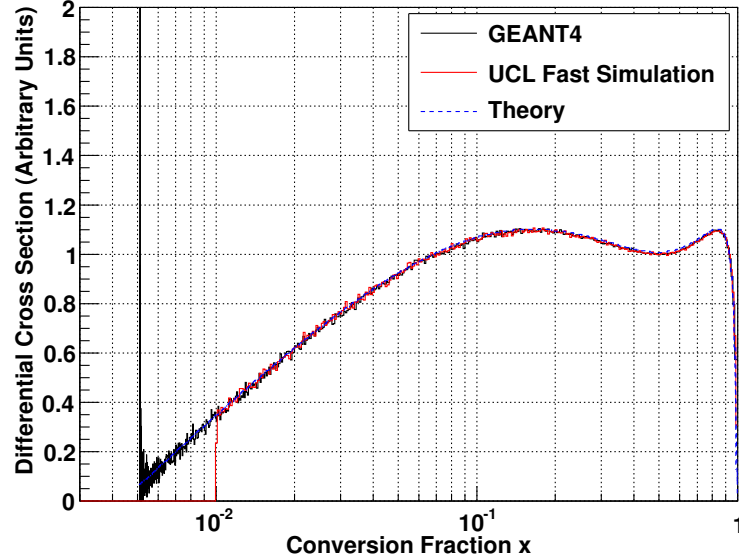


Figure 6.34: UCL Fast Simulation Pair Production Modification A and GEANT4 pair production  $x$ -spectra pseudo-data compared to a theoretical spectrum defined by eq. (5.47) on a logarithmic  $x$ -axis scale. The theoretical spectrum line is partially obscured by the pseudo-data histograms (which it matches closely) but is visible on close examination. The incident photon beam energy was 100 MeV. The differential cross section is given in arbitrary units and the theoretical spectrum is normalised to the GEANT4 pseudo-data histogram in the region  $0.01 < x < 0.1$ . Excellent agreement is observed between GEANT4 and UCL Fast Simulation Pair Production Modification A across the entire  $x$ -range. Note the UCL Fast Simulation Pair Production Modification A spectrum appears to vanish below  $x = 0.01$ , this is because sub 1 MeV electrons are not propagated and hence not recorded in the spectrum. However, pair production events for  $x$ -values below 0.01 are still being generated and the positron (which necessarily has an energy greater than 1 MeV) from such events is propagated. Similarly for events with  $x$ -values greater than 0.99 only the electron is propagated, as the positron will have an energy less than 1 MeV and hence be discarded.

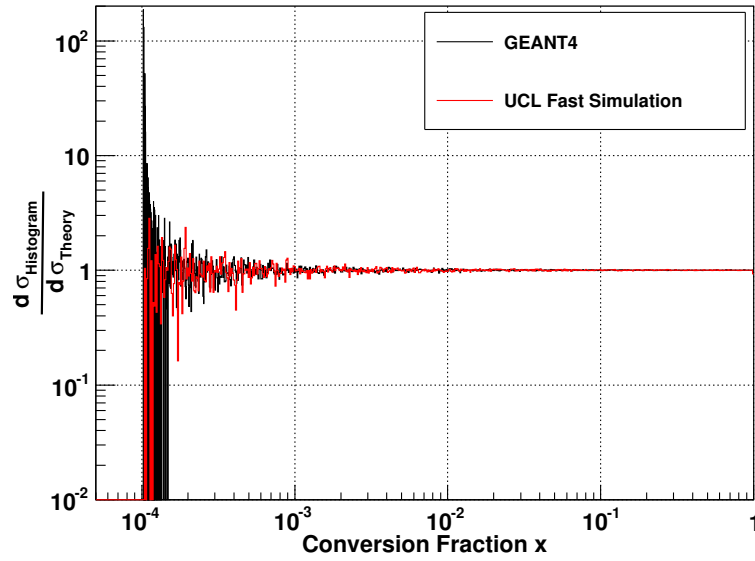


Figure 6.35: The ratio of GEANT4 and UCL Fast Simulation Pair Production Modification A  $x$ -spectra pseudo-data to the theoretical spectrum given by eq. (5.47) on logarithmic axis scales. The incident photon beam energy was 5 GeV. The theoretical spectrum is normalised to the GEANT4 pseudo-data histogram in the region  $0.01 < x < 0.1$ .

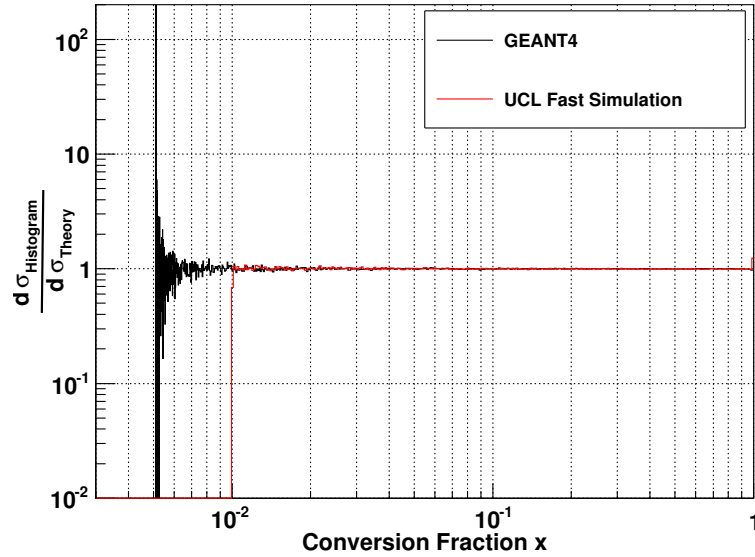


Figure 6.36: The ratio of GEANT4 and UCL Fast Simulation Pair Production Modification A  $x$ -spectra pseudo-data to the theoretical spectrum given by eq. (5.47) on logarithmic axis scales. The incident photon beam energy was 100 MeV. The theoretical spectrum is normalised to the GEANT4 pseudo-data histogram in the region  $0.01 < x < 0.1$ .

tion of that total cross section that is Compton scattering/pair production. In the case that a pair production event is selected, an  $x$  is then drawn from the pair production differential cross section  $x$ -spectrum.

The total photon interaction cross section is determined for each photon in UCL Fast Simulation by first finding the high energy total photon interaction cross section limit, given by eq. (5.59). Note the fraction of photon interactions which are not pair production is negligible in this high energy limit, hence it is valid to use the pair production total cross section as the total photon interaction cross section in this limit. Then the cross section is scaled according to the ratio:

$$\frac{\text{Total Photon Interaction Cross Section at the Incident Photon Energy}}{\text{Total Photon Interaction Cross Section in the High Energy Limit}} \quad (6.4)$$

The numerator and denominator of this ratio are both determined from National Institute of Standards and Technology (NIST) experimental data [84]. (The NIST data is given for a range of incident photon energies; the numerator is determined by logarithmic interpolation of the NIST data and the highest incident photon energy data point is used to determine the denominator.) Note the denominator of this ratio is not, in fact, equal to the theoretical limit given by eq. (5.59); we are in effect using the NIST data but scaling it such as to ‘peg’ it to this theoretical high energy limit.

The total photon interaction cross section is used to generate the probability  $P$ , for a photon to interact in a given logical layer. This probability is exactly given by:

$$P = 1 - \exp\left(-\frac{x}{L}\right) \quad (6.5)$$

where  $x$  is the thickness of the logical layer and  $L$  is the collision length in the absorber, defined as  $L = 1/(\rho\sigma)$  with  $\rho$  being the density of the absorber (silicon) and  $\sigma$  being the total photon interaction cross section in the absorber in units of  $\text{cm}^2/\text{g}$ . If this macroscopic unit of cross section is multiplied by a density (in  $\text{g}/\text{cm}^3$ ) we get units of  $\text{cm}^{-1}$ , i.e. the correct units for the inverse of mean free path; thus this unit of cross section obeys the relation  $\ell = (\rho\sigma)^{-1}$ , where  $\ell$  is mean free path,  $\rho$  density and  $\sigma$  total

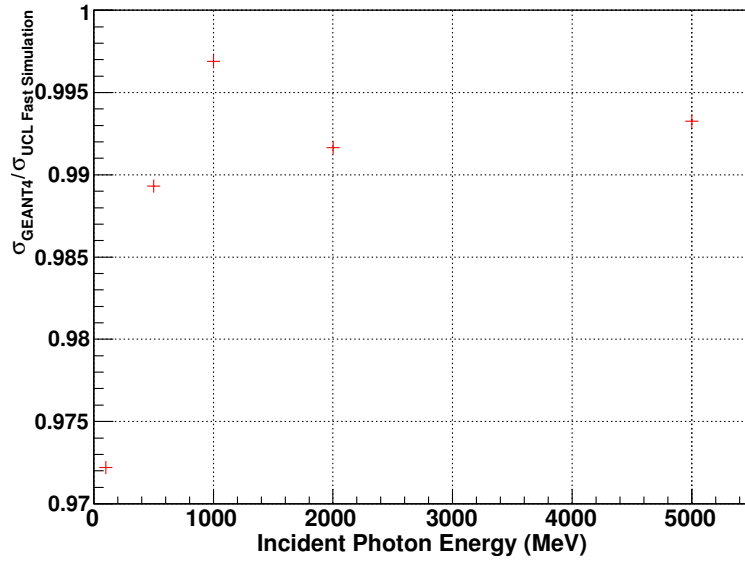


Figure 6.37: The ratio of the GEANT4 pair production total cross section to the UCL Fast Simulation Pair Production Modification A pair production total cross section, both calculated from test beam pseudo-data, plotted as a function of incident photon energy. Note the increased discrepancy between GEANT4 and UCL Fast Simulation at a 100 MeV incident photon energy.

cross section. In the case of a thin slice where  $x/L \ll 1$ , this can be approximated as:

$$P = \frac{x}{L}. \quad (6.6)$$

This approximation is used in UCL Fast Simulation. Each photon interaction generated is randomly determined to be either a pair production or a Compton scattering according to the ratio of the cross sections of these two processes at the given incident photon energy, which is also determined from NIST experimental data [84]. If a photon interaction is generated within a given logical layer no further interactions are simulated in that layer, even if the initial interaction is only a Compton scattering.

Figure 6.37 is a plot of the ratio  $\sigma_{\text{GEANT4}} / \sigma_{\text{UCL Fast Simulation Pair Production Modification A}}$ , calculated from test beam pseudo-data, as a function of incident photon energy. We see agreement to within 1.5% apart from at 100 MeV. In fig. 6.38 GEANT4's total cross section parameterisation is compared to NIST data and the total cross section formulation used by UCL Fast Simulation Pair Production Modification A, as a function

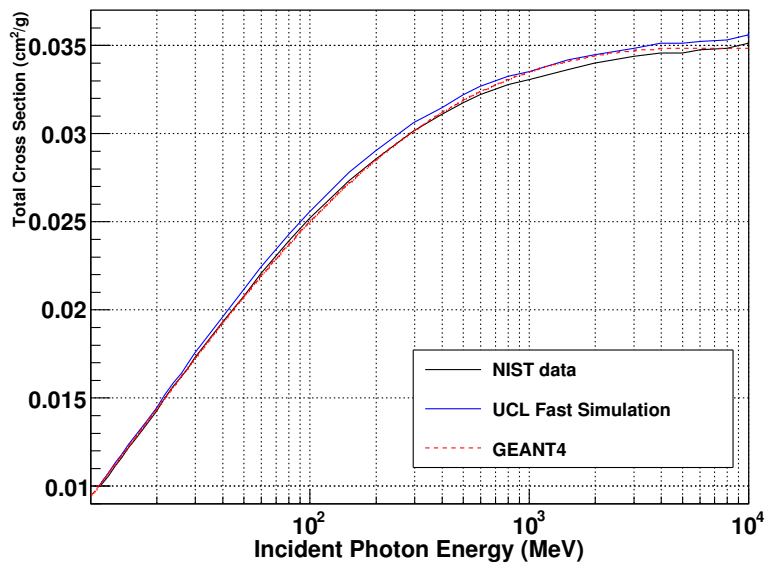


Figure 6.38: The GEANT4 pair production total cross section compared to NIST data and the UCL Fast Simulation Pair Production Modification A formulation of total cross section, as a function of incident photon energy. Cross sections are given in units of  $\text{cm}^2/\text{g}$ . Note the significant discrepancy between the GEANT4 pair production total cross section parameterisation and the UCL Fast Simulation Pair Production Modification A formulation close to  $\sim 100$  MeV.

of incident photon energy. Figure 6.38 explains the energy dependence of the ratio  $\sigma_{\text{GEANT4}}/\sigma_{\text{UCL Fast Simulation Pair Production Modification A}}$  seen in fig. 6.37. It can be seen that the GEANT4 formulation is in closer agreement to UCL Fast Simulation Pair Production Modification A for some energies and to NIST data for other energies.

It was decided to change the implementation of the total photon interaction cross section in UCL Fast Simulation in light of these results. It was preferred to use an implementation that continued to use experimental data specific to the absorber of interest, silicon, rather than use the  $Z$  dependent fit to data across a range of elements adopted by GEANT4. The new procedure is to take the total photon interaction cross section for each photon directly from the NIST data, eliminating the use of eq. (5.59) entirely. The splitting of photon interactions into pair production and Compton scattering is unaltered. This new implementation is henceforth referred to as UCL Fast Simulation Pair Production Modification B and also includes all changes made in UCL Fast Simulation Pair Production Modification A. Note this modification, while labelled

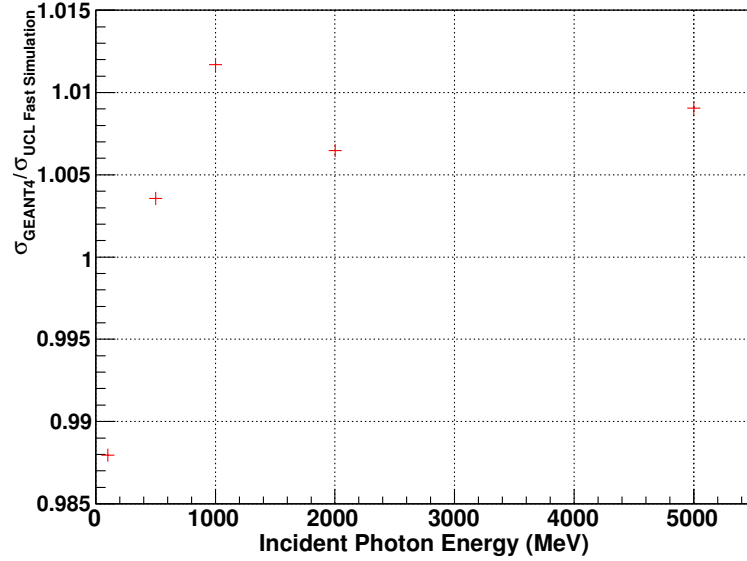


Figure 6.39: The ratio of the GEANT4 pair production total cross section to the UCL Fast Simulation Pair Production Modification B pair production total cross section, both calculated from test beam pseudo data, plotted as a function of incident photon energy. Note the level of agreement is within 1.5%; the disagreement seen is to be expected, as the NIST data used doesn't exactly match the GEANT4 parameterisation of pair production total cross section.

as a 'Pair Production Modification', will affect the total cross section for both pair production and Compton scattering.

Figure 6.39 is a plot of the ratio  $\sigma_{\text{GEANT4}} / \sigma_{\text{UCL Fast Simulation Pair Production Modification B}}$ , calculated from test beam pseudo-data, as a function of incident photon energy. We see agreement to within 1.5%. Note the level of agreement has not improved at all energies compared to UCL Fast Simulation Pair Production Modification A - however this is expected as GEANT4's parameterisation doesn't exactly match NIST experimental data. This new implementation of the pair production total cross section is seen as satisfactory.

## Chapter 7

# Modelling the Composition of the CDF Run II Inner Detector

### 7.1 Overview

The modelling of Bremsstrahlung and pair production in UCL Fast Simulation originally made the assumption that the entire CDF Run II silicon tracker consisted of silicon only. In reality this is not the case; in addition to the silicon sensors themselves, there are a variety of electronic components and support structures [36].

As discussed previously in section 4.6.1, UCL Fast Simulation models the material in the silicon tracker using the material map SiliMap [52]. For each bin of each logical layer SiliMap provides the mean specific radiation length  $X_0$ , mean energy loss constant  $C_{dE/dx}$  and mean excitation potential  $I_0$ . The geometry of each layer is also known, hence for a given particle trajectory the total integrated radiation length and the total integrated energy loss constant may be calculated. However the material composition of each logical layer is not provided.

The Bremsstrahlung differential cross section  $y$ -spectrum is, in general, dependent on the media being traversed. The GEANT4 4.9.2 model (see eq. (5.27)) of the Bremsstrahlung differential cross section  $y$ -spectrum is dependent on the  $Z$ ,  $X_0$  and electron density ( $n_e$ ) of the medium being traversed. Hence it is not generally possible to model exactly the Bremsstrahlung  $y_{\text{eff}}$ -spectrum without knowing the material composition of

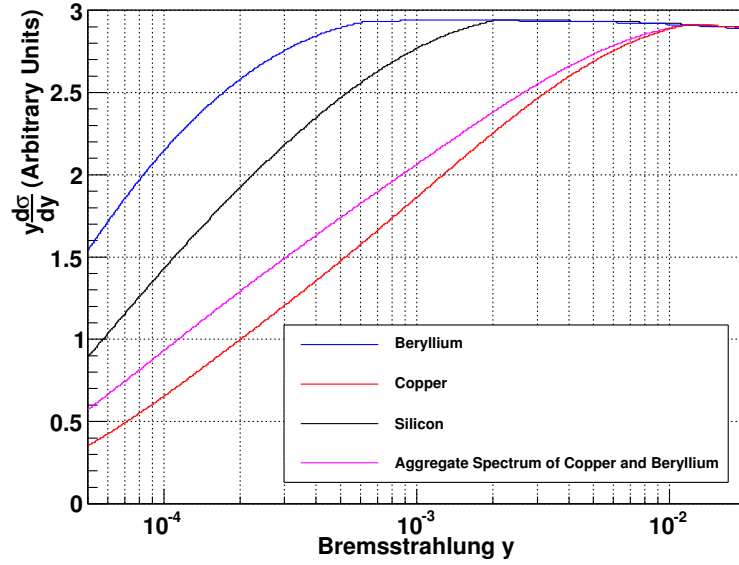


Figure 7.1: Comparison of the energy weighted differential cross section (i.e.  $y \frac{d\sigma}{dy}$ )  $y$ -spectra of Bremsstrahlung occurring in beryllium, silicon and copper. Also compared is the aggregate theoretical differential cross section  $y$ -spectrum of beryllium and copper, where the weighting of each element's spectrum has been determined by the thickness of the element (divided by the elements radiation length) required by a two element model of a layer of pure silicon. This approximates the pseudo-data spectrum we would expect from an actual Cu/Be Model of a layer of pure silicon in UCL Fast Simulation. For  $y$ -values above  $\sim 0.02$  the beryllium, silicon, and copper spectra are all in good agreement. The region where LPM/dielectric suppression is important begins at higher values of  $y$  for 'heavier' elements. This is to be expected as the upper bound for the region where LPM/dielectric suppression is appreciable is inversely proportional to  $E_{LPM-2}$ , which itself is linearly dependent on the radiation length of the medium being traversed.

the silicon tracker.

Figure 7.1 is a plot of  $y \frac{d\sigma}{dy}(y)$ , the energy weighted Bremsstrahlung differential  $y$ -spectrum, for the theoretical GEANT4 4.9.2 model of 40 GeV electrons where the interaction medium is variously silicon, beryllium and copper. While theoretically the Bremsstrahlung differential cross section  $y$ -spectrum is dependent on the medium being traversed across the entire  $y$ -range, the only non-negligible difference is observed in the  $y$  region where LPM/dielectric suppression is important. This region has a higher upper  $y$ -bound for heavier (higher  $Z$ ) elements.

## 7.2 Simple Estimate of the Effect on the $W$ Mass Measurement

The systematic shift on the  $W$  mass that would be generated by switching UCL Fast Simulation from modelling Bremsstrahlung in the CDF Run II silicon tracker as occurring exclusively in silicon to occurring exclusively in copper was estimated. This estimate was made using the technique of iteratively retuning the important simulation parameters before generating  $W$  mass templates to fit for the shift. This method is similar to that described in section 8.1. This indicated the systematic shift in the fitted  $W$  mass to be  $16.8 \pm 1.6$  MeV/ $c^2$ . The uncertainty quoted here is the statistical uncertainty on the  $W$  mass fit only, and does not include an estimate of the systematic uncertainty on the shift due to the statistical uncertainty on the retuned simulation parameters. Although modelling the CDF Run II silicon tracker as comprising entirely of copper is clearly unrealistic, the size of the shift shows that the composition of the CDF Run II silicon tracker is potentially significant to this analysis, and requires further consideration.

## 7.3 Modelling the Composition of the Silicon Tracker using a Two Element Model

An accurate model of the composition of the CDF Run II silicon tracker could in principle be produced from the detailed component by component model of the CDF Run II detector used by the GEANT3 based CdfSim. However this was not practical for this analysis. Instead we studied modelling each logical layer of the detector defined by SiliMap as a combination of two different elements, a light element and a heavy element. Specific elements must be chosen for the light and heavy elements; this choice will be discussed later. The composition of each logical layer in terms of the two elements is derived by using the total integrated radiation length for the layer and total integrated energy loss constant for the layer as constraints. This is henceforth referred to as a ‘two element model’.

Approximating each logical layer as two sublayers, a sublayer of material A and a sublayer of material B, the equations relating the properties of these sublayers to the total properties of the layer provided by SiliMap are:

$$\left( \sum_i x_i C_{dEdx,i} \right) = x C_{dEdx,MatA} + y C_{dEdx,MatB} \quad (7.1)$$

$$\left( \sum_i \frac{x_i}{X_{0,i}} \right) = \frac{x}{X_{0,MatA}} + \frac{y}{X_{0,MatB}} \quad (7.2)$$

where:

$\left( \sum_i x_i C_{dEdx,i} \right)$  : true total integrated energy loss constant of the layer (provided by SiliMap)

$\left( \sum_i \frac{x_i}{X_{0,i}} \right)$  : true total integrated radiation length of the layer (provided by SiliMap)

$x$  : physical thickness of sublayer of material A

$y$  : physical thickness of sublayer of material B

$C_{dEdx,MatA}$  : energy loss constant of material A

$C_{dEdx,MatB}$  : energy loss constant of material B

$X_{0,MatA}$  : radiation length of material A

$X_{0,MatB}$  : radiation length of material B

Note that  $\left( \sum_i x_i C_{dEdx,i} \right)$  and  $\left( \sum_i \frac{x_i}{X_{0,i}} \right)$  are both given by SiliMap as single values; the summation over elements occurred when the persistent look-up table was originally compiled from a scan of the CdfSim detector geometry in GEANT3. Also note that while this method could generally be applied to any two materials, we only use it for cases where material A and material B are both pure elements.

Combining eqs. (7.1) and (7.2) and eliminating either  $x$  or  $y$ , we derive the following

equations for the thickness of the material A and material B sublayers:

$$x = \frac{\left(\frac{\sum_i x_i C_{dEdx,i}}{C_{dEdx,MatB}} - X_{0,MatB}\right) \left(\sum_i \frac{x_i}{X_{0,i}}\right)}{\frac{C_{dEdx,MatA}}{C_{dEdx,MatB}} - \frac{X_{0,MatB}}{X_{0,MatA}}} \quad (7.3)$$

$$y = \frac{\left(\frac{\sum_i x_i C_{dEdx,i}}{C_{dEdx,MatA}} - X_{0,MatA}\right) \left(\sum_i \frac{x_i}{X_{0,i}}\right)}{\frac{C_{dEdx,MatB}}{C_{dEdx,MatA}} - \frac{X_{0,MatA}}{X_{0,MatB}}} \quad (7.4)$$

This method relies on the assumption that all the materials comprising a layer can be accurately represented (with regards to the simulation of the Bremsstrahlung differential cross section  $y$ -spectrum) as the sum of a single specific ‘light’ element and a single specific ‘heavy’ element. It also assumes that elements with similar properties (with regards to Bremsstrahlung) will have similar radiation lengths and energy loss constants. If a layer were in fact comprised entirely of the specific ‘light’ element and specific ‘heavy’ element being used as material A and material B, then this method would capture the composition of the layer with perfect accuracy. However if either of these assumptions is not at least approximately true for elements abundant in the silicon tracker, this method will not necessarily provide an accurate model of the Bremsstrahlung differential cross section  $y$ -spectrum. Careful investigation has shown that this method is the only consistent and viable method to derive the thickness of the two elements for a simple two element model.

The Bremsstrahlung differential cross section  $y$ -spectrum used in UCL Fast Simulation for Bremsstrahlung interactions occurring in non-silicon elements is a modified version of UCL Fast Simulation Bremsstrahlung Modification C (which is itself based on the GEANT4 4.9.2 Bremsstrahlung model). The values of  $Z$ ,  $X_0$  and  $n_e$  in UCL Fast Simulation Bremsstrahlung Modification C are replaced with the values for the element being modelled. The GEANT4 4.9.2 Bremsstrahlung total cross section model is dependent on the properties of the medium being traversed, however we do not tune the total cross section for each element being modelled to pseudo-data from GEANT4 4.9.2 in a test beam setup as we did for silicon (see section 6.2.7); instead we modify the total cross section for each element being modelled such that the element’s Bremsstrahlung

differential cross section  $y$ -spectrum is normalised to the silicon Bremsstrahlung differential cross section  $y$ -spectrum in the high- $y$  region where LPM/dielectric suppression is negligible. Hence the only changes in the Bremsstrahlung total cross section between different media that we model will be due to changes in the LPM/dielectric suppression. This will therefore only affect the number of low- $y$  Bremsstrahlung events that occur. Such events will usually enter the first bin of the three bin  $E/p$  distribution used to tune the material scale tuning factor (see section 4.6.2) for UCL Fast Simulation, as will events where no Bremsstrahlung has occurred. Therefore changes in the LPM/dielectric suppression should not directly impact on the material scale tuning factor. Changes in the LPM/dielectric suppression will modify the shape of the  $E/p$  peak, hence may have an effect on the fitted energy scale and resolution values, for example. We neglect to model other changes to the total cross section; changes to the total Bremsstrahlung cross section that occur due to differences in the differential cross section in the high- $y$  region would affect the number of events entering the high  $E/p$  tail of the  $E/p$  distribution. This would alter the fitted material scale factor, hence retuning the material scale would to first order absorb the effect of any such changes.

Note that all other matter effects simulated in UCL Fast Simulation, i.e. pair production, Compton scattering and ionisation, are not affected by the two element model and continue to be simulated under the approximation that the material is entirely silicon.

## 7.4 Variants of the Two Element Model Implemented

Two variants of the two element model are implemented in UCL Fast Simulation, henceforth referred to as the Cu/Be Model and the Si/Cu-Si/Be Model. Only one model can be applied in a particular run of the simulation; hence a compile time switch in the code allows us to choose which model is applied.

UCL Fast Simulation Bremsstrahlung Modification C's total cross section for interactions occurring in copper is rescaled such that the integral of its differential cross section for interactions occurring in copper (for a 40 GeV incident electron energy) in

the region  $0.05 < y < 1$  (the high- $y$  region) matches that of GEANT4 4.9.2 for interactions occurring in silicon (for the same incident electron energy). The rescaling factor was derived using a test beam comparison (similar to those described previously<sup>1</sup>). In fig. 7.2 UCL Fast Simulation Bremsstrahlung Modification C (including the rescaled total Bremsstrahlung cross section) test beam  $y_{\text{eff}}$ -spectrum pseudo-data for interactions occurring in copper is compared to GEANT4 4.9.2 test beam  $y_{\text{eff}}$ -spectrum pseudo-data for interactions occurring in silicon. As expected the spectra agree in the high- $y$  region, but the LPM/dielectric suppression is different. The integrated differential cross sections of these two pseudo-data histograms in the region  $0.05 < y < 1$  agree to within 0.25%. Ratio plots (not shown) were also generated and confirm the excellent agreement between the GEANT4 4.9.2 and UCL Fast Simulation Bremsstrahlung Modification C test beam  $y_{\text{eff}}$ -spectra pseudo-data from fig. 7.2 in the high- $y$  region. Comparisons were also made between UCL Fast Simulation Bremsstrahlung Modification C test beam  $y_{\text{eff}}$ -spectrum pseudo-data for interactions occurring in copper and GEANT4 4.9.2 test beam  $y_{\text{eff}}$ -spectrum pseudo-data for interactions occurring in copper and in this case excellent agreement of the normalised  $y_{\text{eff}}$ -spectra was observed for all  $y$ -values as expected. A total cross section rescaling factor was derived and validated for beryllium by a similar technique.

#### 7.4.1 Cu/Be Model

The Cu/Be Model uses copper as the ‘heavy’ element and beryllium as the ‘light’ element. The motivation for choosing beryllium and copper for the two elements is:

- They are both relatively abundant as passive materials within the CDF Run II silicon tracker.
- The Bremsstrahlung differential cross section  $y$ -spectrum for beryllium is similar to that of silicon, as can be seen in fig. 7.1, so beryllium is a good generic ‘light’ element.

---

<sup>1</sup>For the derivation of the rescaling factor for copper it is of particular importance that the number of UCL Fast Simulation and GEANT4 4.9.2 electrons fired at the target in the test beam setup is the same.

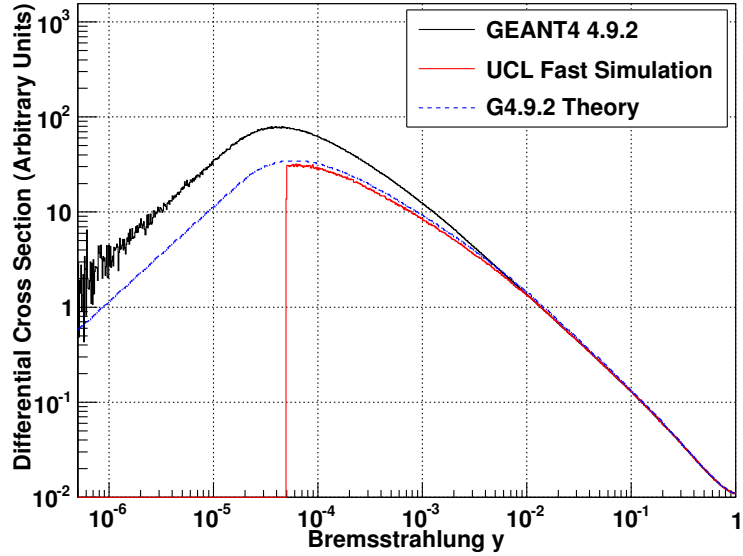


Figure 7.2: GEANT4 4.9.2 and UCL Fast Simulation Bremsstrahlung Modification C  $y_{\text{eff}}$ -spectra pseudo-data compared to a theoretical spectrum defined by eq. (5.27) on logarithmic axis scales. The incident electron beam energy is 40 GeV. The medium traversed is silicon for the GEANT4 4.9.2 pseudo-data. The medium traversed is copper for the theoretical spectrum and the UCL Fast Simulation Bremsstrahlung Modification C pseudo-data. The differential cross section is given in arbitrary units and the theoretical spectrum is normalised to the UCL Fast Simulation Bremsstrahlung Modification C pseudo-data histogram in the region  $0.1 < x < 0.6$ . The UCL Fast Simulation Bremsstrahlung Modification C total cross section for interactions occurring in copper has been scaled such that the integral of the differential cross section in the region  $0.05 < y < 1$  matches that of GEANT4 4.9.2.

- Beryllium is the ‘lightest’ element used in significant quantities in the silicon tracker. It was originally believed copper was the ‘heaviest’ element used in significant quantities in the silicon tracker, though later research showed this to be untrue.

This model will accurately model beryllium-like and copper-like layers, and also layers that are a mixture of copper and beryllium. The flaw in the Cu/Be Model is that it will model elements such as silicon and aluminium inaccurately, because while such elements have a similar differential cross section  $y$ -spectrum to beryllium, they have dissimilar values for  $X_0$  and  $C_{dEdx}$ , skewing the aggregate  $y$ -spectrum produced unnecessarily towards the spectrum of copper for layers of such elements. This can be seen in fig. 7.1.

Each logical layer of SiliMap is modelled as two sublayers of beryllium interlaced with two sublayers of copper. (For the simulation of Bremsstrahlung UCL Fast Simulation divides each SiliMap layer into four sublayers to ensure the accurate simulation of multiple photon emissions occurring within a single layer.) The thickness of each of these sublayers is half the value determined by eqs. (7.3) and (7.4); hence the total thicknesses of beryllium and copper in the layer are that determined by these equations. It is possible for eqs. (7.3) and (7.4) to produce negative values, though never simultaneously. Rough calculations indicate that if the thickness of the ‘heavy’ element required is negative, then the layer is actually likely to be comprised of an element ‘lighter’ (i.e. with a lower atomic number) than the ‘light’ element and if the thickness of the ‘light’ element required is negative, then the layer is actually likely to be comprised of an element ‘heavier’ (i.e. with a higher atomic number) than the ‘heavy’ element. If the thickness of copper required is negative, then we ignore the values of  $x$  and  $y$  produced by eqs. (7.3) and (7.4) and model the logical layer as entirely beryllium (split into four sublayers) with a total thickness sufficient to produce the correct total integrated radiation length for the layer. If the thickness of beryllium required is negative, then we ignore the values of  $x$  and  $y$  produced by eqs. (7.3) and (7.4) and model the logical layer as entirely copper (split into four sublayers) with a total thickness sufficient to produce the correct total integrated radiation length for the layer. The Cu/Be Model is not used in UCL Fast Simulation for the  $W$  mass analysis, so is switched off in the simulation;

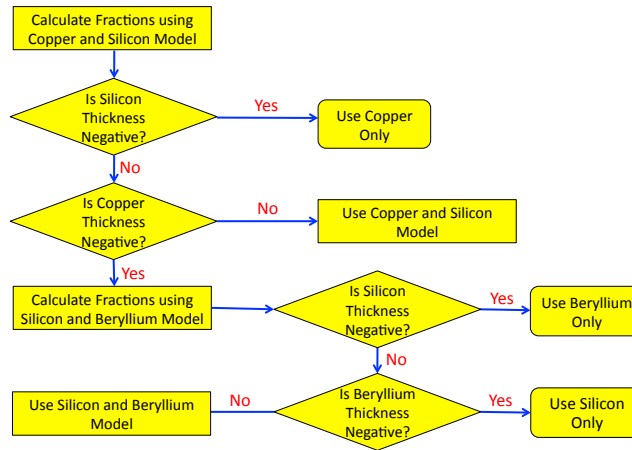


Figure 7.3: The logic of the Si/Cu-Si/Be Model.

however it will be used to generate an estimate of the systematic uncertainty due to the mis-modelling of the composition of the CDF Run II silicon tracker (see section 8.1).

#### 7.4.2 Si/Cu-Si/Be Model

The Si/Cu-Si/Be Model initially uses copper as the ‘heavy’ element and silicon as the ‘light’ element. For layers where the calculated thickness of both elements is positive and for layers where the calculated thickness of silicon is negative the model uses the same logic as the Cu/Be Model, replacing beryllium with silicon. For layers where the calculated thickness of copper is negative the model switches to using silicon as the ‘heavy’ element and beryllium as the ‘light’ element, the model then uses the same logic as the Cu/Be Model, replacing copper with silicon. This logic is summarised in fig. 7.3. The Si/Cu-Si/Be Model is used in UCL Fast Simulation for the  $W$  mass analysis, so is enabled by default in the simulation.

The motivation for this model was to include silicon in addition to beryllium and copper. Hence silicon-like layers would be well modelled in addition to beryllium-like layers and copper-like layers. Layers that are a mixture of either beryllium and silicon or copper and silicon will also be well modelled. Hence overall this would appear to provide a satisfactory model of the composition of the CDF Run II silicon tracker. A weakness

of this model is that it will mis-model layers that are largely a mixture of beryllium-like elements and copper-like elements; this might, for example, be relevant to the modelling of logical layers representing copper wire encased in plastics that consist largely of hydro-carbons. In such cases it will model such layers as being largely silicon, hence not capturing the increased LPM/dielectric suppression required due to the presence of copper. An estimate of the systematic uncertainty on the  $W$  mass measurement due to this mis-modelling is presented in section 8.1.

## 7.5 Modelling of Hybrid Layers in the Silicon Tracker

Based on examination of the CdfSim code and the information given in reference [35] it appears that the Layer 00, SVXII and ISL hybrids consist of very light material such as beryllium and very heavy material such as gold. Modelling the hybrids as a mixture of beryllium and gold would hence be an accurate model of the actual material composition of such hybrids. The standard two element model in Duke Fast Simulation was replaced by our collaborators by a two element model using beryllium and gold for specific regions of specific SiliMap logical layers where the hybrids are located. As they saw a large shift in the measured (blinded)  $Z$  mass in the  $Z \rightarrow ee$  channel upon implementing this (indicating a potentially large shift in the measured  $W$  mass), it was decided to implement such a model in UCL Fast Simulation.

The UCL Fast Simulation Au/Be Model (note all the discussion in the remainder of this section refers to the UCL Fast Simulation model) uses gold as the ‘heavy’ element and beryllium as the ‘light’ element. The logic is the same as for the Cu/Be Model, replacing copper with gold. A total cross section rescaling factor was derived and validated for gold by a similar technique as used for copper in section 7.4. The Au/Be Model is used to replace the Si/Cu-Si/Be Model only when the electron being simulated is traversing one of a specified set of logical layers and the simulated electron’s path at the centre of the logical layer being traversed satisfies specified  $z$  co-ordinate criteria (where the  $z$  co-ordinate is the standard CDF  $z$  co-ordinate along the beam line). The specified set of layers and the specified  $z$  co-ordinate criteria for those layers are

SiliMap Layer Number(s)	$z$ Co-ordinate Criteria for Using Au/Be Model
0	No hybrids in this layer
1 and 2	$ z  > 47.0$ AND $ z  < 51.0$
3	No hybrids in this layer
4 through to 20	$( z  > 10.0$ AND $ z  < 21.0)$ OR $( z  > 40.0$ AND $ z  < 47.0)$
21 and 22	No hybrids in these layers
23	$ z  > 12.0$ AND $ z  < 18.0$
24 and 25	No hybrids in these layers
26	$ z  > 20.0$ AND $ z  < 26.0$
27 and 28	No hybrids in these layers
29	$ z  > 39.0$ AND $ z  < 45.0$
30 and 31	No hybrids in these layers

Table 7.1: The  $z$  co-ordinate criteria for using the Au/Be Model for each logical layer of SiliMap. If the criteria are satisfied then the layer is modelled using the Au/Be Model. If not then the layer is modelled using the Si/Cu-Si/Be Model. Some layers do not contain any hybrids, these are always modelled using the Si/Cu-Si/Be Model. SiliMap layers are numbered from 0 to 31 according to position, starting from the innermost layer (the beam pipe) up to the outermost layer (the COT inner wall).

presented in table 7.1.

It is very important to note the use of the Au/Be Model was a late addition to UCL Fast Simulation Bremsstrahlung modelling and all the other work presented in this chapter and in Chapter 8 predates the introduction of the Au/Be Model. Hence the various versions of UCL Fast Simulation used in the estimation of the systematic uncertainties in section 8.1 do not use the Au/Be Model. As the Au/Be Model was not included in the version of UCL Fast Simulation used in calculating the Bremsstrahlung systematic uncertainties, it is possible that the Au/Be Model's subsequent introduction may have reduced the systematic error due to modelling of the composition of the CDF Run II silicon tracker using a two element model. The dominant contribution to the overall Bremsstrahlung systematic uncertainty is the Cu/Be Model systematic, intended to estimate the error on the measured  $W$  mass due to the mis-modelling of layers that consist of a combination of beryllium-like elements and copper-like elements. The possibility of such mis-modelling is not applicable to layers now being accurately modelled as a mixture of gold and beryllium (and the composition of such layers may be such that they would be particularly poorly modelled by the Si/Cu-Si/Be Model),

hence the error due to such mis-modelling should be reduced.

## Chapter 8

# Bremsstrahlung and Pair

# Production Modelling Systematic

# Uncertainties on the $W$ Mass

# Measurement

## 8.1 Bremsstrahlung Modelling Systematic Uncertainties

The fitting of  $E/p$  distributions is central to the  $W$  mass analysis. Any photons that are radiated in the silicon tracker will reduce the measured momentum of an electron, but will probably be recombined with the electron in the CEM and will not reduce the measured energy of that electron, thus changing the measured  $E/p$ . This is modelled in UCL Fast Simulation but any errors in the modelling of Bremsstrahlung will affect the simulated  $E/p$  distribution. This will result in small errors in the  $E/p$  fitting; these errors will propagate directly to the electromagnetic energy scale determination and hence to the  $W$  mass itself. Hence it is important to estimate the effect the accuracy of UCL Fast Simulation's modelling of Bremsstrahlung will have on the accuracy of the measured  $m_W$ .

To do this we run multiple versions of UCL Fast Simulation. One version will be

the actual simulation model selected for the  $W$  mass analysis, henceforth referred to as the standard simulation. The others will be models that differ from the actual  $W$  mass analysis model by what we believe is the largest reasonable error on our simulation, henceforth referred to as the variant simulations. We use the standard simulation to generate pseudo-data, simulated  $W$  boson decay events at a (realistic) nominal value of  $m_W$ . We run the variant simulation to generate  $W$  mass templates and fit to the pseudo-data generated by the standard simulation. We take the difference between the fitted  $m_W$  and the nominal  $m_W$  of the pseudo-data as a systematic uncertainty on  $m_W$ . Due to the finite Monte-Carlo statistics there will be a statistical uncertainty on this systematic uncertainty. The fits will be performed using the standard least squares technique [43], using the  $W$  boson transverse mass ( $m_T$ ) distribution.

The effects of changes in the simulation on the  $m_W$  measured by the final analysis of the data may be (either partially or entirely) propagated through or absorbed by the retuning of important simulation parameters; thus it is necessary to simulate this retuning when generating systematics by fitting templates to pseudo-data. This is achieved by retuning important simulation parameters in the variant simulations relative to the nominal simulation parameters used in generating standard simulation pseudo-data and then running the variant simulations to generate  $W$  mass templates using these retuned parameters. The simulation parameters that require retuning are the CEM energy scale, the CEM  $\kappa$  (a tunable parameter of the CEM energy resolution model, see section 9.1) and the material scale, all of which are estimated by the least squares technique. The retunings are performed by fitting a standard simulation pseudo-data distribution generated using (realistic) nominal values for the material scale, CEM energy scale and CEM  $\kappa$  to templates generated using the variant simulations. The results of these retuning fits for a particular variant simulation are used as the retuned parameters of that variant simulation.

Material scale, CEM  $\kappa$  and CEM energy scale are all interdependent. For CEM energy scale and CEM  $\kappa$  this is resolved by generating a grid of template points varying both the energy scale and  $\kappa$  and then fitting both parameters iteratively until a stable energy scale and  $\kappa$  combination is found. The interdependence of the material scale and

Simulation Parameter	Formulae for Uncertainty on $m_W$ Due to the Statistical Uncertainty on this Parameter (MeV/c <sup>2</sup> )
CEM Energy Scale	$80400.0 \times \Delta(S_{\text{CEM}})$
CEM $\kappa$	$5386.7 \times \Delta\kappa$
Material Scale	$823.3 \times \Delta(S_{\text{mat}})$

Table 8.1: The formulae used to calculate uncertainties on  $m_W$  shifts due the statistical uncertainties on the various retuned parameters.  $\Delta(S_{\text{CEM}})$ ,  $\Delta\kappa$  and  $\Delta(S_{\text{mat}})$  are respectively the absolute uncertainties on energy scale shifts,  $\kappa$  shifts and material scale shifts. Note these absolute uncertainties are all expected to be significantly less than 1 and thus the uncertainties on  $m_W$  calculated will be small (a few MeV/c<sup>2</sup>). Statistical uncertainties on the CEM energy scale propagate directly to the measured primary electron  $E_T$  and hence  $m_W$ . The formula for  $\kappa$  is derived from the result of a template to pseudo-data  $m_W$  fit where the templates and pseudo-data are generated with different  $\kappa$  values. The main effect of shifts in the material scale on  $m_W$  is expected to be indirectly through changes in the energy scale. The formula for material scale is thus derived from the results of a template to pseudo-data energy scale fit where the templates and pseudo-data are generated with different values of material scale.

the energy scale/ $\kappa$  combination is resolved for each variant simulation by an iterative fitting cycle of a set of energy scale/ $\kappa$  fits, then a material scale fit then another set of energy scale/ $\kappa$  fits; at each step in this cycle new templates are generated using the values from the previous step. The second energy scale/ $\kappa$  combination and the fitted material scale are used as the retuned parameter values for the generation of  $W$  mass templates.

Each retuned simulation parameter has an associated statistical uncertainty on its value due to finite Monte-Carlo statistics. The formulae used to estimate the additional statistical uncertainties on  $W$  mass shifts (that are derived by fitting templates to pseudo-data) due the uncertainties on the various retuned parameters are given in table 8.1.

Note that both when fitting for  $W$  mass and when fitting for simulation parameters it is possible to ‘reverse the fit’ and fit standard simulation templates to variant simulation pseudo-data. We would expect the shift between the fitted value and the nominal value for such reverse fits to be equal in magnitude and opposite in sign to the original fit (henceforth referred to as the forward fit) to within the statistical error on the fit. This is used as a cross-check of the fitting procedure. For material scale the shift used is the

weighted mean of the shift calculated from the forward fit and the shift calculated from the reverse fit (the reverse shift being multiplied by minus one to correct for the reversed sign). For energy scale and  $\kappa$  both the energy scale shift calculated from the forward fit and the  $\kappa$  shift calculated from the forward fit are used if they produce the largest combined resultant estimated shift in  $m_W$  or both the energy scale shift (multiplied by minus one) from the reverse fit and the  $\kappa$  shift (multiplied by minus one) from the reverse fit are used if they produce the largest combined resultant estimated shift in  $m_W$ .

Five systematic uncertainties are considered for the UCL Fast Simulation Bremsstrahlung model, each is intended to estimate the systematic uncertainty on  $m_W$  due to a known uncertainty in the model. Three are linked to the Bremsstrahlung differential cross section  $y$ -spectrum: ‘Half-LPM’, ‘High- $y$  Re-weighted to GEANT4 4.9.0  $y$ -Spectrum’ and ‘High- $y$  Re-weighted to a  $y$ -Spectrum that Approximates the EEDL Tabulated Theoretical Results’; these systematics are described in sections 8.1.1 to 8.1.3. The other two systematics, ‘Silicon Only’ and ‘Cu/Be Model’, are linked to the two element model; these systematics are described in sections 8.1.4 and 8.1.5.

The final retuned CEM energy scales, CEM  $\kappa$ ’s and material scales used to generate  $m_W$  templates for these systematics are presented in tables 8.2 and 8.3. Each value is given as a shift from the nominal value used in the associated standard simulation, along with the associated statistical uncertainty. The final systematic uncertainties on the  $W$  mass measurement, along with the associated total statistical uncertainties on these systematics are presented in table 8.4.

The ‘High- $y$  Re-weighted to GEANT4 4.9.0  $y$ -Spectrum’ systematic uncertainty is thought to be an overly conservative estimate of the effect on  $m_W$  of the mis-modelling of the Bremsstrahlung differential cross section high- $y$  spectral shape by UCL Fast Simulation Bremsstrahlung Modification C. The ‘High- $y$  Re-weighted to a  $y$ -Spectrum that Approximates the EEDL Tabulated Theoretical Results’ systematic uncertainty is thought to give a better estimate of the effect on  $m_W$  of such mis-modelling (see section 8.1.3). The total Bremsstrahlung systematic uncertainty on the  $W$  mass measurement from combining all the systematic uncertainties presented in table 8.4 (ex-

Systematic	CEM Energy Scale Shift	CEM $\kappa$ Shift
1. Half-LPM	$(1.38 \pm 1.18) \times 10^{-5}$	$(0.82 \pm 3.92) \times 10^{-5}$
2. High- $y$ Re-weighted to GEANT4 4.9.0 $y$ -Spectrum	$(-2.931 \pm 0.122) \times 10^{-4}$	$(2.247 \pm 0.381) \times 10^{-4}$
3. High- $y$ Re-weighted to a $y$ -Spectrum that Approximates the EEDL Tabulated Theoretical Results	$(-2.89 \pm 1.19) \times 10^{-5}$	$(2.781 \pm 3.814) \times 10^{-5}$
4. Silicon Only	$(0.24 \pm 1.17) \times 10^{-5}$	$(-1.019 \pm 0.388) \times 10^{-4}$
5. Cu/Be Model	$(1.327 \pm 0.118) \times 10^{-4}$	$(-7.88 \pm 3.79) \times 10^{-5}$

Table 8.2: The final retuned CEM energy scales and CEM  $\kappa$ 's used in the Bremsstrahlung systematics' variant simulations to generate  $m_W$  templates. Each value is given as a shift from the nominal value used in the associated standard simulation, along with the associated statistical uncertainty.

Systematic	Material Scale Shift
1. Half-LPM	$(3.705 \pm 0.991) \times 10^{-3}$
2. High- $y$ Re-weighted to GEANT4 4.9.0 $y$ -Spectrum	$(3.3866 \pm 0.1001) \times 10^{-2}$
3. High- $y$ Re-weighted to a $y$ -Spectrum that Approximates the EEDL Tabulated Theoretical Results	$(9.429 \pm 0.992) \times 10^{-3}$
4. Silicon Only	$(-0.789 \pm 1.230) \times 10^{-3}$
5. Cu/Be Model	$(-4.535 \pm 1.231) \times 10^{-3}$

Table 8.3: The final retuned material scales used in the Bremsstrahlung systematics' variant simulations to generate  $m_W$  templates. Each value is given as a shift from the nominal value used in the associated standard simulation, along with the associated statistical uncertainty.

Systematic	Systematic Uncertainty on $m_W$ (MeV/c <sup>2</sup> )	Statistical Uncertainty on $m_W$ Fit (MeV/c <sup>2</sup> )	Total Statistical Uncertainty on Systematic (MeV/c <sup>2</sup> )
1. Half-LPM	3.745	1.296	1.815
2. High- $y$ Re-weighted to GEANT4 4.9.0 $y$ -Spectrum	33.342	1.294	1.832
3. High- $y$ Re-weighted to a $y$ -Spectrum that Approximates the EEDL Tabulated Theoretical Results	4.732	1.295	1.816
4. Silicon Only	1.833	1.293	1.903
5. Cu/Be Model	12.633	1.293	1.907

Table 8.4: The final Bremsstrahlung systematic uncertainties on the  $W$  mass measurement, along with the associated total statistical uncertainties (from finite Monte-Carlo statistics) on these systematic uncertainties.

cluding the ‘High- $y$  Re-weighted to GEANT4 4.9.0  $y$ -Spectrum’ systematic uncertainty) is  $14.120 \pm 3.722$  MeV/c<sup>2</sup>. This combined systematic uncertainty is higher than anticipated mostly due to the contribution of the ‘Cu/Be Model’ systematic. However the effective ‘Cu/Be Model’ systematic uncertainty may have been reduced by work on modelling hybrid layers as a mixture of gold and beryllium (see section 7.5) that postdates these systematic studies, though without re-running the ‘Cu/Be Model’ systematic study including this new work on hybrid layers in the simulation (which would require extensive computing resources) this is only speculation.

### 8.1.1 Half-LPM

For this systematic the LPM/dielectric suppression factor in UCL Fast Simulation Bremsstrahlung Modification C (see section 6.2.6) is reduced to half its normal value in the variant model. This is achieved by randomly sampling the Bremsstrahlung differential cross section  $y$ -spectrum values from either the normal UCL Fast Simulation Bremsstrahlung Modification C spectrum or from the UCL Fast Simulation Bremsstrahlung Modification C spectrum with no LPM/dielectric suppression (achieved by setting the LPM parameters  $\xi(s) = 1$ ,  $G(s) = 1$ ,  $\phi(s) = 1$  and the dielectric parameter  $S(k) = 1$ ),

with equal probability of either. The total Bremsstrahlung cross section is modified such as to maintain the integral of the differential cross section  $y$ -spectrum in the high- $y$  region  $0.05 < y < 1$ . In the case of this systematic, the standard simulation is not the actual simulation model selected for the  $W$  mass analysis, but UCL Fast Simulation Bremsstrahlung Modification C with no two element model, assuming all the material in the silicon tracker to be silicon. The variant simulation is then this standard simulation modified as detailed above.

This systematic is intended to roughly estimate the possible systematic error resultant from reduced LPM/dielectric suppression due to poorly understood surface effects which are not modelled in UCL Fast Simulation Bremsstrahlung Modification C (or indeed GEANT4 4.9.2). Such surface effects would be most important when modelling thin slices. A slice with a thickness of  $2\% X_0$  is seen as a reasonable example of a thin slice (for silicon  $2\% X_0 \approx 1.87$  mm). Figure 6.25 is a comparison of GEANT4 pseudo-data to SLAC experimental data for a carbon plate with thickness  $2\% X_0$ . The 50% change in LPM/dielectric suppression was derived by careful examination of the data and GEANT4 4.9.2 pseudo-data in this comparison, noting as a useful visual aid that the  $k$ -spectrum without any LPM/dielectric suppression would be a smooth continuation of the GEANT4 4.9.0  $k$ -spectrum from above the LPM cut-off into the region below the LPM cut-off. This change deliberately emphasised the observed discrepancy between the data and GEANT4 4.9.2 pseudo-data in the region  $10 < k < 20$  MeV directly below the LPM cut-off; the energy weighted differential cross section (below the LPM cut-off) is greater for higher  $k$ -values thus this region is the most important region of the LPM/dielectric suppression region to model correctly for the  $W$  mass analysis. Note that in the comparison there is an *increase* in LPM/dielectric suppression in the data compared to the pseudo-data; the reason for this is unknown, we expect a decrease. It would thus have been preferable to consider an increase (by a factor of 2) instead of a decrease in LPM/dielectric suppression; however this was not done. Despite this the ‘Half-LPM’ systematic is considered a reasonable estimate of the systematic uncertainty due to surface effects as the change in the simulation considered is of the correct magnitude, although the sign of the change is not that observed in comparisons to data.

### 8.1.2 High- $y$ Re-weighted to GEANT4 4.9.0 $y$ -Spectrum

For this systematic the high- $y$  region of UCL Fast Simulation Bremsstrahlung Modification C is modified to match the spectral shape of the GEANT4 4.9.0  $y$ -spectrum (for the same incident electron energy) in the variant model. This is implemented by calculating the ratio  $R_{\text{high-}y}(y)$  for each Bremsstrahlung event where the incident electron energy is greater than 1 GeV.  $R_{\text{high-}y}(y)$  is defined:

$$R_{\text{high-}y}(y) = N \frac{d\sigma(y)_{\text{G4.9.0}}}{d\sigma(y)_{\text{G4.9.2}}} \quad (8.1)$$

where  $d\sigma(y)_{\text{G4.9.0}}$  is calculated using eq. (5.9) (the LPM and dielectric effects are deliberately not considered in this calculation);  $d\sigma(y)_{\text{G4.9.2}}$  is calculated using eq. (5.27), setting the LPM parameters  $\xi(s) = 1$ ,  $G(s) = 1$ ,  $\phi(s) = 1$  and the dielectric parameter  $S(k) = 1$  to remove the LPM and dielectric effects.  $N$  is a normalisation factor. Studies show that  $R_{\text{high-}y}(y)$  with  $N = 1$  approaches a limit  $L$  asymptotically as  $y \rightarrow 0$  and that for all energies of interest to this analysis (i.e. between 1 GeV and 150 GeV)  $R_{\text{high-}y}(y) \leq L$  for all values of  $y$ . For the variant model  $N = 1/L$  such that  $R_{\text{high-}y}(y) \rightarrow 1$  as  $y \rightarrow 0$ . For each Bremsstrahlung event where the incident electron energy is greater than 1 GeV we generate a random number  $Q$ , in the interval  $[0, 1]$ . If  $Q > R_{\text{high-}y}(y)$  we reject the Bremsstrahlung event, i.e. no new photons are generated and the energy of the incident electron is not altered. The total Bremsstrahlung cross section is modified such as to maintain the integral of the differential cross section  $y$ -spectrum in the low- $y$  region  $0.0001 < y < 0.005$ . As the total cross section and the  $y$ -spectral shape are weakly interdependent, two iterations of the modification procedure are required to achieved a sufficient level of accuracy. In the case of this systematic, the standard simulation is not the actual simulation model selected for the  $W$  mass analysis, but UCL Fast Simulation Bremsstrahlung Modification C with no two element model, assuming all the material in the silicon tracker to be silicon. The variant simulation is then this standard simulation modified as detailed above.

This systematic is intended to estimate the effect of the uncertainty in the modelling of the  $y$ -spectral shape in the high- $y$  region. Comparisons have shown neither the

GEANT4 4.9.2 model nor the GEANT4 4.9.0 model of the Bremsstrahlung differential cross section  $y$ -spectrum in the high- $y$  region accurately match the EEDL tabulated theoretical results [72, 73] (which we consider to be the most accurate source of applicable Bremsstrahlung differential cross section  $y$ -spectrum information available) across the entire  $y$ -range (see fig. 6.27). However in the region where the tabulated theoretical results deviate from both GEANT4 models, the tabulated theoretical results give cross section values between those of the GEANT4 4.9.2 model and the GEANT4 4.9.0 model. Thus switching between the two GEANT4 models can be interpreted as the largest reasonable error in the simulation of the high- $y$  region; this systematic is an estimate of the effect of such a switch.

### 8.1.3 High- $y$ Re-weighted to a $y$ -Spectrum that Approximates the EEDL Tabulated Theoretical Results

For this systematic the high- $y$  region of UCL Fast Simulation Bremsstrahlung Modification C is modified such that the  $y$ -spectrum spectral shape (for all energies above 1 GeV) approximately matches the EEDL tabulated theoretical results (for an incident electron energy of 100 GeV) in the variant model.

This is implemented by calculating the ratio  $R_{\text{high-}y}(y)$  for each Bremsstrahlung event where the incident electron energy is greater than 1 GeV, where  $R_{\text{high-}y}(y)$  is defined in eq. (8.1) in the ‘High- $y$  Re-weighted to GEANT4 4.9.0  $y$ -Spectrum’ systematic uncertainty described above. This allows us to calculate the ‘ratio’  $R_{\text{EEDL-high-}y}(y)$ , defined as:

$$\begin{aligned}
 R_{\text{EEDL-high-}y}(y) &= R_{\text{high-}y}(y) & (y < y_{\text{cutoff-EEDL}}) & \quad (8.2) \\
 R_{\text{EEDL-high-}y}(y) &= R_{\text{high-}y}(y_{\text{cutoff-EEDL}}) & (y \geq y_{\text{cutoff-EEDL}}) &
 \end{aligned}$$

where  $y_{\text{cutoff-EEDL}} = 0.0743$ . The  $y_{\text{cutoff-EEDL}}$  value was decided upon, from inspection of fig. 8.1 (see below), as a value which produces a  $y$ -spectrum that is a good approximation of the EEDL tabulated theoretical results. For each Bremsstrahlung event where the incident electron energy is greater than 1 GeV we generate a random number  $Q$ , in the

interval  $[0, 1]$ . If  $Q > R_{\text{EEDL-high-}y}(y)$  we reject the Bremsstrahlung event, i.e. no new photons are generated and the energy of the incident electron is not altered.

The total Bremsstrahlung cross section is modified such as to maintain the integral of the differential cross section  $y$ -spectrum in the low- $y$  region  $0.0001 < y < 0.005$ . Two iterations of the modification procedure are required to achieved a sufficient level of accuracy; the first iteration starting from the final cross section of the variant simulation in the ‘High- $y$  Re-weighted to GEANT4 4.9.0  $y$ -Spectrum’ systematic described above.

In the case of this systematic, the standard simulation is not the actual simulation model selected for the  $W$  mass analysis, but UCL Fast Simulation Bremsstrahlung Modification C with no two element model, assuming all the material in the silicon tracker to be silicon. The variant simulation is then this standard simulation modified as detailed above.

The EEDL tabulated theoretical results with incident electron energies closest to 40 GeV comprise either 100 GeV or 12.2474 MeV; it is unclear how to correctly interpolate between these for intermediate energies. Figure 8.1 is a plot comparing the ratios  $\frac{d\sigma_X}{d\sigma_{\text{GEANT4 4.9.2 } y\text{-spectrum}}}$  where  $X$  is variously: EEDL tabulated theoretical Bremsstrahlung  $y$ -spectra for incident electron energies of 100 GeV and 12.2474 MeV; the GEANT4 4.9.0 theoretical differential cross section  $y$ -spectra as given by eq. (5.9) for incident electron energies of 100 GeV, 40 GeV and 12.2474 MeV. A linear  $x$ -axis scale is used. All other details of this figure are the same as for fig. 6.27. The EEDL tabulated theoretical Bremsstrahlung  $y$ -spectrum and GEANT4 4.9.0 theoretical Bremsstrahlung  $y$ -spectrum for 12.2474 MeV roughly agree (unfortunately this is only partially visible in the plot presented here due the  $y$ -axis range used; it is more clearly observed in other versions of this plot using a greater  $y$ -axis range, however these are otherwise less informative and are not included in this thesis for the sake of brevity); while possibly insufficiently accurate for the purposes of this analysis, GEANT4 4.9.0 would appear to roughly capture the incident electron energy dependence of the EEDL tabulated theoretical results. The GEANT4 4.9.0 theoretical differential cross section  $y$ -spectra for incident electron energies of 100 GeV and 40 GeV (the later being the typical energy of an electron that is the primary daughter particle of a  $W$  boson decay) are extremely similar (in comparison to

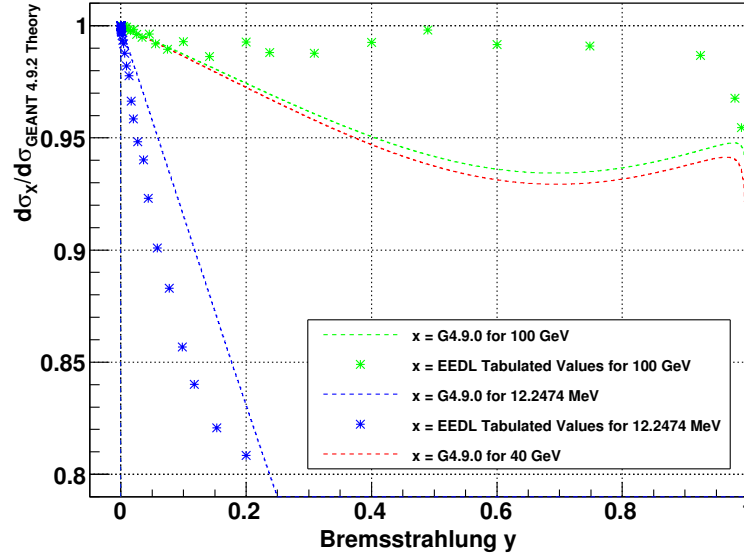


Figure 8.1: The ratios  $\frac{d\sigma_X}{d\sigma_{\text{GEANT4 4.9.2 } y\text{-spectrum}}}$ , where  $X$  is variously: EEDL tabulated theoretical Bremsstrahlung  $y$ -spectra for incident electron energies of 100 GeV and 12.2474 MeV; the GEANT4 4.9.0 theoretical differential cross section  $y$ -spectra as given by eq. (5.9) for incident electron energies of 100 GeV, 40 GeV and 12.2474 MeV. The GEANT4 4.9.2  $y$ -spectrum is the GEANT4 4.9.2 theoretical differential cross section  $y$ -spectrum as given by eq. (5.27). The medium is silicon. A linear  $x$ -axis scale is used. Note the vertical line from 0 to 1 at  $y = 0$  is an artefact of the routine used to generate this plot and has no physical meaning. All other details of this figure are the same as for fig. 6.27. Note the very rough agreement between the EEDL tabulated theoretical values for an incident electron energy of 12.2474 MeV and the GEANT4 4.9.0 model for the same incident electron energy, and the similarity between the GEANT4 4.9.0 model for an incident electron energy of 40 GeV and the GEANT4 4.9.0 model for an incident electron energy of 100 GeV. Further discussion is given in the main text.

the  $y$ -spectrum for 12.2474 MeV) so it would appear reasonable to assume hypothetical EEDL tabulated theoretical results for an incident electron energy of 40 GeV would be very similar to those for an incident electron energy of 100 GeV. This is the justification for the use of the EEDL tabulated theoretical results for an incident electron energy of 100 GeV as a basis for the variant model for all incident electron energies above 1 GeV.

This systematic is intended to estimate the effect of the uncertainty in the modelling of the  $y$ -spectral shape in the high- $y$  region and is considered as an alternative to the ‘High- $y$  Re-weighted to GEANT4 4.9.0  $y$ -Spectrum’ systematic uncertainty described above (which upon calculation was found to be considerably greater than expected). For roughly  $y \geq 0.2$ , the difference between the GEANT4 4.9.0 model and the EEDL

tabulated theoretical results (which we consider to be the most accurate source of applicable Bremsstrahlung differential cross section  $y$ -spectrum information available) is significantly greater than that between the GEANT4 4.9.2 model and the EEDL tabulated theoretical results (see fig. 6.27); thus the systematic ‘High- $y$  Re-weighted to GEANT4 4.9.0  $y$ -Spectrum’ is considered to produce an overly conservative estimate of the systematic uncertainty from mis-modelling of the Bremsstrahlung high- $y$  spectrum. Instead in this systematic we consider switching between the GEANT4 4.9.2 model and a model that approximates the EEDL tabulated theoretical results as the largest reasonable change in the simulation of the high- $y$  region and estimate the effect of such a switch.

Though we believed the EEDL tabulated theoretical results to be more accurate than the GEANT4 4.9.2 model, the version of UCL Fast Simulation used for the final analysis of the data was not changed to use the model that approximates the EEDL tabulated theoretical results (as used by the variant simulation in this systematic) because it is not possible to validate this model using test beam pseudo-experiments and it may not be a robust model of the  $y$ -spectrum. This model is inaccurate as it only approximates the EEDL tabulated theoretical results roughly at a single energy of 100 GeV. The EEDL tabulated theoretical results are not smooth (possibly due to statistical fluctuations produced by a Monte-Carlo technique used in their generation) and thus may be inaccurate. Thus overall this model will only give a rough approximation of the true differential cross section  $y$ -spectrum at best; if we were to use this model for the final data analysis then we would still need to use the systematic described in this section as an estimate of the residual systematic uncertainty due to the inaccuracy of this model. The systematic difference between this model and UCL Fast Simulation Bremsstrahlung Modification C (the model of Bremsstrahlung in the version of UCL Fast Simulation used for the final analysis of the data) is small; thus we continue to use UCL Fast Simulation Bremsstrahlung Modification C, which has been validated against GEANT4 4.9.2 using test beam pseudo-experiments, is believed to be robust and precisely produces the known ultra high energy limit differential cross section  $y$ -spectrum.

#### 8.1.4 Silicon Only

For this systematic UCL Fast Simulation Bremsstrahlung Modification C with no two element model, assuming all the material in the silicon tracker to be silicon, is the variant simulation. The standard simulation is the actual simulation model selected for the  $W$  mass analysis. This systematic is intended to roughly estimate the possible systematic error due to the imperfect nature of the two element model as a model of the composition of the silicon tracker.

#### 8.1.5 Cu/Be Model

For this systematic UCL Fast Simulation Bremsstrahlung Modification C with the Cu/Be Model (see section 7.4.1) as the two element model is the variant simulation. The standard simulation is the actual simulation model selected for the  $W$  mass analysis (i.e. the Si/Cu-Si/Be Model as the two element model). As discussed previously this systematic is intended to estimate the systematic error due to the known weakness of the Si/Cu-Si/Be Model in the case of layers that consist of a combination of beryllium-like elements and copper-like elements (e.g. plastic coated copper cabling).

### 8.2 Pair Production Modelling Systematic Uncertainties

It is important to estimate the effect the accuracy of UCL Fast Simulation's modelling of pair production will have on the accuracy of the  $W$  mass measurement. The modelling of pair production is thought to be less important than Bremsstrahlung to the  $W$  mass analysis because photons are not the primary daughter particles of  $W$  decays. However the exact effect of pair production mis-modelling on the measured  $W$  mass is hard to predict from basic arguments. We generate estimates of the systematic uncertainties on  $m_W$  due to pair production mis-modelling using the techniques detailed in section 8.1.

Two systematic uncertainties are considered for the UCL Fast Simulation pair production model. They are intended to estimate the systematic uncertainties on  $m_W$  due to known uncertainties in the model. The systematics are 'Basic Spectrum' and 'Pegged Total Cross Section'; details of these systematics are given in sections 8.2.1 and 8.2.2.

Systematic	CEM Energy Scale Shift	CEM $\kappa$ Shift
1. Basic Spectrum	$(0.71 \pm 1.19) \times 10^{-5}$	$(-3.92 \pm 3.92) \times 10^{-5}$
2. Pegged Total Cross Section	$(0.97 \pm 1.19) \times 10^{-5}$	$(8.28 \pm 3.83) \times 10^{-5}$

Table 8.5: The final retuned CEM energy scales and CEM  $\kappa$ 's used in the pair production systematics' variant simulations to generate  $m_W$  templates. Each value is given as a shift from the nominal value used in the associated standard simulation, along with the associated statistical uncertainty.

Systematic	Material Scale Shift
1. Basic Spectrum	$(-0.602 \pm 1.213) \times 10^{-3}$
2. Pegged Total Cross Section	$(0.474 \pm 1.189) \times 10^{-3}$

Table 8.6: The final retuned material scales used in the pair production systematics' variant simulations to generate  $m_W$  templates. Each value is given as a shift from the nominal value used in the associated standard simulation, along with the associated statistical uncertainty.

The final retuned CEM energy scales, CEM  $\kappa$ 's and material scales used to generate  $m_W$  templates for these systematics are presented in tables 8.5 and 8.6. Each value is given as a shift from the nominal value used in the associated standard simulation, along with the associated statistical uncertainty. The final systematic uncertainties on the  $W$  mass measurement, along with the associated total statistical uncertainties on these systematics, are presented in table 8.7. The combined systematic uncertainty on the measured  $W$  mass from both the systematic uncertainties given in table 8.7 is  $2.754 \pm 2.686$  MeV/ $c^2$ , this is considered sufficiently accurate for this analysis. Details of both UCL Fast Simulation Pair Production Modification A and UCL Fast Simulation Pair Production Modification B are given in section 6.4.

### 8.2.1 Basic Spectrum

For this systematic UCL Fast Simulation Pair Production Modification B modified to revert to using eq. (5.46) as the pair production differential cross section  $x$ -spectrum is the variant model. The standard simulation is the actual simulation model selected for the  $W$  mass analysis. This systematic is intended to roughly estimate the possible

Systematic	Systematic Uncertainty on $m_W$ (MeV/c <sup>2</sup> )	Statistical Uncertainty on $m_W$ Fit (MeV/c <sup>2</sup> )	Total Statistical Uncertainty on Systematic (MeV/c <sup>2</sup> )
1. Basic Spectrum	1.505	1.293	1.905
2. Pegged Total Cross Section	2.306	1.293	1.894

Table 8.7: The final pair production systematic uncertainties on the  $W$  mass measurement, along with the associated total statistical uncertainties (from finite Monte-Carlo statistics) on these systematic uncertainties.

systematic error due to imperfection in the modelling of the pair production differential cross section  $x$ -spectrum. It is rather conservative; however given the absence of validation of the GEANT4 model of pair production against external data or pseudo-data such conservatism is necessary.

### 8.2.2 Pegged Total Cross Section

For this systematic UCL Fast Simulation Pair Production Modification A (including the original model of photon interaction total cross section as detailed in section 6.4.3) is the variant model. This model essentially ‘pegs’ the NIST total cross section data to the theoretical high energy limit given by eq. (5.59). The standard simulation is the actual simulation model selected for the  $W$  mass analysis. This systematic is intended to roughly estimate the possible systematic error due to imperfection in the modelling of the pair production (and Compton scattering) total cross section.

## 8.3 Total Combined Systematic Uncertainty from Bremsstrahlung and Pair Production

The total Bremsstrahlung systematic uncertainty on the  $W$  mass measurement in the electron channel is estimated as  $14.120 \pm 3.722$  MeV/c<sup>2</sup>. The total pair production systematic uncertainty on the  $W$  mass measurement in the electron channel is estimated as  $2.754 \pm 2.686$  MeV/c<sup>2</sup>. The combined Bremsstrahlung and pair production systematic uncertainty on the  $W$  mass measurement in the electron channel is estimated as  $14.4 \pm$

4.6 MeV/c<sup>2</sup>. Though all these numbers have been derived specifically for UCL Fast Simulation, it is expected they would apply equally to any similar simulation used for the measurement of the  $W$  mass. The baseline analysis of the CEM energy scale considered the ‘High- $y$  Re-weighted to a  $y$ -Spectrum that Approximates the EEDL Tabulated Theoretical Results’ systematic. The two element model systematics were not applicable to the baseline analysis as Duke Fast Simulation uses a different two element model. The pair production systematics were disregarded in the baseline analysis of CEM energy scale as they were small compared to other uncertainties considered and statistically consistent with zero uncertainty (and thus the  $m_W$  shifts generated for such systematics could very plausibly be largely due to finite Monte-Carlo statistics).

## Chapter 9

# Determination of the Electron CEM Energy Scale for the CDF Run II $W$ Mass Measurement

### 9.1 Overview of CEM Energy Scale Calibration

The accurate determination of the CEM energy scale is critical to measuring the  $W$  mass in the electron channel. The measurement of  $p_T^e$  is linearly dependent on the CEM energy scale;  $m_T$  is dependent on  $p_T^\ell$  both directly and through  $\cancel{p}_T$ . Thus any change in the CEM energy scale will propagate (approximately linearly) to  $m_T$ . The CEM energy scale can be determined by two independent methods. Comparing the results of the two methods provides a stringent test of the accuracy of many aspects of our simulation, while the subsequent combination of the two results (by calculating their weighted mean) provides a more statistically accurate determination of the CEM energy scale than either method would in isolation.

In simulated events generated by UCL Fast Simulation an overall energy scale factor  $S_{\text{CEM}}$  is applied to the reconstructed electron energy. A random smearing factor is also applied to reconstructed electron energies to simulate the CEM resolution; this is

sampled from a normal distribution with a standard deviation  $\sigma_E$ , defined as:

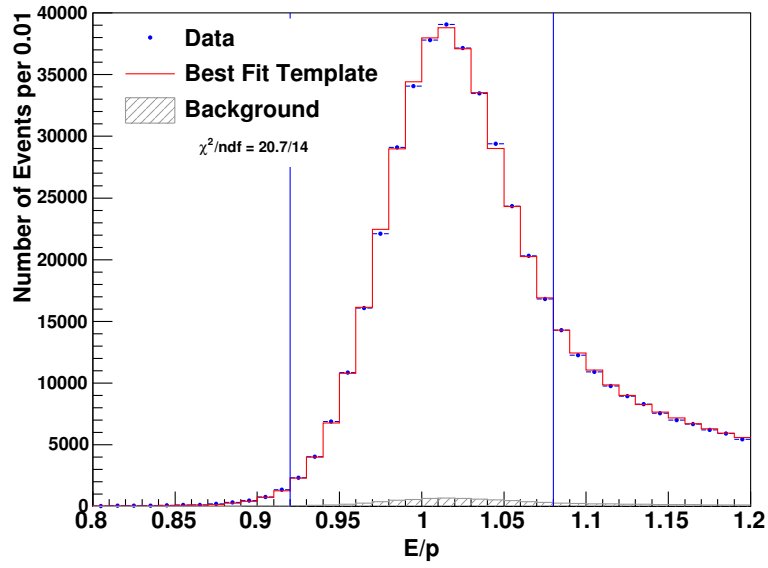
$$\sigma_E^2 = \left( \frac{0.126}{\sqrt{E_T}} \right)^2 + \kappa^2. \quad (9.1)$$

where the first term is the stochastic smearing term measured by a test beam during the commissioning of CDF and  $\kappa$  is a tuning factor specific to this analysis.  $S_{\text{CEM}}$  and  $\kappa$  are determined by fitting simulated templates to data.  $S_{\text{CEM}}$  and  $\kappa$  are interdependent and thus must be determined through an iterative fitting cycle, i.e. a first fit is used to estimate  $S_{\text{CEM}}$  for a fixed value of  $\kappa$ , a second fit is then used to estimate  $\kappa$  with  $S_{\text{CEM}}$  fixed at the value determined in the previous step and so forth till both parameters converge on a stable value. Fits to two different distributions (described below) are separately used to determine values for  $S_{\text{CEM}}$  and  $\kappa$ . The consistency of the two determinations is evaluated. The final values of  $S_{\text{CEM}}$  and  $\kappa$  used are the weighted averages of the values from the two determinations. The two distributions used are:

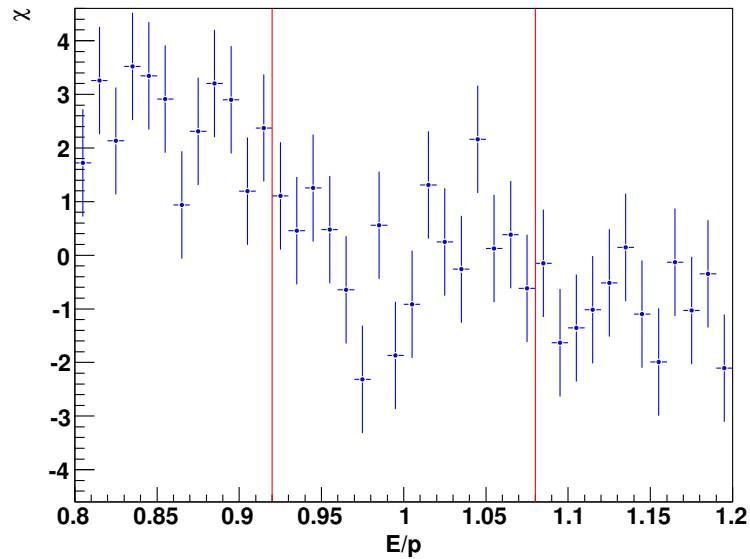
- $E/p$  in  $W \rightarrow e\nu$  events: An  $E/p$  calibration uses an iterative cycle of fits to the  $E/p$  distribution of electron channel  $W$  events in fine bins in the peak region  $0.92 < E/p < 1.08$  to estimate  $S_{\text{CEM}}$  and  $\kappa$ . An  $E/p$  background distribution is added to the templates for this fit; this background is produced using the same techniques that are used to produce backgrounds for fits to estimate  $m_W$ . In essence  $E/p$  calibration sets the calorimeter energy scale by utilising the very accurately calibrated COT momentum scale. It is the more statistically precise of the two methods. Figure 9.1 is an example of a comparison of the best fitting template to data for an  $E/p$  calibration. (The exact UCL Fast Simulation setup and results of this example are discussed later.)
- $Z \rightarrow e^+e^-$  invariant mass: A  $Z \rightarrow e^+e^-$  calibration uses an iterative cycle of fits to the  $m_{ee}$  distribution (of electron channel  $Z$  events) in fine bins in the peak region  $81 < m_{ee} < 101 \text{ GeV}/c^2$  to estimate  $S_{\text{CEM}}$  and  $\kappa$ . In these fits the value of  $Z$  mass used in HORACE is the current world average; this value is held constant. Figure 9.2 is an example of a comparison of the best fitting template to data for a  $Z \rightarrow e^+e^-$  calibration. (The exact UCL Fast Simulation setup and results of

this example are discussed later.)

The comparison of the results of the two methods can be interpreted as a measurement of the mass of the  $Z$  boson. The world average value of the  $Z$  mass is used in UCL Fast Simulation's event generation code. The energy scale determined from  $Z \rightarrow e^+e^-$  mass fits is linearly dependent on this mass value but the energy scale determined from  $W \rightarrow e\nu$   $E/p$  fits is completely independent of this mass value. Thus hypothetically any difference in the scales determined by the two methods could be absorbed by shifting the value of the  $Z$  mass used in the simulation in linear proportion to the difference and thus we report such differences in energy scale as shifts in the measured value of  $m_Z$  from the world average value according to the relation  $\Delta(m_Z) = -\Delta(S_{\text{CEM}}) \times (m_Z)_{\text{world average}}$ , where  $\Delta(S_{\text{CEM}}) = (S_{\text{CEM}})_{Z \rightarrow e^+e^- \text{ mass}} - (S_{\text{CEM}})_{W \rightarrow e\nu E/p}$  and  $(m_Z)_{\text{world average}} = 91.1876 \text{ GeV}/c^2$  [14]. The  $Z \rightarrow e^+e^-$  mass CEM energy scale fits are blinded by applying an unknown fixed offset sampled from a uniform distribution with a range of  $\pm \frac{75 \text{ MeV}/c^2}{(m_Z)_{\text{world average}}}$  to the fitted CEM energy scale (thus effectively blinding the  $Z$  mass measurement by  $\pm 75 \text{ MeV}/c^2$ ). This blinding is applied to the external output of the fitting code only; internally the fitting code uses the unblinded value when setting the fixed energy scale value for kappa fits during an iterative energy scale and kappa fit cycle. (Note the blinded value is used nowhere in UCL Fast Simulation itself; the blinding is applied only to the value fitted by comparing UCL Fast Simulation templates to data.) This blinding is intended to prevent the simulation being 'fine-tuned' to return the known world average  $m_Z$ , while still allowing us to see if our measurement of  $m_Z$  is discrepant from the world average by hundreds of MeV (i.e. grossly erroneous). The blinding will be removed when we are confident in our simulation and believe we are making an accurate measurement of the  $Z$  mass. *If* our unblinded value of  $m_Z$  is consistent with the world average then we can claim we have successfully made a satisfactory blinded measurement of the  $Z$  mass and freeze (i.e. make no further changes to) our simulation of the CEM energy scale for use in the overall  $W$  mass measurement. If our unblinded value is *not* consistent with the world average then we must continue working on our simulation till we can make a satisfactory

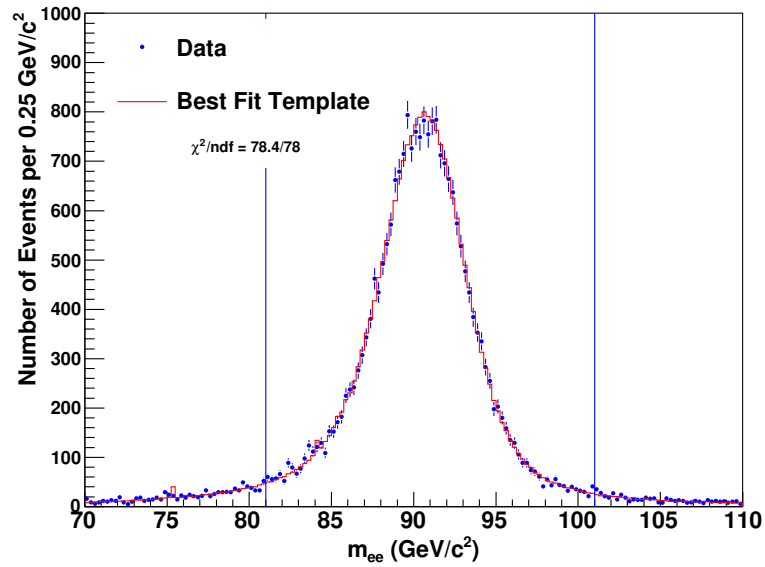


(a)

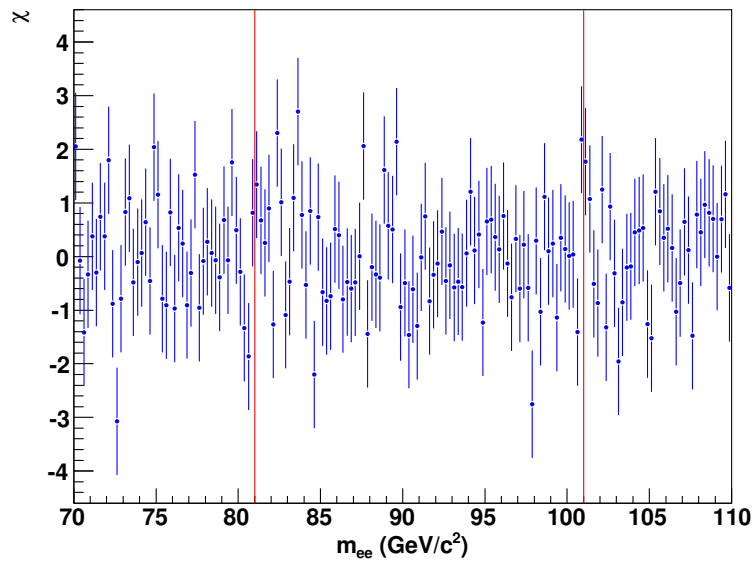


(b)

Figure 9.1: The  $E/p$  distribution of the best fitting template from the  $W \rightarrow e\nu$   $E/p$  CEM energy scale fit compared to the equivalent data distribution (a) and the  $\chi$  distribution for this comparison (b). ( $\chi = (n - m)/\sqrt{\sigma_n^2 + \sigma_m^2}$  where  $n$  is the number of observed data events in the bin,  $m$  is the number of simulation events in the bin,  $\sigma_n = \sqrt{n}$  is the error on the number of data events in the bin and  $\sigma_m$  is the error on the number of simulation events in the bin.) The templates are generated using the UCL leakage, coil energy loss and non-linearity models; the results of this fit are given in section 9.3.5. A contribution from background is included in the template  $E/p$  distribution; this background contribution (normalised to the data) is also plotted as a separate histogram in (a).



(a)



(b)

Figure 9.2: The  $m_{ee}$  distribution of the best fitting template from the  $Z \rightarrow e^+e^-$  mass CEM energy scale fit compared to the equivalent data distribution (a) and the  $\chi$  distribution for this comparison (b). The templates are generated using the UCL leakage, coil energy loss and non-linearity models; the results of this fit are given in section 9.3.5. No background is added to this distribution;  $Z \rightarrow e^+e^-$  backgrounds are negligible.

measurement of  $m_Z$ ; however we will no longer be able to claim such a measurement was blinded.

Prior to the calorimeter energy scale determination any variation in the calorimeter energy scale as a function of East-West symmetrised calorimeter tower number is removed by performing a separate  $W \rightarrow e\nu$   $E/p$  fit for the set of electrons reconstructed in each particular symmetrised calorimeter tower<sup>1</sup>. The fits are otherwise similar to the inclusive  $E/p$  fit described above. The reconstructed energies of electrons in data are corrected according to the results of these tower-by-tower  $E/p$  fits to remove any observed dependence of the energy scale on tower number.

## 9.2 CEM Energy Scale Analysis using UCL Fast Simulation

UCL Fast Simulation has been developed over a number of years by the UCL CDF group, much of its code being inherited from a prior measurement of the  $W$  boson width [79]. Since many simulation parameters are at least weakly interdependent (sometimes only through alterations in the  $W$  and  $Z$  event samples occurring because of events moving across cut boundaries) the simulation has been roughly retuned on a regular basis as various aspects of it have been developed.

This chapter presents the final retuning of parameters related to the CEM energy scale and the final CEM energy scale fits using both the  $Z \rightarrow e^+e^-$  mass and  $W \rightarrow e\nu$   $E/p$  methods. The analysis was performed twice using two different versions of UCL Fast Simulation. The first attempt produced a  $Z$  mass measurement that was inconsistent (with the world average  $Z$  mass) for all possible values of the  $Z \rightarrow e^+e^-$  mass CEM energy scale blinding. Thus several changes were made to UCL Fast Simulation and the analysis was repeated. The second attempt produced a blinded  $Z$  mass measurement that was consistent for some possible values of the  $Z \rightarrow e^+e^-$  mass CEM energy scale blinding. Thus the  $Z \rightarrow e^+e^-$  mass energy scale result from the second

---

<sup>1</sup>As noted previously, the CDF central calorimeter was split into two barrels, the East and West barrels, by the  $z = 0$  plane. The barrels were mirror images of each other; thus we define a symmetrised tower as a particular tower in the East barrel and its mirror image in the West barrel.

attempt was unblinded to produce a final  $Z$  mass measurement and a final set of CEM energy scale results.

The starting point for this final tuning cycle is UCL Fast Simulation including (at least) rough values for all the parameters necessary to run the code. The final calibrations of the tracker momentum scale (see section 4.7) from Duke Fast Simulation (which has a more detailed model of the COT than UCL Fast Simulation) are incorporated into UCL Fast Simulation. The recoil model (see section 4.8) parameters used are old and may not reflect recent changes to the simulation but as the recoil modelling has little effect on the determination of the CEM energy scale these will be sufficient.

The first attempt at the analysis used UCL Fast Simulation's default leakage model, coil energy loss model and non-linearity model. Several parameters were retuned: a new set of tower-by-tower  $W \rightarrow e\nu$   $E/p$  CEM energy scale fits were performed and the results applied as corrections to the data (see section 9.3.1); the tuning of the material scale was checked (see section 9.3.2); and a new non-linearity was fitted (see section 9.3.4). The  $W \rightarrow e\nu$   $E/p$  CEM energy scale was fitted separately for events with negatively and positively charged tracks as a consistency check and the results of this were satisfactory (see section 9.3.3). The CEM energy scale results from this first attempt are presented in section 9.3.5, along with the resultant blinded  $Z$  mass measurement.

The second attempt at the analysis adopted the leakage model, coil energy loss model and non-linearity model used in Duke Fast Simulation (see sections 9.4.1 and 9.4.2). Our collaborators at Duke have already managed to produce a  $Z$  mass consistent with the world average using Duke Fast Simulation; this simulation used very different parameterisations from UCL Fast Simulation of the leakage, coil energy loss and non-linearity. All three of these elements of the simulation are critical to the CEM energy scale measurement. The UCL Fast Simulation models of these effects were sufficiently accurate for the previous analysis of  $W$  boson width [79]; the leakage and coil energy loss are modelled by sampling from distributions generated by (GEANT3 based) CdfSim, while the non-linearity is modelled using the simplest possible form. However the second CDF II  $W$  mass analysis utilises a much larger ( $\sim 10$  times larger) dataset than this previous analysis and thus these parameterisation may not be sufficiently accurate for

this higher statistics dataset. The Duke Fast Simulation models of these effects are based on detailed test beam studies using GEANT4 and may provide the higher level of accuracy required by this analysis. Thus it was thought possible that replacing the standard UCL parameterisations of these simulation elements in UCL Fast Simulation with their Duke counterparts might reduce the  $Z$  mass discrepancy; this proved to be correct. The tower-by-tower energy scale fits were repeated using the modified UCL Fast Simulation and the new corrections applied to the data (see section 9.4.3); the new CEM energy scale fits used this new corrected data. The CEM energy scale results from this second attempt are presented in section 9.4.4, along with the resultant blinded  $Z$  mass measurement. Using this setup the blinded  $Z$  mass value was consistent with the world average value to within the maximum blinding offset, thus was unblinded. The final unblinded results (including the resultant unblinded  $Z$  mass measurement) are presented in section 9.5.

## 9.3 Analysis using UCL Leakage, Coil Energy Loss and Non-Linearity Models

### 9.3.1 Tower-by-Tower Energy Scale and $\kappa$ Fits

A set of tower-by-tower  $W \rightarrow e\nu$   $E/p$  CEM energy scale fits (as described in section 9.1) were performed. The results of these fits are presented in table 9.1. The energy scales were applied as corrections to both the  $W$  and  $Z$  datasets; as they are a parameterisation of the calorimeter resolution, the  $\kappa$  values cannot be applied as corrections to data. The tower-by-tower  $W \rightarrow e\nu$   $E/p$  CEM energy scale fits were then repeated using the corrected data; the residual tower-by-tower energy scale variation was observed to be statistically insignificant. It is possible to apply the  $\kappa$  values as tower-by-tower corrections to the resolution modelling in the simulation. Tests showed the effect of applying such tower-by-tower  $\kappa$  corrections is minimal ( $\sim 2$  MeV/ $c^2$ ); thus they were not used.

Symmetrised Tower Number	Fitted CEM Energy Scale	Statistical Uncertainty on CEM Energy Scale	Fitted CEM $\kappa$	Statistical Uncertainty on CEM $\kappa$	$\chi^2$ /ndf of Energy Scale Fit
0	1.02260	0.00032	0.0128	0.0008	18.3/14
1	1.02517	0.00022	0.0075	0.0009	14.8/14
2	1.02722	0.00024	0.0050	0.0012	23.7/14
3	1.02314	0.00024	0.0	0.0018	14.9/14
4	1.02221	0.00026	0.0014	0.0032	13.3/14
5	1.01922	0.00028	0.0074	0.0011	8.7/14
6	1.01712	0.00029	0.0070	0.0016	19.9/14
7	1.01092	0.00036	0.0132	0.0010	13.4/14
8	1.00571	0.00045	0.0144	0.0013	11.0/14

Table 9.1: Tower-by-tower  $W \rightarrow e\nu$   $E/p$  CEM energy scale and CEM  $\kappa$  fit results. The energy scales are applied as corrections to both the  $W$  and  $Z$  datasets.

### 9.3.2 Material Scale Fits

A material scale fit (as described in section 4.6.2) was performed using data that incorporated the tower-by-tower CEM energy scale corrections. The fitted value of material scale is:

$$S_{\text{mat}} = 1.0057 \pm 0.0040 \quad (\chi^2/\text{ndf} = 2.2/1)$$

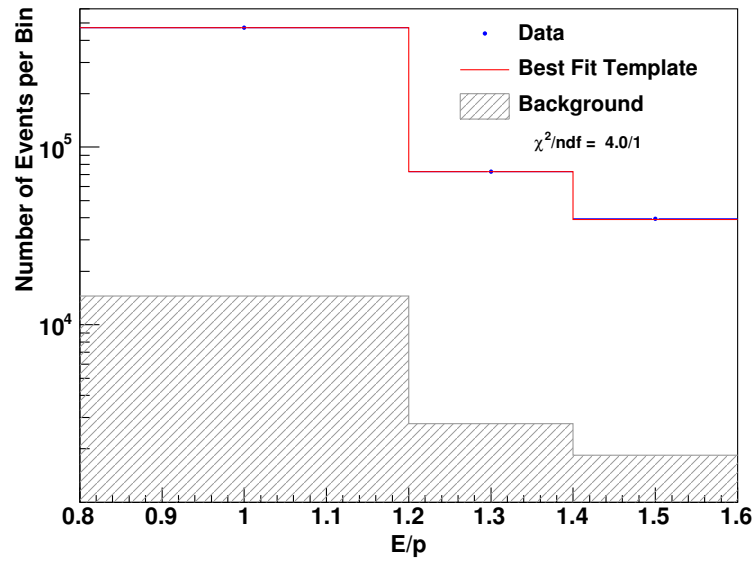
Figure 9.3 is a comparison of the best fitting template to data for this fit.

As a consistency check a material scale fit was also performed using  $Z \rightarrow e^+e^-$  three bin  $E/p$  templates and data. No background was added to this fit as  $Z \rightarrow e^+e^-$  backgrounds are negligible; it was otherwise similar to the standard fit using  $W \rightarrow e\nu$  events. The fitted value of the material scale using  $Z$ 's is:

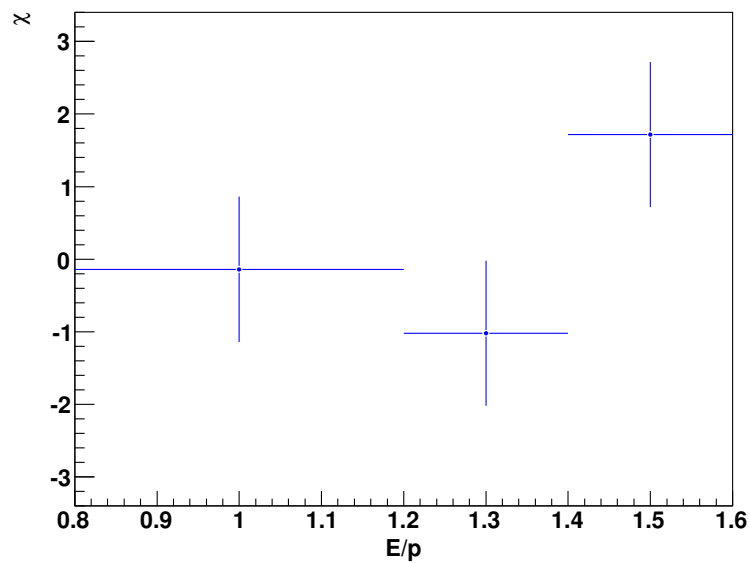
$$(S_{\text{mat}})_Z = 1.0008 \pm 0.0122 \quad (\chi^2/\text{ndf} = 2.4/1)$$

Figure 9.4 is a comparison of the best fitting template to data for this fit. The fitted value of  $(S_{\text{mat}})_Z$  is statistically consistent with  $S_{\text{mat}}$  to within  $1\sigma$ .

We would choose to use  $S_{\text{mat}}$  in our simulation and not the weighted average of  $S_{\text{mat}}$  and  $(S_{\text{mat}})_Z$ ; the statistical accuracy of  $S_{\text{mat}}$  alone is sufficient and it is preferable to use a calibration specifically tuned for the  $W$  boson events alone. However it was

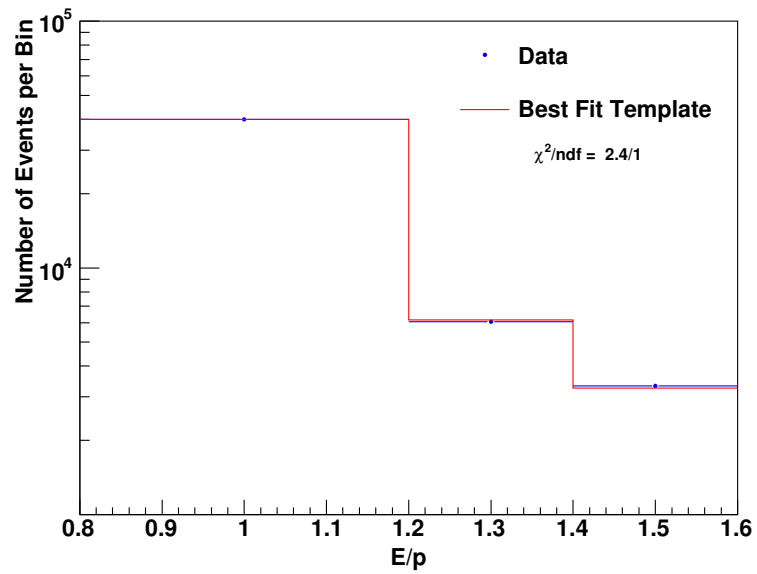


(a)

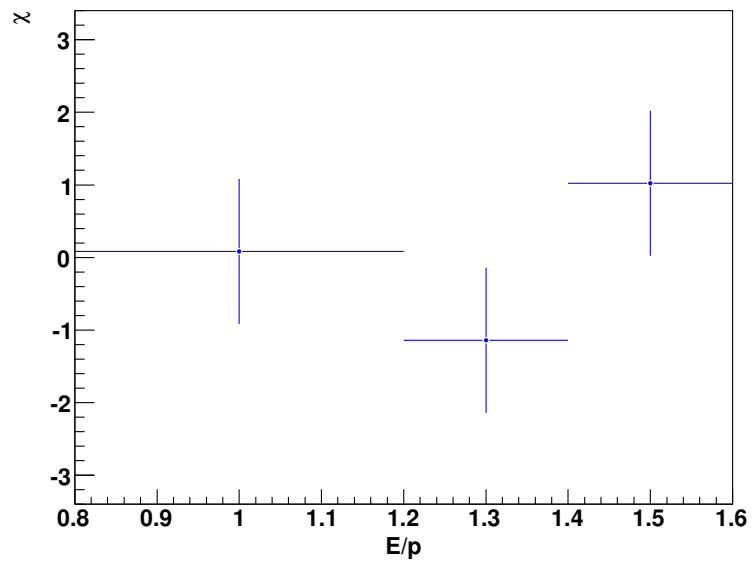


(b)

Figure 9.3: The three binned  $E/p$  distribution of the best fitting template from the material scale fit (using  $W$  events) compared to the equivalent data distribution (a) and the  $\chi$  distribution for this comparison (b). A contribution from background is included in the template  $E/p$  distribution; this background contribution (normalised to the data) is also plotted as a separate histogram in (a). Note the difference between the best fit template  $\chi^2$  and the  $\chi^2$  quoted on the fitted  $S_{\text{mat}}$  is expected, as the later is the value of the minimum of the fitted  $\chi^2$  parabola and does not correspond to a particular template.



(a)



(b)

Figure 9.4: The three binned  $E/p$  distribution of the best fitting template from the material scale fit using  $Z$  events compared to the equivalent data distribution (a) and the  $\chi$  distribution for this comparison (b). No background is added to this distribution;  $Z \rightarrow e^-e^+$  backgrounds are negligible.

decided to continue using the value used in the simulation prior to this set of material scale fits of  $S_{\text{mat}} = 1.0025$ , as concurrent studies had already begun using this old value when this new material scale fit was made. This value of  $S_{\text{mat}}$  is statistically consistent to within  $1\sigma$  with the new value.

### 9.3.3 Separate $W \rightarrow e^+\nu$ and $W \rightarrow e^-\nu$ CEM Energy Scale Fits

As a consistency check, the  $W \rightarrow e\nu$   $E/p$  CEM energy scale and  $\kappa$  are fitted with the additional selection requirement of the electron having a negatively charged track being applied in the event selection procedure for both the simulation and for the data. This is repeated with the selection requirement altered to the electron having a positively charged track.

The  $W \rightarrow e\nu$   $E/p$  CEM energy scale and  $\kappa$  fitted for negatively charged tracks is:

$$\begin{aligned}(S_{\text{CEM}})_{-} &= 1.02026 \pm 0.00013 & (\chi^2/\text{ndf} = 16.5/14) \\ (\kappa)_{-} &= 0.0080 \pm 0.0005 & (\chi^2/\text{ndf} = 16.5/14)\end{aligned}$$

The  $W \rightarrow e\nu$   $E/p$  CEM energy scale and  $\kappa$  fitted for positively charged tracks is:

$$\begin{aligned}(S_{\text{CEM}})_{+} &= 1.02003 \pm 0.00013 & (\chi^2/\text{ndf} = 15.3/14) \\ (\kappa)_{+} &= 0.0075 \pm 0.0005 & (\chi^2/\text{ndf} = 15.3/14)\end{aligned}$$

The  $\kappa$  fit results are consistent within their statistical uncertainty. The  $W \rightarrow e\nu$   $E/p$  CEM energy scale and  $\kappa$  fitted including both negatively charged and positively charged tracks (using templates generated by combining the sets of templates used for the above fits) is:

$$\begin{aligned}S_{\text{CEM}} &= 1.02012 \pm 0.00009 & (\chi^2/\text{ndf} = 17.3/14) \\ \kappa &= 0.0077 \pm 0.0004 & (\chi^2/\text{ndf} = 18.3/14)\end{aligned}$$

$(S_{\text{CEM}})_{-}$  and  $(S_{\text{CEM}})_{+}$  differ by approximately  $1.25\sigma$ , with the inclusive result being

approximately midway between them. The most likely cause of this difference is residual imperfections in the COT magnetic field modelling that still remain after track curvature corrections have been applied. Statistical fluctuations alone are also a plausible explanation for the difference. Though such imperfections should be corrected, their effect on the CEM energy scale calibration tends to cancel when fitting both negatively and positively charged tracks simultaneously (as can be observed in this case) and thus such corrections were not pursued as part of this calibration.

### 9.3.4 UCL Particle-by-Particle Calorimeter Non-Linearity

It is possible that the calorimeter energy scale, the ratio of the reconstructed energy measured in the CEM to the true energy of electrons, varies as a function of the electron energy itself. This is the calorimeter energy scale non-linearity, usually referred to simply as the non-linearity. The non-linearity could potentially arise from a number of physical sources. The most likely source is that light from higher energy showers travels less distance to the PMT than light from lower energy showers because higher energy showers peak at greater depths than lower energy showers and thus light from higher energy showers is less affected by absorption in the ageing wavelength shifting fibres that it passes through. This source would depend on the energy of the individual incident particles and not the reconstructed energy; thus we apply the non-linearity to the energy of particles before simulating clustering. Two potential sources of non-linear CEM response, absorption of energy in the TOF and solenoid coil and longitudinal leakage of energy into the hadronic calorimeter, are explicitly modelled by our simulation and thus are not expected to contribute significantly to the non-linearity. (Though any minor residual mis-modelling of these effects may be absorbed into the non-linearity.)

The  $E/p$  distribution split into individual 2.5 GeV  $E_T$  slices (where  $E$  and  $E_T$  are the reconstructed energy and reconstructed transverse energy respectively) is sensitive to any possible non-linearity. To fit a non-linearity on a per-particle basis it is necessary to replace the normal template fitting procedure with a specific non-linearity fitting procedure as outlined here. In the simulation the reconstructed transverse energy of an electron comprises the transverse energy of all the particles that are clustered to form

that electron. If we apply a first order per-particle non-linearity then the reconstructed energy of a cluster is:

$$E_T = \sum_i (a + b \times E_T^{e,\gamma}) E_T^{e,\gamma} \quad (9.2)$$

where  $E_T^{e,\gamma}$  are the transverse energies of  $i$  individual electrons/photons in the cluster,  $a$  is a linear scale factor (however as it is fitted as part of the non-linearity it is referred to as the non-linearity scale) and  $b$  is a non-linearity slope factor. This can be rewritten as:

$$E_T = a \sum_i E_T^{e,\gamma} + b \sum_i (E_T^{e,\gamma})^2 \quad (9.3)$$

High statistics sets of  $W \rightarrow e\nu$  and  $Z \rightarrow e^+e^-$  pseudo-data are generated using UCL Fast Simulation, recording for each simulated cluster  $\sum_i E_T^{e,\gamma}$  and  $\sum_i (E_T^{e,\gamma})^2$  (and also  $p_T$ ) thus allowing for the reconstructed transverse energies of electrons (and thence the  $E/p$  values of such electrons) to be re-computed as functions of non-linearity scale and slope. (The random smearing factor applied to re-computed energies is identical to that used in the original simulation, as is the underlying energy added to them.) The simulated  $E/p$  distributions for each  $E_T$  slice within the range of  $E_T$  values allowed by cuts can thus be calculated as a function of non-linearity scale and slope too. These distributions are then compared to their data equivalents for both  $W$  and  $Z$  events. The comparisons are made within the range  $0.9 < E/p < 1.1$ . The  $\chi^2$  for each slice is calculated. The values of the non-linearity slope and scale are estimated as those values that give the minimum aggregate  $\chi^2$  for all  $E_T$  slices for both  $W$  and  $Z$  events within a two dimensional slope and scale parameter space. The non-linearity is then applied on a per-particle basis to simulated events.

A particle-by-particle non-linearity fit was performed using data that incorporated the tower-by-tower CEM energy scale corrections. The values of the non-linearity scale and slope factor obtained are:

$$a = 0.99921 \pm 0.00009 \quad (\chi^2/\text{ndf} = 223.6/160)$$

$$b = 0.000385 \pm 0.000009 \text{ GeV}^{-1}$$

As  $a$  and  $b$  are fit simultaneously, they share a single  $\chi^2/\text{ndf}$  value. The  $\chi^2/\text{ndf}$  achieved is relatively poor, this probably indicates imperfect modelling of the fitted  $E_T$  slice  $E/p$  distributions. One source of mis-modelling in these distributions is that no backgrounds are added. Ideally an  $E_T$ -dependent background contribution should be added to each slice, however such backgrounds have not been generated. Not adding backgrounds may be the source of the poor  $\chi^2/\text{ndf}$  obtained. Figures 9.5 and 9.6 are comparisons of the best fit simulation pseudo-data and data  $E/p$  distributions for individual  $E_T$  slices for  $W$  events and  $Z$  events respectively. Figure 9.7 compares the mean  $E/p$  of each  $E_T$  slice for data, best fitting simulation pseudo-data and simulation pseudo-data with zero non-linearity applied; this is a control distribution for the particle-by-particle non-linearity fit. Figure 9.8 makes the same comparison by plotting the ratio of the mean data  $E/p$  of each  $E_T$  slice to the mean simulation  $E/p$  of each  $E_T$  slice, for both the best fit simulation pseudo-data and the simulation pseudo-data with zero non-linearity applied. Both figures show  $W$  events and  $Z$  events on separate plots.

In fig. 9.8 it can clearly be seen that the  $W$  event results for the best fit non-linearity are aligned to one to a high degree of accuracy, while the  $Z$  event results are almost entirely below one (and not as accurately aligned). This indicates that this fit is dominated by the internal substructure (with respect to  $E_T$ ) of the  $W$  events (i.e. the slope required to fit the difference in energy scale across the range of  $W$  event  $E_T$  slices); applying this non-linearity flattens out that internal substructure (and to a limited extent the substructure of the  $Z$  events) but does not resolve the essential difference between  $W$  and  $Z$  events. (This essential difference between  $W$  and  $Z$  events is that they require a different  $E/p$  CEM energy scale; this is visible in fig. 9.8(b) where the ratio of best fitting pseudo-data to data is significantly less than one for the majority of the  $E_T$  slices considered.)

The value of non-linearity slope given above differs by  $1.1\sigma$  from the value (of  $b = 0.000375 \text{ GeV}^{-1}$ ) used in the simulation prior to this set of non-linearity fits. This prior value was actually the value used to generate the energy scale templates used in section 9.3.5; the use of this older value was accidental. Testing showed that setting  $b = 0$  had little effect on either the measured  $W \rightarrow e\nu$   $E/p$  CEM energy scale or

$Z \rightarrow e^+e^-$  mass CEM energy scale and thus the dependence of the measured  $Z$  mass on the non-linearity slope is very weak; thus the effect of this mistake on the fits in the aforementioned section was estimated to be negligible. The logarithmic non-linearity slope calculation in section 9.4.1 uses the correct value of  $b = 0.000385 \text{ GeV}^{-1}$  from the set of fits presented in this section.

### 9.3.5 CEM Energy Scale Results

As discussed above, the templates used for the fits presented in this section use UCL Fast Simulation with a non-linearity slope parameter of  $b = 0.000375 \text{ GeV}^{-1}$  and a material scale of  $S_{\text{mat}} = 1.0025$ . The data used in the fits in this section includes the tower-by-tower energy scale corrections given in section 9.3.1.

The  $W \rightarrow e\nu$   $E/p$  CEM energy scale fit results are:

$$S_{\text{CEM}} = 1.02010 \pm 0.00009 \quad (\chi^2/\text{ndf} = 19.2/14)$$

$$\kappa = 0.0072 \pm 0.0004 \quad (\chi^2/\text{ndf} = 18.6/14)$$

Figure 9.1 is a comparison of the best fitting template to data for this fit.

As a consistency check an  $E/p$  CEM energy scale fit was also performed using  $Z \rightarrow e^+e^-$   $E/p$  templates and data. The fitted value of  $Z \rightarrow e^+e^-$   $E/p$  CEM energy scale is:

$$S_{\text{CEM}} = 1.01913 \pm 0.00031 \quad (\chi^2/\text{ndf} = 10.4/14)$$

$$\kappa = 0.0072 \pm 0.0013 \quad (\chi^2/\text{ndf} = 10.6/14)$$

There is a  $3.0\sigma$  discrepancy between this result and the standard  $W \rightarrow e\nu$   $E/p$  energy scale result.

The blinded  $Z \rightarrow e^+e^-$  mass CEM energy scale fit results are:

$$S_{\text{CEM}} = 1.01882 \pm 0.00023 \quad (\chi^2/\text{ndf} = 78.5/78)$$

$$\kappa = 0.0140 \pm 0.0007 \quad (\chi^2/\text{ndf} = 78.4/78)$$

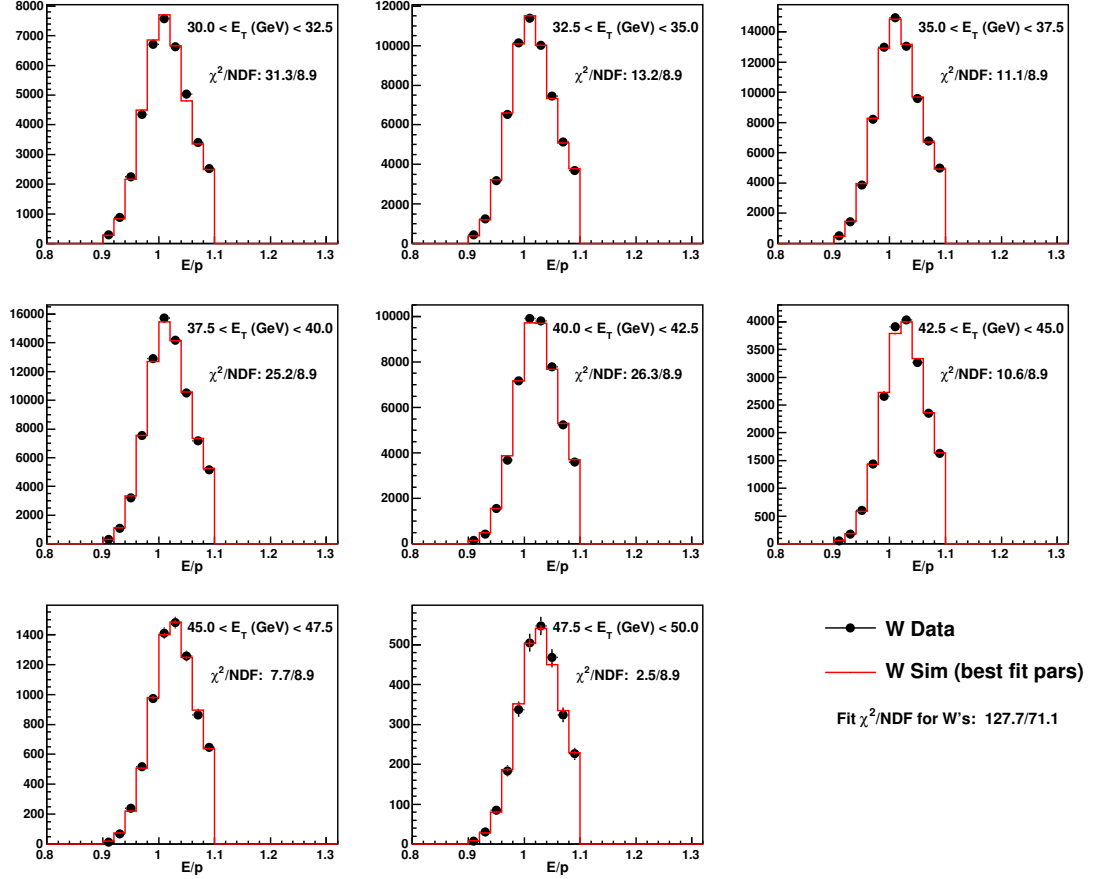


Figure 9.5: The particle-by-particle non-linearity best fit simulation pseudo-data and data  $E/p$  distributions of individual  $E_T$  slices for  $W$  events. The  $y$  variable is number of events per 0.02 units  $E/p$ . No background is added. The  $\chi^2$  of individual slices is calculated in the region  $0.9 < E/p < 1.1$ . The fit estimates the non-linearity slope parameter and an energy scale by minimising the combined total  $\chi^2$  of all the  $E_T$  slices in the range  $30 < E_T < 50$  GeV for  $W$  events (as shown in this figure) and  $30 < E_T < 55$  GeV for  $Z$  events (see fig. 9.6). The total number of degrees of freedom of the fit is the total number of bins considered (180) in the fit subtracting one for each  $E_T$  slice considered in the fit (for the normalisation of that slice) and subtracting two for the number of parameters being estimated; the total number of degrees of freedom of the fit is thus calculated as 160. We calculate the number of degrees of freedom of each of the individual  $E_T$  slices by dividing the total number of degrees of freedom of the fit by the number of slices being considered (18) and calculate the total number of degrees of freedom of a channel as the sum of the numbers of degrees of freedom of all of the individual  $E_T$  slices from that channel. Thus the number degrees of freedom of individual slices and the total number of degrees of freedom for all  $W$  events slices are fractional, however the total number of degrees of freedom for the  $W$  and  $Z$  event slices combined is an integer (160).

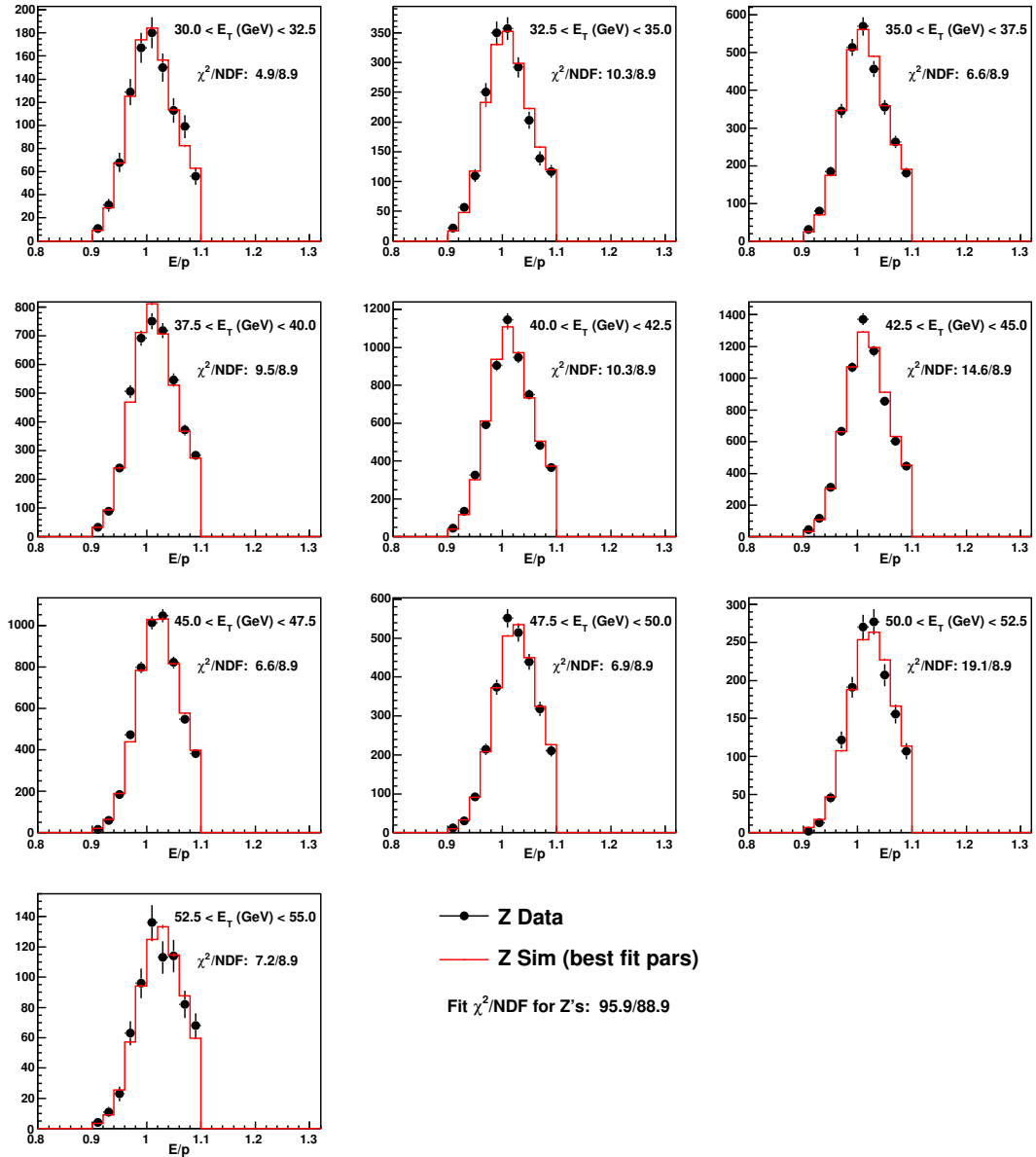
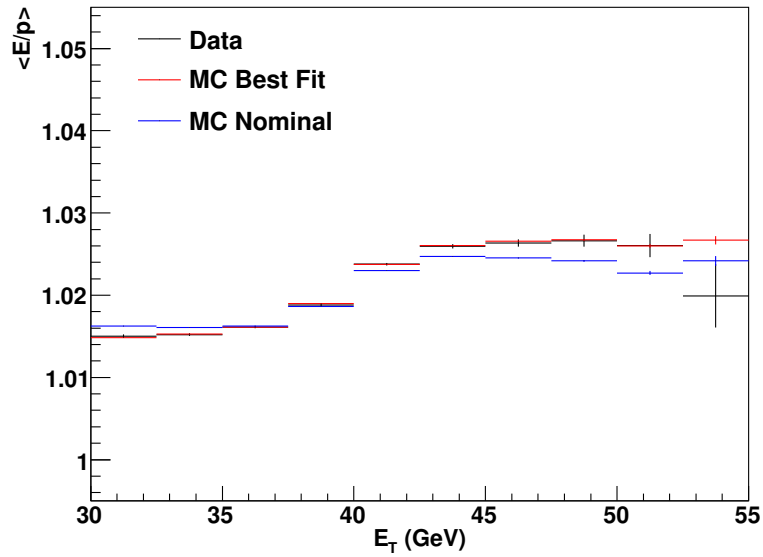
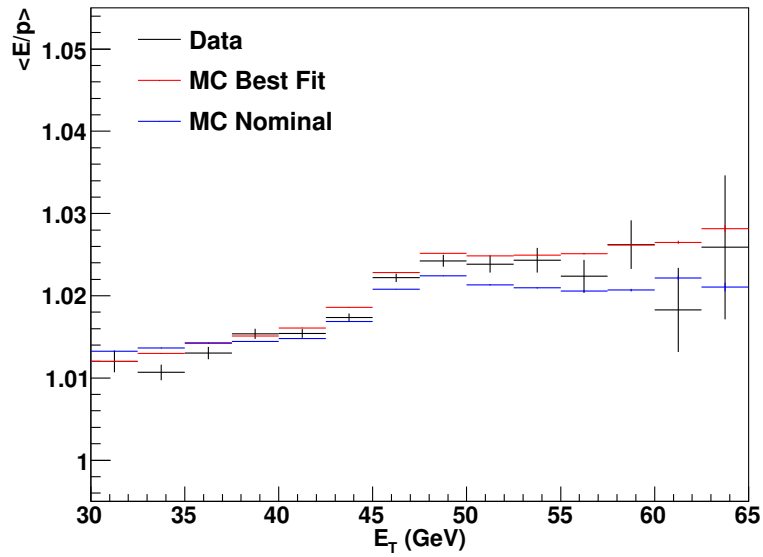


Figure 9.6: The particle-by-particle non-linearity best fit simulation pseudo-data and data  $E/p$  distributions of individual  $E_T$  slices for  $Z$  events. The  $y$  variable is number of events per 0.02 units  $E/p$ . No background is added. The  $\chi^2$  of individual slices is calculated in the region  $0.9 < E/p < 1.1$ . The fit estimates the non-linearity slope parameter and an energy scale by minimising the combined total  $\chi^2$  of all the  $E_T$  slices in the range  $30 < E_T < 50$  GeV for  $W$  events (see fig. 9.5) and  $30 < E_T < 55$  GeV for  $Z$  events (as shown in this figure). The number degrees of freedom of individual slices and the total number of degrees of freedom for all  $Z$  event slices are fractional, however the total number of degrees of freedom for the  $W$  and  $Z$  event slices combined is an integer (160) (see the caption of fig. 9.5 for further explanation).

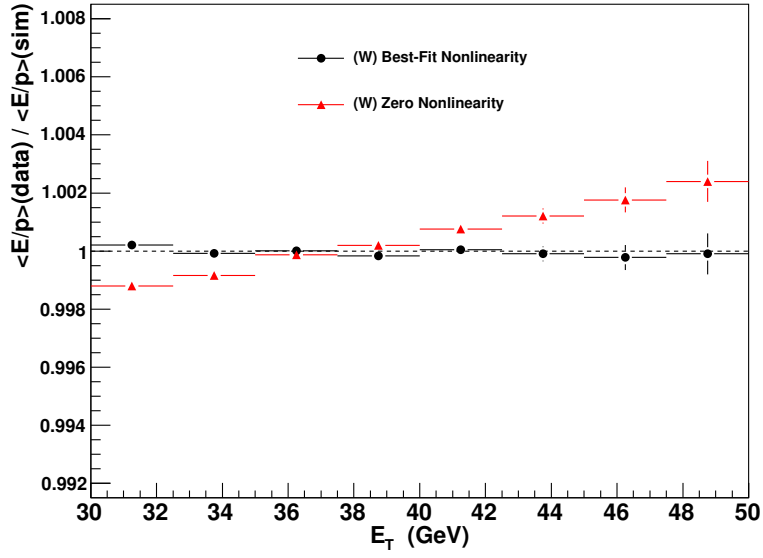


(a)

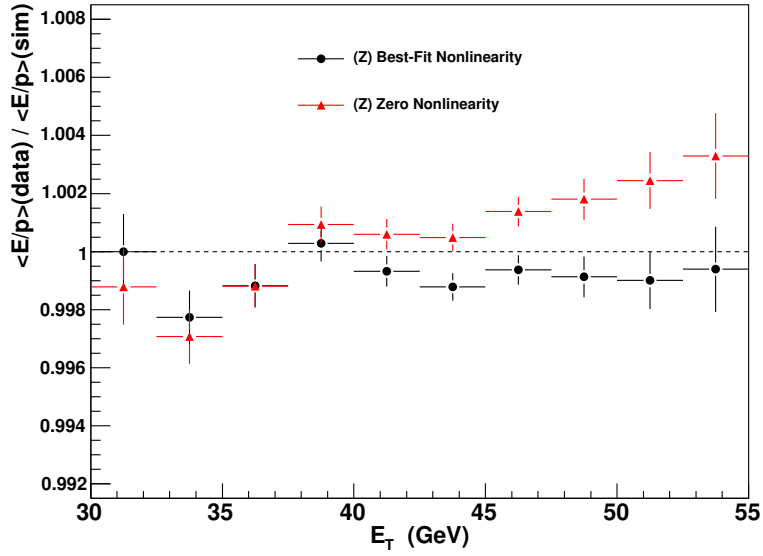


(b)

Figure 9.7: Mean  $E/p$  of each  $E_T$  slice plotted against slice  $E_T$  for  $W$  events (a) and  $Z$  events (b); this is a control distribution for the particle-by-particle non-linearity fit. Values are plotted for data, the best fitting simulation pseudo-data ('MC Best Fit') and simulation pseudo-data with zero non-linearity applied ('MC Nominal').



(a)



(b)

Figure 9.8: Ratio of the mean  $E/p$  of each  $E_T$  slice for simulation pseudo-data to that for data plotted against slice  $E_T$  for  $W$  events (a) and  $Z$  events (b); this is a control distribution for the particle-by-particle non-linearity fit. Values are plotted using the best fitting simulation pseudo-data ('Best-Fit Nonlinearity') and simulation pseudo-data with zero non-linearity applied ('Zero Nonlinearity').

Figure 9.2 is a comparison of the best fitting template to data for this fit. Combining the  $W \rightarrow e\nu$   $E/p$  CEM energy scale fit result and the  $Z \rightarrow e^+e^-$  mass CEM energy scale fit result gives a blinded measurement of the  $Z$  mass of:

$$\Delta(m_Z) = -116.7 \pm 22.5 \text{ MeV}/c^2$$

where the error is calculated by combining the statistical error on both scale fits using standard error propagation techniques. (The negative sign indicates we are measuring a  $Z$  mass that is less than the world average.) Given the range of the blinding, this shows an inconsistency of between  $1.85\sigma$  and  $8.52\sigma$  with the world average. As the measured  $Z$  mass was inconsistent with the world average by more than  $1\sigma$  even for the most favourable value of the blinding, it was decided further blinded energy scale fits should be performed after modifying the modelling of the leakage, coil energy loss and non-linearity. This is detailed in the next section.

## 9.4 Analysis using Duke Leakage, Coil Energy Loss and Non-Linearity Models

### 9.4.1 Duke Particle-by-Particle Calorimeter Non-Linearity with a Logarithmic Form

Duke Fast Simulation uses a particle-by-particle non-linearity that varies logarithmically with the energy of the incident particle [1, 85]. It is based on GEANT4 test beam studies of the calorimeter the Duke group have performed. This ‘Duke’ non-linearity is only applied directly to electrons. The Duke non-linearity for electrons (as a scale factor correction) is:

$$(\Delta S)_{\text{non-linearity}} = c \log(E_T/p) \tag{9.4}$$

where  $c$  is a non-linearity slope parameter and  $p$  is the non-linearity pivot. This non-linearity can be related to the ‘linear’ non-linearity previously used by UCL Fast Simulation by Taylor expanding around the pivot; this allows us to relate the logarithmic

non-linearity slope  $c$ , to the linear non-linearity slope  $b$  by the relation  $c = bp$ . It is assumed that all photons are converted to electron-positron pairs by pair production and this conversion is explicitly simulated; the Duke non-linearity is then applied to the electrons and positrons created individually and the resultant  $\Delta S$  values combined additively to produce an overall scale factor correction to apply to the photon.

We replace our default non-linearity in UCL Fast Simulation with the Duke non-linearity. We combined the Duke non-linearity additively with the Duke leakage and coil energy loss scaling factor to produce a combined Duke leakage, coil energy loss and non-linearity scale factor  $S_{\text{comb}}$ , that is applied on a particle-by-particle basis:

$$S_{\text{comb}} = 1 + (\Delta S)_{\text{leakage/coil energy loss}} + (\Delta S)_{\text{non-linearity}} \quad (9.5)$$

We use the linear non-linearity slope fitted in section 9.3.4 ( $b = 0.000385 \text{ GeV}^{-1}$ ) to calculate a slope parameter for the Duke non-linearity using  $c = bp$ , with  $p = 36.9 \text{ GeV}$  (this pivot value being set as the roughly the average energy of primary electrons in simulated  $W \rightarrow e\nu$  events before clustering). This calculation yields  $c = 0.0142$ .

#### 9.4.2 Duke Leakage and Coil Energy Loss Model

Duke Fast Simulation uses a leakage model based on GEANT4 test beam studies of the calorimeter the Duke group have performed [86, 87]. The leakage is characterised by  $f_l$ , the fraction of the energy of an incident particle leaking from the CEM to the hadronic calorimeter. The leakage is only applied directly to electrons. For a 50 GeV electron incident on calorimeter tower 0,  $f_l$  is sampled from the gamma distribution  $\Gamma(x) = x^5 e^{-x}$ , where  $x = (\log(f_l) - \mu)/\sigma$  (where  $\mu$  and  $\sigma$  are the mean and standard deviation respectively of distributions generated in GEANT4 test beam studies for this particular energy and calorimeter tower). For electrons with different incident electron energies and/or incident on different calorimeter towers the same basic distribution is sampled from (the distribution for a 50 GeV electron incident on calorimeter tower 0) but the sampled  $f_l$  is then modified by adding a correction factor that depends upon the incident energy of the electron and the thickness of the CEM calorimeter tower it

was incident upon. This correction factor is given by:

$$\Delta \log_{10} f_l = 0.125 \times \log_2 \left( \frac{E}{50 \text{ GeV}} \right) - 0.075 \times \Delta(x_0/0.59) \quad (9.6)$$

where  $E$  is the incident energy of the electron and  $x_0$  the thickness in radiation lengths of the CEM tower it was incident upon. The  $x_0$  is taken from a table compiled by the Duke group and corrected for the thickness of material the particle passes through upstream of the CEM front-plate. For electrons with  $E < 50$  GeV a further correction is additionally applied to the sampled  $f_l$ . This further correction  $(\Delta \log_{10} f_l)_{\text{LE}}$  is sampled from a Gaussian with a mean  $\mu_G = 0.2z$  and a standard deviation  $\sigma_G = 0.17z$ , where  $z = |\log_{10}(E/50 \text{ GeV})|$ . It is then applied alongside the first correction thus:

$$\log_{10} f_l = \log_{10}(f_l)_{\text{sampled}} + \Delta \log_{10} f_l + (\Delta \log_{10} f_l)_{\text{LE}} \quad (9.7)$$

The amount of light produced by the scintillators in the CEM (thus the measured energy of particles) is proportional (to first order) to the quantity of energy deposited in those scintillators  $E_s$ . The fraction of the total energy deposited in the calorimeter that is deposited in those scintillators is the scintillator sampling fraction  $f_s = E_s/[E(1 - f_l)]$ .  $f_s$  is dependent on the leakage; this variation is modelled by a (tower geometry dependent) parameterisation of test beam pseudo-data to generate a correction to the detected energy of particles in the CEM. This correction is applied as an additional multiplicative scaling to the leakage fraction  $f_l$ . (Even though  $f_s$  is not actually a form of leakage it is convenient to include it in  $f_l$  as it depends upon the true leakage fraction.)

For photons  $f_l$  is calculated by first generating a conversion to an electron-positron pair by pair production then calculating individual  $f_l$ 's for both the electron and positron. The overall leakage fraction for the photon is then calculated thus:

$$f_l = (E_+ f_{l+} + E_- f_{l-})/E \quad (9.8)$$

where  $f_+/f_-$  and  $E_+/E_-$  are respectively the individual leakage fraction and individual

energy of the positron/electron.

Duke Fast Simulation also models energy loss in the solenoid coil (and other material between the active volume of the COT and the active volume of the CEM) using a parameterisation based on GEANT4 test beam studies of the calorimeter. This model includes the variations of such energy loss with tower geometry and is different for electrons and photons. This model calculates  $f_c$ , the fraction of a particle's energy lost in the solenoid coil (and other material between the active volume of the COT and the active volume of the CEM) for each particle. This is combined additively with the leakage fraction to produce  $(\Delta S)_{\text{leakage/coil energy loss}} = f_c + f_l$  and then applied on a particle-by-particle basis in conjunction with the non-linearity (as described in section 9.4.1).

We replace our default leakage and coil energy loss models with their Duke equivalents.

### 9.4.3 Tower-by-Tower Energy Scale and $\kappa$ Fits

A set of tower-by-tower  $W \rightarrow e\nu$   $E/p$  CEM energy scale fits (as described in section 9.1) were performed. The templates were generated using the Duke leakage, coil energy loss and non-linearity models. (For historical reasons, the value of the non-linearity slope parameter used to generate these templates was not the value calculated in section 9.4.1 but instead  $c = 0.0052$ . This applies only to these templates; templates for fits described in subsequent sections use the value given in section 9.4.1. The effect of this on the results obtained is believed to be negligible.) The results of these fits are presented in table 9.2. The baseline data is the same as used in section 9.3.1. The energy scales were applied as corrections to both the  $W$  and  $Z$  datasets; as they are a parameterisation of the calorimeter resolution, the  $\kappa$  values cannot be applied as corrections to data. The tower-by-tower  $W \rightarrow e\nu$   $E/p$  CEM energy scale fits were then repeated using the corrected data; the residual tower-by-tower energy scale variation was observed to be statistically insignificant.

Symmetrised Tower Number	Fitted CEM Energy Scale	Statistical Uncertainty on CEM Energy Scale	Fitted CEM $\kappa$	Statistical Uncertainty on CEM $\kappa$	$\chi^2$ /ndf of Energy Scale Fit
0	1.04332	0.00032	0.00824	0.00110	15.4/14
1	1.04594	0.00023	0.00069	0.00134	24.6/14
2	1.04630	0.00023	0.00053	0.00136	25.7/14
3	1.04252	0.00024	0.00032	0.00132	27.9/14
4	1.04403	0.00026	0.00004	0.00201	14.0/14
5	1.04208	0.00029	0.00385	0.00235	9.4/14
6	1.04536	0.00031	0.00421	0.00185	22.6/14
7	1.04394	0.00036	0.01142	0.00104	10.9/14
8	1.05010	0.00048	0.01469	0.00128	6.5/14

Table 9.2: Tower-by-tower  $W \rightarrow e\nu$   $E/p$  CEM energy scale and CEM  $\kappa$  fit results using the Duke leakage, coil energy loss and non-linearity models. The baseline data is the same as used in section 9.3.1. The energy scales are applied as corrections to both the  $W$  and  $Z$  datasets. Note the poor  $\chi^2$ /ndf values obtained for towers 1, 2, 3 and 6; this may indicate mis-modelling of these particular towers in UCL Fast Simulation.

#### 9.4.4 CEM Energy Scale Results

The templates used for the fits presented in this section use UCL Fast Simulation with the Duke leakage, coil energy loss and non-linearity models with a logarithmic non-linearity slope parameter of  $c = 0.0142$  and a material scale of  $S_{\text{mat}} = 1.0025$ . The data used in the fits in this section includes the tower-by-tower energy scale corrections given in section 9.4.3.

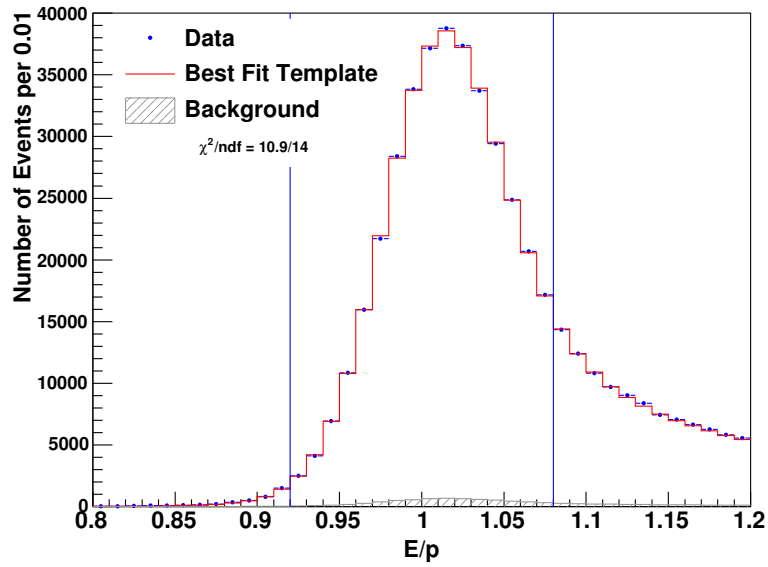
The  $W \rightarrow e\nu$   $E/p$  CEM energy scale fit results are:

$$S_{\text{CEM}} = 1.04463 \pm 0.00009 \quad (\chi^2/\text{ndf} = 11.2/14)$$

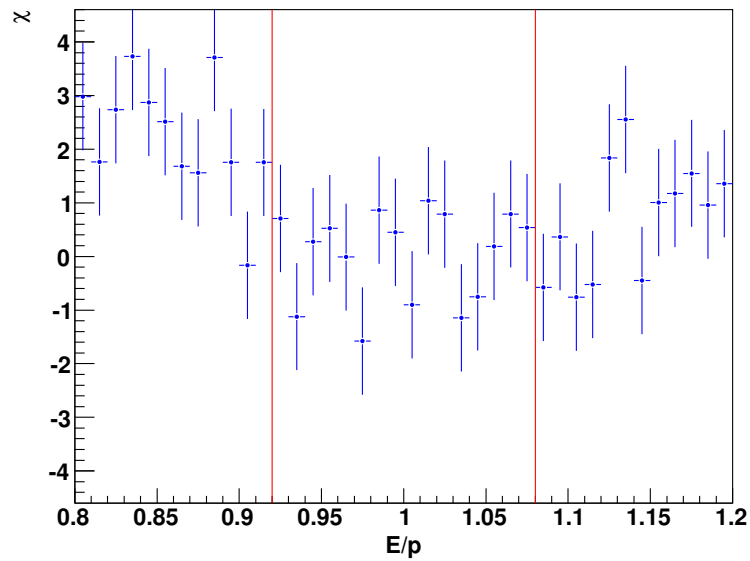
$$\kappa = 0.0032 \pm 0.0008 \quad (\chi^2/\text{ndf} = 11.2/14)$$

Figure 9.9 is a comparison of the best fitting template to data for this fit.

As a consistency check an  $E/p$  CEM energy scale fit was also performed using  $Z \rightarrow e^+e^-$   $E/p$  templates and data. The fitted value of  $Z \rightarrow e^+e^-$   $E/p$  CEM energy



(a)



(b)

Figure 9.9: The  $E/p$  distribution of the best fitting template from the  $W \rightarrow e\nu$   $E/p$  CEM energy scale fit compared to the equivalent data distribution (a) and the  $\chi$  distribution for this comparison (b). The templates are generated using the Duke leakage, coil energy loss and non-linearity models; the results of this fit are given in the text. A contribution from background is included in the template  $E/p$  distribution; this background contribution (normalised to the data) is also plotted as a separate histogram in (a).

scale is:

$$S_{\text{CEM}} = 1.04369 \pm 0.00031 \quad (\chi^2/\text{ndf} = 9.5/14)$$

$$\kappa = 0.0002 \pm 0.0033 \quad (\chi^2/\text{ndf} = 9.4/14)$$

Figure 9.10 is a comparison of the best fitting template to data for this fit. There is a  $2.9\sigma$  discrepancy between this energy scale result and the standard  $W \rightarrow e\nu$   $E/p$  energy scale result. It is very unlikely this discrepancy is entirely due to statistical fluctuations; there would appear to be some mis-modelling of either the  $Z \rightarrow e^+e^-$   $E/p$  distribution or the  $W \rightarrow e\nu$   $E/p$  distribution. It is very likely the discrepancy is either entirely due to such mis-modelling or due to a combination of such mis-modelling and statistical fluctuations.

The blinded  $Z \rightarrow e^+e^-$  mass CEM energy scale fit results are:

$$S_{\text{CEM}} = 1.04390 \pm 0.00027 \quad (\chi^2/\text{ndf} = 75.8/78)$$

$$\kappa = 0.0114 \pm 0.0015 \quad (\chi^2/\text{ndf} = 75.9/78)$$

Figure 9.11 is a comparison of the best fitting template to data for this fit. Combining the  $W \rightarrow e\nu$   $E/p$  CEM energy scale fit result and the  $Z \rightarrow e^+e^-$  mass CEM energy scale fit result gives a blinded measurement of the  $Z$  mass of:

$$\Delta(m_Z) = -66.6 \pm 26.0 \text{ MeV}/c^2$$

where the error is calculated by combining the statistical error on both scale fits using standard error propagation techniques. The consistency of this blinded measurement depends on the blinding offset. If the blinding offset is between  $-75$  MeV and  $-40.6$  MeV, this shows a measurement of the  $Z$  mass that is consistent with the world average. Other values of the blinding offset will give  $Z$  mass measurements that are inconsistent with the world average; the inconsistency will range linearly from  $1\sigma$  for a blinding offset of  $-40.6$  MeV to  $5.45\sigma$  for a blinding offset of  $+75$  MeV. Due to the possible consistency with the world average  $Z$  mass it was decided to unblind.

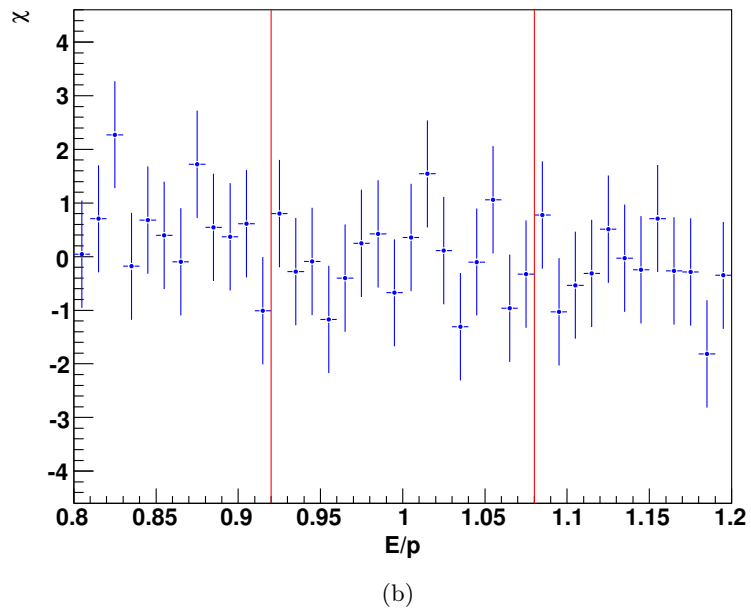
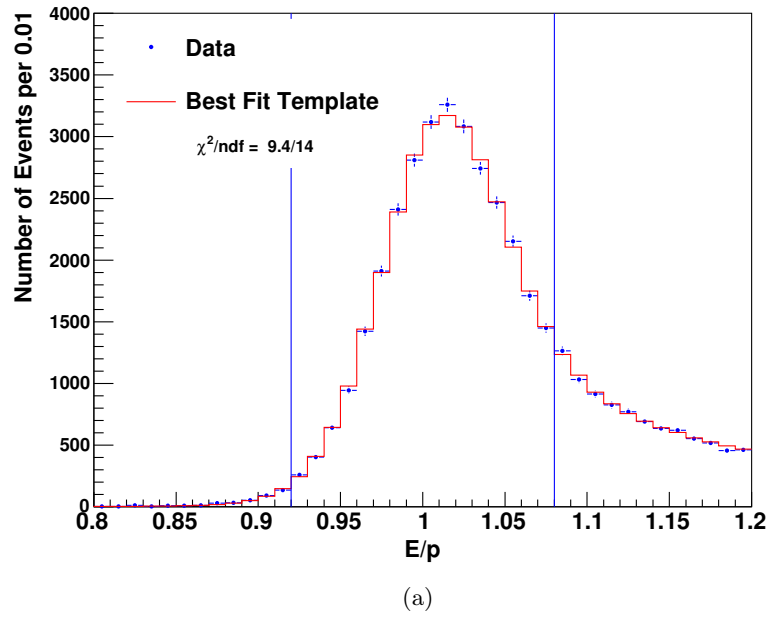
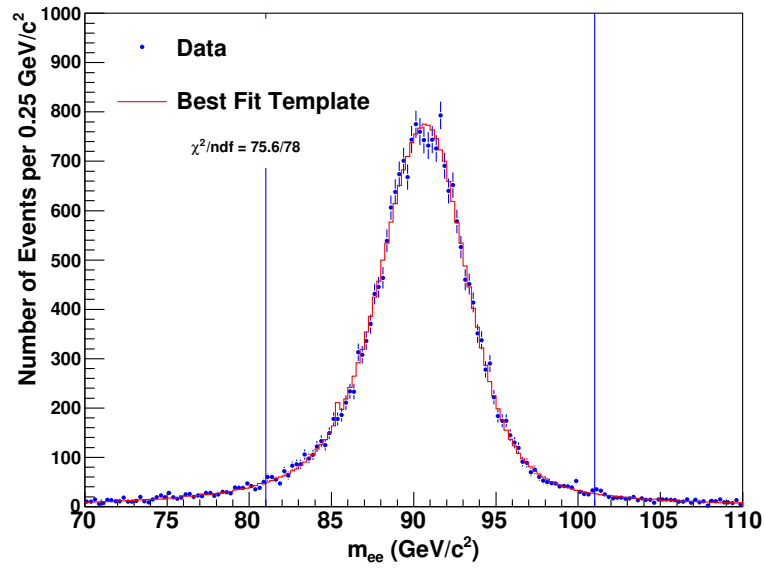
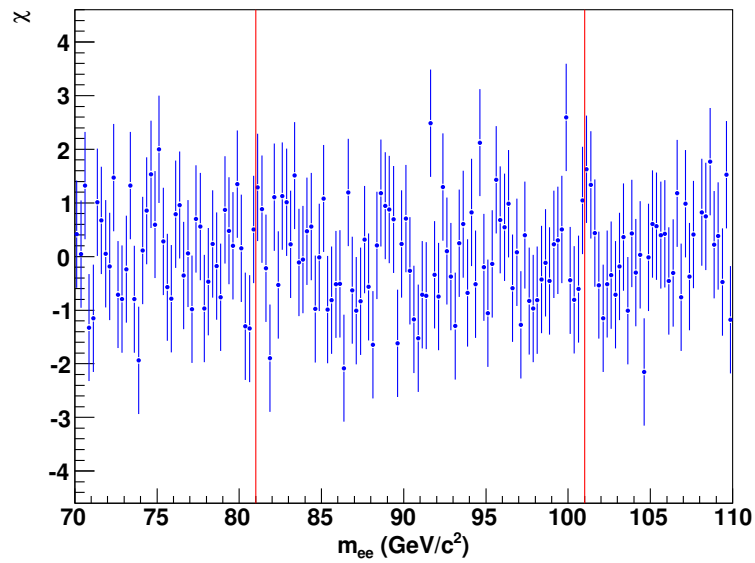


Figure 9.10: The  $E/p$  distribution of the best fitting template from the  $Z \rightarrow e^+e^- E/p$  CEM energy scale fit compared to the equivalent data distribution (a) and the  $\chi$  distribution for this comparison (b). The templates are generated using the Duke leakage, coil energy loss and non-linearity models; the results of this fit are given in the text. No background is added to this distribution;  $Z \rightarrow e^-e^+$  backgrounds are negligible.



(a)



(b)

Figure 9.11: The  $m_{ee}$  distribution of the best fitting template from the  $Z \rightarrow e^+e^-$  mass CEM energy scale fit compared to the equivalent data distribution (a) and the  $\chi$  distribution for this comparison (b). The templates are generated using the Duke leakage, coil energy loss and non-linearity models; the results of this fit are given in the text. No background is added to this distribution;  $Z \rightarrow e^+e^-$  backgrounds are negligible.

## 9.5 Final CEM Energy Scale Calibration Results

As the  $Z$  mass measured in section 9.4.4 was consistent for some values of the blinding, it was decided this result was satisfactory and should be unblinded. Thus the final result uses the Duke leakage, coil energy loss and non-linearity models with a logarithmic non-linearity slope parameter of  $c = 0.0142$  and a material scale of  $S_{\text{mat}} = 1.0025$  (and the tower-by-tower data corrections of section 9.4.3). The  $E/p$  CEM energy scale fits (both the standard fit using  $W \rightarrow e\nu$  events and the fit using  $Z \rightarrow e^+e^-$  events) are not blinded, thus the results are those given in section 9.4.4.

The final unblinded  $Z \rightarrow e^+e^-$  mass CEM energy scale fit results are:

$$S_{\text{CEM}} = 1.04390 \pm 0.00027 \quad (\chi^2/\text{ndf} = 75.8/78)$$

$$\kappa = 0.0113 \pm 0.0015 \quad (\chi^2/\text{ndf} = 75.9/78)$$

Notice this the same fit as given in section 9.4.4 with the blinding removed. (Thus fig. 9.11 is a comparison of the best fitting template to data for this fit.) Upon unblinding it became clear there was a mistake in the blinding code and the blinding offset had been applied to  $\kappa$  and not  $S_{\text{CEM}}$ . (Thus in effect the blinding offset on  $S_{\text{CEM}}$  was zero.) Since this was only discovered after removing the blinding, the analysis was still effectively blinded as we *believed* there to be a blinding offset applied. Combining the  $W \rightarrow e\nu$   $E/p$  CEM energy scale fit result and the  $Z \rightarrow e^+e^-$  mass CEM energy scale fit result gives an unblinded measurement of the  $Z$  mass of:

$$\Delta(m_Z) = -66.6 \pm 26.0 \text{ MeV}/c^2$$

where the error is calculated by combining the statistical error on both scale fits using standard error propagation techniques. This value is inconsistent with the world average value by  $2.56\sigma$ . This inconsistency could be due to a statistical fluctuation, however given its magnitude it is likely this inconsistency is due to either residual mis-modelling of the data by UCL Fast Simulation or a combination of residual mis-modelling and a statistical fluctuation. Possible causes of this inconsistency are discussed in the next

section.

## 9.6 Possible Causes of the Inconsistent $Z$ Mass Measurement

Possible causes of the discrepancy between the measured  $Z$  mass and the world average are:

- Statistical fluctuations: the discrepancy in the  $Z$  mass measurement is not so large that statistical fluctuations alone are an implausible explanation. It is also possible that statistical fluctuations are the cause of part of the discrepancy, with some other effect causing the remainder of the discrepancy.
- Backgrounds: as no backgrounds are applied to  $Z$  fits, backgrounds are in principle a possible cause of the discrepant  $Z$  mass measurement; however investigation has shown the effect of a plausible degree of mis-modelling of the backgrounds is almost negligible, so it seems very unlikely that this is the case.
- QED corrections in HORACE: it is possible that the modelling of QED corrections by HORACE is inaccurate. The modelling of QED corrections has been thoroughly validated by other members of the CDF  $W$  mass working group, so it seems unlikely to be the source of the  $Z$  mass discrepancy. Given the complexity of these corrections, further validation of them is beyond the scope of this thesis.
- COT modelling: UCL Fast Simulation does not model individual hits within the COT. This could lead to mis-modelling of the momentum measurement of electrons, however it is unclear how this would generate a discrepancy in the  $Z$  mass measurement.
- Curvature corrections: UCL Fast Simulation models the effect of the finite beam spot size on beam constrained momentum measurements. If Bremsstrahlung occurs in the silicon tracker the ‘kink’ in the electron’s track will reduce the accuracy of the beam constrained momentum measurement; this is also modelled in UCL

Fast Simulation. The same effect may also occur when Bremsstrahlung occurs in the COT, however in this case its exact effect depends on how many of the COT hits are before/after the kink and how the fitting algorithm interprets this. An ad-hoc model of this is used in UCL Fast Simulation; there are some doubts as to the veracity of this model. As the measurement of momentum is vital to accurate  $E/p$  energy scale calibrations, mis-modelling of this effect could be the cause of the discrepancy in the  $Z$  mass measurement. Investigations indicate that further adjustment of the current parameterisation of this would not have a major impact on the measured  $Z$  mass but is possible a completely new parameterisation of this effect is required to model it accurately.

- Energy loss in the COT and silicon tracker: the modelling of pair production and Bremsstrahlung has been extensively validated while the effect of Compton scattering is estimated to be negligible (the magnitude of the uncertainties estimated for pair production modelling is small for gross changes in the model and the effect of pair production is expected to be considerably greater than that of Compton scattering) and ionisation should affect electrons in  $W$  and  $Z$  events almost equally; thus it seems unlikely the modelling of any of these is the cause of the discrepant  $Z$  mass measurement. It is possible that there are problems with the accuracy of our material map.
- Leakage and coil energy loss modelling: the Duke models of leakage and coil energy loss were based on extensive GEANT4 modelling of the calorimeter, however it is possible there remains some residual mis-modelling of these effects or that these models have been incorrectly translated to UCL Fast Simulation.
- Non-linearity: the average energy of primary electrons in  $Z$  events is higher than in  $W$  events, thus increases in the non-linearity slope are naively expected to increase the difference in energy between  $Z$  and  $W$  events. This would increase the difference between the results of the two method of measuring the CEM energy scale. However investigation indicates that changing the non-linearity slope does not affect the measured  $Z$  mass significantly for either the linear or logarithmic

non-linearity models and so we conclude that naive expectations are not valid. For  $W \rightarrow e\nu$   $E/p$  energy scale fits a narrow  $E/p$  window is used, thus (generally) only events where the energy loss by the primary electron prior to reaching the calorimeter is small are used in this fit. Thus in this fit the main effect of the non-linearity is on the primary electron. However the non-linearity pivot value is set to the average energy (before recombination) of the primary electron in  $W$  events<sup>2</sup>, thus to first order the effect of non-linearity corrections on this fit will be minimal.

For  $Z \rightarrow e^+e^-$  mass energy scale fits a wider range of  $E/p$  values is accepted, thus events where the energy loss prior to arrival is large are used in this fit; for such events the non-linearity corrections applied to the secondary particles have a significant effect on the measured cluster energy. The average energies of  $Z$  event primary electrons will be greater than those of  $W$  events and thus greater than the pivot, however it appears that (aggregated over all the events included in the fit window) the increase in energy applied to the primary electron of  $Z$  events is cancelled out by the energy removed from secondary particles (which will have energies below the pivot) and thus the overall effect of the non-linearity corrections on this fit is small. For the linear UCL non-linearity testing shows the  $Z \rightarrow e^+e^-$  mass energy scale does not shift when the non-linearity is turned on/off entirely; the  $W \rightarrow e\nu$   $E/p$  energy scale is also very insensitive to gross changes in the linear non-linearity slope value. For the logarithmic non-linearity both the  $W \rightarrow e\nu$   $E/p$  energy scale and the  $Z \rightarrow e^+e^-$  mass energy scale vary weakly with the non-linearity slope, however this variation approximately cancels out in comparisons between the two scales (even for a gross 50% change in the non-linearity slope). However turning the logarithmic non-linearity on/off entirely changes the measured  $Z$  mass by about 10 MeV/c<sup>2</sup> (turning the logarithmic non-linearity off increases the  $Z$  mass discrepancy).

---

<sup>2</sup>A non-linearity pivot is used in both the linear UCL non-linearity and the logarithmic Duke non-linearity. For the linear non-linearity it is a technical detail used to ensure the value of the non-linearity scale  $a$  does not deviate significantly from 1 and is not fundamental to the physics model; thus for simplicity it was omitted from the description of the linear UCL non-linearity given in section 9.3.4.

Thus overall it appears that further tuning of the non-linearity scale, perhaps fitting the non-linearity slope value specifically for the Duke non-linearity, might fine tune the CEM energy scale but it is unlikely an error in the non-linearity slope value is the cause of the discrepant measurement of the  $Z$  mass. It also appears unlikely that returning to the linear non-linearity and altering the non-linearity slope could improve the accuracy of the  $Z$  mass measurement. It is possible a further tweaking of the form of the logarithmic parameterisation (perhaps changing how it treats low energy particles) could improve the accuracy of the  $Z$  mass measurement.

- Smearing: there is a large discrepancy in the  $\kappa$  values obtained from  $E/p$  and  $Z \rightarrow e^+e^-$  mass fits. The reason for this is unknown but is possibly due to the mis-modelling of smearing in either the calorimeter or COT. The  $\chi^2/\text{ndf}$  values achieved in energy scale and  $\kappa$  fits are satisfactory; thus it does not seem that any mis-modelling of smearing effects is distorting the shape of the  $E/p$  distribution. Hence it seems unlikely that any such mis-modelling of smearing is the cause of the discrepant measurement of the  $Z$  mass. However it is possible the discrepant  $\kappa$  values are due to some major unknown flaw in the simulation; in this case the same flaw might be the cause of the discrepant measurement of the  $Z$  mass.
- Underlying energy: the same underlying energy correction is used for  $Z$  and  $W$  events, specifically that derived from  $W$  data. It is possible there is a non-negligible difference in the underlying energy distribution of  $W$  and  $Z$  events due to the differing selection cuts of the two event samples thus using the same correction for  $Z$  events as  $W$  events does not correctly model the underlying event energy and causes the discrepant measurement of the  $Z$  mass observed. However this is thought to be unlikely as Duke Fast Simulation, which has successfully made a measurement of the  $Z$  mass consistent with the world average, also applies the same correction to  $W$  and  $Z$  events.
- Unknown bug in UCL Fast Simulation: a logical flaw in the simulation's application of one or more of the intended physics models is possible. The good  $\chi^2/\text{ndf}$

values achieved would appear to preclude any gross errors, but given the high level of precision we are attempting to achieve in the  $Z$  mass measurement even relatively minor bugs could be the cause of the discrepancy.

## Chapter 10

# Conclusions and $W$ Mass

## Measurement Results

### 10.1 Conclusions

Two possible models for Bremsstrahlung in UCL Fast Simulation have been considered, the GEANT4 4.9.0 and GEANT4 4.9.2 models. Both have been implemented in the simulation and the modelling validated against the respective versions of GEANT4 using test beam pseudo-experiments; this validation showed the implementation of both models to be satisfactory. The models differ in the low and high photon energy regions of the Bremsstrahlung photon emission energy spectrum. Comparison of the two models to data and tabulated theoretical results shows the GEANT4 4.9.2 model to be more accurate in the low energy region. The high energy region is complex and neither model fully captures the tabulated theoretical results for this region. We choose to use the GEANT4 4.9.2 model by default in UCL Fast Simulation. The systematic uncertainty arising from residual Bremsstrahlung mis-modelling was estimated by considering: different models of the soft photon region for which the LPM effect is significant and different models of the hard photon Bremsstrahlung spectrum. Aside from the sources of uncertainty considered, the UCL Fast Simulation model of Bremsstrahlung is believed to be robust and accurate.

Originally it was assumed that the entire CDF Run II silicon tracker was composed

of silicon for the purpose of calculating the Bremsstrahlung photon emission energy spectrum. As tests showed this was possibly inaccurate, it was decided to model each layer of the material map used (SiliMap) as a combination of two elements: either silicon and copper (for layers where elements heavier than silicon are indicated to be present) or silicon and beryllium (for layers where elements lighter than silicon are indicated to be present), based on the properties of the layer stored in the material map. The systematic uncertainties arising from two possible changes in the material description were estimated.

The combined systematic uncertainty on the  $W$  mass measurement from uncertainties in the modelling of Bremsstrahlung is  $6.2 \pm 3.2 \text{ MeV}/c^2$ . Note that this total does *not* include a larger systematic shift that is observed if a different two-element model using only copper and beryllium is employed. (The total systematic uncertainty *including* this larger systematic is  $14.1 \pm 3.7 \text{ MeV}/c^2$ .) Whether or not there remains a significant systematic uncertainty due to the material description requires further study: it is likely to be the case that this systematic difference is significantly reduced when the SVX-II hybrid layers are separately modelled as a mixture of heavy and light elements.

The GEANT 4.9.0 model of the pair production electron emission energy spectrum has been implemented in UCL Fast Simulation and validated using virtual test beam pseudo-experiments. We use a pair production total cross section taken directly from experimental data. The total systematic uncertainty on the  $W$  mass measurement from pair production was estimated as  $2.8 \pm 2.7 \text{ MeV}/c^2$ . The pair production model in UCL Fast Simulation is believed to be robust and accurate.

The CEM energy scale has been calibrated by two independent methods; two attempts at this calibration were made. The first attempt, that used the standard version of UCL Fast Simulation produced a blinded  $Z$  mass that was not consistent with the world average for any possible value of the blinding offset and thus was unsatisfactory. The second attempt used UCL Fast Simulation modified to include models of the leakage, coil energy loss and non-linearity taken from Duke Fast Simulation. This second attempt produced a blinded  $Z$  mass that was consistent with the world average for some possible values of the blinding offset, thus was satisfactory. This second measurement of

the  $Z$  mass was then unblinded; the unblinded  $Z$  mass differed from the world average by  $66.6 \pm 26.0$  MeV/ $c^2$ , a  $2.5\sigma$  discrepancy. Various reasons for this discrepancy have been discussed but the cause of the discrepancy remains unclear. While discrepant with the world average, this result shows there is no gross error in the modelling of the physics important to measuring the  $Z$  mass using UCL Fast Simulation. This is an independent cross-check of  $Z$  mass modelling for the second CDF Run II  $W$  mass analysis.

## 10.2 $W$ Mass Measurement Results

The  $W$  mass analysis was completed in early 2012 by the entire  $W$  mass analysis group [2, 4]. The default simulation for this analysis was Duke Fast Simulation but this thesis contributed important cross-checks which showed the robustness of the Bremsstrahlung and pair production models used in the analysis. The unblinded  $W$  mass measurement for the electron channel is:

$$m_W = 80406 \pm 25 \text{ MeV}/c^2$$

This value was obtained by combining the  $m_W$  values obtained from the transverse mass, electron transverse energy and reconstructed neutrino transverse momentum fits for the electron channel (taking into account correlations). The individual  $m_W$  values obtained are given in table 10.1; figs. 10.1 to 10.3 are comparisons of the best fitting templates to data for these fits (and their muon channel counterparts). The systematic uncertainties on  $m_W$  for each of these fits are given in table 10.2. The unblinded  $W$  mass measurement for the muon channel is:

$$m_W = 80374 \pm 22 \text{ MeV}/c^2$$

This value was obtained by combining the  $m_W$  values obtained from the transverse mass, muon transverse momentum and reconstructed neutrino transverse momentum fits for the muon channel (taking into account correlations). The individual  $m_W$  values

Charged Lepton	Kinematic Distribution	Fit Result (MeV)	$\chi^2/\text{ndf}$
Electron	Transverse Mass	$80408 \pm 19$	52/48
Electron	Electron $E_T$	$80393 \pm 21$	60/62
Electron	Neutrino $p_T$	$80431 \pm 25$	71/62
Muon	Transverse Mass	$80379 \pm 16$	57/48
Muon	Muon $p_T$	$80348 \pm 18$	58/62
Muon	Neutrino $p_T$	$80406 \pm 22$	82/62

Table 10.1: The individual  $m_W$  values fitted using the transverse mass, lepton transverse momentum and reconstructed neutrino transverse momentum distributions in the electron and muon channels for the second CDF Run II  $W$  mass measurement. The uncertainties quoted are the statistical uncertainties on the fits themselves. Values taken from reference [88].

obtained are given in table 10.1; figs. 10.1 to 10.3 are comparisons of the best fitting templates to data for these fits (and their electron channel counterparts). For brevity the systematic uncertainties for each of these fits are omitted from this thesis; they are given in reference [88]. The final combined  $W$  mass measurement using both channels is:

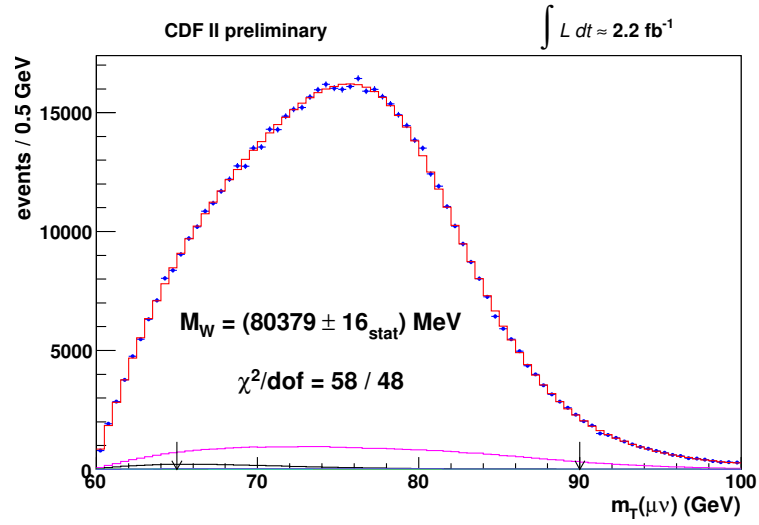
$$m_W = 80387 \pm 19 \text{ MeV}/c^2$$

This is notably more accurate than the original goal set of a  $25 \text{ MeV}/c^2$  uncertainty. This is the single most accurate determination of the  $W$  mass to date, and is more accurate than the current world average (prior to including this result). The central value is consistent with the current world average ( $m_W = 80399 \pm 23 \text{ MeV}/c^2$ ). The combined electron and muon channel uncertainties on  $m_W$  for this new result are given in table 10.3.

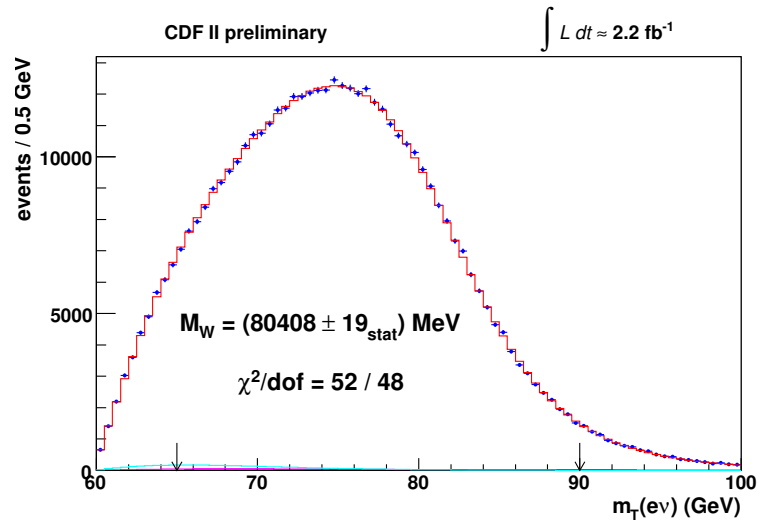
The world average value of  $m_W$  including this new result is:

$$m_W = 80390 \pm 16 \text{ MeV}/c^2$$

This new results reduces the (95% confidence level) upper limit of the indirect SM Higgs mass predicted by electroweak constraints from  $m_H < 161 \text{ GeV}/c^2$  to  $m_H < 145 \text{ GeV}/c^2$ . The  $m_W$  and  $m_t$  constraints on the SM Higgs mass including both this new result and other recent results are presented in fig. 10.4. The updated world average

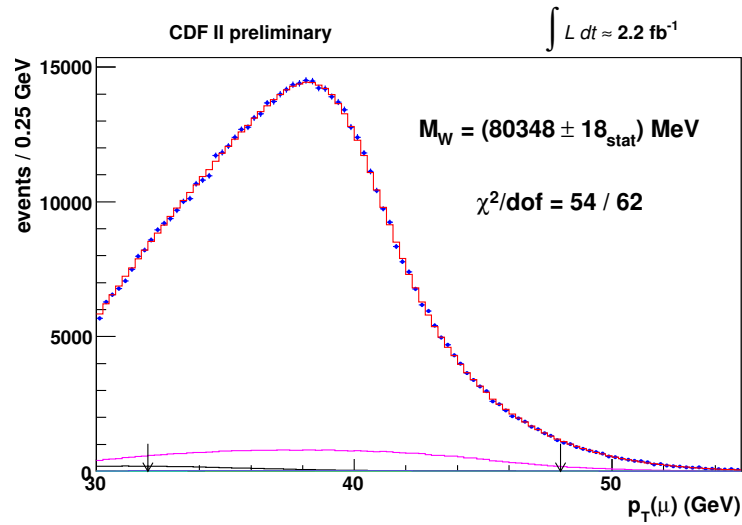


(a)

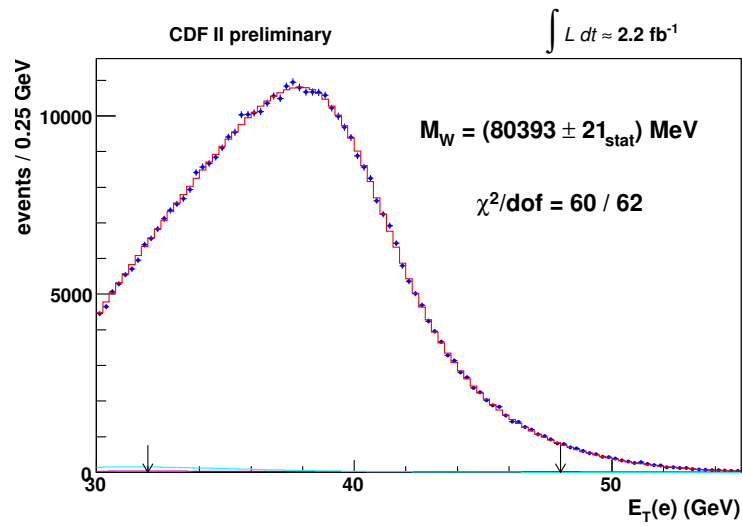


(b)

Figure 10.1: The transverse mass distribution of the best fitting template (red histogram) compared to the equivalent data distribution (blue points) for the muon channel (a) and electron channel (b)  $m_W$  fits using this kinematic variable. The background contributions added to the templates are shown in the same plots, including the  $Z \rightarrow \ell^+\ell^-$  background (magenta histogram) and hadronic jet background (cyan histogram). The fit window is indicated with arrows. Reproduced from reference [88].

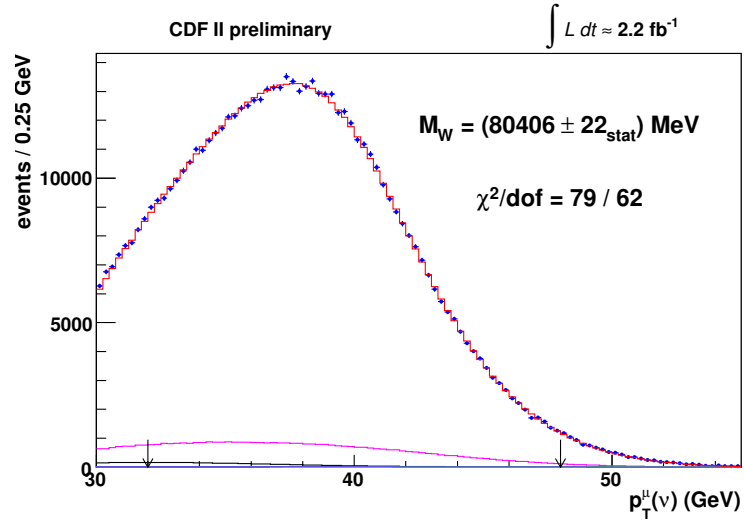


(a)

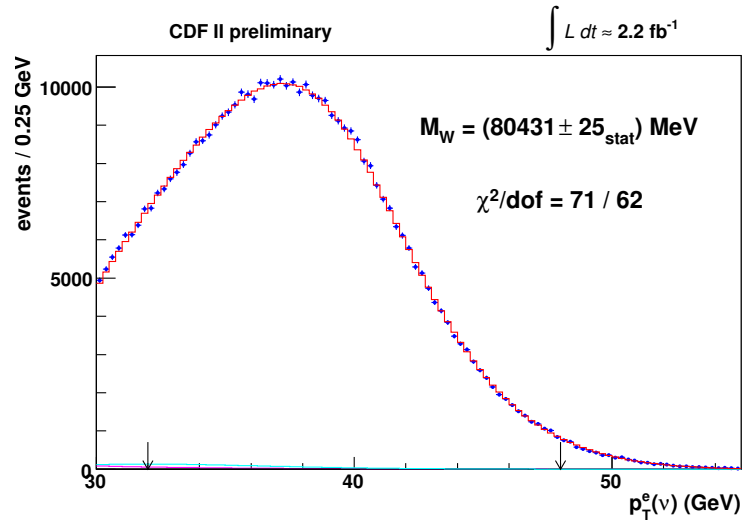


(b)

Figure 10.2: The lepton transverse momentum (transverse energy for electrons) distribution of the best fitting template (red histogram) compared to the equivalent data distribution (blue points) for the muon channel (a) and electron channel (b)  $m_W$  fits using this kinematic variable. The background contributions added to the templates are shown in the same plots, including the  $Z \rightarrow \ell^+\ell^-$  background (magenta histogram) and hadronic jet background (cyan histogram). The fit window is indicated with arrows. Reproduced from reference [88].



(a)



(b)

Figure 10.3: The reconstructed neutrino transverse momentum distribution of the best fitting template (red histogram) compared to the equivalent data distribution (blue points) for the muon channel (a) and electron channel (b)  $m_W$  fits using this kinematic variable. The background contributions added to the templates are shown in the same plots, including the  $Z \rightarrow \ell^+\ell^-$  background (magenta histogram) and hadronic jet background (cyan histogram). The fit window is indicated with arrows. Reproduced from reference [88].

Source	Uncertainty on $m_T$ fit (MeV/ $c^2$ )	Uncertainty on electron $E_T$ fit (MeV/ $c^2$ )	Uncertainty on neutrino $p_T$ fit (MeV/ $c^2$ )
Electron Energy Scale	10	10	10
Electron Energy Resolution	4	4	7
Recoil Energy Scale	5	6	2
Recoil Energy Resolution	7	5	11
$u_{\parallel}$ Efficiency	0	2	3
Lepton Removal	3	0	6
Backgrounds	4	3	4
$p_T(W)$ Model	3	9	4
Parton Distributions	10	9	11
QED Radiation	4	4	4
Total	18	19	22

Table 10.2: Electron channel uncertainties on  $m_W$  fits for the second CDF Run II  $W$  mass analysis. Separate values are given for each of the three kinematic distributions used to fit  $m_W$ : the transverse mass distribution, the electron transverse energy distribution and the reconstructed neutrino transverse momentum distribution. Adapted from reference [88].

Source	Uncertainty (MeV/ $c^2$ )
Lepton Energy Scale and Resolution	7
Recoil Energy Scale and Resolution	6
Lepton Removal	2
Backgrounds	3
$p_T(W)$ Model	5
Parton Distributions	10
QED Radiation	4
$W$ Boson Statistics	12
Total	19

Table 10.3: Combined electron and muon channel uncertainties on  $m_W$  for the second CDF Run II  $W$  mass analysis. Adapted from reference [4].

$m_W$  remains consistent with a SM Higgs boson with a low mass ( $\sim 125 \text{ GeV}/c^2$ ); such a low mass Higgs boson has not yet been excluded by direct searches and may have been hinted at by recent direct searches at the LHC and the Tevatron.

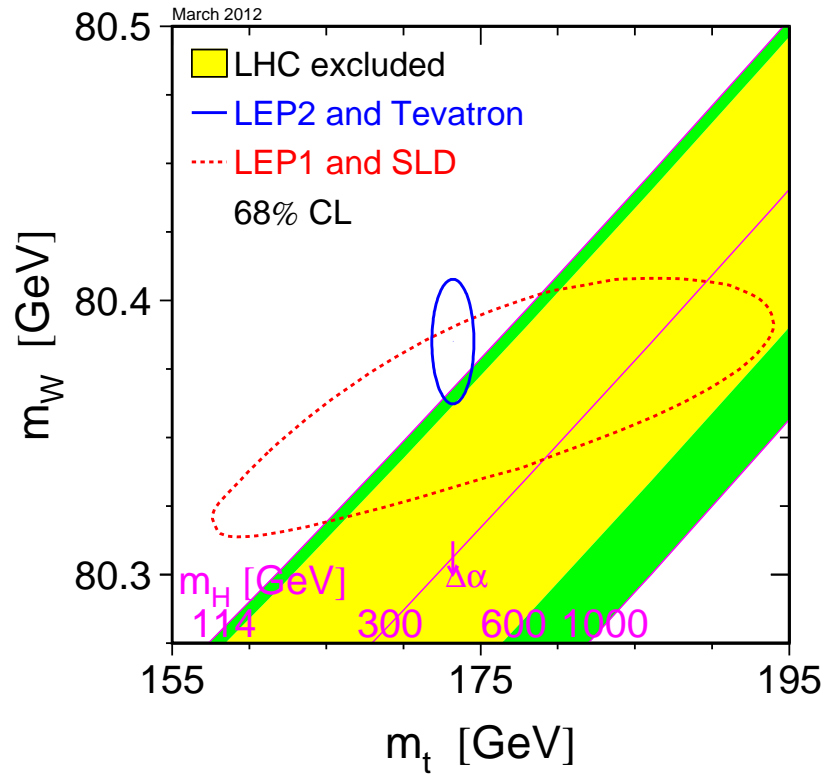


Figure 10.4: Diagram showing the 68% confidence level limit imposed on the SM Higgs boson mass through a combination of  $m_W$  and  $m_t$  measurements by LEP II and the Tevatron (blue, by direct measurements of  $m_W$  and  $m_t$ ), including the new CDF Run II measurement of the  $W$  mass; and LEP I and SLD (red, by indirect measurements of  $m_W$  and  $m_t$ ). The upper edge of the green area is the lower bound on the Higgs boson mass imposed by direct searches at LEP. If the fit were to lay in the region above this bound the Minimal Supersymmetric Standard Model would be favoured. The yellow band within the green area is imposed by direct searches at the Tevatron and LHC. The lower edge of the green area is imposed as an upper bound on the Higgs boson mass, since for Higgs boson masses above  $1 \text{ TeV}/c^2$ , the SM and its formulae do not make sense. This figure is an updated version of fig. 3.4. Reproduced from reference [89].

## Appendix A

# The CDF Run II Electromagnetic Clustering Algorithm

The CDF Run II electromagnetic clustering algorithm for the CEM is as follows:

- All of the CEM towers within each  $\phi$  wedge are placed in an ordered list according to the energy recorded in them starting with the tower with the highest recorded energy.
- The first tower on the list is considered to be the seed tower and the energies recorded in the two adjacent towers in the same  $\phi$  segment are individually added to the energy of the seed tower if they are above 100 MeV. Additionally the ‘two tower energy’ is also recorded for each cluster; this comprises the total energy of the seed tower and (possibly) one adjacent tower. The adjacent tower used in the calculation of the two tower energy must be one that has been added to the cluster; if both adjacent towers have been added to the cluster then the adjacent tower closest to the energy weighted centre of the electromagnetic shower in the seed tower is used.
- The seed tower and the adjacent towers are then removed from the list.
- The process is then repeated using the first element of the reduced list as the new seed tower and only adding the energy of adjacent towers if they are still on the

list and pass the energy cut.

- Repetition of the process continues till no towers remain on the list.

Both for data and simulation, the  $W$  mass analysis defines the energy of a cluster as being the two tower energy of that cluster (in place of the default ‘three tower’ energy).

## Appendix B

# Non Iterative Method for the Evaluation of LPM and Dielectric Variables

First a variable  $s'$  is defined in analogy to the equation for  $s$  (eq. (5.33)) but without the  $\xi(s)$  dependence:

$$s' = \sqrt{\frac{E_{\text{LPM-2}k}}{8E(E-k)}}. \quad (\text{B.1})$$

Then we can redefine  $\xi$  as a function of  $s'^1$ :

$$\xi(s') = 2 \quad (s' \leq \sqrt{2}s_1) \quad (\text{B.2})$$

$$\xi(s') = 1 + h - \frac{0.08(1-h)[1-(1-h)^2]}{\ln \sqrt{2}s_1} \quad (\sqrt{2}s_1 < s' \ll 1) \quad (\text{B.3})$$

$$\xi(s') = 1 \quad (s' \geq 1) \quad (\text{B.4})$$

where  $h = \ln(s')/\ln(\sqrt{2}s_1)$ . This redefinition is valid because  $\xi$  varies slowly with  $s$ .

Then we can calculate  $s$  according to the equation:

$$s = \frac{s'}{\sqrt{\xi(s')}} \quad (\text{B.5})$$

---

<sup>1</sup>The exact meaning of the  $\ll$  notation in the inequality on the second line is obscure, but it appears to imply a non-strict inequality.

A modification is then applied to account for the interaction of the LPM and dielectric suppression mechanisms.  $s'$  is transformed into  $\hat{s}$  thus:

$$\hat{s} = s \cdot \left( 1 + \frac{k_p^2}{k^2} \right) \quad (\text{B.6})$$

Then we recalculate  $\xi$  using eqs. (5.34) to (5.36), substituting  $\hat{s}$  for  $s$ :

$$\xi(\hat{s}) = 2 \quad (\hat{s} < s_1) \quad (\text{B.7})$$

$$\xi(\hat{s}) = 1 + \ln(\hat{s})/\ln(s_1) \quad (s_1 < \hat{s} < 1) \quad (\text{B.8})$$

$$\xi(\hat{s}) = 1 \quad (\hat{s} \geq 1) \quad (\text{B.9})$$

Equations (5.31) and (5.32) can be approximated by the polynomials:

$$\phi(s) = 1 - \exp \left[ -6s(1 + (3 - \pi)s) + s^3 / (0.623 + 0.796s + 0.658s^2) \right] \quad (\text{B.10})$$

$$\psi(s) = 1 - \exp \left[ -4s - 8s^2 / (1 + 3.96s + 4.97s^2 - 0.05s^3 + 7.5s^4) \right] \quad (\text{B.11})$$

$$G(s) = 3\psi(s) - 2\phi(s) \quad (\text{B.12})$$

These approximations are accurate to within 0.15%. Substituting  $\hat{s}$  for  $s$  and neglecting insignificant terms where possible we can obtain simpler polynomials, the form of which depends on the value of  $\hat{s}$ . For  $\hat{s} < 0.1$  the form is<sup>2</sup>:

$$\phi(\hat{s}) = 6\hat{s} - 18.84955592153876\hat{s}^2 + 39.47841760435743\hat{s}^3 - 57.69873135166053\hat{s}^4 \quad (\text{B.13})$$

$$G(\hat{s}) = 37.69911184307752\hat{s}^2 - 236.8705056261446\hat{s}^3 + 807.7822389\hat{s}^4 \quad (\text{B.14})$$

For  $0.1 \leq \hat{s} < 0.415827397755$  no further simplification is possible and eqs. (B.10) to (B.12) should be used directly (substituting  $\hat{s}$  for  $s$ ). For  $0.415827397755 \leq \hat{s} <$

---

<sup>2</sup>All numerical values here are quoted to the same number of significant figures as given in the reference from which they were taken.

1.9516 the form is:

$$\phi(\hat{s}) = 1 - \exp \left[ -6\hat{s} (1 + (3 - \pi) \hat{s}) + \hat{s}^3 / (0.623 + 0.796\hat{s} + 0.658\hat{s}^2) \right] \quad (\text{B.15})$$

$$G(\hat{s}) = \tanh \left( -0.16072300849123999 + 3.7550300067531581\hat{s} - 1.7981383069010097\hat{s}^2 \right. \\ \left. + 0.67282686077812381\hat{s}^3 - 0.1207722909879257\hat{s}^4 \right) \quad (\text{B.16})$$

Note eq. (B.16) is not a simplification of eq. (B.12), but an alternative parameterisation for  $G(s)$ . It is not made clear in the GEANT4 4.9.2 code how this parameterisation is derived. For  $\hat{s} \geq 1.9516$  the form is:

$$\phi(\hat{s}) = 1 - 0.0119048/\hat{s}^4 \quad (\text{B.17})$$

$$G(\hat{s}) = 1 - 0.0230655/\hat{s}^4 \quad (\text{B.18})$$

Finally if  $\xi\phi > 1$  and/or  $\hat{s} > 0.57$  we must apply:

$$\xi = 1/\phi \quad (\text{B.19})$$

This ensures the Bremsstrahlung differential cross section (eq. (5.27)) is not inflated above its non LPM value.

## Appendix C

# Details of the Pair Production

## Sampling and Rejection Procedure

Integrating then sampling directly from the  $x$ -spectrum used by UCL Fast Simulation Pair Production Modification A/B is a time consuming process, and due to the energy dependence of this spectrum must be reprocessed for each individual photon. It is easier to sample from eq. (5.46), which is not energy dependent, hence can be integrated during initialisation just once. Then the ratio:

$$S = \frac{d\sigma_{\text{eq. (5.47)}}(x)}{d\sigma_{\text{eq. (5.46)}}(x)} \quad (\text{C.1})$$

is calculated for the value of  $x$  sampled and the incident photon energy in question. A random number  $r$ , in the range  $0 \leq r < 1$ , is generated using a uniform distribution. If  $r \geq S$  then the value of  $x$  sampled from eq. (5.46) is rejected. If the value is not rejected then the sampled value of  $x$  is used for this interaction. If the value is rejected, the procedure is repeated, sampling a new value of  $x$  and testing for rejection against a new random number. This continues till a value of  $x$  is not rejected, or until 5 sampling and rejection cycles have occurred, at which point a value of  $x$  is sampled from eq. (5.46) and used without testing for rejection. This procedure produces the same spectrum as eq. (5.47), although minor differences could in theory occur because of naively sampling from eq. (5.46) if no  $x$  is found within 5 cycles. However test beam

results show that for energies of interest to us this effect is negligible. The overall normalisation of eq. (5.47) (because we treat total cross section separately, the absolute normalisation of eq. (5.47) is not relevant) must always be set to be less than eq. (5.46) for all  $x$  for the sampling procedure to be valid. We set the normalisation by integrating eq. (5.47) once during initialisation for a 5 GeV incident photon energy in the range  $0.1 < x < 0.9$  and normalising to eq. (5.46) integrated over the same range. We then scale down the normalised eq. (5.47) produced by a ‘safety factor’ of 10/11. Testing shows this normalised eq. (5.47)  $x$ -spectrum is then less than eq. (5.46) for all  $x$  at all incident photon energies.

# Bibliography

- [1] I. Bizjak et al. “ $E/p$ -based Calibration of the CEM for the  $W$  mass measurement using 2.3 fb<sup>-1</sup> dataset”. CDF Note 10620. CDF Collaboration, 2011.
- [2] D. Beecher et al. “Measurement of the  $W$  Boson Mass using 2.2/fb of CDFII data”. CDF Note 10755. CDF Collaboration, 2012.
- [3] I. Bizjak et al. “The Modelling of Bremsstrahlung and Pair Production for the Second CDF Run II  $W$  Mass Measurement”. CDF Note 10495. CDF Collaboration, 2011.
- [4] T. Aaltonen et al. “Precise measurement of the  $W$  boson mass at CDF II”. Accepted for publication by Phys. Rev. Lett. 2012.
- [5] J. Cranshaw et al. “A Calibration Database Schema for CDF II”. CDF Note 5088. CDF Collaboration, 2002.
- [6] D. H. Perkins. *Introduction to High Energy Physics*. 4th ed. Cambridge University Press, 2000.
- [7] M. E. Peskin and D. V. Schroeder. *An Introduction To Quantum Field Theory*. Westview Press, 1995.
- [8] R.K. Ellis, W.J. Stirling, and B.R. Webber. *QCD and collider physics*. Cambridge University Press, 1996.
- [9] S. Weinberg. “A Model of Leptons”. *Phys. Rev. Lett.* **19** (1967), 1264–1266.
- [10] A. Salam. “Weak and Electromagnetic Interactions”. Elementary Particle Theory, Proceedings Of The Nobel Symposium Held 1968 At Lerum, Sweden. 1968, 367–377.

- [11] S. L. Glashow, J. Iliopoulos, and L. Maiani. “Weak Interactions with Lepton-Hadron Symmetry”. *Phys. Rev.* **D2** (1970), 1285–1292.
- [12] P. W. Higgs. “Broken symmetries, massless particles and gauge fields”. *Phys. Lett.* **12** (1964), 132–133.
- [13] P. W. Higgs. “Spontaneous Symmetry Breakdown without Massless Bosons”. *Phys. Rev.* **145** (1966), 1156–1163.
- [14] K. Nakamura et. al. (Particle Data Group). “Review of Particle Physics”. *J. Phys.* **G37** (2010), 075021.
- [15] M. B. Green, J. H. Schwarz, and E. Witten. *Superstring theory*. 2 vols. Cambridge University Press, 1987.
- [16] J. G. Polchinski. *String Theory*. 2 vols. Cambridge University Press, 1998.
- [17] H. Georgi and S. L. Glashow. “Unity of All Elementary-Particle Forces”. *Phys. Rev. Lett.* **32** (1974), 438–441.
- [18] S. Weinberg. *The Quantum Theory of Fields, Volume III: Supersymmetry*. Cambridge University Press, 2000.
- [19] F. T. Cole et al. “A Report On The Design Of The Fermi National Accelerator Laboratory Superconducting Accelerator”. FERMILAB-DESIGN-1979-02. Fermi National Accelerator Laboratory, 1979.
- [20] S.D. Holmes, ed. “Tevatron Run II Handbook”. FERMILAB-TM-2484-1998. Fermi National Accelerator Laboratory. 1998.
- [21] F. Abe et al. “Observation of top quark production in anti-p p collisions”. *Phys. Rev. Lett.* **74** (1995), 2626–2631.
- [22] S. Abachi et al. “Observation of the Top Quark”. *Phys. Rev. Lett.* **74** (1995), 2632–2637.
- [23] “CDF Discoveries And Other Highlights”. CDF Collaboration. 2011. URL: <http://www-cdf.fnal.gov/physics/highlights.html> (visited on Sept. 6, 2011).
- [24] F. Abe et al. “The CDF detector: an overview”. *Nucl. Instrum. Meth.* **A271** (1988), 387–403.

- [25] R. Blair et al. “The CDF-II detector: Technical design report”. FERMILAB-PUB-96-390-E. Fermi National Accelerator Laboratory, 1996.
- [26] A. Sill for the CDF Collaboration. “CDF Run II silicon tracking projects”. *Nucl. Instrum. Meth.* **A447** (2000), 1–8.
- [27] T. Affolder et al. “CDF Central Outer Tracker”. *Nucl. Instrum. Meth.* **A526** (2004), 249–299.
- [28] R. D. Erbacher. “Calorimetry in CDF Run II”. Proceedings 31st International Conference on High Energy Physics (ICHEP 2002), Amsterdam, The Netherlands, 24-31 Jul 2002. FERMILAB-CONF-02/251-E.
- [29] L. Balka et al. “The CDF central electromagnetic calorimeter”. *Nucl. Instrum. Meth.* **A267** (1988), 272–279.
- [30] S. Bertolucci et al. “The CDF central and endwall hadron calorimeter”. *Nucl. Instrum. Meth.* **A267** (1988), 301–314.
- [31] G. Ascoli et al. “CDF central muon detector”. *Nucl. Instrum. Meth.* **A268** (1988), 33–40.
- [32] A. Artikov et al. “Design and construction of new central and forward muon counters for CDF II”. *Nucl. Instrum. Meth.* **A538** (2005), 358–371.
- [33] D. Acosta et al. “The CDF Cherenkov luminosity monitor”. *Nucl. Instrum. Meth.* **A461** (2001), 540–544.
- [34] E. Gerchtein. “Description of the Beam Pipe in the CDF Geometry System for Run II”. CDF Note 5849. CDF Collaboration, 2002.
- [35] L. Chen and A. Connolly. “Material Estimates for SVXII Hybrids and Portcards”. CDF Note 5355. CDF Collaboration, 2000.
- [36] L. Vacavant. “GEANT Description of the CDF Inner Tracker Passive Material”. CDF Note 5825. CDF Collaboration, 2002.
- [37] S. Chuang et al. “Estimate of the amount of material in the CDF tracker using high-Pt electrons”. CDF Note 6573. CDF Collaboration, 2004.

- [38] K. Anikeev et al. “Calibration of Energy Loss and Magnetic Field using  $J/\psi$  Events in Run II”. CDF Note 5958. CDF Collaboration, 2002.
- [39] “Passive Material Simulation Validation Plots”. CDF Internal Webpage. CDF Collaboration. (Visited on May 13, 2011).
- [40] A. Sirlin. “Radiative corrections in the  $SU(2)_L \times U(1)$  theory: A simple renormalization framework”. *Phys. Rev.* **D22** (1980), 971–981.
- [41] T. Aaltonen et al. “First run II measurement of the  $W$  boson mass at the Fermilab Tevatron”. *Phys. Rev.* **D77** (2008), 112001.
- [42] J. Alcaraz et al. “The LEP Electroweak Working Group”. 2011. URL: <http://lepewwg.web.cern.ch/LEPEWWG/> (visited on Sept. 6, 2011).
- [43] R. J. Barlow. *Statistics: A Guide to the Use of Statistical Methods in the Physical Sciences*. Wiley, 1989.
- [44] Y. Zeng et al. “Muon Channel Backgrounds to the  $W$  Boson Mass Measurement”. CDF Note 10655. CDF Collaboration, 2012.
- [45] D. Beecher. “PDF and QCD effects in the precision measurement of the  $W$  boson mass at CDF”. PhD thesis. University College London, 2011.
- [46] C.M. Carloni Calame et al. “Precision electroweak calculation of the charged current Drell-Yan process”. *JHEP* **0612** (2006), 16.
- [47] C.M. Carloni Calame et al. “Precision electroweak calculation of the production of a high transverse-momentum lepton pair at hadron colliders”. *JHEP* **0710** (2007), 109.
- [48] G.A. Ladinsky and C.P. Yuan. “The Nonperturbative regime in QCD resummation for gauge boson production at hadron colliders”. *Phys.Rev.* **D50** (1994), 4239.
- [49] C. Balazs and C.P. Yuan. “Soft gluon effects on lepton pairs at hadron colliders”. *Phys.Rev.* **D56** (1997), 5558–5583.
- [50] F. Landry et al. “Tevatron Run-1  $Z$  boson data and Collins-Soper-Sterman resummation formalism”. *Phys.Rev.* **D67** (2003), 073016.

- [51] J. Pumplin et al. “New generation of parton distributions with uncertainties from global QCD analysis”. *JHEP* **07** (2002), 012.
- [52] K. Rinnert. “A Fast-Access Material Map for the SVX II/ISL Silicon Tracking Volume at CDF 2 ”. CDF Note 5846. CDF Collaboration, 2004.
- [53] V. Bartsch et al. “Direct Measurement of the  $W$  Boson Width”. CDF Note 8668. CDF Collaboration, 2007.
- [54] T. W. Vine. “A direct measurement of the  $W$  decay width”. PhD thesis. University College London, 2008.
- [55] I. Bizjak et al. “COT Momentum Scale for the  $W$  Mass Analysis”. CDF Note 10106. CDF Collaboration, 2010.
- [56] S. A. Malik. “Precision Measurement of the Mass and Width of the  $W$  Boson at CDF”. PhD thesis. University College London, 2009.
- [57] W. E. Burcham and M. Jobes. *Nuclear and Particle Physics*. Prentice Hall, 1995.
- [58] C. Amsler et al. “Review of particle physics”. *Phys. Lett.* **B667** (2008), 1.
- [59] Y.-S. Tsai. “Pair production and Bremsstrahlung of charged leptons”. *Rev. Mod. Phys.* **46** (1974), 815–851.
- [60] P. L. Anthony et al. “Bremsstrahlung suppression due to the Landau-Pomeranchuk-Migdal and dielectric effects in a variety of materials”. *Phys. Rev.* **D56** (1997), 1373–1390.
- [61] A. B. Migdal. “Bremsstrahlung and Pair Production in Condensed Media at High Energies”. *Phys. Rev.* **103** (1956), 1811–1820.
- [62] “GEANT4 4.9.1 Physics Reference Manual”. Available at: <http://geant4.cern.ch/UserDocumentation/UsersGuides/PhysicsReferenceManual/BackupVersions/V9.1/fo/PhysicsReferenceManual.pdf>. 2007. (Visited on Sept. 6, 2011).
- [63] S. M. Seltzer and M. J. Berger. “Bremsstrahlung spectra from electron interactions with screened atomic nuclei and orbital electrons”. *Nucl. Instrum. Meth.* **B12** (1985), 95–134.

- [64] H. W. Koch and J. W. Motz. “Bremsstrahlung Cross-Section Formulas and Related Data”. *Rev. Mod. Phys.* **31** (1959), 920–955.
- [65] J. C. Butcher and H. Messel. “Electron number distribution in electron-photon showers in air and aluminium absorbers”. *Nucl. Phys.* **20** (1960), 15–128.
- [66] V. M. Galitsky and I. I. Gurevich. *Il Nuovo Cimento* **32** (1964), 1820.
- [67] “GEANT4 4.9.0 Source Code”. Available at: <http://geant4www.triumf.ca/lxr/>. (Visited on Sept. 6, 2011).
- [68] “GEANT4 4.9.2 Physics Reference Manual”. Available at: <http://geant4.web.cern.ch/geant4/UserDocumentation/UsersGuides/PhysicsReferenceManual/BackupVersions/V9.2.Rev01/fo/PhysicsReferenceManual.pdf>. 2009. (Visited on Sept. 6, 2011).
- [69] T. Stanev et al. “Development of ultrahigh-energy electromagnetic cascades in water and lead including the Landau-Pomeranchuk-Migdal effect”. *Phys. Rev.* **D25** (1982), 1291–1304.
- [70] S. Klein. “Suppression of Bremsstrahlung and pair production due to environmental factors”. *Rev. Mod. Phys.* **71** (1999), 1501–1538.
- [71] M. L. Ter-Mikaelian. *High-energy Electromagnetic Processes in Condensed Media*. Wiley, 1972.
- [72] S. T. Perkins, D. E. Cullen, and S. M. Seltzer. “Evaluated Electron Data Library”. Available at: <http://www-nds.iaea.org/epdl97/>. (Visited on Sept. 6, 2011).
- [73] S. T. Perkins, D. E. Cullen, and S. M. Seltzer. “Tables and graphs of electron-interaction cross sections from 10 eV to 100 GeV derived from the LLNL Evaluated Electron Data Library (EEDL),  $Z = 1-100$ ”. UCRL-50400-Vol.31. Lawrence Livermore National Lab, 1991.
- [74] H. Bethe and W. Heitler. “On the Stopping of Fast Particles and on the Creation of Positive Electrons”. *Royal Society of London Proceedings Series A* **146** (1934), 83–112.

- [75] J. A. Wheeler and W. E. Lamb. “Influence of Atomic Electrons on Radiation and Pair Production”. *Phys. Rev.* **55** (1939), 858–862.
- [76] J. A. Wheeler and W. E. Lamb. “Influence of Atomic Electrons on Radiation and Pair Production”. *Phys. Rev.* **101** (1956), 1836.
- [77] S. D. Drell and J. D. Walecka. “Electrodynamic Processes with Nuclear Targets”. *Ann. Phys.* **28** (1964), 18–33.
- [78] J. W. Motz, H. A. Olsen, and H. W. Koch. “Pair Production by Photons”. *Rev. Mod. Phys.* **41** (1969), 581–639.
- [79] T. Aaltonen et al. “A Direct measurement of the W boson width in  $p\bar{p}$  collisions at  $\sqrt{s} = 1.96$  TeV”. *Phys. Rev. Lett.* **100** (2008), 071801.
- [80] S. Agostinelli et al. “G4: a simulation toolkit”. *Nucl. Instrum. Meth.* **A506** (2003), 250–303.
- [81] A. Schällicke et al. “Improved Description of Bremsstrahlung for High-Energy Electrons in Geant4”. *IEEE Nuclear Science Symposium Conference Record*. N37-1. 2008, 2788–2791.
- [82] P. L. Anthony et al. “An Accurate Measurement of the Landau-Pomeranchuk-Migdal Effect”. *Phys. Rev. Lett.* **75** (1995), 1949–1952.
- [83] P. L. Anthony et al. “Measurement of Dielectric Suppression of Bremsstrahlung”. *Phys. Rev. Lett.* **76** (1996), 3550–3553.
- [84] M. J. Berger et al. “XCOM: Photon Cross Sections Database”. Available at: <http://physics.nist.gov/PhysRefData/Xcom/Text/XCOM.html>. (Visited on Sept. 6, 2011).
- [85] C. Hays, A. V. Kotwal, and R. Shekhar. “A Study of Non-Linear Response in the Central Electromagnetic Calorimeter using GEANT4”. CDF Note 10181. CDF Collaboration, 2010.
- [86] C. Hays, A. Kotwal, and R. Shekhar. “A Model based on GEANT4 for Electron Response in the Central Electromagnetic Calorimeter”. CDF Note 10135. CDF Collaboration, 2010.

- [87] C. Hays, A. Kotwal, and R. Shekhar. “A Model based on GEANT4 for Photon Response in the Central Electromagnetic Calorimeter”. CDF Note 10156. CDF Collaboration, 2010.
- [88] “Measurement of the W Boson Mass with 2.2/fb of Data at CDF II”. CDF Collaboration. 2012. URL: <http://www-cdf.fnal.gov/physics/ewk/2012/wmass/> (visited on May 2, 2012).
- [89] J. Alcaraz et al. “The LEP Electroweak Working Group”. 2012. URL: <http://lepewwg.web.cern.ch/LEPEWWG/> (visited on Mar. 20, 2012).